Complex Dynamic Source Modeling of Large Earthquakes Constrained by Bayesian Inversion and Observations

Taufiqurrahman

München 2023

Complex Dynamic Source Modeling of Large Earthquakes Constrained by Bayesian Inversion and Observations

Taufiqurrahman

Dissertation zur Erlangung des
Doktorgrades an der Fakultät für Geowissenschaften
der Ludwig–Maximilians–Universität
München

vorgelegt von
Taufiqurrahman

München, den 05.07.2023

Erstgutachter: Prof. Dr. Heiner Igel
Zweitgutachter: Prof. Dr. Alice-Agnes Gabriel
Tag der mündlichen Prüfung: 20.12.2023

Summary

Dynamic rupture models provide valuable insights into earthquake source dynamics, particularly in cases where direct observations are scarce or non-existent. These multi-physics simulations combine earthquake rupture along a fault, governed by frictional constitutive laws, with seismic wave propagation described by the linear elastic wave equation. Numerical models must incorporate realistic media and complex source geometry to represent the earthquake process accurately. This dissertation expands the framework within the dynamic rupture software SeisSol to build complex dynamic source models to shed light on fault friction, rheology, and the dynamics of earthquakes based on the outcomes of the Bayesian dynamic source inversions.

The first study aims to improve the understanding and assessment of seismic hazards by integrating advancements in physics-based earthquake simulations, high-performance computing, and data-driven earthquake imaging. The study employs 3D dynamic rupture modeling and broadband ground motion synthetics to analyze the 2016 Mw 6.2 Amatrice, Italy earthquake. It uses a smooth, best-fitting model from Bayesian dynamic rupture source inversion of strong-motion data, augmented with fractal fault roughness, frictional heterogeneities, viscoelastic attenuation, and topography, to simulate the ground motion observations.

The second study presents data-assimilated 3D dynamic rupture models of California's most significant earthquakes in over 20 years: the Mw 6.4 Searles Valley and Mw 7.1 Ridgecrest sequence. The researchers use supercomputing to find the link between the two earthquakes and explain various datasets with earthquake physics, elucidating the mechanics of complex fault systems and earthquake sequences.

The third study uses 3D simulations of dynamic rupture and seismic wave propagation to derive families of dynamic models based on a detailed kinematic rupture model from the Mw 6.5 Norcia earthquake on October 30th, 2016. The study confirms the usefulness of these kinematic models and categorizes dynamic rupture scenarios into families that are consistent with seismic and geodetic data, as well as geological requirements.

By reconciling dense earthquake recordings, three-dimensional regional structures, and stress models, the research demonstrates the efficacy of a joint physics-based and data-driven approach in determining the mechanics of complex fault systems and earthquake sequences. This comprehensive approach combines advancements in physics-based earthquake simulations and data-driven earthquake imaging to understand complex earthquake phenomena better and assess seismic hazards, with the potential for a transformative impact on future geohazard mitigation.

Contents

List of Figures

List of Tables

Chapter 1

Introduction

Earthquakes, which are prominent manifestations of faulting due to plate tectonics, have seen considerable advancements in our understanding of the physical processes governing their occurrence and rupture propagation over the past few decades. Seismologists are mainly focused on dynamic fault weakening during seismic rupture initiation and propagation, a fundamental aspect of the field. Various approaches, such as frictional lab experiments, dynamic earthquake physics modeling, and interpreting observed seismograms through forward and inverse modeling, all contribute to comprehending frictional failure across fault zones that generate seismic waves. Current research primarily aims to enhance our understanding of the latter two areas.

Large earthquakes exhibit complexities on both spatial and temporal scales, with evidence of intricate rupture propagation from real earthquake studies and laboratory experiments. These complexities involve delays at barriers, fault bends, or branched faults. Both types of studies confirm such complexities. Moreover, under favorable conditions, ruptures can transition from sub-shear to super-shear. Dynamic source simulations have proven effective in modeling earthquake rupture temporal and geometrical complexities. These complexities may arise from frictional and stress heterogeneity across the fault, surface reflections, or complex friction laws. Phenomena such as slip reactivation, rupture jumps, changes in the rupture propagation direction, and rupture delays exemplify these complexities.

Computational performance on the petaflop scale or beyond is essential to generate dynamically consistent predictions of strong ground-motion excitation in earthquake scenarios. Dynamic source analysis cannot be the starting point; constraints on rupture behavior from slip inversions and quantifying uncertain modeling parameters are crucial.

Practical earthquake source analysis involves iterative steps that progressively refine the source rupture process image (e.g., [69]). Typically, investigations begin with point-source interpretations like earthquake location and centroid moment tensor inversion. The former uses high-frequency data to determine rupture nucleation location, while the latter offers low-frequency point-source approximation for overall slip timing, location, and mechanism.

Slip inversion helps infer additional information about rupture propagation and slip spatial distribution. The low-frequency approximation is enriched by a high-frequency

component, either synthetic or empirical, allowing broadband strong ground motion modeling to constrain further specific earthquake features (e.g., [1]). Ultimately, dynamic rupture earthquake scenarios can be developed based on observational constraints. Each stage carries some uncertainty, which must be considered when interpreting the rupture process.

1.1 Earthquake dynamic rupture modeling

Dynamic rupture modeling links small-scale rock friction lab experiments and large-scale earthquake observations, enhancing our understanding of earthquake nucleation, propagation, and healing. Recent studies on specific, well-documented earthquakes have significantly improved our knowledge of rupture processes due to advancements in the accuracy of models that simulate rupture dynamics. However, understanding earthquake source processes remains challenging due to the intricate nature of geological settings, numerous factors influencing recorded ground motions, inaccessibility of in-situ observations from seismogenic zones several kilometers deep, and the limited occurrence of large, intensely radiating earthquakes. Research has shown that earthquake source processes are highly dependent on factors such as fault geometry, frictional constitutive relationships, off-fault rheology, fault strength, and stress state (e.g., [63] [161] [183] [64]).

Constructing physics-based earthquake source models consistent with rupture dynamics can be approached in several ways. The dynamic inversion method optimizes the initial stress and frictional parameter distribution along the fault to best fit observed data. However, due to computational challenges, such inversions are difficult to achieve, with only a few studies conducted so far (e.g., [169] [61]). Often, simplistic parameterization is used, such as models with only one or two patches featuring desired dynamic parameters (e.g., [223] [196]). A more general approach involves building dynamic models from inferred kinematic source models (e.g., [168] [159] [102]) or analyzing stresses translated from earthquake kinematic models in terms of the governing friction law (e.g., [26] [84] [23]). This information is then used to constrain a detailed dynamic model of the studied earthquake.

The open-source software package SeisSol (`http://www.seissol.org/`) enables realistic source physics simulations of three-dimensional seismic wave propagation, accommodating complex fault setups, fault roughness, modern friction laws, and off-fault plasticity in elastic, viscoelastic, and viscoplastic media. Based on the ADER-DG method [49], SeisSol ensures high-order accuracy in space and time, allowing precise modeling of seismic waves traveling long distances with minimal dispersion errors. It features unstructured tetrahedral meshing for complex fault zone geometry, Earth structure, rapid mesh generation, and efficient, high-performance computing (e.g., [165] [246] [224, 226]).

Large-scale dynamic ruptures forward scenarios, such as the 1992 Landers, the 1994 Northridge, the potential Husavik-Flatey-Fault system, the 2004 Sumatra-Andaman, the 2016 Kaikoura, and the 2018 Palu earthquakes, have been studied, including synthetic ground shaking in the engineering frequency band (0-10 Hz). These studies have pro-

vided insights into fault mechanics, demonstrating that considering geometrical complexity, realistic fault properties, and velocity models impacts earthquake source dynamics and synthetic ground shaking.

1.2 Bayesian inference in source inversions

Earthquake studies are becoming increasingly data-rich, but there still needs to be more models that accurately capture the full spatiotemporal scales of fault movements. Bayesian approaches, which assimilate diverse observational data to constrain model parameters, have been applied to kinematic slip inversions (e.g., [198] [152] [52]). These highly nonlinear methods, called dynamic earthquake source inversions, require fine-grained predictive models to fit data containing specific information about the faulting process, such as observed strong motion waveforms.

Dynamic source inversions focus on iterative sampling the spatial distribution of starting stress and frictional parameters, collectively known as the model's dynamic parameters, to minimize the mismatch between synthetic and actual seismograms. However, due to the significant computational workload, there have only been a few attempts made so far [39] [61] [169]. Recently, Gallovic et al. [71, 72] presented a novel method to constrain fault friction parameters and stress conditions governing earthquake rupture within a Bayesian framework, successfully applying it to the 2016 Mw 6.2 earthquake in Amatrice, Italy. This method combines simple, efficient finite-difference dynamic rupture simulations with a parallel tempering Monte Carlo process to sample the posterior probability density function, requiring hundreds of thousands to millions of dynamic simulations. Although the method quantifies uncertainties as a primary advantage, it has limitations, including restrictions to near-vertical, planar faults, the absence of topography, and structural fault complexity.

Dynamic source inversions are performed in a relatively low-frequency band ($<$0.5Hz) where detailed crustal models are not required. A broader frequency range ($<$ 10Hz) should be considered for seismic hazard and earthquake engineering applications. Preliminary extensions to broadband modeling ($\sim$5Hz, [72] [244]) appear promising. However, they suggest depletion of high-frequency radiation in the source, even for stations with weak site effects. As scattering of seismic waves in complex media elongates waveforms but does not increase high-frequency radiation [105, 104], the source itself must generate sufficient high-frequency energy. Dynamic rupture simulations resolving small-scale geometric fault complexities reveal the importance of fault surface roughness described by self-similar power-law random fields on both rupture propagation and radiated waves (e.g., [51] [207]). The complexity of dynamic model parameter distribution is crucial for explaining mid-to-high frequency content in observed strong ground motions (e.g., [231]).

Increasing the earthquake source's high-frequency content is one of many necessary elements to explain high-frequency ground motions accurately. Realistic 3D media should also be considered, including random scattering, topography, and site effects. Furthermore, Withers et al. ([245]) showed that increasing the complexity of the velocity model (3D features with random scattering) reduces ground motion variability due to decreased

wavefield coherency. Including realistic 3D models' effects in kinematic slip inversion prevents spurious artifacts in rupture evolution ([67]). The effects of 3D models in dynamic source inversion are yet to be explored.

1.3 Main objectives and outline

Our research objective is to foster the understanding of geophysical processes controlling earthquake rupture propagation and hazard mitigation in a data-driven manner, utilizing recent developments in high-performance computing and Bayesian frameworks. This work contributes to developing the community-driven open-source software package SeisSol and the improved understanding of parameters and conditions influencing rupture dynamics, ground motions, and displacements in realistic multi-physics simulations.

Chapter 2 presents a study on the 2016 Mw 6.2 Amatrice, Italy earthquake. A new approach is proposed to simulate data-fused broadband ground motion synthetics using 3D dynamic rupture modeling. It augments a smooth, best-fitting model from Bayesian dynamic rupture source inversion of strong motion data with fractal fault roughness, frictional heterogeneities, viscoelastic attenuation, and topography. The study demonstrates that 3D data-constrained fully dynamic rupture synthetics show good agreement with observed ground-motion metrics up to 5 Hz, contributing to non-ergodic, physics-based seismic hazard assessment.

Chapter 3 presents data-assimilated three-dimensional dynamic rupture models of California's most significant earthquakes in over 20 years: the Mw 6.4 Searles Valley and Mw 7.1 Ridgecrest sequence. The models use supercomputing to find the link between the two earthquakes and explain strong motion, teleseismic, field mapping, high-rate global positioning system, and space geodetic datasets with earthquake physics. The study shows that a joint physics-based and data-driven approach can be used to determine the mechanics of complex fault systems and earthquake sequences, which will have a transformative impact on future geohazard mitigation.

Chapter 4 presents a study of the 2016 Central Italy earthquake sequence, characterized by significant rupture complexity across multiple faults in an extensional tectonic regime. It uses 3D dynamic rupture and seismic wave propagation simulations to constrain families of spontaneous dynamic models informed by a high-resolution kinematic rupture model of the Mw 6.5 October 30th, 2016, Norcia earthquake. The study validates the viability of kinematic models and classifies spontaneous dynamic rupture scenarios that match seismic and geodetic observations and geological constraints.

Chapter 2, 3, and 4 have been published as:

- Taufiqurrahman, T., Gabriel, A.-A., Ulrich, T., Valentová, L., & Gallovič, F. (2022). Broadband dynamic rupture modeling with fractal fault roughness, frictional heterogeneity, viscoelasticity and topography: The 2016 Mw 6.2 Amatrice, Italy earthquake. *Geophysical Research Letters*, 49, e2022GL098872. `https://doi.org/10.1029/2022GL098872`

- Taufiqurrahman, T., Gabriel, Li, D., A.-A., Ulrich, T., Li, B., Carena, S., Verdecchia, A., & Gallovič, F. (2023). Dynamics, interactions, and delays of the 2019 Ridgecrest rupture sequence. *Nature*, 618, 308–315, `https://doi.org/10.1038/s41586-023-05985-x`

- Tinti, E., Casarotti, E., Ulrich, T., Taufiqurrahman, T., Li, D., & Gabriel, A.-A. (2021). Constraining families of dynamic models using geological, geodetic and strong ground motion data: The Mw 6.5, October 30th, 2016, Norcia earthquake, Italy. *Earth and Planetary Science Letters*, 576, 117237, `https://doi.org/10.1016/j.epsl.2021.117237`

Chapter 2

Broadband Dynamic Rupture Modeling with Fractal Fault Roughness, Frictional Heterogeneity, Viscoelasticity and Topography: The 2016 Mw 6.2 Amatrice, Italy Earthquake

2.1 Abstract

Advances in physics-based earthquake simulations, utilizing high-performance computing, have been exploited to better understand the generation and characteristics of the high-frequency seismic wavefield. However, direct comparison to ground motion observations of a specific earthquake is challenging. We propose a new approach to simulate data-fused broadband ground motion synthetics using 3D dynamic rupture modeling of the 2016 Mw 6.2 Amatrice, Italy earthquake. We augment a smooth, best-fitting model from Bayesian dynamic rupture source inversion of strong-motion data (<1 Hz) with fractal fault roughness, frictional heterogeneities, viscoelastic attenuation, and topography. The required consistency to match long periods allows us to quantify the role of small-scale dynamic source heterogeneities, such as the 3D roughness drag, from observational broadband seismic waveforms. We demonstrate that 3D data-constrained fully dynamic rupture synthetics show good agreement with various observed ground-motion metrics up to ∼5 Hz and are an important avenue toward non-ergodic, physics-based seismic hazard assessment.

2.2 Introduction

Simulations of broadband (>1 Hz) ground motions are of great importance to seismologists and the earthquake engineering community. Even though we often lack detailed knowledge of the subsurface and earthquake source processes at small scales, it is essential to understand the generation and characteristics of the high-frequency seismic wavefield coinciding with most buildings' resonance frequencies. Broadband ground motions have been successfully simulated using hybrid techniques (e.g., [81]; [142]; [209]) that combine low-frequency

deterministic ground motion synthetics with stochastically generated high-frequency components. While classical kinematic approaches are tremendously useful specifically for seismic hazard assessment and engineering, they do not guarantee a physically consistent source description and do not permit data-driven inferences on the fundamentals of how faults slip co-seismically, specifically on smaller scales ([26]; [143]; [217]). Dynamic rupture models provide mechanically viable correlations among macroscopic earthquake rupture parameters, such as slip rate and rupture time, rooted in laboratory-derived friction laws and elastodynamics ([82]; [199]; [202]). Nevertheless, mainly due to the associated computational demands at high frequencies, fully dynamic rupture scenarios have rarely been validated against real seismograms in a broad frequency range.

Hybrid synthetic waveforms lack deterministic information at higher frequencies and pose challenges in the realistic parameterization of wave propagation and earthquake rupture. Indeed, high-frequency radiation may arise, for instance, from acceleration and deceleration of the rupture front [139] caused by fault kinks, segmentation, or roughness (e.g., [27]; [207]), frictional or stress heterogeneities (e.g., [186]; [231]) or from off-fault damage (e.g., [158]; [251]). Additionally, the radiated wavefield is scattered by complex topography and structural heterogeneities (e.g., [92]; [105]; [171]; [212]).

Recent advances in high-performance computing allow deterministic 3D regional-scale broadband simulations to resolve frequencies up to 10 Hz [97, 171, 187, 199]. Such simulations often assume a kinematic, thus predefined, finite earthquake source representation. In distinction, dynamic rupture models offer physically self-consistent descriptions of the earthquake rupture process. Generic dynamic rupture simulations across rough faults (both in 2D or 3D [25, 27, 51, 207, 244]) are characterized by highly complex rupture processes translating into ground motion synthetics that can match empirical ground-motion prediction equations (GMPEs).

The 24 August 2016, Mw 6.2 Amatrice earthquake [34, 148] is the first in the Amatrice-Visso-Norcia earthquake sequence in the Central-Northern Apennine system of NW-SE aligned normal faults. It was the sequence's most destructive event, causing extensive damage to surrounding buildings and infrastructure [149]. The earthquake was recorded by a remarkably dense network of strong ground motion instruments, including 20 near-source stations within a radius of 50 km from the earthquake epicenter (Figure 2.1, Table 2.1 in 2.9). The two closest stations, in Amatrice (AMT) and Norcia (NRC), are located only a few kilometers away from the fault.

The source process of the Amatrice event has been imaged using seismic data [172, 218], geodetic data (e.g., [31, 237]), or both [35, 116], suggesting pronounced source heterogeneities. However, kinematic finite-fault inversions are challenged by inherent non-uniqueness [70, 143, 182, 208, 215]. Dynamic source inversions recovering friction parameters and the initial state of fault stress offer a data-driven source description compatible with earthquake physics (e.g., [169]) but require a sufficiently simple dynamic rupture model to reduce the computational cost of the forward problem. A Bayesian dynamic inversion using the Parallel Tempering Monte Carlo algorithm [71, 197] was applied to the Amatrice earthquake, utilizing band-pass filtered (between 0.05 and 0.5–1 Hz) strong ground motion data by Gallovič et al. [72]. Assuming a 1D medium with planar topog-

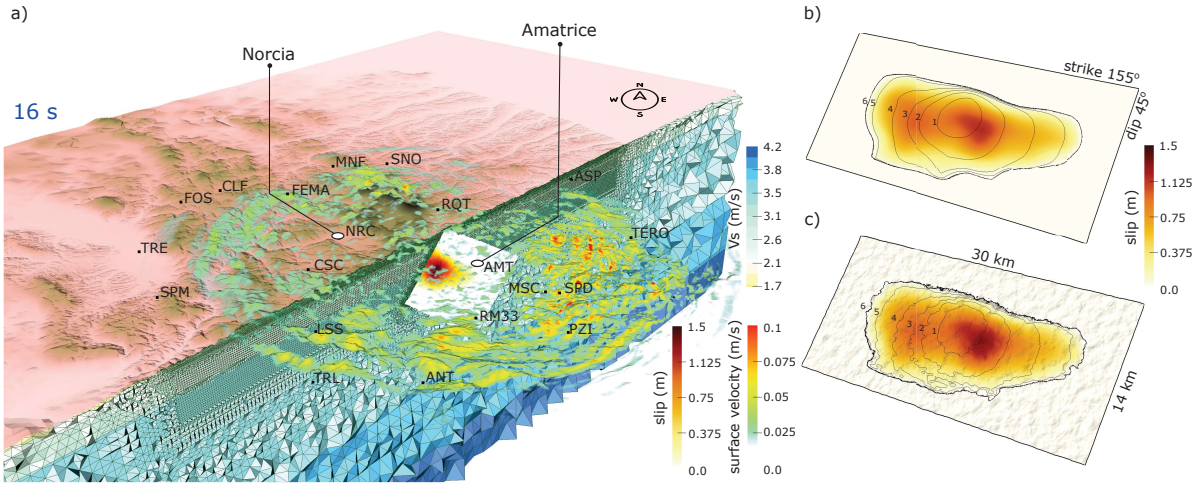

Figure 2.1: (a) Three-dimensional dynamic rupture model setup of the 2016 Mw 6.2 Amatrice, Central Italy, earthquake. Snapshot of the absolute surface velocity at a simulation time of 16 s. The model is discretized by an unstructured tetrahedral mesh refined in the vicinity of the fault and the high-resolution topography. Twenty strong-motion stations used in this study are marked in black (see Table 2.1 in 2.9). Mesh elements are colored by shear wave velocity (V_s). (b, c) Fault slip for the smooth Bayesian dynamic source inversion reference model (b) and the broadband dynamic rupture model (c). Black curves represent rupture front contours every 1 s.

raphy, the best-fitting model was used to predict ground motions up to higher frequencies than considered in the inversion (up to ∼5 Hz). Yet this approach poorly matched the high-frequency content, presumably most sensitive to unresolvable small-scale features of the rupture process.

We propose a new approach to simulate data-fused broadband ground motion synthetics using 3D dynamic rupture modeling. Our starting point is the best-fitting model from the Bayesian dynamic source inversion of the Amatrice earthquake (Figure 2.1b, hereafter named "reference model"). We self-consistently augment this smooth reference model by adding fault roughness, small-scale frictional heterogeneities, viscoelastic attenuation, and topography, yielding realistic high-frequency radiation without disrupting the large-scale characteristics of the reference model. The synthetic near-field ground motions show good agreement with various observed ground-motion metrics up to frequencies of ∼5 Hz.

2.3 Ingredients for broadband dynamic rupture modeling

While a wide range of mechanisms may enhance high-frequency radiation, the here selected processes have been proposed to be first-order relevant [25, 56, 171, 207, 212, 244] and are reasonably well constrained beyond the case of the Amatrice earthquake. For example, [27] find that fault roughness, and not material heterogeneity, dominates the dynamic rup-

ture process. [138] discuss that large-scale topography can have locally stronger effects on modeled ground motions than 3D subsurface structure. Contrary to the latter, the topography is typically well-constrained by observations and readily available in high resolution. Viscoelastic attenuation is important to capture the decay of seismic energy with increasing propagation distance [100, 246]. Computational advances [97, 180] now allow us to show in fully dynamic rupture models of a real earthquake that fault roughness, frictional heterogeneity, topography, and attenuation have complementary effects. Dynamic rupture source complexity enhances high-frequency generation, while topography effects elongate the synthetic coda signals, together yielding more realistic ground motions.

We build our model upon Bayesian dynamic rupture inversion of the 2016 Amatrice earthquake following the approach of Gallovič et al. [71] with the improved forward solver FD3D-TSN [180], which was verified in a suite of dynamic rupture benchmarks [89]. The inversion is performed for a 30 km long and 14 km wide planar fault governed by a slip-weakening friction law [101, 162]. The dynamic rupture slip rate functions along the fault are convolved with pre-calculated Green's functions representing impulse responses of the medium. In this step, the fault is dipping at 45°, embedded in the 1D velocity structure of [1] with a flat free surface. The dynamic models are characterized by three spatially heterogeneous parameters: (a) the initial shear stress along dip τ_i, (b) the friction drop, $\mu_s - \mu_d$, with μ_s and μ_d the static and dynamic friction coefficient respectively, and (c) the slip-weakening distance D_c. Yielding occurs when the shear stress τ reaches the fault strength $\tau_s = \mu_s \sigma_n$, where σ_n is assumed as linearly depth-dependent normal stress with a gradient of 8.52 MPa/km and a minimum value of 0.1 MPa. The initial along-strike shear stress $\tau_{strike0}$ is assumed to be zero. The dynamic friction coefficient μ_d is fixed to 0.4, and frictional cohesion of 0.5 MPa is assumed everywhere on the fault. The best-fitting model from the Bayesian inversion represents the reference model of this study. We then perform high-resolution enhanced 3D dynamic rupture simulations using the open-source software package SeisSol (`https://github.com/SeisSol/SeisSol`), resolving seismic wavefield up to 5 Hz (locally up to 10 Hz) within 50 km distance of the fault using an unstructured, statically adaptive mesh consisting of 80 million tetrahedral elements (Figure 2.1a, Text 2.9.1 in 2.9).

2.3.1 Fault roughness

The reference model's dynamic parameters are first bilinearly interpolated from their 1.75 km along-dip and 2.3 km along-strike reference resolution into a denser 25 m sampled grid (see Figure 2.2, column a). Next, we adapt the fault morphology to adhere to a band-limited self-similar (Hurst exponent $H = 1$) fractal surface. The amplitude-to-wavelength ratio α of natural faults ranges between 10^{-4} and 10^{-2} ([178]), and we here use $\alpha = 10^{-2}$ allowing direct comparability to earlier studies ([25, 56, 207, 244]). This nearly upper limit of roughness may be related to the presumably immature fault system hosting the Amatrice earthquake [172], as suggested from regional slow long-term slip rates [65], the young age of post-orogenic extension in the Apennines and the decoupling effect of multiple décollement levels and strong rheological contrasts (e.g., [13, 221]).

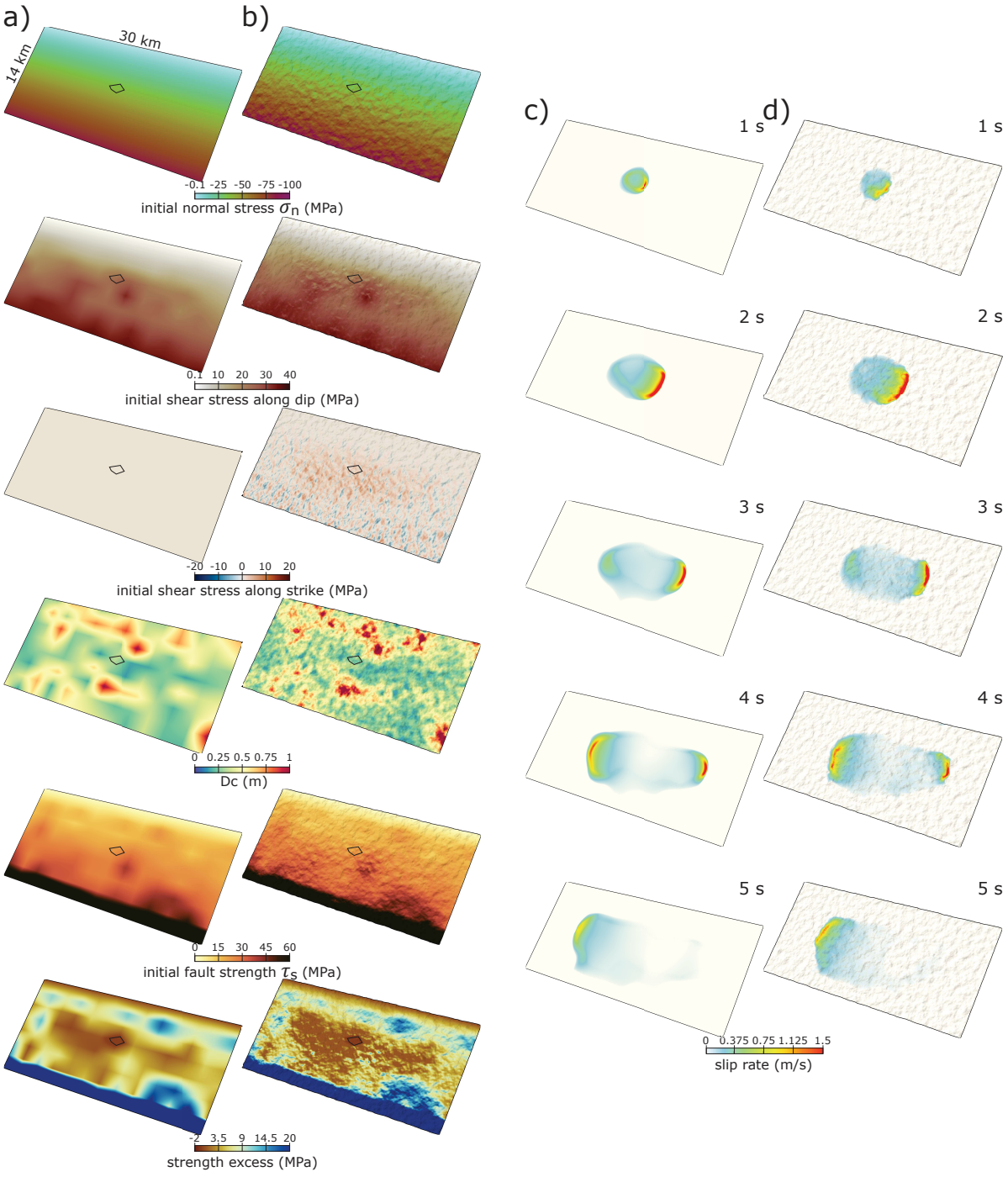

Figure 2.2: (a, b) Comparison of dynamic parameters used in the reference model (a), and the broadband rough fault model (b). Fractal heterogeneity is also added to the distribution of slip weakening distance (D_c). The black contour marks the nucleating negative strength excess area. (c, d) Dynamic rupture propagation in the reference (c) and broadband (d) rough fault models of the Amatrice earthquake. Snapshots of the absolute fault slip rates illustrate the similar space-time evolution in both models.

The fractal surface wavelengths are band-limited between λ_{min} and λ_{max}. Choosing $\lambda_{min} = 200$ m balances resolution requirements and computational cost for our setup and aligns with previous 3D fault roughness studies [57, 207]. Our choice of $\lambda_{max} = 2$ km is motivated by the ~ 2 km spatial resolution of the dynamic parameters in the reference model.

2.3.2 3D roughness drag and heterogeneous initial stresses

Shear and normal stresses are dynamically perturbed by fault roughness during rupture propagation. The general scaling of the 'roughness drag' [51], an additional shear resistance to slip, was derived for a 1D rough fault in a 2D quasi-static boundary perturbation analysis by Fang & Dunham [56] as

$$\tau_{\text{drag}}^{2D} = 8\pi^3\alpha^2 G^*\Delta(1/\lambda_{\text{min}} - 1/\lambda_{\text{max}}) \approx 8\pi^3\alpha^2 G^*\Delta/\lambda_{\text{min}} \tag{2.1}$$

with Δ being the fault slip, λ_{min} the minimum roughness wavelength, and $G^* = G/(1-\nu)$, where G and ν are shear modulus and Poisson's ratio, respectively, and $\lambda_{\text{max}} \gg \lambda_{\text{min}}$.

To preserve the overall characteristics of the reference scenario while incorporating fault roughness, we must compensate the roughness drag in the initial loading by increasing the reference initial shear tractions as $\tau_{\text{dip}} = \tau_{\text{dip0}} + \tau_{\text{drag}}^{3D}$ and $\tau_{\text{strike}} = \tau_{\text{strike0}} + \tau_{\text{drag}}^{3D}$. We thus attempt to numerically approximate the roughness drag (following Dunham et al. [51], but for the first time based on 3D dynamic rupture models) as

$$\tau_{\text{drag}}^{3D} = C\tau_{\text{drag}}^{2D} \tag{2.2}$$

where C is a dimensionless coefficient. In Text 2.9.2, we demonstrate in numerical experiments that C can be approximated from τ_{drag}^{2D} using characteristics of the reference model slip distribution. For our choice of $n = 4$ elements to resolve $\lambda_{\text{min}} = 200$ m, we obtain C of ~ 0.44. The average value of τ_{drag}^{3D} across the rupture area is ~ 1.4 MPa. Our lower τ_{drag}^{3D} is intuitive since the material off a 3D roughness feature can also deform perpendicular to slip in distinction to the 2D case. We caution that while τ_{drag}^{2D} is defined for 2D in-plane quasi-static rupture, proper analytical treatment of the 3D (dynamic) roughness drag is very complex. The formulation of the roughness drag is based on stationary statistics and thus applies in the slipping (or slipped) region well behind the rupture front, challenging analytical extensions to account for rupture front curvature, inertia, or slip gradients in the vicinity of the rupture front. This motivates our empirical approach (see also Text 2.9.2). We account for the 3D roughness drag while preserving the smooth reference initial stress distribution by loading the rough fault with a heterogeneous regional stress tensor: we first adapt the smooth reference initial fault loading to balance roughness drag, then expose the now rough fault to the adapted loading (Text 2.9.3). As a result, the broadband model features roughness-induced small-scale fluctuations of the initial shear and normal

tractions (Figure 2.2b), consisting of both releasing and restraining slopes that bring the fault closer and farther from failure, respectively (Figure 2.6).

2.3.3 Frictional heterogeneity

We perturb the smooth variation of the reference characteristic frictional slip weakening distance D_c^0, the spatially most variable dynamic parameter in the reference Bayesian dynamic inversion. The relative standard deviation of D_c is on the order of 50% [72], highlighting its importance as a proxy for unaccounted geometrical and geological features. We use a band-limited fractal distribution. We prescribe $D_c = \max(0.14 \text{ m}, D_c^0(1+\epsilon))$, where 0.14 m is the minimum value of D_c^0, and ϵ follows a fractal distribution of amplitude-to-wavelength ratio $\alpha = 10^{-4}$ generated from a different random seed than the one used for the fault roughness. Including small-scale heterogeneous D_c in our broadband model is a proxy for frictional or stress asperities that have been shown to be important for high-frequency radiation in previous work (e.g., [186]; [74]). Heterogeneous D_c contributes to radiating additional energy due to fault-local acceleration and deceleration.

2.3.4 Topography and viscoelasticity

In our broadband dynamic rupture, the flat free surface used in the inversion is superseded by high-resolution topography data sampled to 150 m resolution [57]. The modeled 3D domain spans 300 × 300 km horizontally and extends to a depth of 150 km to avoid any undesired reflections from the (imperfectly) absorbing boundaries. We incorporate the 1D velocity model, with $V_p = 1.86V_s$, and viscoelastic attenuation, with $Q_p = 2Q_s$, inferred by Ameri et al. [1], see Table 2.2. Accounting for topography and viscoelasticity is complementary to including dynamic source heterogeneity. Realistic 3D topography scattering redistributes seismic energy to later arrival times enhancing synthetic seismogram coda signals, an effect that cannot be obtained when considering source complexity only.

2.4 Broadband rupture dynamics and ground-motion validation

2.4.1 Rupture dynamics

We compare the broadband dynamic rupture model, incorporating fault roughness, small-scale D_c variation, and topography to the reference model with a planar fault, a flat free surface, and smoothly varying initial conditions, in terms of fault slip (Figures 2.1b, c), slip rate space-time evolution (Figures 2.2c, d), and moment rate release (Figure 2.7).

Figures 2.1b,c and 2.2c,d demonstrate similar large-scale slip evolution. The seismic moment of the broadband model is 2.8×10^{18} Nm, corresponding to $M_w = 6.24$, which is comparable to the reference model with 2.6×10^{18} Nm seismic moment ($M_w = 6.20$). We highlight that both models recover the remarkably weak and slow nucleation phase

[218, 72], as was also inferred for the Norcia earthquake [215]. The nucleation is followed by bilateral rupture, which is slower towards the NW than towards the SE in both models. At smaller scales, the broadband model features decoherence of rupture fronts [207]. Locally fluctuating rupture speeds are due to acceleration and deceleration at releasing and restraining slopes, heterogeneous initial shear and normal traction, and D_c heterogeneity. Peak slip rates are increased by ∼15% in the broadband model, while both models feature pulse-like ruptures, and rise time remains largely unaffected.

Comparisons of moment rate releases (Figure 2.7a), moment rate spectra (Figure 2.7b), and the second time-derivative of moment rate releases (Figure 2.7c) illustrate the effects of the fault roughness, heterogeneous loading, and D_c on the high-frequency rupture radiation. While the two distinct episodes of moment rate release are well recovered, its first peak is about 20% higher in the broadband model than the reference model (Figure 2.7a), reflecting the increase in negative strength excess in the nucleation region required for broadband self-sustained spontaneous dynamic rupture across the rough, frictionally heterogeneous fault.

2.4.2 Ground motions

Figure 2.3 compares the observed three-component velocity and acceleration waveforms recorded at the 20 strong-motion stations (Figure 2.1, [135]) with synthetics from the broadband dynamic rupture model. The overall agreement in terms of waveform shape and duration is good for both velocity and acceleration waveforms. The synthetic amplitudes fit velocity recordings very well at most stations (Figure 2.3a). Nevertheless, the modeled acceleration amplitudes are significantly underestimating some station components (Figure 2.3b, e.g., NRC, MNF, FOS, ASP). Analogous plots for the reference model and the rough, heterogeneous fault model without topography are shown in Figures 2.8 and 2.9, respectively. We isolate the effect of using small-scale heterogeneous D_c in comparison to the smoothly varying D_c from [72] in Figure 2.7 (moment rates) and Figure 2.10 (synthetics).

To highlight the role of the fault roughness, frictional heterogeneity, and topography, Figure 2.4 compares observed EW velocity and acceleration waveforms and Fourier Amplitude Spectra (FAS) with synthetics of three models: the reference, the broadband rough fault model with topography, and the broadband rough fault model without topography. All components and stations are shown in Figures 2.11-2.17. The synthetic waveforms of the broadband models match long-period data (0.05-0.5 Hz) equally well as the reference model. Nevertheless, the reference model provides waveforms clearly depleted at high frequencies. A general trend is that fault roughness and topography enhance and elongate waveforms at high frequencies, respectively, although not to the same extent at all stations. The increase in high-frequency content in the broadband waveforms without topography (green) is clearly limited in duration compared to the same model incorporating topography (red). High-frequency ground motions are amplified early-on by fault roughness, while topography-induced scattered waves prolong their duration. The combination of both effects is most pronounced in the central and SE part of the hanging wall

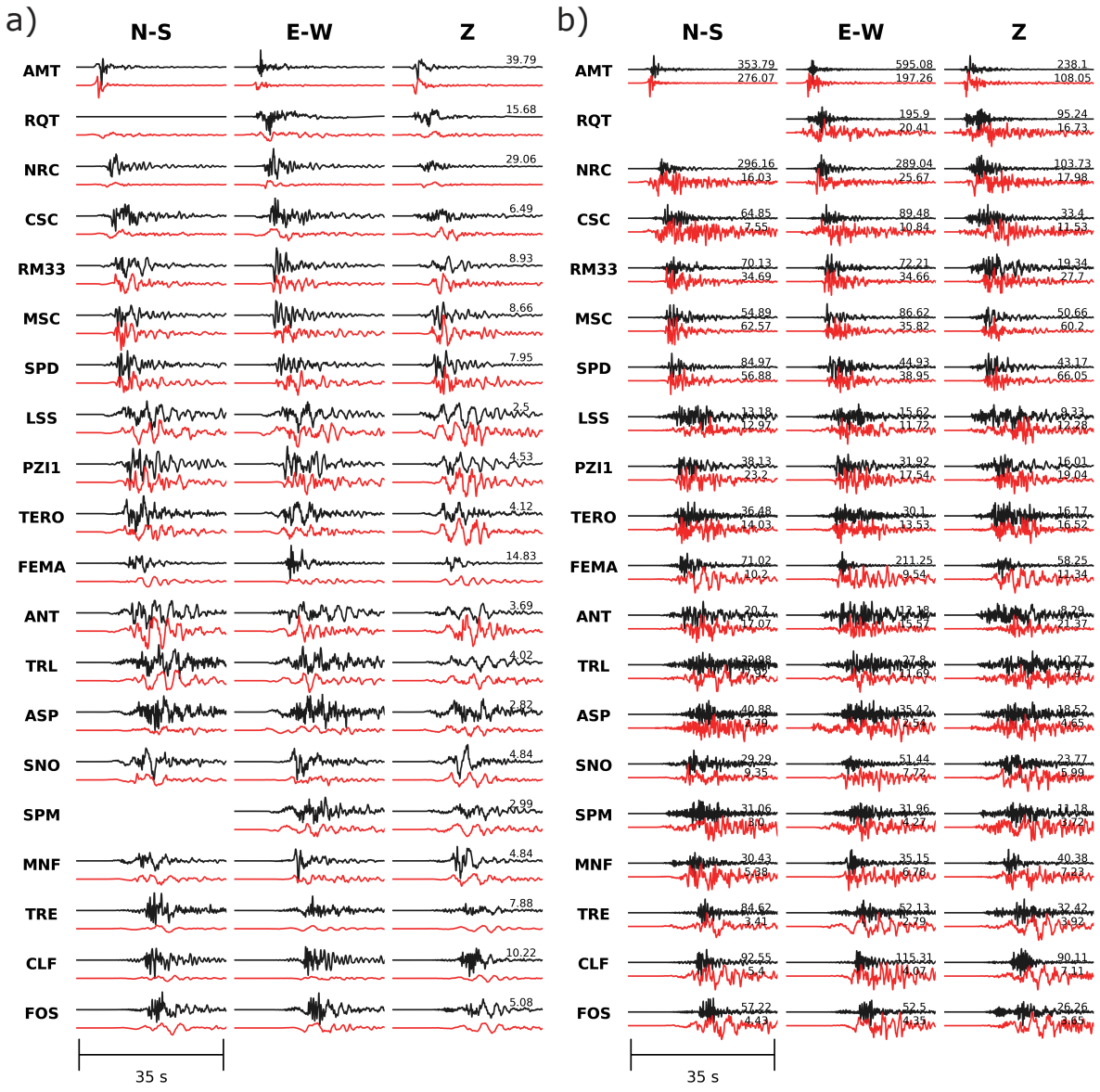

Figure 2.3: Comparison of observed (black) and simulated (red) components (NS, EW, and Z) of (a) ground velocity (in cm/s) and (b) acceleration (in cm/s^2) band-pass filtered between 0.05 and 5 Hz for all 20 stations (Figure 1), ordered by epicentral distance. Synthetics are from the broadband dynamic rupture scenario incorporating fault roughness, D_c heterogeneity, and topography. Both observed and synthetic waveforms are scaled by their maximum value, which is indicated on the right-hand side of each plot. Velocity waveforms are scaled by the maximum value of the observed records at each station, while acceleration waveforms are scaled component-wise.

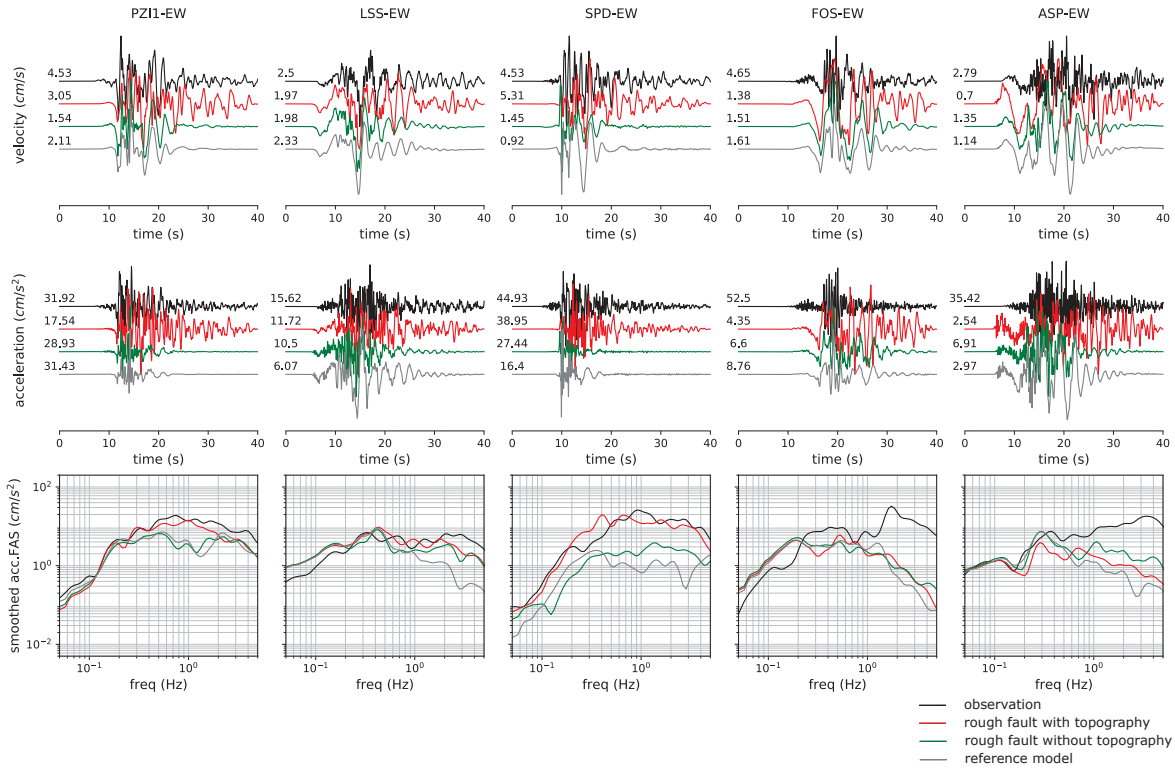

Figure 2.4: Comparison of EW component of broadband synthetic ground-velocity (top) and acceleration (middle) waveforms from the broadband rough fault model with topography (red), the broadband rough fault model without topography (green), and the reference model (gray) compared with observations (black) at five selected stations (see Figure 1). All waveforms are scaled by their maximum values, indicated on the left-hand side of each trace. (bottom) Smoothed Fourier amplitude spectra of the acceleration waveforms using the method of Konno & Ohmachi [117]. The observed data are tapered with a 35 s cosine window.

region (see, e.g., stations PZI1, LSS, and SPD in Figure 2.4 and 2.12, or MSC, AMT, and ANT in Figure 2.11, 2.14, 2.15, and 2.17). At some stations (e.g., stations FOS and ASP), our broadband synthetic spectra are improved yet underestimate the observed spectra at frequencies higher than 1 Hz. We may speculate that larger station-source distances, as for FOS and ASP, and local subsurface complexity such as basin edge effects render more realistic 3D velocity models than used here, important for physics-based broadband modeling. Similarly, fully considering site effects may amplify high-frequency waveform spectra.

Animations of the three components of the velocity wavefield for the reference and broadband models are shown in Movies 2.9.5. They illustrate how seismic waves are both reflected and scattered upon propagating across sharp topographical features like mountains and hills, which explains the prolonged duration of the seismic signal for several receivers (e.g., stations LSS & SPD, Figure 2.4). Although viscoelastic attenuation is generally important to capture the decay of seismic energy during topography scattering, a

comparison between our models with and without attenuation in Figure 2.18 shows relatively minor effects (e.g., for stations SPD, PZI1, TERO).

Figures 2.19 and 2.20 quantify the fit of the synthetic ground motions of the broadband and reference models with observations using Goodness-of-fit (GOF) metrics [160], including peak ground velocity and displacement, spectral acceleration, Fourier amplitude spectra, energy duration, and cumulative energy (Text 2.9.4). The broadband model with topography fits the observations better (GOF 45-65) than the reference model (GOF 35-55) and the broadband model without topography (GOF 40-60).

Figure 2.21 details the model bias and standard deviation over the 0.5-10 s period range, averaged over 20 stations used in this study. In general, a near-zero model bias over a specific period suggests that simulated ground motions match observations reasonably well at given frequencies. The reference model fits the observations only at periods longer than 2 s. Compared to the reference model, the fit of the broadband model without topography (Figure 2.21b) is improved (30-40% lower bias) at periods shorter than 2 s. The broadband model with topography shows an even better fit (40-50% lower bias than the reference model, Figure 2.21c). However, while both broadband models preserve a perfect fit at periods longer than 2 s, some synthetics still underestimate the observations at periods shorter than 2 s, as discussed above.

2.5 Discussion

Recorded broadband ground motions are widely used in earthquake engineering to inform the performance-based design of structures. Typically, generic strong-motion waveforms that fit specific ground motion metrics are selected from a strong-motion database for that purpose [103]. Also, probabilistic seismic hazard analyses often rely on such so-called ergodic ground-motion models (GMMs, e.g., [167]). Yet, these may not reflect the conditions of a specific region of interest. Regional synthetic broadband ground motions from 3D dynamic rupture inversions, which offer a physically consistent representation of earthquakes, can sample conditions that are not sufficiently constrained in empirical models towards the development of non-ergodic, physics-based GMMs [79, 58, 153, 242, 243].

Our proposed broadband dynamic rupture models can be extended to account for other distinctive regional characteristics, such as a listric or segmented fault geometry, 3D velocity models including low velocity layers and basins, and fault zone plasticity [190]. They may also inform PSHA-targeted kinematic rupture generators while inherently ensuring realistic scaling of earthquake characteristics (e.g., [199]). Our models emphasize the need to include i) small-scale source characteristics to enhance the high-frequency source radiation during the rupture propagation, and ii) topography to increase the duration due to scattering. The duration of the latter effect is controlled by viscoelastic attenuation.

We carefully analyze the effects of adding roughness to a flat fault model. We counterbalance the consequent 3D roughness drag by increasing initial shear traction by τ_{drag}^{3D} (equation 2.2), calculated using the spatially variable slip amplitude Δ of the reference model. We explored an alternative model (not presented here), with constant Δ equal to

the peak slip of the reference model (1.14 m). It generates a higher average τ_{drag}^{3D} of about 3.3 MPa (cf. 1.4 MPa, Section 2.2). It may be possible to identify alternative satisfying models based on constant Δ. Nevertheless, the here presented approach of constraining Δ by the spatially variable reference fault slip appears superior due to its simpler and better constrained parametrization.

Our proposed approach to enhance smooth slip models for broadband dynamic-rupture simulations is independent of the data and generation process of the starting smooth source model. Besides the dynamic source inversion used here, kinematic slip models can serve as a reference model as well (e.g., [138]). However, the choices required for conversion in the latter approach may lead to several families of plausible dynamic rupture scenarios that need additional (e.g., geological) constraints to be distinguished [215].

Although our rough fault model with topography improves the waveform fit at high frequencies, some synthetics still underestimate the observations. Additionally, a good fit of shape, duration, and amplitude characteristics of broadband velocity waveforms up to 5 Hz does not necessarily translate into capturing broadband acceleration amplitudes equally well, a challenge identified in kinematic source modeling as well (e.g., [107]).

More complete matching of the observed records at periods < 2 s may, in the future, be enabled by: (i) considering smaller length scales (λ_{min}) of fault surface roughness, potentially further increasing high-frequency radiation at the cost of increased computational demands; (ii) incorporating larger-scale non-planar fault geometry such as a listric fault geometry which has been, for instance, suggested from satellite data ([222]) and which may modulate peak ground velocities as a consequence of curvature focusing effect [163]; (iii) probing and quantifying the variability of the predicted shaking using alternative models from the Bayesian ensemble of the dynamic rupture inversion, and (iv) incorporating a more realistic Earth model to capture path and local site conditions, i.e., 3D velocity models, small-scale scattering media [105, 27], site corrections [187], or non-linear soil effects [192] and (v) off-fault damage [158, 251].

In particular, low-velocity sedimentary basins [126, 170] can significantly amplify the amplitude and duration of ground motions, which may lead to improved synthetics for stations with strong site-effects, e.g., CLF with site-class D (Table 2.1). However, accounting for these mechanisms in sufficient detail (at scales down to $\sim$100 m or less) in observationally constrained 3D broadband dynamic rupture models poses additional computational and observational challenges, and their relevance for matching real earthquake recordings remains open to debate.

2.6 Conclusion

We present a novel approach for broadband dynamic rupture modeling constrained from low-frequency data towards generating physics-based, non-ergodic ground motion synthetics validated by observations. We generate broadband dynamic rupture models of the 2016 Mw 6.2 Amatrice earthquake by combining large-scale heterogeneous stress and frictional parameters, inferred from the best-fitting model of a Bayesian dynamic rupture inversion,

with small-scale self-similar fault roughness and frictional (slip weakening distance) heterogeneity, topography, and viscoelastic seismic attenuation. We empirically quantify the 3D roughness drag governing rupture dynamics on small scales by counterbalancing its effective dynamic stress perturbations. We obtain dynamic rupture scenarios that successfully reproduce the low-frequency (<1 Hz) source characteristics of the inverted dynamic model. The combined small-scale heterogeneities of the fault geometry, frictional strength and loading enhance high-frequency source radiation. Topography elongates the synthetic waveforms by enhancing coda effects. In combination, we obtain more realistic high-frequency (up to ∼5 Hz) synthetics comparable with observed strong motion records. Our work demonstrates 3D physics-based, broadband earthquake ground-motion simulations that are tightly constrained by data-driven dynamic earthquake source inversion and allows us to quantify the first-order role of large- and small-scale dynamic source heterogeneities in the broadband seismic wavefield. Challenging future developments may focus on including 3D and site-specific wave propagation effects towards realistic fully physics-based acceleration synthetics suitable for engineering applications.

2.7 Data availability

We use the software package SeisSol, available at `https://github.com/SeisSol/SeisSol`, branch 'Norcia_sequence', commit 181fc85d5c405a8c44fe21869fe736ab1f0206d5. Input files required to run broadband dynamic rupture simulations can be downloaded from `https://zenodo.org/record/7194965`. The reference dynamic rupture model parameters from the Bayesian inversion are available at `https://github.com/fgallovic/fd3d_tsn_pt/tree/master/example/20160824-Amatrice`. The topography data from the Shuttle Radar Topography Mission (SRTM) is retrieved using the SRTM.py python package (`https://github.com/tkrajina/srtm.py`). Observed strong ground motion waveforms recorded by the Rete Accelerometrica Nazionale (RAN) and the Rete Sismometrica Nazionale, operated by the Italian Department of Civil Protection (DPC) and the Istituto Nazionale di Geofisica e Vulcanologia (INGV) were downloaded from the Engineering Strong-Motion database (`https://esm.mi.ingv.it/`, [135, 123]).

2.8 Acknowledgements

We would like to express our gratitude to Eric Dunham for his valuable insights and discussions regarding Text 2.9.2 in Supporting Information S1. We would also like to thank Germán Prieto, the Associate Editor, and two anonymous reviewers for their helpful feedback and comments.

This work was made possible by the support of the German Research Foundation (DFG, GA 2465/2-1). Additional funding was provided by the European Union's Horizon 2020 research and innovation program, including the TEAR ERC Starting Grant (852992), ChEESE (grant agreement No. 823844), DT-Geo (grant agreement No. 101058129), and

Geo-Inquire (grant agreement No. 101058518). Funding was also received from DFG (GA 2465/3-1), NSF (EAR-2121666), and SCEC (awards 20046 and 21010).

We are grateful to the Gauss Centre for Supercomputing e.V. for providing computing time on the GCS Supercomputer SuperMUC-NG at Leibniz Supercomputing Centre through project pr63qo. Additionally, we thank the King Abdullah University of Science and Technology (KAUST) Supercomputing Laboratory for computing time on Shaheen II through project k1343.

2.9 Supporting information

2.9.1 Numerical discretization and resolution

Our high-resolution 3D dynamic rupture simulations are performed using the open-source software package SeisSol (`https://github.com/SeisSol/SeisSol`), which resolves seismic wave excitation locally up to 10 Hz and ground motions up to at least 5 Hz within 50 km distance of the fault. SeisSol is based on the Arbitrary high-order DERivative Discontinuous Galerkin (ADER-DG) method [49, 166, 165].

The dimensions of the model are 300 km × 300 km × 150 km (depth). We gradually increase the element size towards a maximum edge length of 10 km at the domain edges to reduce computational cost without sacrificing accuracy in the region of interest. This region is a highly resolved subdomain spanning 50 km × 50 km horizontally and 10 km in depth, centered at the hypocenter. There, the high-order accurate element edge lengths range from 150 to 350 m, adapted to the 1D velocity model and requiring at least two elements resolving the shortest wavelengths [113], computed for a target frequency of 5 Hz.

We adapt the planar fault to adhere to band-limited fractal surface morphology characterized by wavelengths ranging from $\lambda_{\min} = 200$ m to $\lambda_{\max} = 2$ km. At least $n = 2$ elements per wavelength $\lambda_{\min}$ are required to capture the complexity of the band-limited rough fault model without aliasing with SeisSol, which uses unstructured tetrahedral meshes. In this study, the rough fault is generated using the Fourier transform method. The rough fault can, therefore, be viewed as a weighted sum of sinusoids, which are here approximated by piece-wise bilinear functions due to SeisSol's geometrically linear triangles representing fault surfaces. We note that this leads to an artificial enhancement of the shorter wavelength content of the rough geometry.

For example, a 2-node approximation of a sine wave of wavelength λ can be decomposed into the sum of sinusoids of wavelength λ and its multiples λ/p. By using higher n, we decrease the artificial short-wavelengths content of wavelengths shorter than λ_{min}. The rough fault geometry then better resembles a band-limited fractal distribution. Low n (i.e., 2 to 4) are sufficient to capture the effects of fault roughness on earthquake dynamics and ground motions and promote well-balanced numerics by limiting the number of elements with dynamic rupture boundaries. Even higher n would allow the discrete fault geometry to approach curvilinear approaches (e.g., [54]) and for a better control of the amplitude spectrum of fault roughness at short wavelengths.

For our choice of $n = 4$, the fault is discretized using 50 m sized elements, ensuring that the process zone size and thus rupture dynamics are sufficiently resolved everywhere on the fault [43, 247]. We measure the minimum process zone size, the region behind the rupture front where the fault strength drops from its static to dynamic level, as being equal to 200 m. The resulting mesh has more than 80 million tetrahedral elements (Figure 2.1a) and is generated using Simmodeler (`https://www.simmetrix.com/simmodeler/`, [106]). Simulating 40 s of a broadband Amatrice dynamic rupture earthquake scenario using SeisSol with fifth-order accuracy in space and time (i.e., basis functions of polynomial order $p = 4$) and double precision requires 4 hours on 256 nodes of the SuperMUC-NG supercomputer.

2.9.2 Empirical quantification of the 3D roughness drag

We empirically approximate the roughness drag τ^{3D}_{drag} (Equation 2.2) using systematic dynamic rupture simulations varying C, the minimum roughness wavelength λ_{min}, and the number of elements n resolving λ_{min}. Equation 2.2 defines C as the dimensionless coefficient for empirical approximation of the 3D roughness drag. We find the preferred scenario for each parameterisation by comparing the space-time evolution of dynamically self-sustained rupture along the fault, seismic moment, peak seismic moment release, and timing of the peak seismic moment release to the reference model. We find that approximating C, as

$$C \approx m\lambda_{\text{min}} + b \tag{2.3}$$

i.e., a linear function with slope $m = 0.001$ and intercept $b = 0.315(1 - 1/n)$, allows us to recover broadband models matching the reference model for a range of broadband dynamic rupture models and discretizations (Figure 2.5a). Figure 2.5b shows all analyzed and the preferred values of intercept b for varying number of elements n per λ_{min}.

We note that the weak dependence of C on element size n in Equation 2.3 is unexpected for well-posed and well-resolved simulations. In this study, we choose to sample the minimum wavelength of the roughness with 4 elements (see Text 2.9.1). This choice, combined with using non-curved elements, leads to slightly different geometrical representations of the targeted fractal fault roughness, specifically for the shortest roughness scales. The here provided relationship takes this practicality into consideration.

Our numerical estimate leads to a lower 3D roughness drag than inferred for 2D. Intuitively, a reduction in roughness drag in our 3D dynamic rupture simulations compared to 2D makes sense, as the deforming material which is attempting to slide past a roughness feature can also deform perpendicular to slip, while the roughness feature will be bounded in that perpendicular (mode III) direction. Besides dimensional considerations, we note that the differences between the 2D static analysis of τ^{2D}_{drag} and our 3D dynamic rupture simulations may additionally be caused by differences between the dynamic character of our models vs. the static analytical derivations.

Finally, our prescribed roughness is isotropic in dip and strike directions. An important question that we do not study is how the roughness drag can be quantified when the

surface has anisotropic roughness, and thus involves both mode II and mode III to different extents. For an isotropic, self-similar rough surface, it makes intuitively sense to form the same parameter combination in 3D as was derived in the 2D expression, having units of roughness drag and being proportional to α^2 (as is required).

2.9.3 Adaption of the reference initial loading to account for the 3D roughness drag

We adapt the reference loading, which is prescribed as smoothly varying fault local initial tractions, to an equivalent globally defined Cartesian background stress allowing for geometry-induced small-scale traction heterogeneities. In this way, we can also account for the above quantified 3D roughness drag while preserving the smooth reference initial stress distribution. We build a heterogeneous stress tensor from τ_{dip}, τ_{strike}, and σ_n (see Section 2.2). The reference coordinate system of our model has the x-axis aligned with fault strike and the y-axis horizontal, pointing away from the hanging wall. We load the fault by an initial stress tensor (σ_{ij}) defined in a fault coordinate system (x, u, v) aligned with the planar reference model fault. v points up-dip, and u is oriented normally to the fault such that (x, u, v) forms a right-handed coordinate system. We set $-\sigma_{uv} = \tau_{dip}$, $-\sigma_{xu} = -\sigma_{xv} = \tau^{3D}_{\text{drag}}$ to compensate for the 3D roughness drag effects on all initial shear stresses components, and $-\sigma_{xx} = -\sigma_{vv} = -\sigma_{uu} = \sigma_n$ (assuming compressive normal stresses being negative). This stress tensor is finally rotated by 45°, the dip angle of the planar reference fault, with respect to the x-axis to the reference coordinate system. The resulting heterogeneous initial loading features roughness-induced small-scale fluctuations of the initial shear and normal tractions (Figure 2b), consisting of both releasing and restraining slopes, in which the fault is brought closer (resp. farther away) from failure (Fig S2a).

Due to the added τ^{3D}_{drag} term, the initial shear traction may exceed the initial fault strength locally. To prevent instantaneous failure across the fault, we limit τ_{dip} and τ_{strike} to be at least 0.5 MPa lower than fault strength everywhere on the fault except the nucleation area. Rupture is initiated in an area of negative strength excess of ∼1 km radius located 16 km along-strike and 7 km down-dip (highlighted by a black line in Figure 2.2a,b). We empirically find that in the such modified rough fault model, 30% higher negative strength excess ($\tau_s - \tau_0$) of ∼1.3 MPa is required to model the dynamically very sensitive weak nucleation from the reference model.

2.9.4 Goodness of fit of broadband and reference ground motion

We quantify the fit between observations and synthetic ground-motions for all models (reference, broadband without topography, and broadband with topography) using Goodness-of-fit (GOF) metrics [160]. We compute the average GOF of 0.05–5 Hz bandpass filtered signals using the following metrics:

- peak ground velocity (PGV)

- peak ground displacement (PGD)
- spectral acceleration (SA) at periods 0.5-10 s
- Fourier amplitude spectra (FS)
- energy duration (DUR)
- cumulative energy (ENER)

We do not consider peak ground acceleration (PGA) because it is susceptible to site effects, which we do not account for in this study. Note that in our GOF computations, we exclude station RQT, for which no NS-component recording is available, and station CLF because of its strong broadband site-effect (class D).

Figure 2.18 shows the distribution of average GOF at all station components for the reference and both rough fault models. The histograms in Figure 2.18 show the prevalence of fairly good values (GOF 45-65) for both reference and rough fault models. The rough fault model with topography fits the observations generally better than the reference model and the rough fault model without topography for all components, with an average GOF of 55, 65 and 55 for EW, NS and Z components, respectively. The best fit stations (GOF > 55 for all components) are PZI, LSS and TERO, located SE from the fault. Figure 2.19 details the average GOF for each station, component, and model. GOF values near or below 35 are observed at stations NRC and FEMA (EW components), stations NRC, ASP, and TRE (NS components), and station MNF (Z component).

We also calculate residuals r_j of spectral accelerations using the natural logarithm of the ratio of the observation O_j and synthetics S_j for each site j as a function of period T_i,

$$r_j(T_i) = \log[O_j(T_i)/S_j(T_i)] \tag{2.4}$$

Here, O_j and S_j are calculated as the geometric mean of the horizontal components. Mean model bias b for number of stations $N = 20$ is defined as

$$b(T_i) = \frac{1}{N}\sum r_j(T_i) \tag{2.5}$$

with its standard deviation σ calculated as

$$\sigma(T_i) = [\frac{1}{N}\sum (r_j(T_i) - b(T_i))^2]^{1/2} \tag{2.6}$$

The model bias for the three tested models are shown in Figure 2.19.

2.9.5 Movies

Below are additional movies as supporting information:

- Absolute slip rate (m/s) across the fault for the reference and the broadband rough fault models:

  `https://drive.google.com/file/d/1TXFbNAshgfduapUGMWZWi413tgzwZNN5/view?usp=sharing`

- Top view of fault parallel (u) ground surface velocity for the reference model:

  `https://drive.google.com/file/d/1qbwnd5iFs5R8AAA2by1Q3NGSrC-SkKcY/view?usp=sharing`

- Top view of fault normal (v) ground surface velocity for the reference model:

  `https://drive.google.com/file/d/1I1yi9le_BusxM6ZGYCtYf4CQ0S0HluRQ/view?usp=sharing`

- Top view of vertical (w) ground surface velocity for the reference model:

  `https://drive.google.com/file/d/1yAvXXEsGGwVRQKeOhJXG8J1o_jkwQAIf/view?usp=sharing`

- Top view of fault parallel (u) ground surface velocity for the broadband rough fault model with topography:

  `https://drive.google.com/file/d/1xdlG5_KPVXe52AogYztJnBFoZcW9czAQ/view?usp=sharing`

- Top view of fault normal (v) ground surface velocity for the broadband rough fault model with topography:

  `https://drive.google.com/file/d/1PSDfvSM5bS-WO-U_Ls0-wp-oHZC5JGJz/view?usp=sharing`

- Top view of vertical (w) ground surface velocity for the broadband rough fault model with topography:

  `https://drive.google.com/file/d/1aIHHXBIBf9VNnDBJkhjZKWBqiavWCG8H/view?usp=sharing`

Code	Station Name	Long.	Lat.	R_{jb} (km)	Site Class (EC8)
AMT	Amatrice	42.6325	13.2866	0.0	B
RQT	Arquata del Tronto	42.813	13.311	4.3	A
NRC	Norcia	42.7925	13.0964	2.6	B
CSC	Cascia	42.719	13.0122	12.3	B
RM33	Pellescritta	42.50898	13.21452	9.7	B
MSC	Mascioni	42.5268	13.3508	9.4	B
SPD	Sella Pedicate	42.5151	13.371	11.3	B
LSS	Leonessa	42.5582	12.9689	23.1	A
PZI1	Pizzoli	42.4356	13.3262	17.9	B
TERO	Teramo	42.62279	13.60393	19.2	A
FEMA	Monte Fema	42.9621	13.04976	14.8	A
ANT	Antrodoco	42.4182	13.0786	24.2	A
TRL	Terminillo	42.4613	12.9323	30.5	B
ASP	Ascoli Piceno	42.848	13.6479	30.9	B
SNO	Sarnano	43.0371	13.3041	19.7	B
SPM	Spoleto	42.7232	12.7512	31.5	A
MNF	Monte Fiegni	43.0596	13.1844	20.9	A
TRE	Trevi	42.8765	12.7358	30.5	C
CLF	Colfiorito	43.03671	12.92043	27.1	D
FOS	Foligno Seggio	43.0146	12.8351	29.8	B

Table 2.1: Strong motion stations at which ground motion waveforms are compared in this study. All 20 stations are within a radius of 50 km from the Mw 6.2 Amatrice event epicenter. R_{jb} is the Joyner-Boore distance and site classification according to EC8 [55].

Depth (km)	Vp (km/s)	Vs (km/s)	ρ (g/cm^3)	Qp	Qs
0	3.16	1.70	2.50	200	100
1	4.83	2.60	2.84	400	200
2	5.76	3.10	2.94	400	200
5	6.51	3.50	3.15	400	200
27	7.00	3.80	3.26	600	300
42	7.80	4.20	3.50	800	400

Table 2.2: 1D Velocity model [1] assumed in this study.

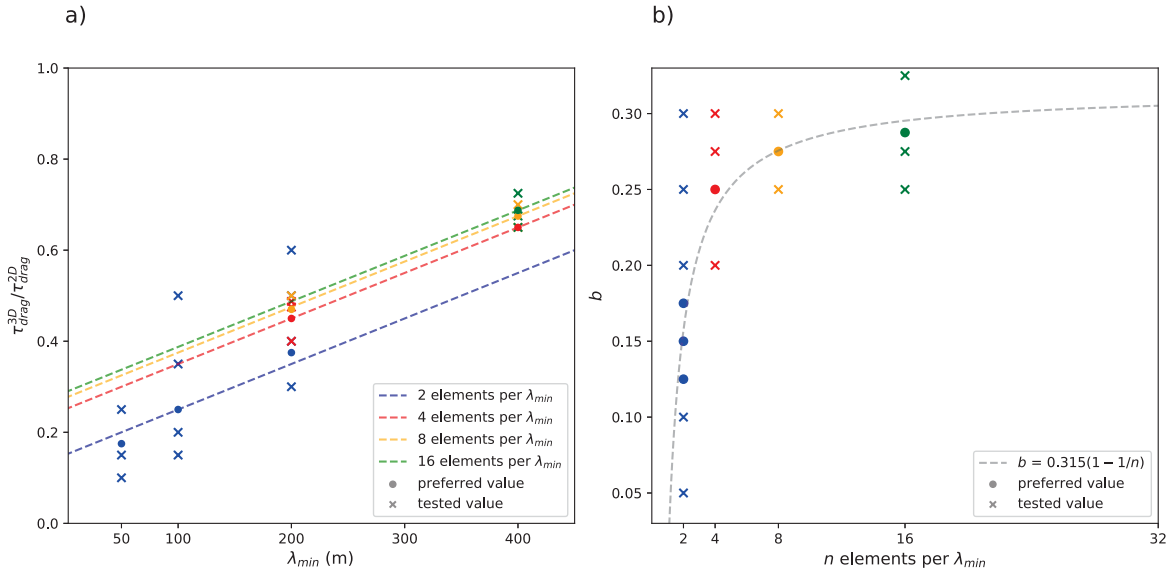

Figure 2.5: Tested and preferred values of coefficient C (Equation 2.2), relating τ^{3D}_{drag} to τ^{2D}_{drag} (Equation 2.1), for varying minimum roughness wavelength λ_{min}. The preferred values of C (shown by full circles) are identified by comparing the moment rate release of the rough fault model to the reference model (a). Tested and preferred values of intercept parameter b (Equation 2.3) for varying number of elements n per λ_{min} are shown in (b). The dashed line corresponds to the fitted function of b.

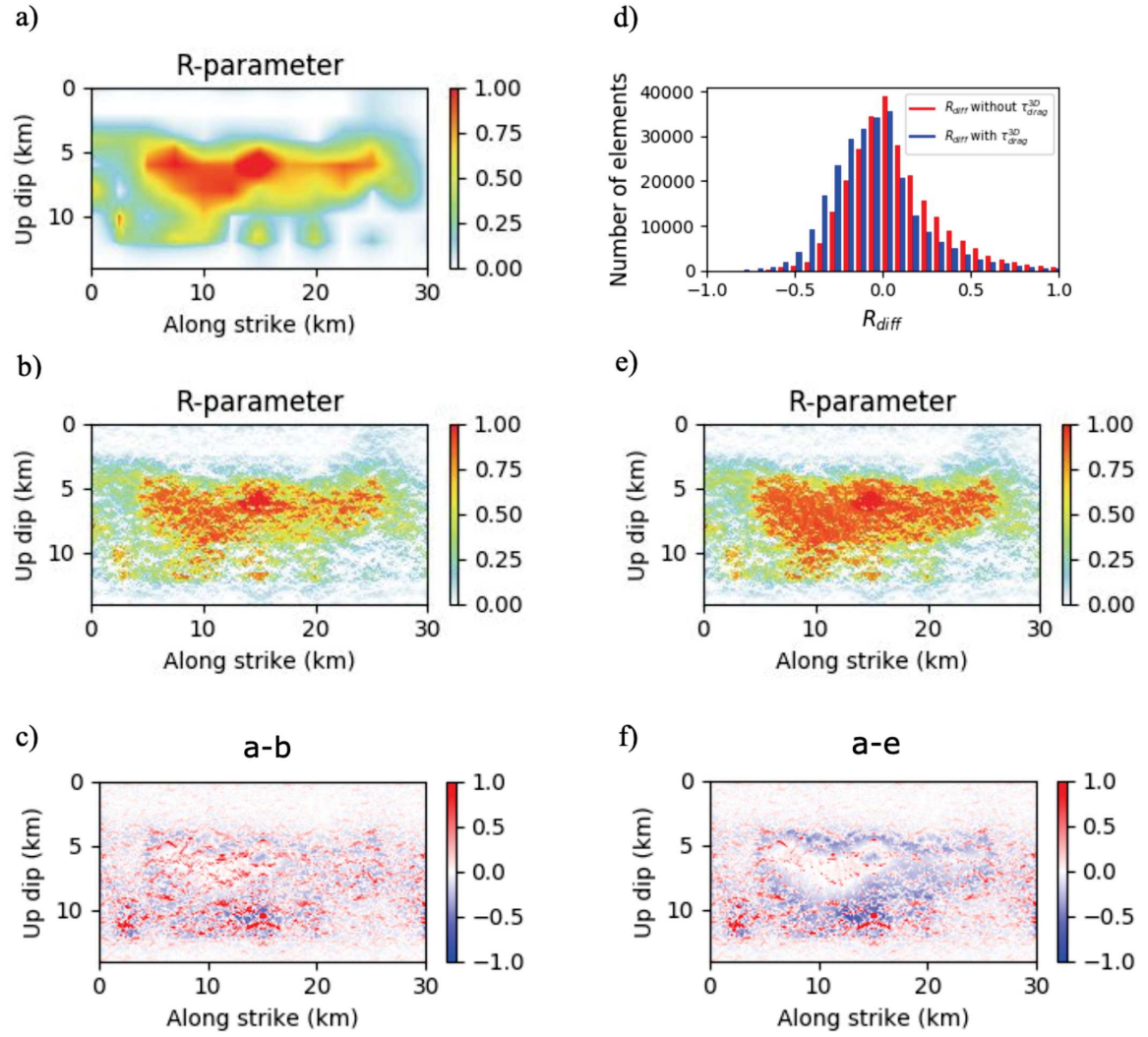

Figure 2.6: Comparison of the relative prestress ratio R for the planar reference model and the rough fault broadband model with and without roughness drag correction. We define the relative prestress ratio R following Aochi & Madariaga [11] as the ratio of the potential stress drop $\Delta\tau$ to the full breakdown strength drop $\Delta\tau_b$, $R = \Delta\tau/\Delta\tau_b = (\tau_0 - \mu_d\sigma_n)/((\mu_s - \mu_d)\sigma_n)$. $R = 1$ indicates a critically stressed fault. (a) R for the reference model, the broadband model (b) without and (e) with τ^{3D}_{drag}; (c) difference of the R-parameter between (a) and (b), (f) difference of the R-parameter between (a) and (e); and (d) histogram of (c) and (f).

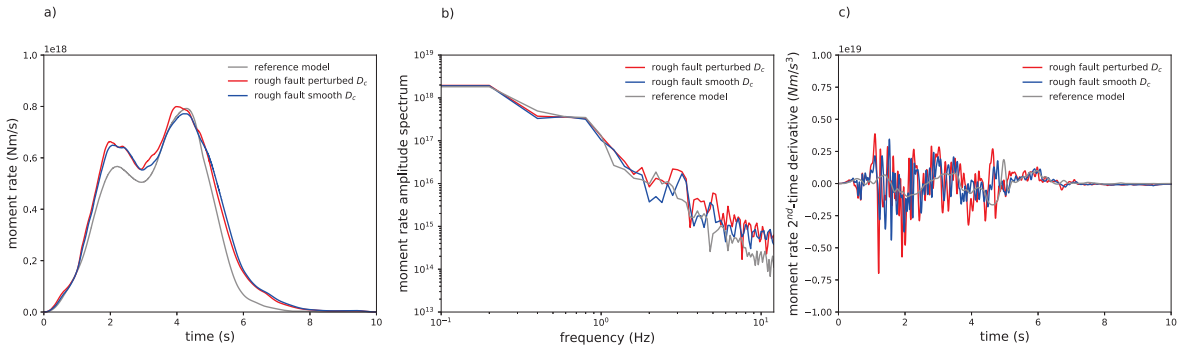

Figure 2.7: (a) Moment rate release, (b) moment rate spectrum, (c) the 2nd time derivative of the moment rate release. Gray curves correspond to the reference model. Red and blue curves correspond to the broadband rough fault model with and without D_c perturbations, respectively.

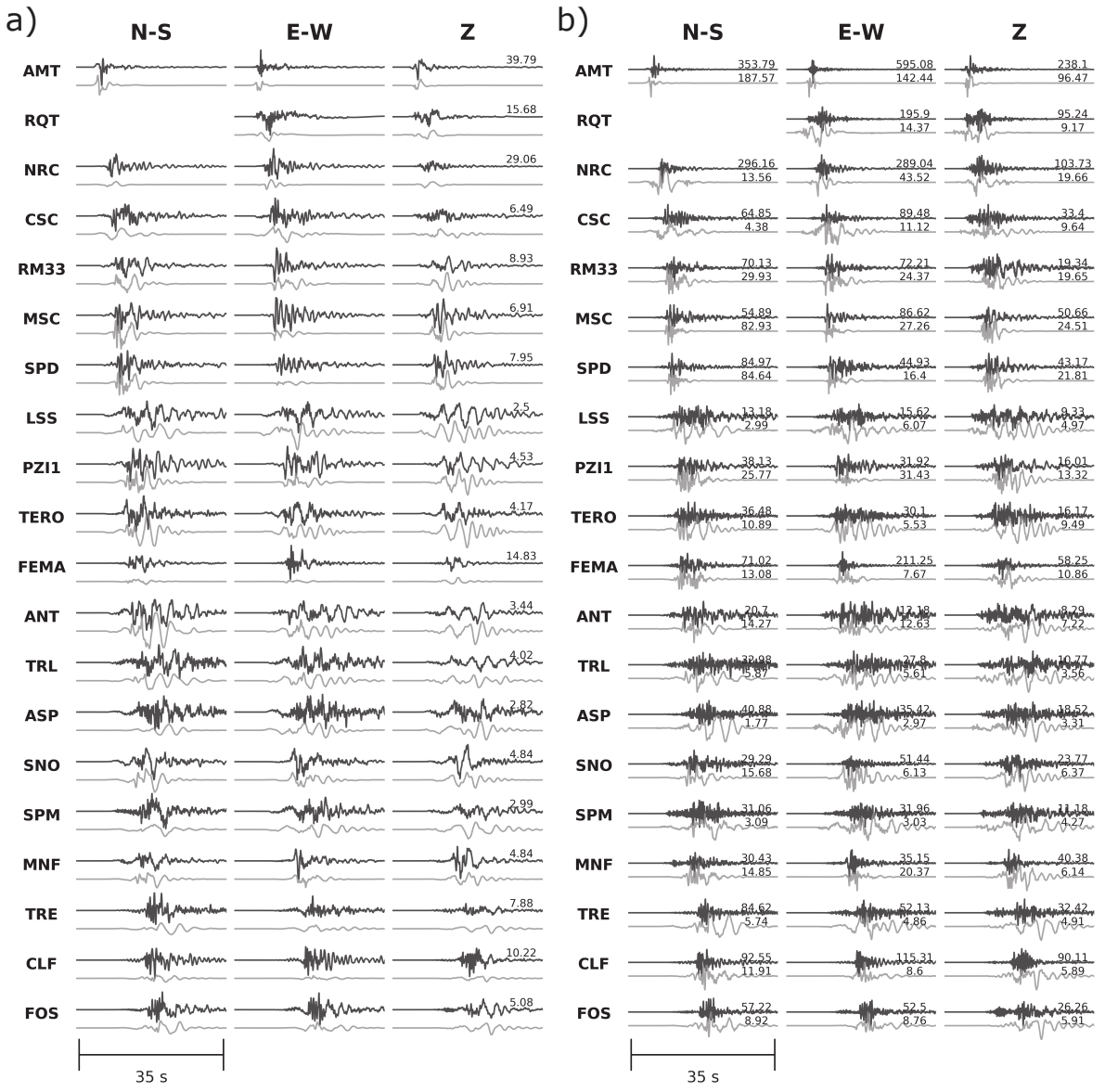

Figure 2.8: Comparison of observed (black) and simulated (gray) broadband three-component (NS, EW, and Z) of (a) ground-velocity (in cm/s) and (b) acceleration (in cm/s^2) waveforms at 20 selected stations (Figure 2.1), ordered by the epicentral distance. Synthetics are from the reference dynamic rupture scenario based on a planar fault. Both observed and synthetic velocity waveforms are scaled by the maximum value of the observed records at each station, indicated on the right-hand side of each plot, while acceleration waveforms are scaled component-wise. Observed and synthetic waveforms are band-pass filtered between 0.05 and 5 Hz.

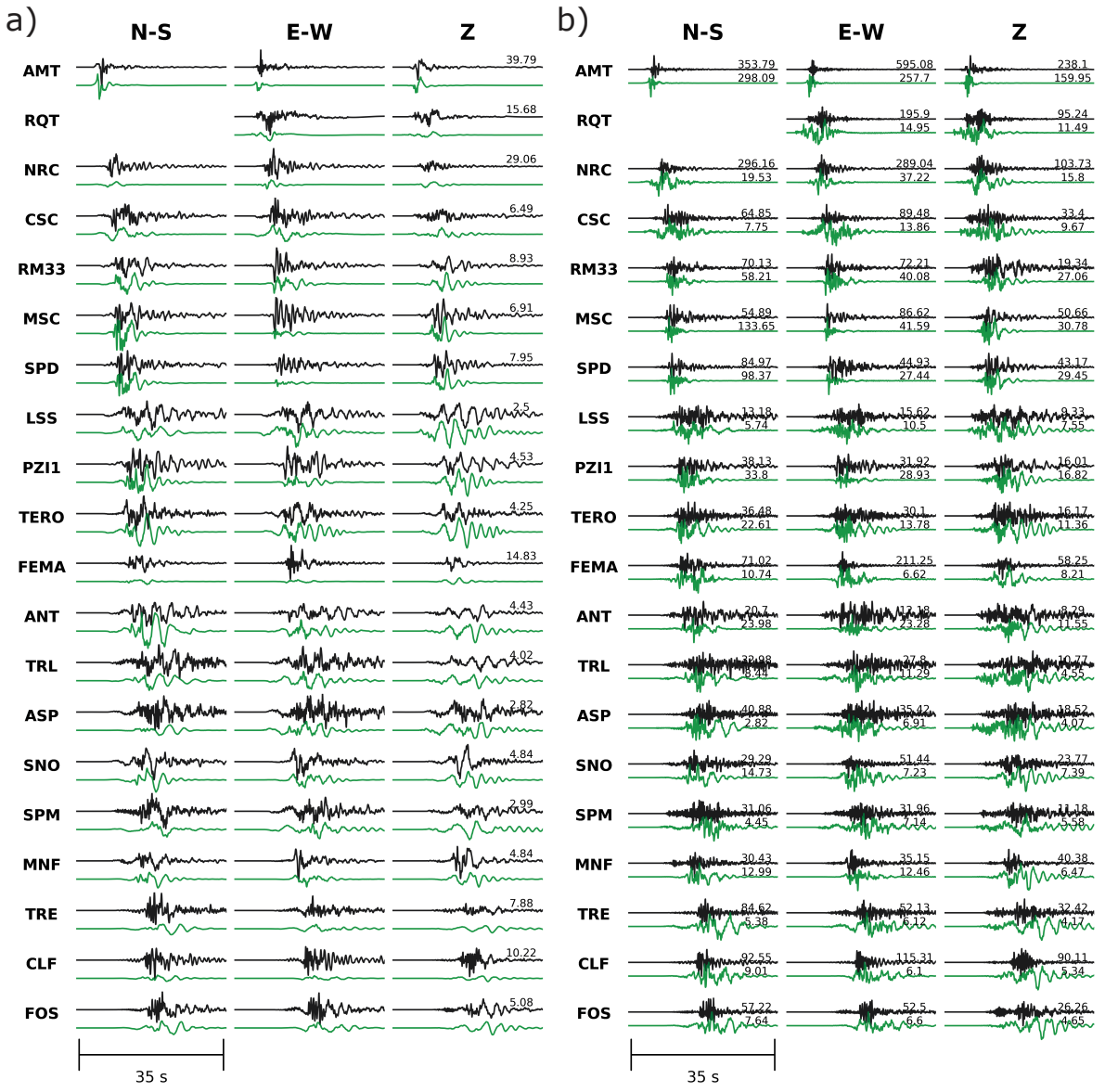

Figure 2.9: Comparison of observed (black) and simulated (green) broadband three-component (NS, EW, and Z) of (a) ground-velocity (in cm/s) and (b) acceleration (in cm/s^2) waveforms at 20 selected stations (Figure 2.1), ordered by epicentral distance. Synthetics are from the rough fault dynamic rupture scenario without topography. Both observed and synthetic velocity waveforms are scaled by the maximum value of the observed records at each station, indicated on the right-hand side of each plot, while acceleration waveforms are scaled component-wise. Observed and synthetic waveforms are band-pass filtered between 0.05 and 5 Hz.

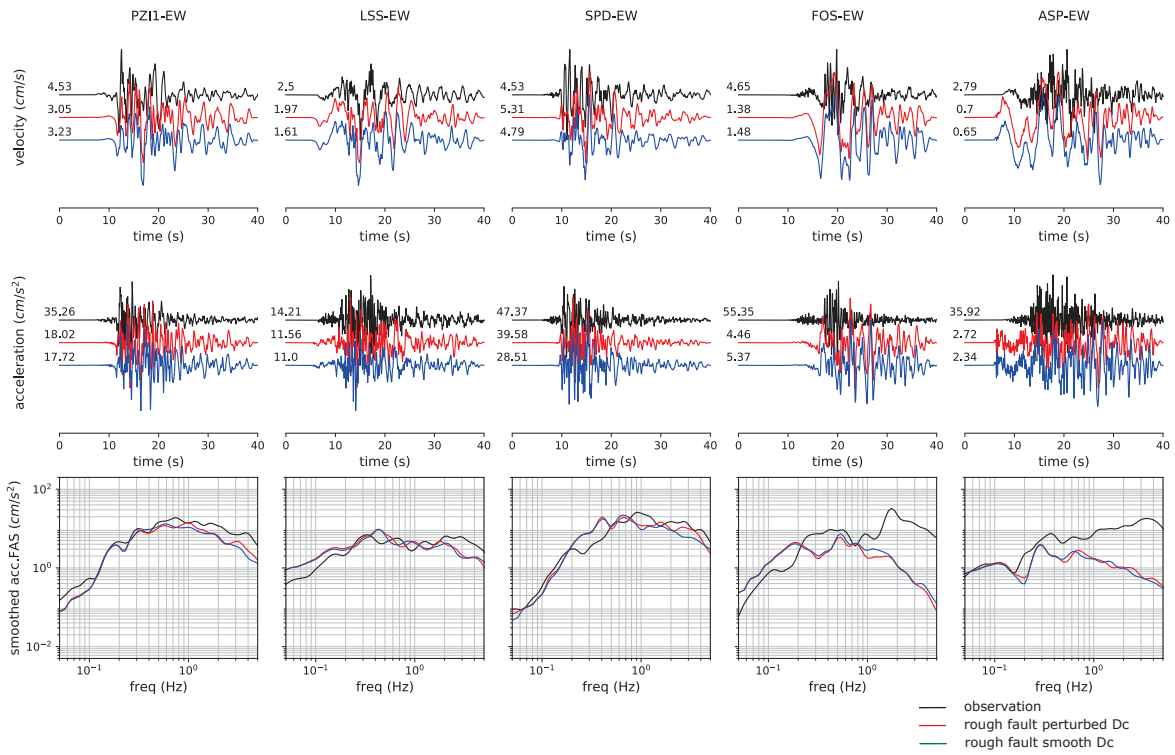

Figure 2.10: Effect of small-scale Dc variations on the synthetics. (top, middle) Comparison of EW component of synthetic ground-velocity (top row) and acceleration (middle row) waveforms from the broadband rough fault model with small-scale Dc perturbations (red), the broadband rough fault model without small-scale Dc perturbations (blue), and the observations (black) at five selected stations (see Figure 2.1). The maximum values of each waveform are indicated on the left-hand side of each trace. (bottom) Smoothed Fourier amplitude spectra (FAS) of the velocity waveforms using the method of Konno & Ohmachi [117]. The observed data are tapered with a 35 s cosine window.

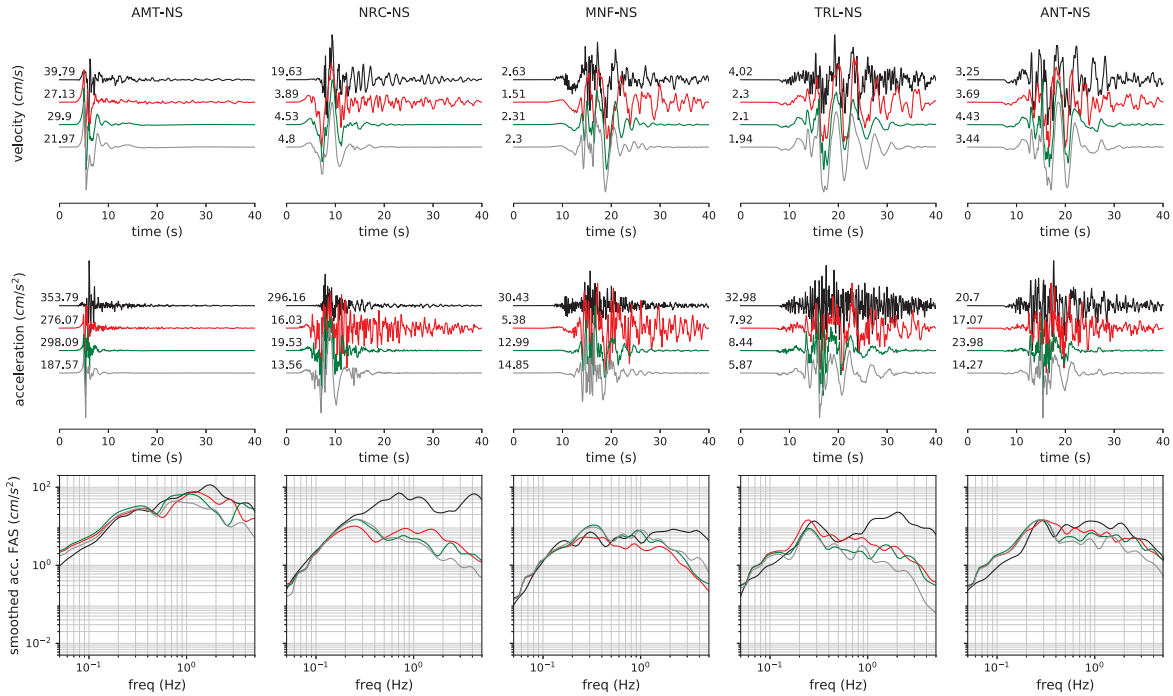

Figure 2.11: Effect of rough fault and topography on the velocity and acceleration waveforms and on the Fourier amplitude spectra. (top, middle) Comparison of synthetic ground-velocity (top row) and acceleration (middle row) waveforms from the broadband rough fault model with topography (red), the broadband rough fault model without topography (green), and the reference model (gray) compared with observations (black). NS component at five selected stations (see Figure 2.1). All waveforms are scaled by their maximum values, indicated on the left-hand side of each plot. (bottom) Smoothed (using the Konno & Ohmachi [117] method) Fourier amplitude spectra (FAS) of the velocity waveforms.

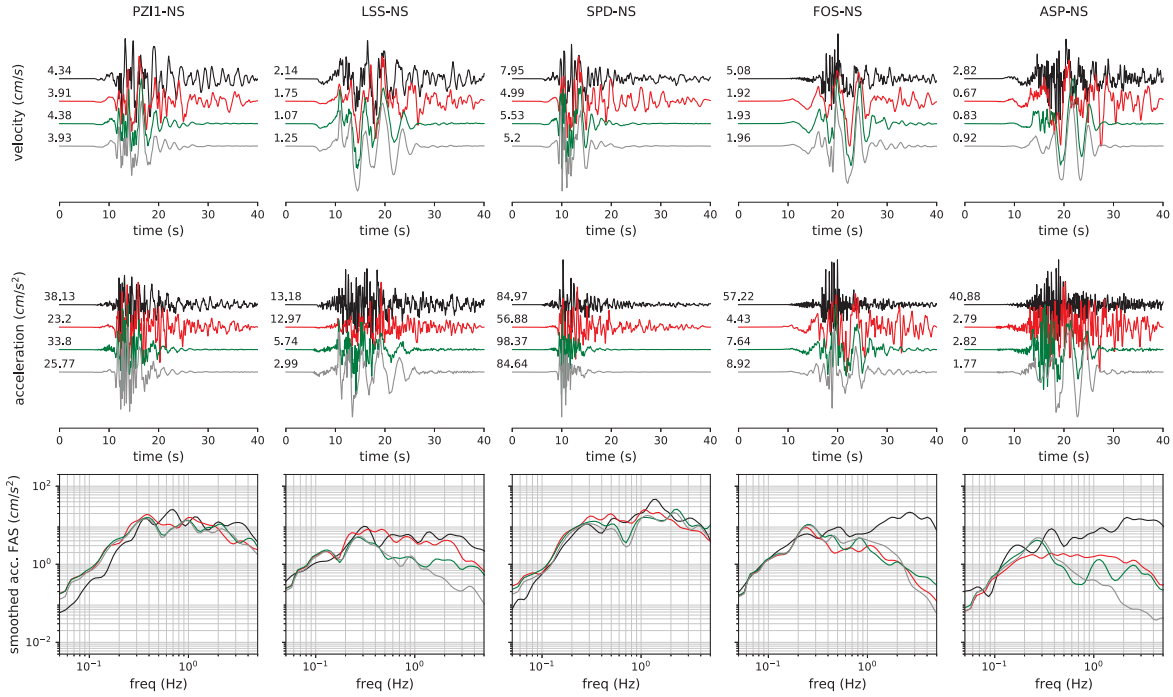

Figure 2.12: Same as Figure 2.8 for stations PZI, LSS, SPD, FOS, and ASP.

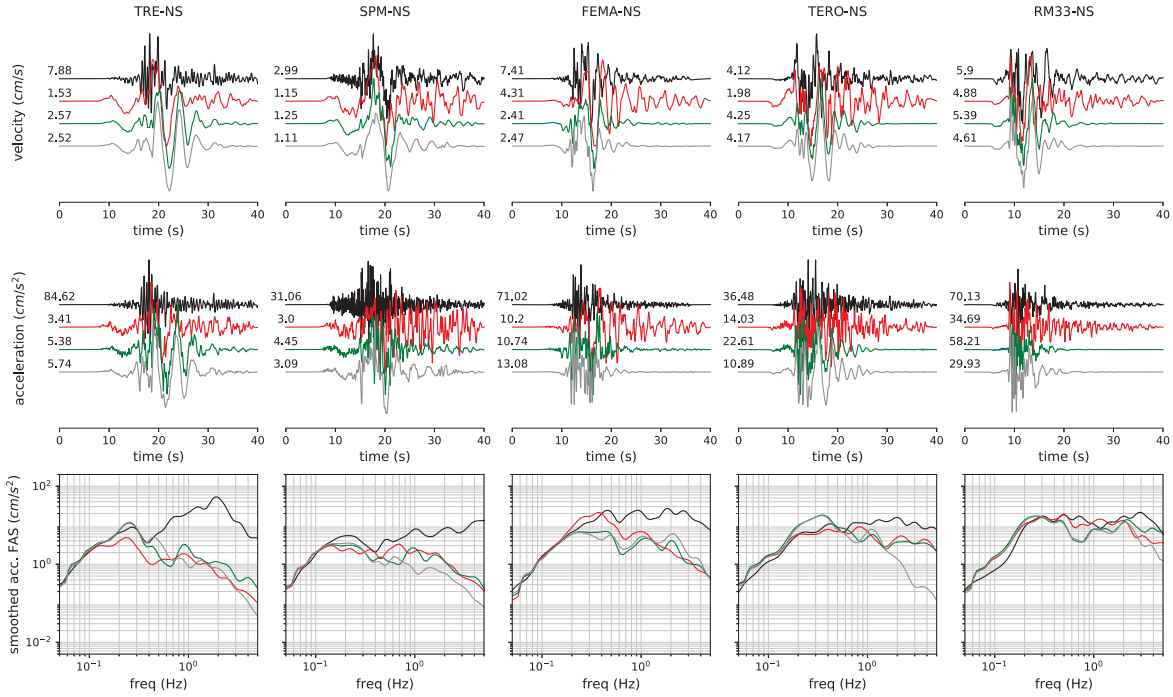

Figure 2.13: Same as Figure 2.8 for stations TRE, SPM, FEMA, TERO, and RM33.

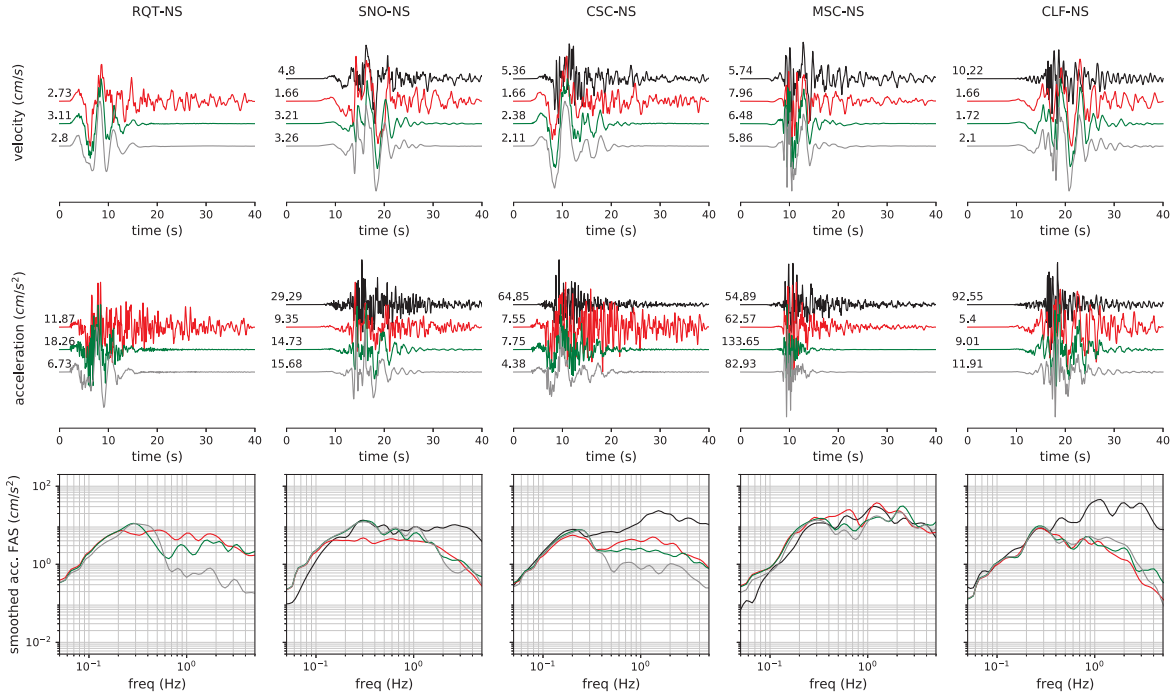

Figure 2.14: Same as Figure 2.8 for stations RQT, SNO, CSC, MSC, and CLF.

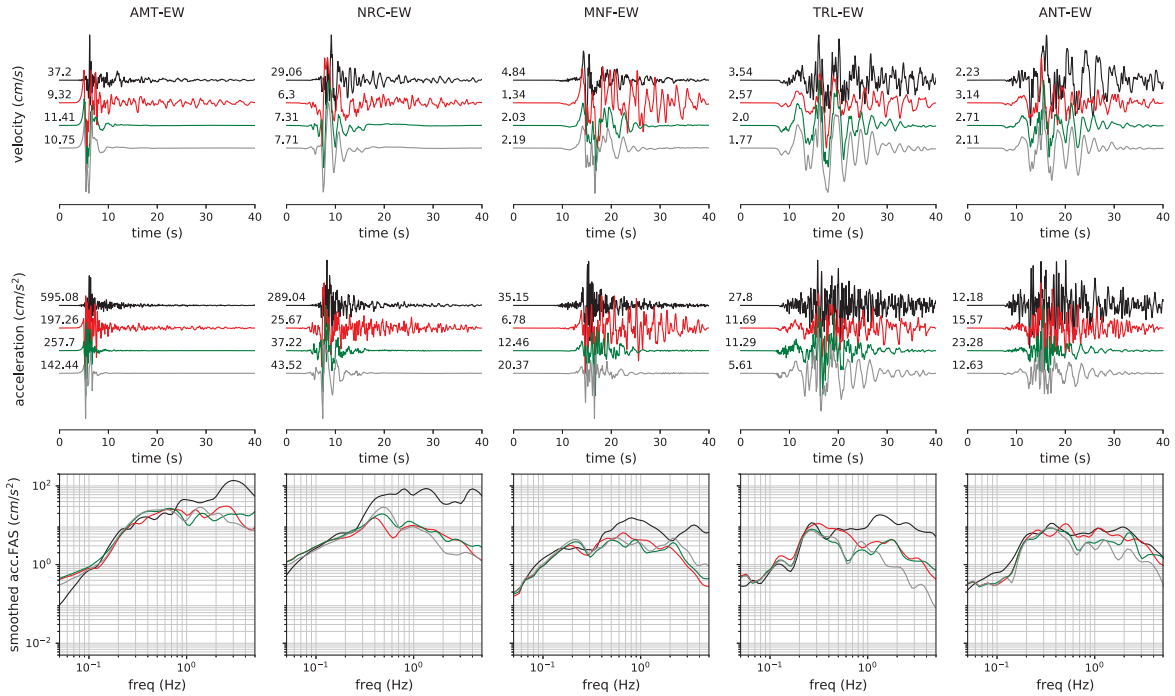

Figure 2.15: Effect of rough fault and topography on the velocity and acceleration waveforms and on the Fourier amplitude spectra. (top, middle) Comparison of synthetic ground-velocity (top row) and acceleration (middle row) waveforms from the broadband rough fault model with topography (red), the broadband rough fault model without topography (green), and the reference model (gray) compared with observations (black). EW component at five selected stations (see Figure 2.1). All waveforms are scaled by their maximum values, indicated on the left-hand side of each plot. (bottom) Smoothed (using the Konno & Ohmachi [117] method) Fourier amplitude spectra (FAS) of the velocity waveforms.

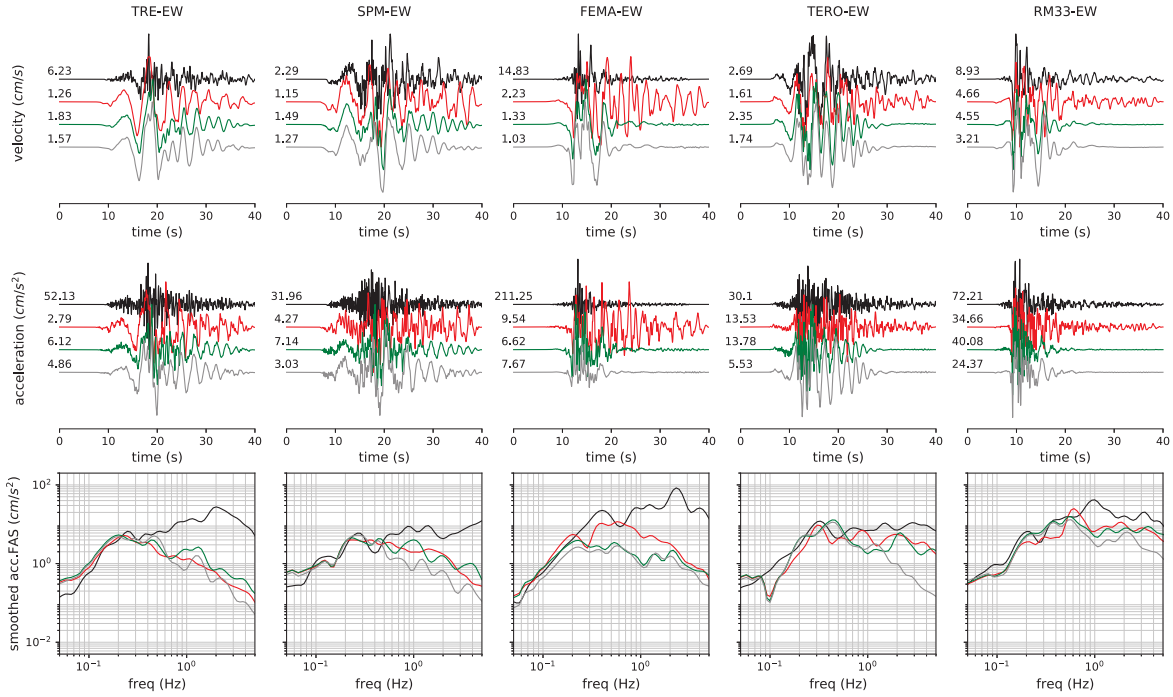

Figure 2.16: Same as Figure 2.13 for stations TRE, SPM, FEMA, TERO, and RM33.

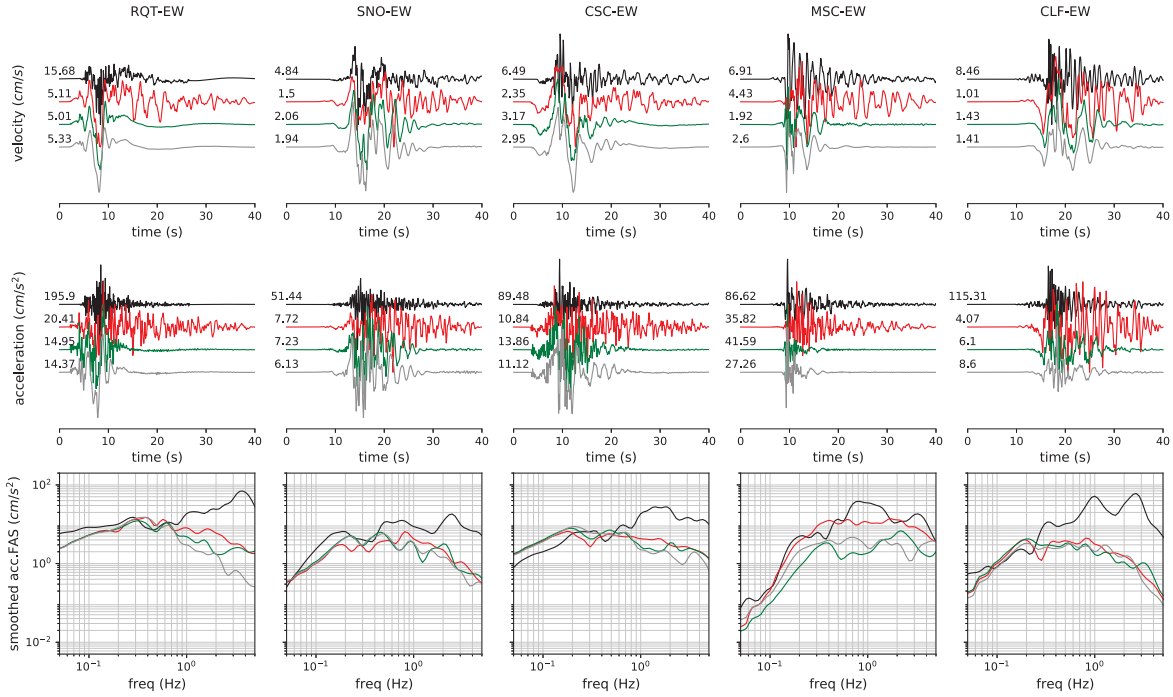

Figure 2.17: Same as Figure 2.13 for stations RQT, SNO, CSC, MSC, and CLF.

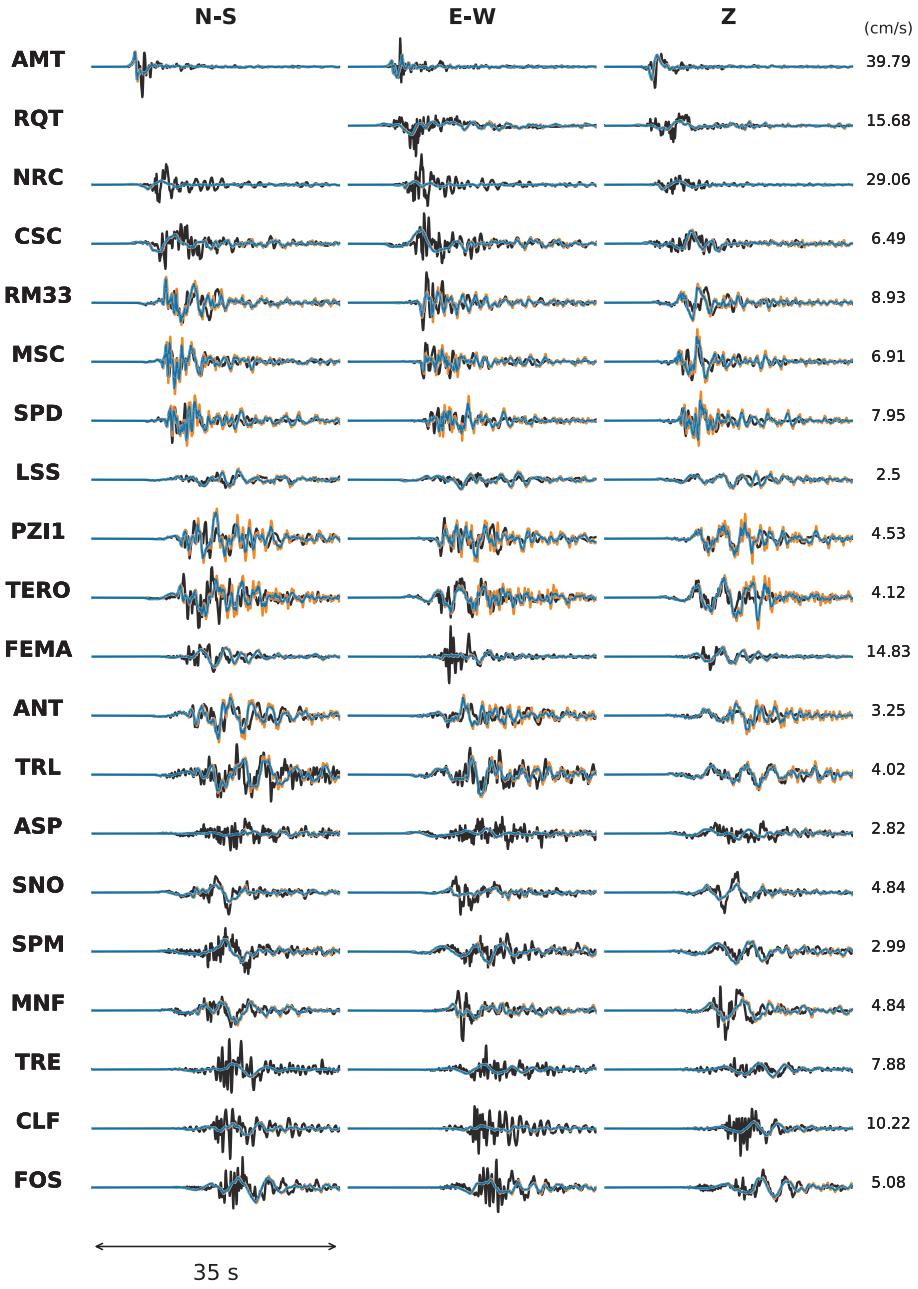

Figure 2.18: Comparison of observed (black) and simulated ground velocities for a planar fault model with topography with (cyan) and without (orange) viscoelastic attenuation at 20 selected stations (Figure 1), ordered by epicentral distance. All observed and synthetic velocity waveforms are scaled by the maximum value of the observed records at each station, indicated in cm/s on the right-hand side of each plot. Observed and synthetic waveforms are band-pass filtered between 0.05 and 5 Hz.

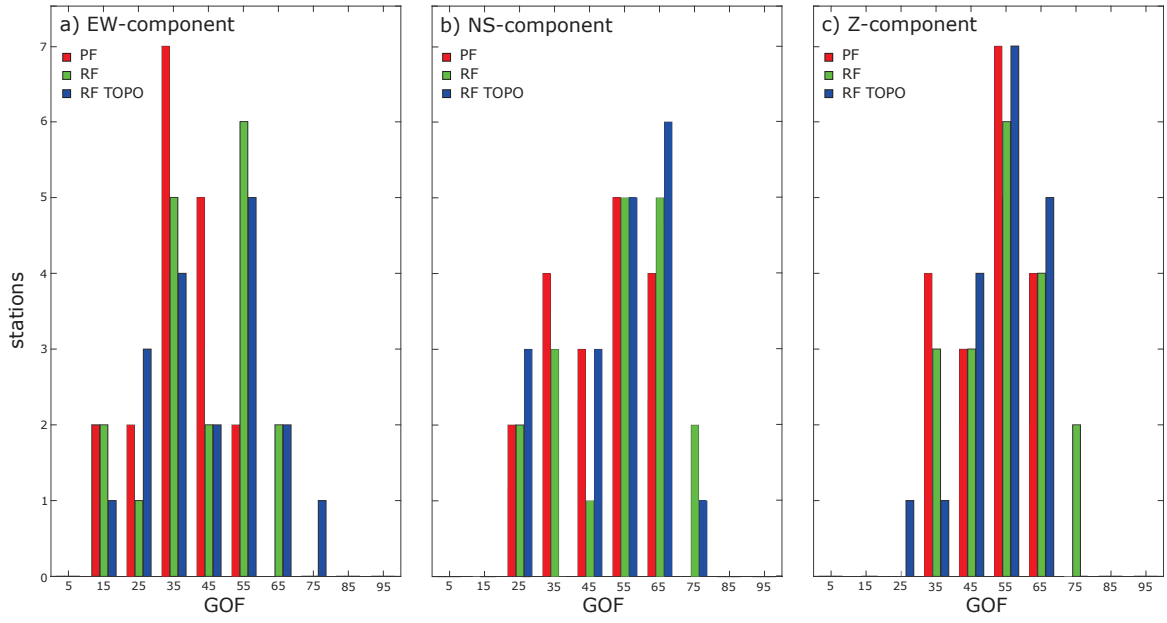

Figure 2.19: Distribution of average Goodness-of-Fit (GOF) for each component and color-coded for the reference model (red), the broadband rough fault model without topography (green), and the broadband rough fault model with topography (blue).

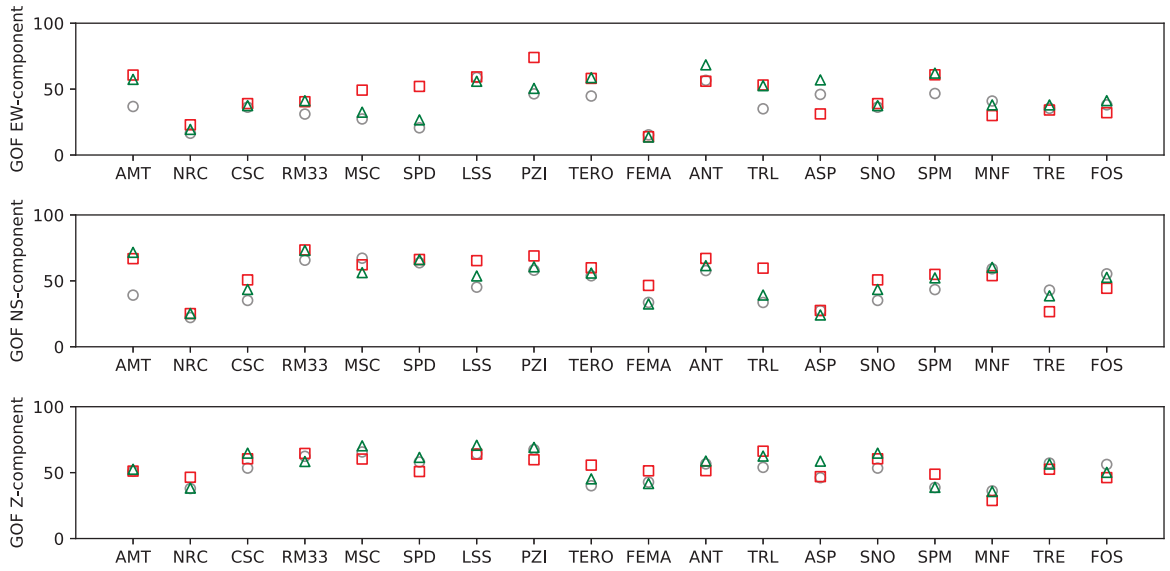

Figure 2.20: Average Goodness-of-Fit (GOF) for each station and component, ordered by epicentral distance, for the reference (gray circles), the broadband rough fault model without topography (green triangles), and the broadband rough fault model with topography (red squares).

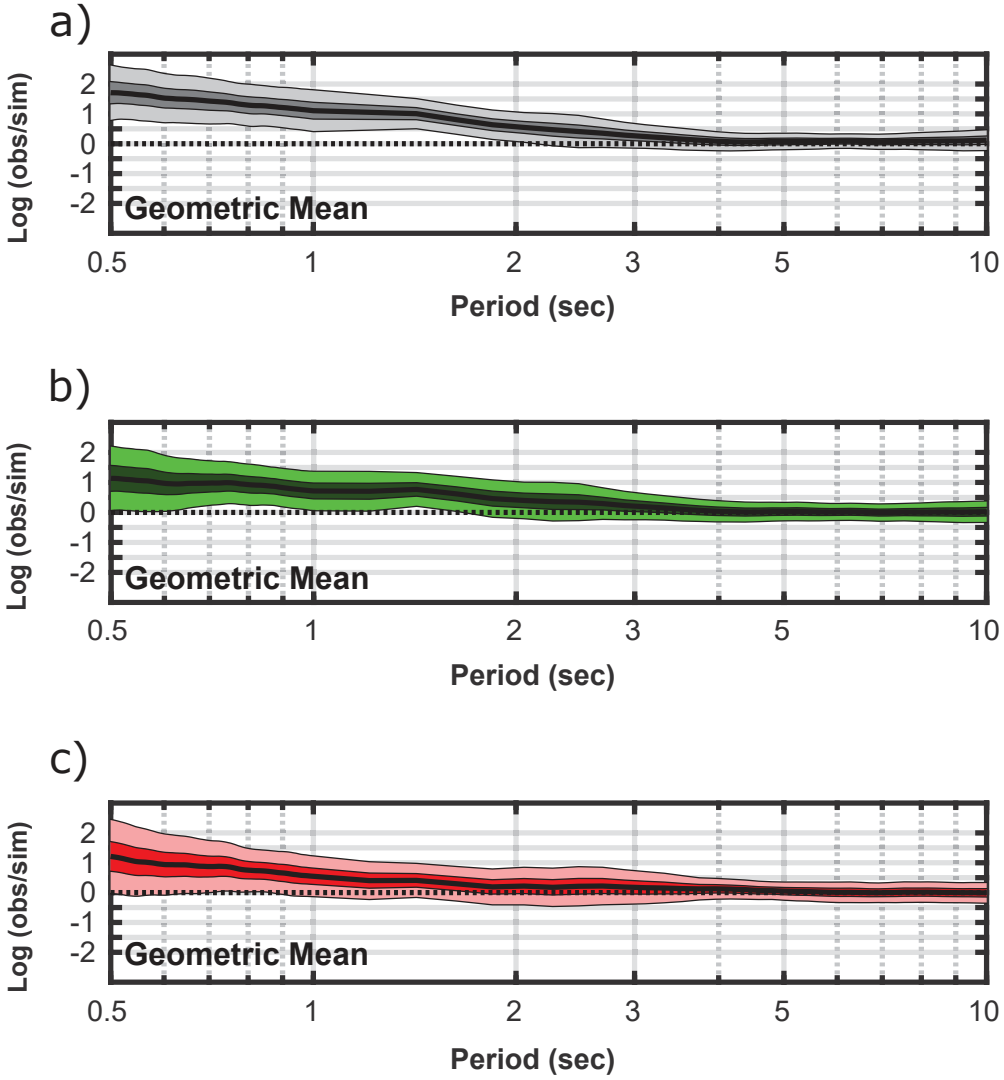

Figure 2.21: The model bias and standard deviation of residuals between observed SA values in the 0.5-10 s period range, averaged over 20 stations and synthetics of (a) reference model, (b) broadband rough fault model without topography, and (c) broadband rough fault model with topography. The bold black line is the median value, the filled area is the 90% confidence interval and the pale filled area is the one-sigma range.

Chapter 3

Dynamics, interactions, and delays of the 2019 Ridgecrest rupture sequence

3.1 Abstract

The observational difficulties and the complexity of earthquake physics have rendered seismic hazard assessment largely empirical. Despite increasingly high-quality geodetic, seismic and field observations, data-driven earthquake imaging yields stark differences and physics-based models explaining all observed dynamic complexities are elusive. Here we present data-assimilated three-dimensional dynamic rupture models of California's biggest earthquakes in more than 20 years: the moment magnitude (Mw) 6.4 Searles Valley and Mw 7.1 Ridgecrest sequence, which ruptured multiple segments of a non-vertical quasi-orthogonal conjugate fault system [189]. Our models use supercomputing to find the link between the two earthquakes. We explain strong-motion, teleseismic, field mapping, high-rate global positioning system and space geodetic datasets with earthquake physics. We find that regional structure, ambient long- and short-term stress, and dynamic and static fault system interactions driven by overpressurized fluids and low dynamic friction are conjointly crucial to understand the dynamics and delays of the sequence. We demonstrate that a joint physics-based and data-driven approach can be used to determine the mechanics of complex fault systems and earthquake sequences when reconciling dense earthquake recordings, three-dimensional regional structure and stress models. We foresee that physics-based interpretation of big observational datasets will have a transformative impact on future geohazard mitigation.

3.2 Introduction

The moment magnitude (Mw) 6.4 Searles Valley foreshock and the Mw 7.1 Ridgecrest mainshock that occurred in California on 4 and 5 July 2019 are prominent examples of large, well recorded earthquakes [189, 95, 87] and provide an opportunity to advance our understanding of the mechanics and regional hazard of active multi-fault systems. The

sequence cascaded across hierarchically interlaced antithetic faults [53], part of the presumably immature Eastern California Shear Zone (ECSZ). The ECSZ accommodates an increasing fraction of regional tectonic forces [256] while developing into a major tectonic boundary. Multiscale block rotation in its transtensional deformation regime leads to ubiquitous conjugate and subparallel strike-slip faulting, which may promote the initiation and segmentation of large earthquakes, which can occur simultaneously or in quick succession [60, 114].

Both earthquakes were highly complex [32], including likely fault reactivation [206, 141]. Peculiarly, the largest events were set apart in time by 34 hours [111, 181] while driving aftershocks, shallow aseismic creep and swarm activity [205, 33]. Numerous inversion-based earthquake models (for example, ref. [238]) use this exceptionally high-quality dataset, but, despite the good coverage of geodetic and seismic observations, the proposed slip models and their interpretations differ starkly. It is still a matter of debate which fault segments actively slipped and which regional conditions promote the general occurrence of conjugate earthquake cascades. Data-driven approaches are inherently limited in their ability to uniquely resolve fault interactions and are specifically challenged by multiple slip episodes occurring close in time and activating partially overlapping fault segments, all common characteristics of earthquake sequences in multi-fault systems. Thus, a unifying approach, capable of jointly explaining independent datasets and intriguing dynamic features, such as the delayed triggering of the mainshock, is required, but remains elusive.

Here we present a tightly data-constrained and physics-based approach that disentangles the competing and non-unique views [238] of the Ridgecrest foreshock and mainshock and their interrelationship, with general implications for the often underestimated hazard posed by multi-fault earthquakes. We address the fundamental questions about the sequence in a data-fused yet physics-based manner, to determine what governs the initiation, propagation and arrest of coseismic slip on immature, geometrically complex faults, how earthquake sequences dynamically interact across multi-fault systems, and the role of heterogeneity in the subsurface and in the ambient stress field, including heterogeneity from historical and recent events, for the dynamics of large earthquakes.

Our supercomputing-empowered three-dimensional (3D) linked foreshock–mainshock dynamic rupture models provide insight into the multi-stage dynamics of how an immature conjugate fault system yields and slides. We reveal foreshock and mainshock dynamics that are characterized by simultaneous rupture of conjugate faults, mixed crack- and pulse-like propagation, and strong interseismic interaction. By combining multidisciplinary and multiscale observations, we constrain the mechanical properties of the fault system to be statically strong but dynamically weak. Dynamic rupture of a statically-strong-yet-dynamically-weak fault system is driven by overpressurized fluids and low dynamic friction in our models. This concept, first proposed to reconcile the San Andreas heat flow paradox [121], allows faults to operate at low average prestress while facilitating multi-fault cascading rupture dynamics [224]. Although dynamic fault weakening may not operate during all natural earthquakes and other mechanisms such as frictional heterogeneity may explain multi-fault ruptures, we show that the interplay of 3D fault stress, strength and geometries remains important even if all faults are dynamically weak.

We demonstrate how a 3D stress model fusing regional tectonics and coseismic and postseismic stress changes of historical earthquakes drives and delays an earthquake sequence through space and time. Our multi-fault model unifies dense strong-motion and teleseismic, field mapping, high-rate Global Navigation Satellite System, and space geodetic foreshock and mainshock datasets with earthquake physics. For comparison in the near- and far-field, we also present a frequency-dependent aftershock-calibrated backprojection analysis [127] and kinematic parametric source inversion (PSI) [86] using strong-motion data, accounting for the geometric fault complexity that we find is required in dynamic modelling.

3.3 From tectonics to dynamic rupture

We apply assimilation methods fusing tectonic, structural, coseismic and interseismic data to jointly inform physics-based dynamic rupture simulations. First, integrating interferometric synthetic aperture radar (InSAR), satellite imagery, relocated seismicity and selected focal mechanisms, we construct [29] (3.7) a non-vertical, quasi-orthogonal cross-cutting 3D fault system (Fig. 3.1). It consists of four geometrically complex fault segments (Supplementary Fig. 3.6), all of which slip coseismically during either the foreshock or the mainshock or both: three northwest–southeast-trending right-lateral faults, F1, F3 and F4, and a conjugate northeast–southwest-trending left-lateral fault, F2. The largest fault, F3, is helically shaped, consistent with the geometry of deep ductile shear localization [129]. We next embed this fault system in a 3D Earth structure combining a 3D community velocity model [125] (3.7) and a two-dimensional (2D) community stress model [253] representing the regional state of stress in the Southern California upper crust (Fig. 3.1a and Supplementary Fig. 3.7). To account for fault-local stress heterogeneity owing to past seismicity, we incorporate a 3D model of the cumulative coseismic and postseismic stress changes of major historical and recent earthquakes spanning approximately the past 1,400 years, extended in the course of this study from ref. [234] (Fig. 3.1b). We combine the resulting heterogeneous ambient stress model with the linear depth dependence of the effective vertical stress (3.7).

There is little consensus about the effective strength of active faults [38]. We demonstrate that a large frictional strength drop, requiring statically strong but dynamically weak faults (Supplementary Table 2), promotes dynamic cascading of rupture across the Ridgecrest system of vastly varying fault orientations. We use a laboratory-based modern friction law (3.7) that features markedly rate-dependent dynamic weakening [45], while being compatible with the high static frictional strength of rocks and multi-fault cascading rupture dynamics [227]. We introduce depth-dependent frictional parameters to account for shallow (above 1.8-km depth) velocity strengthening and along-fault variations in seismogenic depth, as inferred from aftershock locations [189], decreasing from a maximum of about 11 km near the foreshock hypocentre towards north and south (Supplementary Fig. 3.8). Overpressurized fault zone fluids, above the hydrostatic pressure gradient, reduce the apparent strength of faults by decreasing the effective normal stress. Our model

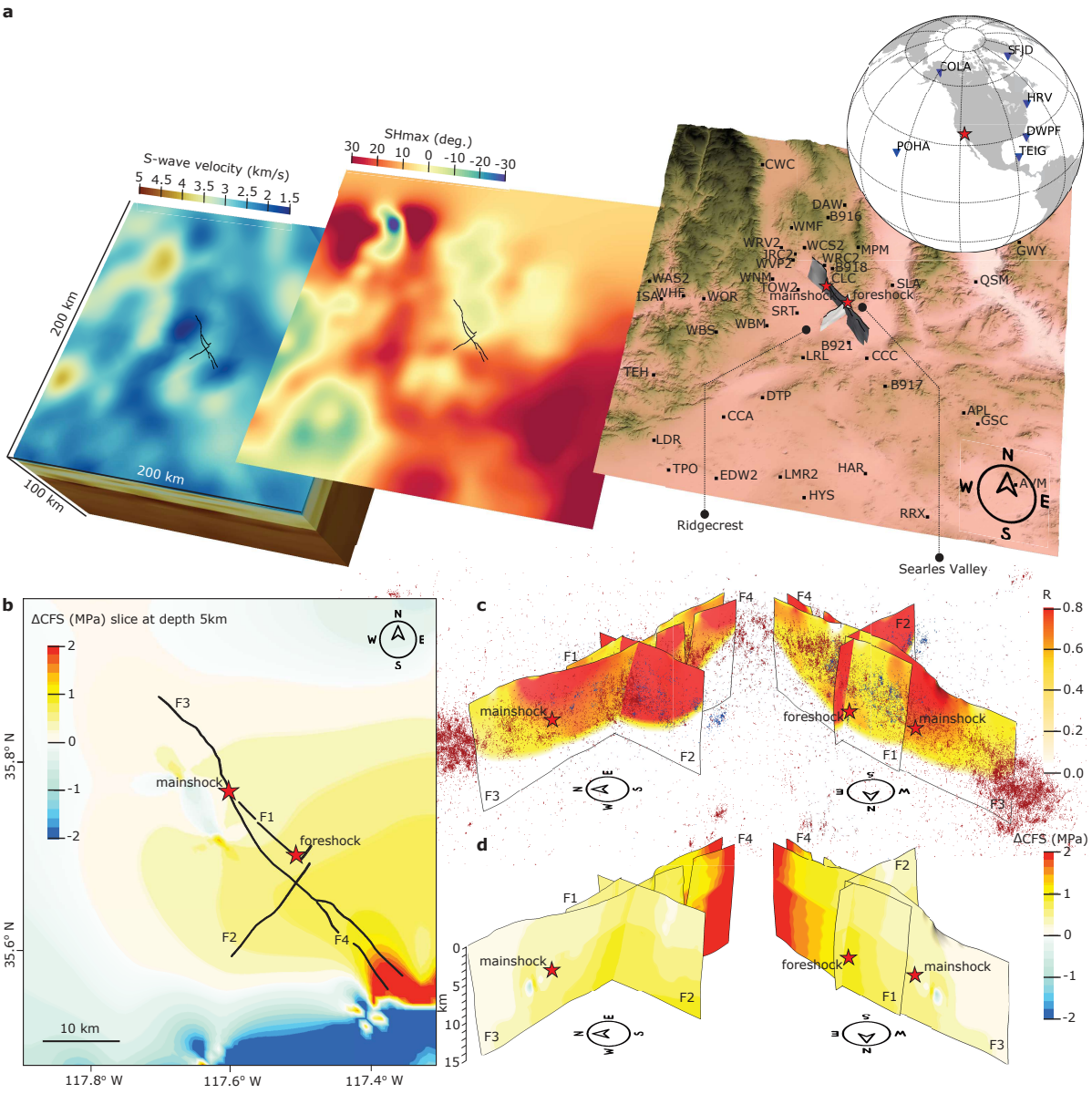

Figure 3.1: Observational constraints for 3D dynamic rupture modelling of the Ridgecrest earthquake sequence. (a) The 3D S-wave velocity model (left; CVM-S4.26 [125]), the 2D model of maximum horizontal stress orientation SHmax (middle; YHSM-2013 [253]) and the study region with geometrically complex fault network (black lines) intersecting topography from SRTM digital elevation model data (right). The chosen strong-motion (black squares) and teleseismic (blue triangles) station locations are shown. (b) The 3D cumulative Coulomb failure stress change ΔCFS owing to major historical and recent earthquakes (Supplementary Table 1 and 3.7), sliced at 5-km depth. (c) Two perspectives of the relative prestress ratio R, which is modulated by fault geometry and heterogeneous ambient stress. The blue and red dots are relocated hypocentres of the foreshock and mainshock aftershocks [189], and the red stars are the foreshock and mainshock hypocentre locations [200]. (d) ΔCFS resolved on the fault network, assuming a rake of -170° on fault segments F1, F3 and F4, and 0° on F2.

suggests that the Ridgecrest fault system is embedded in a region of elevated pore fluid pressure, with fluid pressure higher on the foreshock faults than on the mainshock ones (Supplementary Fig. 3.9).

In dynamic rupture models, the ratio of potential stress drop to frictional breakdown strength (R) is a key parameter controlling earthquake kinematics, dynamic triggering ('cascading') potential and dynamic slip tendency (3.7). We prescribe the prestress relative to strength drop on a virtual, optimally oriented fault within the model domain as $R_0 = 0.8$. This introduces spatially variable relative fault prestress $R \leq R_0$ (Fig. 3.1c), and brings more optimally oriented fault segments locally close to being critically prestressed. The orientation of all regional principal stress components, the relative magnitude of the intermediate principal stress, the choice of R_0, and the cumulative coseismic and postseismic stress changes (Fig. 3.1d) together define the complex 3D pre-sequence stress state that governs the dynamics of the sequence. The conjugate fault F2 and central portions of F3 are well oriented, as illustrated by R locally approaching $R_0 = 0.8$, and simultaneously close to critically prestressed, as the ratio of shear to effective normal prestresses is high (Supplementary Fig. 3.10). In contrast, F1, F4, and the southern and northern parts of F3 show considerably lower R and are therefore further from critical prestress, reflecting geometrical deviation from optimal orientation with respect to the complex 3D stress model.

We use data-inferred key characteristics of both earthquakes, specifically the hypocentre and aftershock locations [189, 200], moment release rate [32, 77, 131], and the delay between foreshock and mainshock, to find the required dynamic parameters R_0, pore fluid pressure and rupture initiation overstress using several systematic dynamic rupture simulations (3.7). We do not invert space geodesy, strong-motion, high-rate global positioning system (GPS) or teleseismic recordings, but use them for retrospective validation of our earthquake source models. Although the need for ad hoc rupture nucleation at prescribed hypocentres is a limitation of dynamic rupture simulations (3.7), analysing the minimum perturbation leading to self-sustained foreshock and mainshock earthquake dynamics matching observations provides insights into the underlying physics of the cascading rupture sequence. We find that our observationally constrained model balances the dynamic viability of sustained foreshock and mainshock dynamic rupture scenarios with realistic stress drop, rupture speed and fault slip.

3.4 Foreshock cross-fault earthquake dynamics

Our earthquake model of the Mw 6.4 Searles Valley foreshock features highly complex dynamics across conjugate faults while failing to coseismically trigger the mainshock. Joint seismological and geodetic [131], and conceptual dynamic [133, 40] models imply a cross-fault rupture path, initiating as deep slip on a right-lateral fault segment (F1; Fig. 3.2a) and continuing on an almost orthogonally interlocked left-lateral segment (F2). Although the F2 surface rupture was traced, satellite images[151] give no indication of the surface rupture along F1.

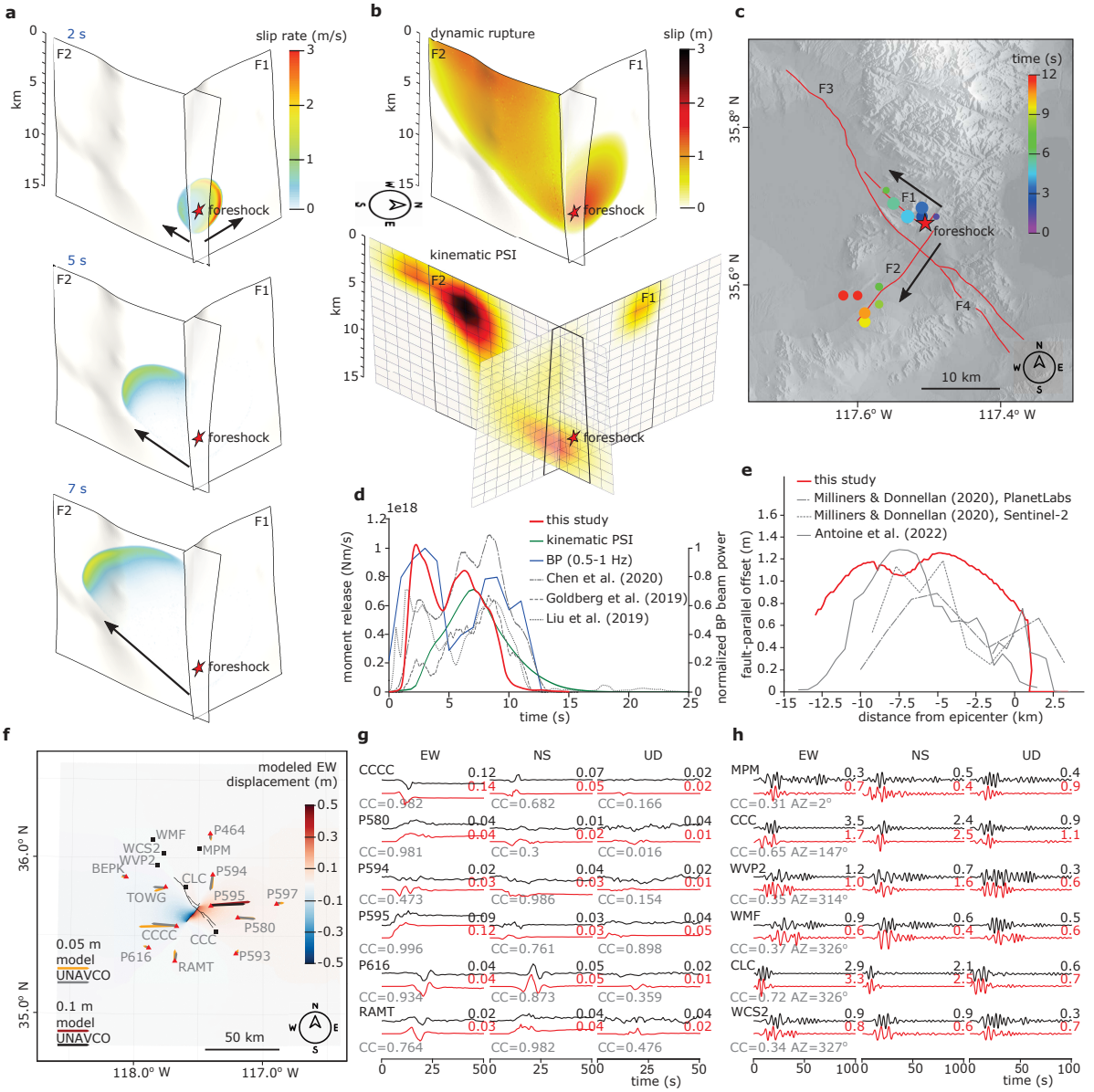

Figure 3.2: Dynamic rupture scenario of the Searles Valley foreshock and comparison with observations. (a) Snapshots of absolute slip rate (see also Supplementary Video 1). (b) Fault slip of the dynamic rupture model (top) and kinematic PSI (bottom). (c) Aftershock-calibrated backprojection (0.5–1 Hz). The black arrows show the rupture directions. (d) Dynamic rupture moment release rate and backprojection beam power (BP) compared with kinematic models [32, 77, 131] including PSI. (e) Fault-parallel surface offsets along F2 (red is from the dynamic rupture model measured orthogonally across the fault trace 400 m from it, and grey is from the optical images using the orbits of PlanetLabs and Sentinel-2 [151]), and on-fault slip estimated from high-resolution optical satellite image correlation [9]. (f) Horizontal coseismic surface deformation. Orange and red vectors are the modelled static horizontal displacements scaled by 0.05 m and 0.1 m. The grey and black vectors show UNAVCO processed data. The red triangles and black squares are the GPS and strong-motion stations shown in g and h. (g) Comparison of 1-Hz continuous GPS observations [146] (black) and synthetics (red) component-wise cross-correlation coefficients (CC, grey; 3.7). (h) Comparison between synthetic (red) and recorded regional seismograms (black), band-pass filtered between 0.1 Hz and 0.3 Hz, sorted by their azimuth relative to the foreshock epicentre. CC (grey) from 300-s three-component waveforms. All time series in g and h are normalized by peak amplitudes (values, top right).

Our spontaneous dynamic rupture simulations reproduce conjugate rupture observations, and find that foreshock–mainshock fault system interactions are important in facilitating the subsequent mainshock dynamics. Rupture initiates (3.7) close to the F1–F2 fault intersection, which may be a general prerequisite for simultaneous rupture of conjugate faults as suggested from field observations [60]. Early and deep right-lateral dynamic rupture across F1 activates the conjugate, critically prestressed left-lateral F2 leading to complex foreshock slip evolution (Fig. 3.2a). At 2 s, rupture takes the form of a near-symmetric, circular crack propagating across both faults, but with higher slip rates (up to about 3 m s^{-1}) on F1 (Fig. 3.2a). At 5 s, slip on F1 spontaneously ceases without reaching the surface owing to this fault's non-optimal orientation and lower-than-critical prestress. In contrast, dynamic rupture on F2 continues to the southwest and up-dip and breaks the surface, until terminated by pronounced stopping phases. Importantly, F2 rupture takes the form of a narrow slip pulse which re-accumulates a significant amount of shear stress across F2, aiding subsequent reactivation[62] during the mainshock.

The physics-based dynamic model agrees with data-driven kinematic models that assume comparable fault geometries. Figure 3.2b showcases the overall agreement of the final slip distribution with a newly inferred kinematic PSI of strong-motion data (3.7). The dynamic rupture model yields depth-confined (8–11 km) right-lateral slip on F1 and widespread left-lateral slip on F2 including pronounced surface rupture (Fig. 3.2b). The maximum fault slip reaches about 1.5 m on F1 near the hypocentre and about 1 m on F2 near the surface. The dynamic rupture scenario generates Mw 6.5, in agreement with observations[32, 77, 131]. Dynamic rupture speed increases from 1.5 km s^{-1} to 2.5 km s^{-1} with distance from the hypocentre, with an average fault-local speed of 2 km s^{-1} (Supplementary Fig. 3.11). Although a direct comparison with observations is challenged by the medium size and multi-fault conjugate dynamics of the foreshock, the fault-local rupture speed agrees with the rupture velocity inferred in the PSI and other kinematic models (2.4–2.6 km s^{-1})[32]. Local differences of the PSI model include lower kinematic slip at depth on F1 and F2 and a more localized slip patch at shallow depth on F2. The latter is probably owing to the Occam's razor principle implicitly preferring simple, localized slip distributions (3.7).

Our aftershock-calibrated backprojection (Supplementary Table 3 and 3.7) of Alaska array data implies orthogonal rupture during the foreshock (Fig. 3.2c), in agreement with our modelled earthquake dynamics. Backprojection captures an approximately 6-km northwest-propagating rupture on F1 followed by rupture to the southwest tip of F2. From beam power analysis (Fig. 3.2d), the inferred high-frequency radiators on F1 and F2 appear equally significant. The normalized backprojection beam power resembles the apparent array moment rate of the dynamic rupture model, specifically its two distinct peaks linked to consecutive slip on F1 and F2. In contrast, dominating slip on F2 is characteristic in other published kinematic models (Fig. 3.2d) and observational moment rates show a weaker early phase than our dynamic model. This may reflect the generally lower sensitivity of kinematic methods to deep slip, especially when overprinted by a dominating, shallow rupture. Contrarily, in our dynamic model, rupture along F1 is required to load and trigger rupture on F2.

The spontaneous dynamic rupture scenario reproduces key characteristics of space geodesy, strong-motion, high-rate GPS and teleseismic recordings. The modelled fault-parallel offsets compare well with subpixel satellite image correlation measurements along the surface rupture of F2 [151] (Fig. 3.2e and Supplementary Fig. 3.12a,b). Also, the modelled static surface deformation is in agreement with geodetic observations from Global Navigation Satellite System and satellite imagery (Fig. 3.2f), and dominated by large, shallow slip on F2. We observe a striking match (Fig. 3.2g) between synthetic and observed near-fault 1-Hz continuous GPS data[146]. The synthetics capture the shape and amplitude of characteristic waveform pulses well, such as the first EW strong pulse at stations CCCC and P595. Synthetic velocity time series agree with regional strong-motion data (Fig. 3.2h and Supplementary Fig. 3.13) and long-period teleseismic recordings (Supplementary Fig. 3.14a).

3.5 Dynamics of the Ridgecrest mainshock

We find that a realistic dynamic rupture scenario of the Ridgecrest mainshock needs to fully account for the stress changes due to the Searles Valley foreshock in addition to the regional complex 3D structure and ambient stress (Supplementary Figs. 3.15-3.17, and 3.7). Modelling both events in the same dynamic rupture simulation, we find that the foreshock does not dynamically trigger the mainshock. The additional shear stress relative to our assumed fault strength and 3D prestress required to activate F3 at the mainshock hypocentre is 18 MPa peak and about 3 MPa averaged across the numerically determined minimal-sized and smooth critical perturbation area (Supplementary Fig. 3.18 and 3.7). Locally higher fluid pressure reducing effective normal stress, a locally statically weaker fault or combinations of heterogeneities may provide equivalent nucleation mechanisms at lower shear- stress increase.

Figure 3a and Supplementary Video 2 illustrate the modelled complex mainshock earthquake dynamics. During the first 5 s, a crack-like rupture expands bilaterally on F3, then smoothly terminates to the north owing to locally lower prestress and less-optimal fault orientation (Supplementary Fig. 3.10). The pronounced stress shadow of the Mw 6.4 foreshock (Fig. 3.4) leads to near-complete termination of southwards rupture in the vicinity of the conjugate F2–F3 intersection, except for decelerated slip at greater depth (at 6.5 s; Fig. 3.3a). This deep, persistent and 'tunnelling' rupture pulse slowly regrows towards the southeast until the northwest segment of F3 is entirely ruptured at 8.5 s. The conjugate segment F2 is re-activated while the main rupture front passes, aided by dynamic frictional restrengthening during the foreshock pulse-like rupture. Shallow parts of F4 are dynamically unclamped and slip during rupture of F3. Spontaneous dynamic rupture accumulates a continuous slip patch spanning F3 (Fig. 3.3b), modulated by the combined effects of fault geometry, ambient stress and structural heterogeneities, and foreshock stress shadows. Similarly to the foreshock, the modelled mainshock slip distribution agrees with kinematic models that assume comparable fault geometries within the range of inherent uncertainties, such as our strong-motion PSI model (Fig. 3.3b). Conjugate fault reactivation

is suggested by our PSI, in our low frequency (0.1–0.5 Hz and 0.25–1 Hz) backprojection results (Fig. 3.3c and Supplementary 14), as well as from joint inversion of InSAR, optical imagery and GPS measurements [141].

Rupture speed increases by about 25% from northwest to southeast and is strongly depth dependent. The average apparent rupture speed is 2.5 km s^{-1} (Supplementary Fig. 3.11) agreeing with our PSI model (2.1–2.4 km s^{-1}) and backprojection (2.5 km s^{-1}) (Supplementary Fig. 3.19d). The moment release rate of our dynamic model, beam power evolution in our backprojection and other kinematic models including PSI (Fig. 3.3d) consistently feature two peaks, which resemble the dynamic delay of F3 rupture when crossing the conjugate intersection with F2 in our model. Our modelled shallow rupture is slower and appears to agree better with data-driven estimates [189, 32, 77, 131], which may be due to less well constrained deeper fault zone geometry and structure.

Our synthetic F3-parallel surface offsets (Fig. 3.3e) reflect the along-strike dynamic rupture variability and peak close to the epicentre, in overall agreement with satellite images [151]. The physics-based model matches coseismic geodetic observations, such as the orientation of the observed GPS displacements (Fig. 3.3f), surprisingly well. Although forward modelling overshoots some static GPS amplitudes, the modelled fault-parallel surface displacements are comparable with satellite imagery (Supplementary Fig. 3.12c,d). The dynamic model reproduces key characteristics of continuous GPS (Fig. 3.3g), strong-motion (Fig. 3.3h and Supplementary Fig. 3.20) and teleseismic waveforms (Supplementary Fig. 3.14b). Pulse-like ground motion, with possibly increased damaging potential, was identified in near-fault observations of both earthquakes [15]. We dynamically reproduce such strong impulsive signals at stations CLC, the closest station to the mainshock epicentre, MPM, WVP2, WMF and WCS2 in the northwest extension of rupture on F3, and CCC, close to the southeast tip of rupture on F4 (Fig. 3.3h), owing to a combination of partially pulse-like rupture, fault reactivation, strong directivity and near-source fling effects.

3.6 Conversations between earthquakes

The average dynamic on-fault stress drop is 4 MPa and 5.4 MPa during spontaneous foreshock and mainshock rupture, respectively, and varies with depth and along-strike for all activated faults (Supplementary Fig. 3.21). This 30%-higher mainshock stress drop directly relates to our dynamic models requiring differences in static pore fluid pressure: the mainshock faults F3 and F4 are governed by an equivalently 30%-lower pore fluid pressure than foreshock faults F1 and F2 (Supplementary Fig. 3.9c) to achieve realistic levels of fault slip, stress drop and dynamically viable rupture cascading for both events in the same model.

Foreshock dynamic rupture induces an absolute shear stress perturbation of at most approximately 0.8 MPa at the mainshock hypocentre (Fig. 3.4a). With peak normal stress changes of about 0.2 MPa additionally clamping and unclamping F3 (inset of Fig. 3.4a), both perturbations are not sufficient to dynamically trigger the mainshock rupture.

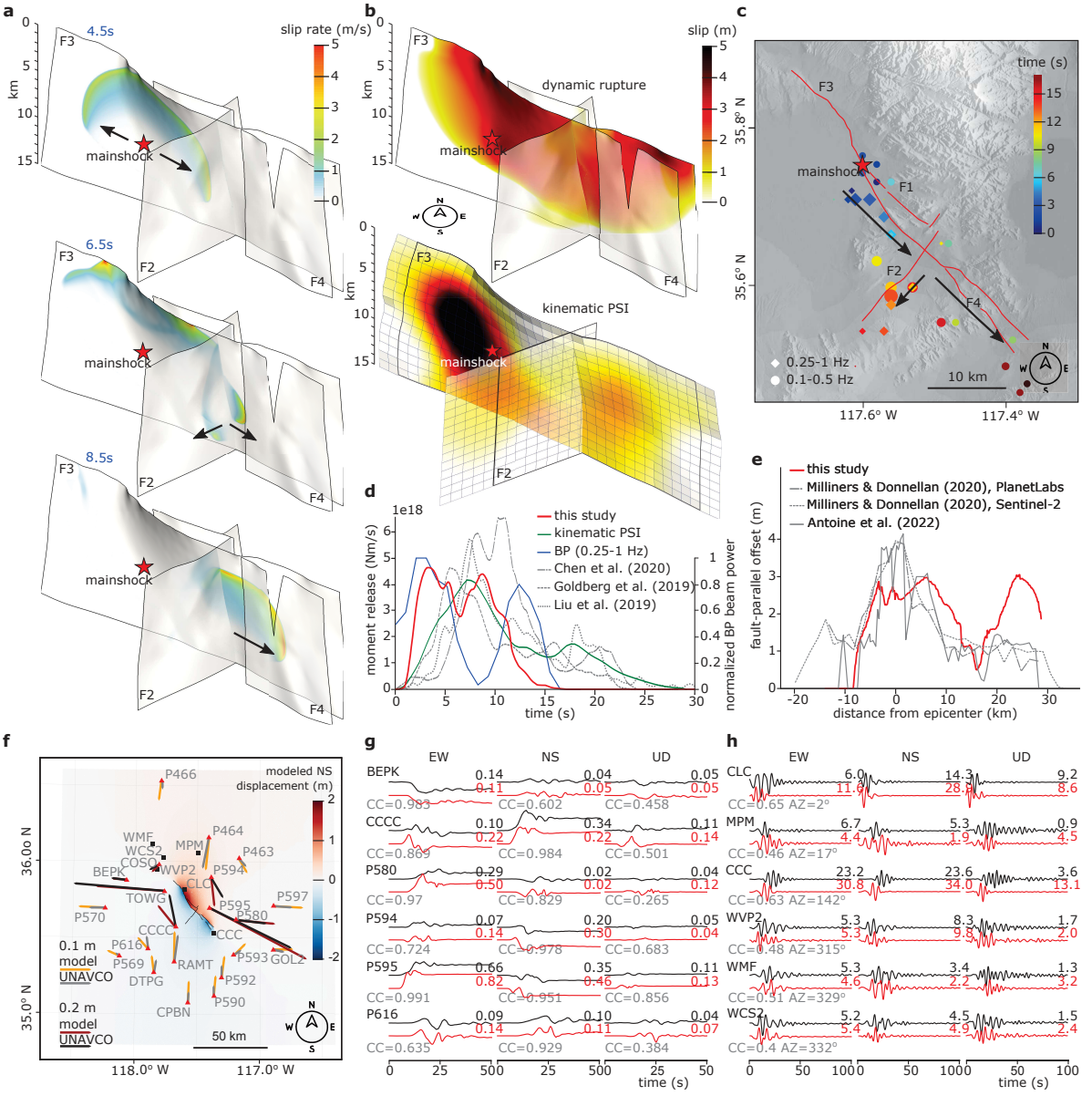

Figure 3.3: Dynamic rupture scenario of the Ridgecrest mainshock and comparison with observations. The details are the same as in Fig. 3.2. (a) Snapshots of absolute slip rate (see also Supplementary Video 2). (b) Fault slip of the dynamic rupture model (top) and kinematic PSI (bottom). (c) Aftershock-calibrated backprojection (based on 0.1–0.5 Hz and 0.25–1 Hz frequency bands, respectively). (d) Dynamic rupture moment release rate and backprojection beam power compared with kinematic models. (e) Fault-parallel surface offsets along F3. (f) Horizontal (NS) coseismic surface deformation. Synthetic horizontal displacement vectors are scaled by 0.1 m and 0.2 m and the underlying map view shows modelled NS displacements. (g) Comparison of synthetic (red) and 1-Hz continuous GPS observations [146] (black). (h) Comparison between synthetic (red) and recorded regional seismograms (black).

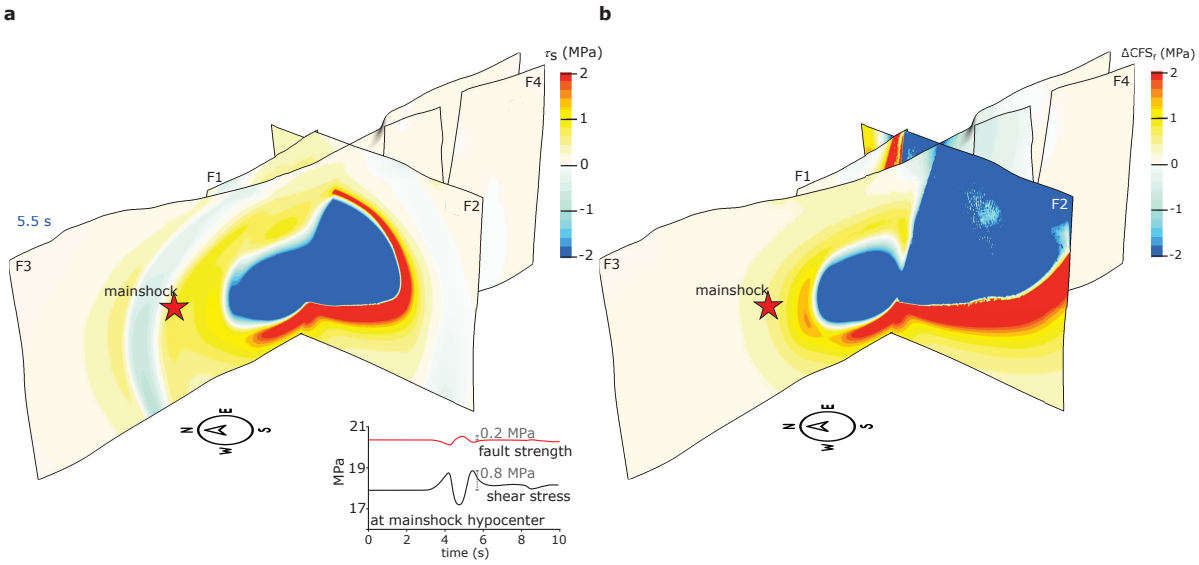

Figure 3.4: Coseismic and postseismic stress changes. (a) Along-strike dynamic shear stress perturbation after 5.5 s of foreshock dynamic rupture. Inset: evolution of dynamic shear stress and fault strength during the first 10 s of foreshock dynamic rupture at the mainshock hypocentre (red star). (b) Post-foreshock scalar Coulomb failure stress changes ΔCFS_f, calculated as $\Delta CFS_f = \Delta\tau - f'\Delta\sigma_n$, where $\Delta\tau$ and $\Delta\sigma_n$ are the total shear and normal fault stress change, and $f' = f(1-\gamma) = 0.4$ is the effective friction coefficient. The colour bar is saturated at ± 2 MPa.

Although our model suggests that dynamic triggering of the mainshock is mechanically inconceivable, it also shows that the complex foreshock Coulomb stress changes bring the mainshock hypocentral area closer to failure: the mainshock hypocentre of F3 is located within a narrow band experiencing positive Coulomb stress change of up to +0.25 MPa (Fig. 3.4b and 3.7).

The modelled foreshock rupture spontaneously terminates on F1, without reaching the surface and within about 3-km horizontal distance to the F3 mainshock hypocentre. This gap in dynamic slip agrees with the inferred gap in relocated aftershocks following the foreshock [189], which was successively filled by a series of moderate-sized earthquakes [220], including an Mw 5.4 earthquake within 2 km of the mainshock hypocentre. The static Coulomb stress changes of this event, however, were found to be negative at the mainshock hypocentre [111], although not well constrained.

Our models do not include stress changes due to aseismic processes such as postseismic slip and deep fault creep. The shear stress carried by afterslip is potentially considerable, implying interaction of coseismic and postseismic slip and their stresses [181]. We analytically estimate [75] (3.7) a peak shear stress increase of 2.5–4.5 MPa for an average afterslip creep front speed of 3 km in 34 h and our assumed effective normal stress of 20.5 MPa at 8-km hypocentral depth. Seamlessly modelling the full spectrum of slip will be important to capture the interactions between foreshocks, mainshocks and aftershocks [255, 179].

The distribution of surface rupture and damage mapped from field and aerial observations [189, 176, 214] (Fig. 3.5a,c) align with our prescribed fault geometries and the modelled dynamically induced off-fault yielding (3.7), which accumulates in the vicinity of complexities in fault system geometry (Fig. 3.5b). The moment contribution of off-fault plastic strain (3.7) in our models is non-negligible, accounting for 3% and 8% of the total seismic moments of the modelled foreshock (Mw 6.45) and mainshock (Mw 7.01), respectively. We observe a shallow slip deficit (SSD) of up to 20% above 2-km depth (inset in Fig. 3.5b), which agrees with joint GPS, ground motion and InSAR inversion [181].

We showcase the sensitivity of our physics-based models in four alternative scenarios including: mainshock dynamic rupture models (1) not accounting for the foreshock stress changes (Supplementary Fig. 3.15); (2) in addition not incorporating the long-term ΔCFS (Supplementary Fig. 3.16); and combined foreshock and mainshock models (3) omitting the long-term ΔCFS (Supplementary Figs. 3.17 and 3.22); and (4) loaded with an alternative community ambient stress model (Supplementary Fig. 3.23). Local rupture dynamics as well as the dynamic activation of segments of the sequence change when key modelling ingredients are altered (Supplementary Fig. 3.24 and 3.7). In particular, not incorporating the long-term ΔCFS prevents correctly capturing the conjugate, partially surface-breaking character of the foreshock rupture.

Using a rate-and-state friction law with strong velocity weakening facilitates the concept of statically strong and dynamically weak faults. If we assumed higher dynamic strength, our relative prestress would decrease (equation ((3.9)) and 3.7). The dynamic rupture cascading potential may then be restored by local stress, strength or pore fluid pressure changes reflecting natural fault zone heterogeneity. For example, concentrating relative prestress at depth would allow us to approximate the expected effects of deep aseismic

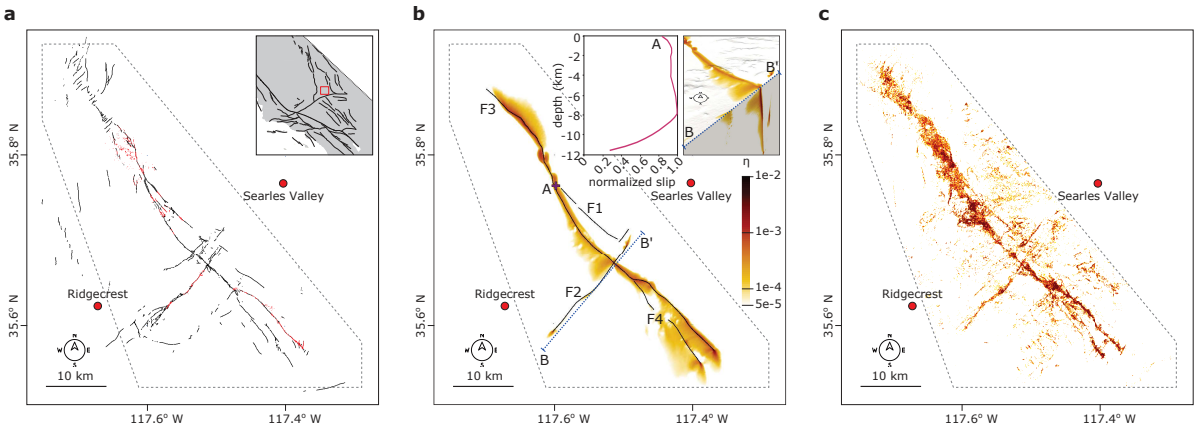

Figure 3.5: Off-fault surface deformation and SSD. (a) Surface rupture mapping from field observations (black) [176] and high-resolution aerial imagery (red) [188]. Inset: location within the ECSZ. (b) Modelled off-fault plastic strain, quantified as η (3.7). Insets: depth profile of normalized slip at the epicentre (red cross at A; left) and cut-away view combining a map view and a vertical slice through the flower-like damage zone (accumulated off-fault plastic strain η; right). (c) Damage proxy map [189] generated from preseismic and postseismic InSAR coherence data.

creep [224, 129].

By assimilating models and data of structural characteristics, tectonic stress, seismogenic depth and long-term stress changes, we constrain multi-fault dynamic rupture scenarios that self-consistently intertwine the 2019 Searles Valley and Ridgecrest multi-fault earthquake dynamics, and unify seismic, geodetic and geological observations. The match with observations, achieved across scales, is remarkable, given that we do not solve an inverse problem. Including small-scale heterogeneities may improve physics-based synthetics at higher frequencies [214]. Our approach demonstrates that data-driven and physics-based modelling can be combined to shed light on the underlying physics of cascading multi-fault earthquake sequences. Our results imply that the long-term and short-term as well as the dynamic and static fault system interaction are crucial for future seismic hazard assessment of active multi-fault systems.

3.7 Methods

3.7.1 Numerical method

We solve the nonlinearly coupled spontaneous dynamic rupture and seismic wave propagation problem with high-order accuracy in space and time using the open-source software SeisSol [49, 24, 97, 184, 230, 118]. SeisSol uses the arbitrary high-order accurate derivative discontinuous Galerkin method [49] and end-to-end optimization for high-performance-computing infrastructure [24, 97, 184, 230, 118]. SeisSol employs fully non-uniform unstructured tetrahedral meshes that statically adapt to geometrically complex 3D geolog-

ical structures, such as non-planar mutually intersecting faults and topography. SeisSol is verified in a wide range of community benchmarks [165] by the Southern California Earthquake Center (SCEC) and US Geological Survey Dynamic Rupture Code Verification project [90, 89].

We link the foreshock and mainshock dynamic rupture earthquake models in the same simulation to account for the dynamic and static stress changes of the foreshock rupture in our scenario of the mainshock. Owing to the lack of intermediate, spontaneous dynamic triggering of the mainshock in our models, we quantify the required additional prestress to initiate the mainshock at the mainshock hypocentre at 100 s after initiating the foreshock. This time span ensures that all transient seismic waves emitted during the foreshock have left the model domain.

3.7.2 Fault geometry

We use a surface fitting technique [29] to generate a 3D geometric model independently of a priori structural interpretation of the conjugate fault network that may have ruptured during the 2019 Ridgecrest sequence (Supplementary Fig. 3.6a). Our fault model is based on relocated earthquake hypocentre locations [189] combined with earthquake focal mechanisms [200] and fault surface traces. We map fault surface traces from a combination of InSAR data [232], public satellite imagery (`https://earth.google.com/web/`) where pre- and post-earthquake images can be compared, private satellite imagery [173], and digital elevation models (`https://apps.nationalmap.gov/viewer/`). To map the foreshock faults, we use only hypocentres and focal mechanisms of those events that occurred in-between the foreshock and mainshock. For the mainshock faults, we use only aftershocks that occurred during the first 48 h after the mainshock. Surface traces are set as 3D fixed constraints. We use the software SKUA-GOCAD as the modelling environment. The model is composed of four geometrically complex fault segments (Fig. 3.1 and Supplementary Fig. 3.6a): three northwest–southeast-trending faults (F1, F3 and F4) and a conjugate northeast–southwest-trending segment (F2). The largest fault, F3, is about 45-km long (Supplementary Fig. 3.1a). Its dip varies from about 80° southwest in its northern part to about 70° northeast south of the mainshock hypocentre, which results in a helical fault geometry [129, 239]. F1, an approximately 15-km-long segment parallel to F3, and F2, an approximately 20-km-long conjugate segment, are the main structures dynamically activated during the foreshock. F4 is an approximately 15-km-long branch in the southwest of F3, and F2, F3 and F4 all slip dynamically during the mainshock. Our constructed faults align with the updated SCEC Community Fault Model (version 5.3, `https://zenodo.org/record/5899364`; Supplementary Fig. 3.1b), including fault representations for the Ridgecrest earthquake sequence [175]. We omit secondary features, such as smaller orthogonal faults that appear as shallow lineations in seismicity [189] and space geodesy [249] (Supplementary Fig. 3.1). Our modelled distributed off-fault plastic strain, however, aligns with regions of observed off-fault damage (Fig. 3.5).

3.7.3 Fault friction

We adopt a strong velocity-weakening rate-and-state friction law [51, 89] that allows reproducing the severe reduction of co-seismic friction observed in laboratory experiments at high slip rates [45]. With this friction law, our fault system is operating at low average shear stress (Fig. 3.10) while dynamically yielding reasonable levels of fault slip and stress drop. This friction law also facilitates rupture cascading across the conjugate fault network and co-seismic complexity such as rupture pulse-to-crack transition and coseismic restrengthening[96, 155][62].

In a rate-and-state framework, frictional fault strength depends upon the state of the fault surface as well as the current slip rate [46, 195].

The strength of each fault is assumed to be proportionate to the magnitude of shear traction τ,

$$\tau = f(V, \Psi)\sigma_n{}' \tag{3.1}$$

where f is the effective friction coefficient, V is slip rate, Ψ is the state variable, and $\sigma_n{}'$ is the effective normal stress. τ and V are parallel and satisfy $\tau V = V\tau$. The instantaneous friction coefficient f depends on V and Ψ and is computed as

$$f(V, \Psi) = a \sinh^{-1}(\frac{V}{2V_0} \exp(\frac{\Psi}{a})) \tag{3.2}$$

where a is the direct-effect parameter and V_0 is the reference velocity. The evolution of Ψ is governed by

$$\frac{d\Psi}{dt} = -\frac{V}{L}(\Psi - \Psi_{\rm ss}(V)) \tag{3.3}$$

where Ψ_{ss} is the steady-state value of the state variable and is given by

$$\Psi_{\rm ss} = a \ln(\frac{2V_0}{V} \sinh(\frac{f_{\rm ss}(V)}{a})). \tag{3.4}$$

The steady-state friction coefficient $f_{\rm ss}$ is

$$f_{\rm ss}(V) = f_{\rm w} + \frac{f_{\rm LV}(V) - f_{\rm w}}{(1 + (V/V_{\rm w})^8)^{1/8}} \tag{3.5}$$

where $f_{\rm LV}$ is the low-velocity friction coefficient which depends on f_0 defined as the steady-state low-velocity friction coefficient at V_0, and is given by

$$f_{\rm LV}(V) = f_0 - (b - a) \ln \frac{V}{V_0}. \tag{3.6}$$

All frictional parameters we prescribe are listed in Table 3.2. We note that we do not directly prescribe the maximum static friction coefficient (μ_s), which dynamically varies across the fault system and may exceed f_0.

Fig. 3.9a shows the depth-dependent direct-effect parameter a and constant evolution-effect parameter b. a linearly increases to 4 km depth, such that the fault frictional behavior transitions from velocity-weakening to velocity-strengthening at 1.8 km depth. The assumed increase of $a - b$ at shallow depth is motivated by (i) direct shear and triaxial experiments [21] showing temperature dependence of this parameter, (ii) models reproducing the variability of shallow creep behaviour in both postseismic and interseismic periods [240] and (iii) previous dynamic rupture modeling [112].

3.7.4 Prestress

We construct an ambient 3D heterogeneous prestress combining observations with simple theoretical analysis and community models.

2D community stress model

We adapt stress as a normalized zero-trace tensor S_{ij} from a 2D community stress model (YHSM-2013[253], provided by the Southern California Earthquake Center, `https://scec.org/research/csm/`).

The YHSM-2013 community stress model is based on damped stress inversion from high-quality SCSN earthquake focal mechanisms from 1981-2010 [253] and provides the time-averaged regional lateral variation of the maximum horizontal compressional stress $SH_{\max}$ and the stress shape ratio ν in our model domain (Fig. 3.7). Stress orientations vary on a range of length scales. Similar to other community stress models, YHSM-2013 can resolve the regional larger-scale heterogeneity (5-10 km) of the ambient stress state, but lacks resolution for local stress heterogeneity at smaller scales.

We use 0.02° (about 2 km) interpolated YHSM-2013 data. Using inverse multiquadratic radial basis function interpolation and a Gaussian filter with a standard deviation for the Gaussian kernel of σ=2 we smooth any sharp transitions within the stress model.

The stress shape ratio ν describes different faulting mechanisms depending on the eigenvalues (S_1, S_2, and S_3; ordered from most compressional to most tensional) of the ambient stress tensor S_{ij}, with

$$\nu = \frac{S_2 - S_3}{S_1 - S_3}. \tag{3.7}$$

When S_2 is vertical, as inferred for the Ridgecrest earthquake region[253], $\nu < 0.5$ characterizes a transpressional regime, $\nu = 0.5$ characterizes a pure strike-slip regime, and $\nu > 0.5$ characterizes a transtensional regime.

Relative fault strength

We use a systematic approach that allows us to constrain the orientation of all principal stresses, the magnitudes of deviatoric stresses[224], and that extends the Mohr-Coulomb theory of frictional failure with dynamic parameters while reducing the large parameter space common in dynamic rupture modeling[215]. We assume that the ambient prestress is 3D heterogeneous and always Andersonian[2], i.e. one principal stress component (S_2) is vertical. We then combine this with the relative fault strength R[11], which is the ratio of the potential stress drop to the full breakdown strength drop. R is defined as

$$R = \frac{\tau - \mu_d \sigma_n'}{(\mu_s - \mu_d)\sigma_n'} \tag{3.8}$$

$R_0 = 1$ indicates a critical prestress level on all optimally-oriented faults. To compute R we assume $\mu_d \approx f_w$, as we observe that the fully weakened friction is typically reached in our simulations, and $\mu_s \approx f_0$ as a conservative assumption, thus,

$$R \approx \frac{\tau - f_{\mathrm{w}} \sigma_n'}{(f_0 - f_{\mathrm{w}})\sigma_n'} \tag{3.9}$$

We note that both approximations may result in locally slightly smaller R than the one we report in Fig. 3.1c for the preferred rupture models and in Fig. 3.22 for alternative scenarios not accounting for the long-term ΔCFS.

The absolute magnitude of all principal stresses can then be fully described by (i) the maximum relative fault strength R_0 of virtual fault segments optimally oriented in the stress field, which constrains the smallest and largest principal stress components, (ii) the pore fluid pressure ratio γ, describing overpressurized fault zone fluids [211], and modulating effective normal stress σ_n' gradients [140], with a hydrostatic state defined as $\gamma = \rho_{\mathrm{water}}/\rho = 0.37$ and higher values of γ corresponding to overpressurized pore fluids and (iii) the stress shape ratio ν.

We compute an ambient depth-dependent prestress tensor, b_{ij}, constrained by $SH_{\max}$, ν, R_0, and γ, by assuming the vertical stress as

$$\sigma_{zz} = \int_0^z \rho(x,y,z')g\,dz' = g\int_0^z \rho(x,y,z')\,dz' = \bar{\rho}(x,y,z)gz \tag{3.10}$$

with $\bar{\rho}(x,y,z) = \frac{1}{z}\int_0^z \rho(x,y,z')\,dz'$ being the density of the 3D heterogeneous overburden (based on the here used CVM-S4.26 velocity model [125]). Fluid pressure is then assumed to be proportional to vertical stress σ_{zz} as $P_f = \gamma\sigma_{zz}$ and the effective vertical stress is $\sigma_{zz}' = (1-\gamma)\sigma_{zz}$.

Long-term Coulomb failure stress changes

We add to the ambient depth-dependent prestress tensor b_{ij}, defined in the previous section, the contribution c_{ij} of coseismic and postseismic Coulomb failure stress changes (ΔCFS)

caused by major historical earthquakes ($M_w \geq 7$) that have occurred in the ECSZ during the last ∼1400 years [234], as well as by recent events of smaller magnitude. This new static stress change model (Fig. 3.25, Table 3.1) accounts for 8 additional historical and recent events compared to earlier published versions [234].

Figs. 3.1b and 3.26a show the associated changes in Coulomb failure stress ΔCFS at 5 km depth, assuming a NW-striking fault plane with strike=318°, dip=88°, and rake=-170°. Prior to the start of the 2019 Ridgecrest sequence, the computed ΔCFS is ∼0.8 MPa at the location of the foreshock hypocenter, but only ∼0.4 MPa at the mainshock hypocenter. We include the two largest events (M_w 5.8 and M_w 4.9) of the 1995 Ridgecrest earthquake sequence, which reduces prestress near the mainshock hypocenter (Fig. 3.1d).

We isolate the contribution of the two 1995 earthquakes by calculating ΔCFS due to only these two events and ΔCFS due to all others (Fig. 3.26). Both occurred in close proximity to the fault system without causing clear surface rupture[94]. The effects of the 1995 M_w 5.8 and M_w 4.9 events are overall local but shadow the hypocentral area of the mainshock, potentially contributing to the delayed triggering. Including previous events in particular on the Garlock fault, leads to positive Coulomb failure stress changes in the foreshock hypocentral area.

We note that we take into account both co- and post-seismic stress changes due to viscoelastic relaxation of the lower crust and upper mantle, which are thought to play an important role at timescales longer than 5 years [233]. Also, we reiterate that we do not compute ΔCFS on an a priori assumed planar fault geometry, but use a full tensor, which allows us to account for the complexity of the conjugate fault network when resolving on-fault stress changes.

Combined 3D heterogeneous prestress for dynamic rupture modelling

The full prestress tensor s_{ij} used in our dynamic rupture models is obtained by combining the ambient prestress tensor b_{ij} and the pre-Ridgecrest long-term stress change tensor c_{ij}. In addition, we apply a depth-modulation function $\Omega(z)$ (Fig. 3.9b), which smoothly tapers deviatoric stresses below the spatially-varying seismogenic depth z_{seis} as:

$$s_{ij}(x,y,z) = \Omega(z)(b_{ij}(x,y,z)) + c_{ij}(x,y,z)) + (1-\Omega(z))\sigma'_{zz}(x,y,z)\delta_{ij} \tag{3.11}$$

with z_{seis} constrained by aftershock locations (Fig. 3.8).

Additional modulation of the depth-dependence of R_0 would allow to account for potential stress concentrations at the bottom of the seismogenic zone induced by deep creep [224, 129]. However, the shape and depth of such stress concentration would be difficult to constrain for our complex fault system.

By performing a few dynamic rupture experiments, we find optimal values of γ and R_0, constrained by the mechanic viability of rupture to cascade along the fault network with realistic amounts of fault slip and stress drop. An approximation of the order of magnitude of the expected dynamic stress drop is $R_0(1-\gamma)\sigma_{zz}(f_0 - f_w)$, with $f_0 = 0.6 \approx \mu_s$ the static

friction coefficient and $f_w = 0.1 \approx \mu_d$ the fully weakened friction, which demonstrates dynamic trade-offs between R_0 and γ[224].

We find that a prescribed R_0= 0.8, as the relative strength of an optimal fault in the complex stress field s_{ij}, is a large enough value to allow for sustained foreshock and mainshock rupture along the conjugate fault system, but small enough to reproduce realistic fault slip and stress drop.

For the foreshock, we find that a fluid pressure ratio of $\gamma = 0.83$, well below lithostatic but above hydrostatic, produces spontaneous rupture of both F1 and F2 with an amount of fault slip consistent with inversion studies [32, 77]. In comparison, a mainshock dynamic rupture simulation based on the same γ fails to dynamically rupture the southern parts of F3 and F4. A higher stress drop is needed to sustain rupture beyond the conjugate F2-F3 intersection. We find that reducing fluid pressure by 30% and assuming $\gamma = 0.77$ on F3 and F4, thus allowing for 30% higher potential stress drop than on F1 and F2, allows spontaneous rupture of the southern parts of F3 and F4, well aligned with observations.

3.7.5 Rupture nucleation

In dynamic rupture models, only a small portion, the critical nucleation zone [193], of the fault needs to reach failure to nucleate a rupture while faults can be prestressed well below critical (Fig. 3.10) and yet break spontaneously. Dynamic rupture simulations typically use prescribed nucleation procedures. 3D earthquake cycle simulations that incorporate spontaneous (aseismic) nucleation and dynamic rupture exist [124, 110, 134, 147] but are methodologically and computationally challenging at the same level of combined geometrical, frictional and structural complexity [109, 229].

Several techniques for nucleating dynamic earthquake ruptures exist, including locally either elevated shear stress, low (effective) static frictional strength or time-weakening forced rupture [4, 20, 99, 91]. We carefully follow established modeling best-practices [66, 89], using a nucleation patch smoothly varying in space and time and acting across a minimal-sized perturbation area, avoiding artifacts and initiating self-sustained spontaneous rupture with minimal perturbation determined in several trial dynamic rupture simulations. In both the foreshock and mainshock scenarios spontaneous dynamic rupture is initiated by progressively increasing on-fault shear traction in a spherical volume of radius $r_{\text{nuc}} = 3.5$ km centered at their respective hypocenters (Table 3.4). The nucleation overstress $\Delta\tau(r,t)$ is given as:

$$\Delta\tau(r,t) = \tau_{\text{nuc}} F(r) G(t) \tag{3.12}$$

with τ_{nuc} the peak value of the overstress and r the radius from the hypocenter. $F(r)$ defines the shape of the overstress perturbation:

$$F(r) = \begin{cases} \frac{1}{2}\sum_{n=1}^{2} \exp\left[-\frac{1}{2}\left(\frac{r}{r_{\text{crit}(n)}}\right)^2\right] & r < r_{\text{nuc}} \\ 0 & r \geq r_{\text{nuc}} \end{cases} \tag{3.13}$$

r_{crit}(n=1) and r_{crit}(n=2) are set to 0.4 km, and 1.6 km, respectively. For both events, we use $\tau_{\mathrm{nuc}} = 18$ MPa, which results in an average nucleation stress of ∼3 MPa over the circular nucleation area (Fig. 3.18). $G(t)$ is a smoothed step function given as:

$$G(t) = \begin{cases} \exp\left[\frac{(t-T_{\mathrm{nuc}})^2}{t(t-2T_{\mathrm{nuc}})}\right] & 0 < t < T_{\mathrm{nuc}} \\ 1 & t \geq T_{\mathrm{nuc}} \end{cases} \tag{3.14}$$

with $T_{\mathrm{nuc}} = 1$ s.

3.7.6 Analytical interpretation of the dynamically required mainshock nucleation stress

We can interpret the additional shear stress required to activate F3 in our dynamic rupture model using an analytical estimate of the shear stress increase carried by afterslip [75], implying interaction of coseismic and postseismic slip and their stresses [181]. We adapt the analytical 1D estimate of the peak shear stress to normal stress ratio f_{p} carried by transient afterslip (Eq. 2.20 of [75]) as

$$f_{\mathrm{p}} \approx f_0 + a \ln \frac{v_r/v_0}{\kappa_0 g(v_{\mathrm{r}}/c_{\mathrm{S}})}, \tag{3.15}$$

where f_0 is the initial fault stress ratio at the ambient fault sliding velocity V_0, the constant near-field prefactor $\kappa_0 \approx 1$, and the universal function[59] $g(v_{\mathrm{r}}/c_{\mathrm{S}}) \approx 1$ for aseismic fronts, v_r is the speed of the transient (afterslip) front, $v_0 = \mu V_0/b\sigma_{\mathrm{n}}$ is a characteristic rupture velocity embodying the dependence on the fault ambient conditions. Assuming v_r to correspond to approximately 3 km in 34 hrs [189], $a = 0.01$ and $b = 0.014$ yields a peak shear stress perturbation at the transient front of 2.5-4.5 MPa for ambient fault slip rates $V_0 = 10^{-12} \ldots 10^{-16}$ m/s.

3.7.7 Sensitivity of the dynamic rupture models

We analyse the sensitivity of the modeled foreshock and mainshock rupture dynamics to key modeling ingredients including the chosen ambient stress setup and the 3D long-term stress changes.

We observe high sensitivity of foreshock rupture dynamics to regional initial conditions, including its simultaneous conjugate rupture, partial surface rupture and lack of co-seismic mainshock triggering. We observe high sensitivity of mainshock rupture dynamics to foreshock slip distributions on F1 and F2, for example, with respect to the mainshock's ability to dynamically overcome the geometric and stress barrier posed by the conjugate F2-F3 fault intersection and activate the southern segment of F3.

Our dynamic rupture scenario of the Ridgecrest mainshock fully accounts for the stress changes due to the Searles Valley foreshock in addition to long-term Coulomb failure stress

changes ΔCFS. We here demonstrate the effects of (i) not incorporating the foreshock stress changes in an alternative mainshock rupture dynamics simulation, shown in Fig. 3.15 and Video S3, and of (ii) omitting both foreshock stresses and ΔCFS in alternative mainshock rupture dynamics simulation (Fig. 3.16, Video S4). In both cases, mainshock rupture dynamics are less complex than in the preferred model (Fig. 3.27).

In the mainshock model without the foreshock stress changes, spontaneously accumulating fault slip is overall larger than in the preferred mainshock model, especially on F3 near the conjugate F2-F3 intersection (Fig. 3.24a). Unlike the preferred model, this scenario features no rupture delay at this intersection. We also see more shallow slip on F2 and F4 and more slip at shallow depth after the F2-F3 intersection.

In the alternative mainshock simulation omitting additionally long-term ΔCFS, fault slip is overall lower and specifically reduced at shallow depth (Fig. 3.24b). We observe less slip to the South of F3, no more slip on F4 and reduced slip on F2. Differences in slip to the South are likely linked to the 1453 M_w7.7 event on the Garlock fault [234]. Rupture duration is here about 2 s shorter, due to the lack of dynamic triggering of F4.

In the alternative combined dynamic rupture models (iii) of foreshock and mainshock presented in Figs. 3.17, 3.22 and Videos S5, S6, we do not incorporate the pre-Ridgecrest long-term 3D stress changes ΔCFS. In this way, we evidence the non-negligible effects of ΔCFS from previous important earthquakes on foreshock and mainshock rupture dynamics. Fig. 3.17 shows the foreshock scenario, which lacks pronounced rupture on F2 (Fig. 3.24c). Differences in the mainshock slip distribution include non-rupture of F4, similar to model (ii). Slip in the southern F3 region is larger than in model (ii) but still reduced with respect to the reference model and not sufficient to dynamically trigger the F4 segment (Fig. 3.24d). Differences in the relative prestress ratio R on all faults highlight the effect of long-term ΔCFS on the relative strength of F2 and on the mainshock hypocentral region at F3 (Fig. 3.22).

Lastly, we analyse the sensitivity to the ambient background stress model by implementing the 3D stress inversion model FM3D [88] instead of YHSM-2013 [253]. YHSM-2013 is a 2D model, which has higher lateral resolution in the Ridgecrest region. The alternative combined dynamic rupture models (iv) of foreshock and mainshock with the same long-term ΔCFS are shown in Fig. 3.23 and Videos S7, S8. In the FM3D foreshock scenario, both F1 and F2 are ruptured with a higher slip magnitude on F2 compared to the reference scenario (Fig. 3.24e). In the FM3D mainshock scenario, dynamic rupture on F3 terminates at the conjugate intersection with F2, highlighting the sensitivity of a mechanically viable realistic mainshock scenario to the foreshock rupture dynamics and especially to the rupture extent on F2 (Fig. 3.24f).

3.7.8 Computational mesh and model resolution

The model domain used to jointly simulate both events accounts for high-resolution topography and is spatially discretized in an unstructured tetrahedral mesh of 27,264,253 million tetrahedral elements. We retrieved topography data from the Shuttle Radar Topography Mission (SRTM, [57]) using the SRTM.py python package `https://github.`

`com/tkrajina/srtm.py`. The spatially-adaptive mesh resolution is set to an element edge length of h =75 m close to all faults and gradually coarsened away from the fault surfaces. The mesh is also refined near topography, and set to h =500 m element edge lengths at the free surface. We use the WGS84 / UTM Mercator 11S projection.

Simulating 200 seconds physical simulation time on this computational mesh using high-order basis functions of polynomial order p =4, leading to a 5th order space-time accurate numerical scheme for wave propagation, typically requires ∼19.5 hours on 250x48 Skylake cores of the SuperMUC-NG supercomputer (Leibniz Supercomputing Center, Germany). Our chosen h, p resolution resolves the seismic wavefield up to at least 2 Hz in the near source region. Each dynamic rupture element face consists of $(p + 2)^2$ Gauss integration points, enabling sub-elemental resolution of rupture dynamics[247]. The size of the area behind the rupture front in which shear stress decreases from its static to its dynamic value is the process zone width. In the dynamic rupture models presented, we measure the median process zone width as 6.1 km, while for 95% of the ruptured fault elements it is larger than 515 m, which is well resolved by our chosen discretisation.

3.7.9 3D velocity model and viscoelastic attenuation

We embed all faults in the SCEC 3D velocity model CVM-S4.26 (Fig. 3.1a), which is based on unmodified 3D tomography [125]. Our simulations use viscoelastic rheologies to model intrinsic attenuation [228]. The P-wave and S-wave quality factors (Q_P and Q_S) follow established empirical relationships, assuming $Q_\mathrm{S} = 50\ c_\mathrm{S}$ (for c_S in km/s) and $Q_\mathrm{P} = 2\ Q_\mathrm{S}$ [42, 80].

3.7.10 Off-fault plasticity

Our model accounts for non-linear off-fault plasticity (Fig. 3.5b) which, in combination with near-surface velocity-strengthening behavior, permits realistic estimates of the shallow slip deficit (SSD) and near-field ground motion in the presence of complex fault geometries. We assume a non-associated Drucker-Prager elasto-viscoplastic rheology to model off-fault damage [247], parameterized by bulk internal friction coefficient and 3D variable plastic cohesion. We use a uniform bulk friction coefficient of 0.7 and define plastic cohesion C_plast as everywhere proportional to the 3D heterogeneous shear modulus [191] $\mu(x, y, z)$ (in Pa):

$$C_\mathrm{plast} = 10^{-4}\mu(x, y, z) \tag{3.16}$$

The onset of plastic yielding is not instantaneous but governed by viscoplastic relaxation with a relaxation time T_v set to 0.05 s, which ensures convergence of simulation results with mesh refinement [247].

In our models, the total seismic moment $M_{0,t}$ is the sum of the moment due to slip on the fault, $M_{0,e}$, and $M_{0,p}$, the moment contribution of distributed off-fault plastic strain quantified as η, a scalar quantity measuring the accumulated off-fault plastic strain at

the end of the foreshock or mainshock dynamic rupture simulations. Following previous analysis [8, 136, 63, 225] we compute the contribution of plastic strain to the total seismic moment as:

$$M_{0,\mathrm{p}} = \sum_{i=1}^{N} \mu V \eta \tag{3.17}$$

with μ being the rigidity, V the volume of each tetrahedral element i and

$$\eta(t) = \int_0^t \sqrt{\frac{1}{2}\dot{\epsilon}_{ij}^{p}\dot{\epsilon}_{ij}^{p}}\mathrm{d}t \tag{3.18}$$

and $\dot{\epsilon}_{ij}^{p}$ being the inelastic strain rate. The contribution of plastic strain to the total moment is small but non-negligible specifically for the mainshock scenario (where $M_{0,\mathrm{p}}$ $/M_{0,\mathrm{t}} \approx 8\%$).

3.7.11 Backprojection

To image the rupture processes of the Searles Valley foreshock and the Ridgecrest mainshock sequence, we assume a grid of possible source locations covering the latitude range 34°N to 37.5°N, and longitude range -120°W to -116°W, with 0.05° grid spacing in both latitude and longitude. We use the relatively dense array data from Alaska. Only stations with relatively high average coherence (> 0.6) of the P-wave are selected to avoid interference of low-quality signals and noise. We use the Ridgecrest mainshock as a reference event and apply a cross-correlation method using 20 s of P-wave onset aligned recordings, filtered between 0.1 to 1 Hz to calculate the waveform coherency. Based on this, 268 stations from the Alaska array are selected. Azimuth coverage ranges from 320° to 348°, and epicentral distances range from 30° to 45°, which ensures that P and S phases are well separated.

Stations at regional distance have also been used to perform back-projection of both events [248], which is overall in agreement with our results. While regional back-projection is feasible with respect to the short duration of both earthquakes, close proximity and rupture complexity of the sequence may challenge regional BP resolution and stability. We use the 1D velocity model ak135 [115] to calculate theoretical travel times from the source grid to each seismic station. We image the rupture process of both events using a sliding time back-projection technique, with 6 s long time windows and 1 s time steps.

We apply a calibration method [76] to reduce location uncertainties, which are mainly due to (non-accounted for) non-constant source depths, heterogeneous 3D velocity structures, and anisotropy along the source to station travel paths. For calibrating, we use 14 earthquakes larger than $M_{\mathrm{w}}4.5$ occurring between July 4th and 12th, 2019, including the foreshock and mainshock events (see Table 3.3).

For the Searles Valley foreshock, we use low frequency (0.5-1 Hz) data to guarantee high coherence of the wave front. Our back-projection images rupture on F1 for 6 s and rupture on F2 within the following 6 s (Fig. 3.2c). We interpret that F2 rupture is initiated at

the hypocenter jointly with F1 rupture, and that F2 breaks in a continuous manner away from the hypocenter. Dynamic triggering from the west side of F2 is unlikely, given the distance from the hypocenter. Rupture directivity effects from F1 towards the array may result in artificially elevated amplitudes in the filtered frequency range [128] rendering the first 6 s of rupture on F2 challenging to resolve. Back-projection results, here and in [252], suggest that F1 ruptured at about 1 km/s and F2 at about 1.5 km/s. Beam power reaches its first and higher energy peak at about 2-3 s, during F1 rupture. Then energy radiation drops, aligned with F1 rupture terminating in the dynamic rupture scenario. Beam power reaches a second peak at 8-9 s after the estimated rupture onset, which resembles the dynamic rupture model reaching the south-western end of the F2 segment.

For the Ridgecrest mainshock, the higher signal to noise ratio of recorded waveforms guarantees coherent signals up to 2 Hz, and allows to perform multi-frequency back-projection. Higher frequency (1-2 Hz) BP shows continuous rupture from the epicenter to the southern tip of F3, while lower frequency (0.1-0.5 and 0.25-1 Hz) results show also reactivation of F2 (Fig. 3.3c). BP beam power features two peaks for multiple frequency ranges. The first peak is associated with rupture on F3 to the North of the conjugate F2-F3 intersection and is more sensitive to higher frequencies. We associate the second peak with the reactivation of F2 and the rupture of the SE segment of F3. The frequency-dependence of our back-projection results is likely due to the effect of rupture directivity and rupture speed variation [254, 128]. The F3 rupture in backwards-array direction towards the SE, results in lower characteristic frequency at the array because of the Doppler effect. On the other hand, a faster rupture speed can increase the characteristic frequency and counteract the Doppler effect. A faster rupture speed in the SE part of F3 (Fig. 3.19), crossing the conjugate intersection, is also observed from local array-based back-projection [248].

3.7.12 Kinematic PSI

We image rupture kinematics of both events from seismic waveforms using the kinematic Parametric Slip Inversion (PSI) method by [86]. We use all available seismic stations within 130 km distance from the fault. The rupture is assumed to propagate along prescribed fault segments at spatially variable speed. Slip rates are described as Yoffe functions [217] with spatially varying rise times. The slip distribution is parameterized using spline interpolation from a variable set of control points. The rake angles are allowed to vary smoothly. Synthetic waveforms are calculated by discretizing the segments into subfaults of 1.5×1 km and convolving their moment-rate functions with the respective Green's functions precalculated in the GIL7 1D velocity model [164] using Axitra [41]. We band-pass filter both data and synthetics between 0.05 and 0.5 Hz.

The inverse problem is formulated in a Bayesian framework [86]. The prior probability density function (PDF) on the number of slip control points k follows a reciprocal distribution, $p(k) \propto k^{-1}$. By this means, it serves as "Occam's razor", preferring implicitly simple, localized slip distributions. Other priors are generally uniform (PDF) in relatively wide ranges (e.g., ±45 degrees for the rake angle). The data uncertainty is described by a multivariate Gaussian function with a full covariance matrix. It includes a component

accounting for the uncertainty of Green's functions due to imperfect description of the velocity model [85]. The posterior samples are obtained by a Markov Chain Monte Carlo (MCMC) method, namely the parallel tempering technique [197].

We assume two planar faults for the foreshock, approximating the fault geometries of F1 and F2 for simplicity. The mainshock model includes the two fault segments F2 and F3, and honors the deflected F2 geometry. The results shown in the main text in Figs. 3.2b and 3.3b correspond to the best-fitting model and serve as an example from the ensemble of solutions obtained by the MCMC sampling.

While smooth initial conditions lead to relatively smooth slip distribution in the dynamic models, the self-adapting spatial parameterization in the kinematic models tends to localize the slip due to the Occam's razor constraint (as the data does not require otherwise). It is challenging to disentangle fault slip across conjugate fault intersections in kinematic methods due to the proximity of faults and the similar radiation pattern of, e.g., right-lateral F1 and left-lateral F2 segments in the foreshock. Therefore, the uncertainty is more significant for both models in the vicinity of the conjugate fault segment intersection. For example, PSI shows a smaller fault slip on F1 around the hypocenter but a bit larger slip on F2 closer to the surface for the foreshock. Similarly, minor slip patches are rather uncertain due to their little contribution to the waveforms. In some cases, such as the one at the NW end of the foreshock's F1, the inferred slip might be projectedfrom coinciding secondary, unaccounted faults.

3.7.13 Geodetic data analysis

We obtained the processed static GPS vector data from UNAVCO (`https://www.unavco.org/highlights/2019/ridgecrest.html`). We compare our modeled surface displacements at selected stations with observational data as shown in Fig. 3.2f and 3.3f. To avoid contamination by remnant seismic waves propagating throughout the model domain, we extract the synthetic surface displacements at 100 s after dynamic rupture nucleation in both foreshock and mainshock models. We calculate the maximal possible value of cross-correlation (CC) between the observed and synthetic time series component-wise to account for the different signal-to-noise ratios in the horizontal and vertical components.

Our modeled co-seismic GPS displacements of the Searles Valley foreshock match observational recordings well at most stations, with notable overshooting amplitudes at near-fault stations CCCC and P595 (Fig. 3.2f). For the mainshock, we also observe overall good agreement except for small overshooting displacements at station P595, P580 and P594 (Fig. 3.3f).

Stations CCCC and P595 are close to the terminations of faults in our prescribed fault geometry, and the observed discrepancies may reflect a more gradual rupture arrest along F2 than captured in our model. Additional discrepancies may by associated with secondary faults off the main fault identified with optical imaging [249], [151] but not explicitly incorporated in our model.

3.7.14 Teleseismic waveforms

We generate synthetic broadband seismograms at 6 teleseismic stations (of the IU network) around the events (Fig.3.1a and 3.14) using the Instaseis [48] Green's function database and the PREM model incorporating anisotropic effects and accurate to a shortest period of 2 s. The sources for the synthetic teleseismic waveforms are calculated by translating the fault slip time histories of the foreshock and mainshock dynamic rupture models into a respective double-couple point source, that we then use in Instaseis. The observed teleseismic data were downloaded from IRIS using Obspy [119].

The teleseismic synthetics fit the foreshock (Fig. 3.14a, average cross-correlation coefficient of $\sim$0.73) and mainshock (Fig. 3.14b, average cross-correlation coefficients $\sim$0.75) observations well in the long period range considered (50–500 s). The simplifying choice of a 1D PREM-based teleseismic Green's function database may explain some of the remaining differences.

Acknowledgements

We thank M. Bader, L. Krenz, S. Wolf, R. Dorozhinskii and the group of hardware-aware algorithms and software for high- performance computing at TUM for decade-long collaboration; N. Schliwa, J. Biemiller, C. Nicholson and S. A. Wirp for discussions; and S. Antoine for sharing surface offset data. This work was supported by the European Union's Horizon 2020 Research and Innovation Programme (TEAR grant number 852992) and Horizon Europe (ChEESE-2P grant number 101093038, DT-GEO grant number 101058129 and Geo-INQUIRE grant number 101058518), the National Science Foundation (grant number EAR-2121666), the German Research Foundation (DFG projects GA 2465/2-1 and GA 2465/3-1) and the Southern California Earthquake Center (SCEC award 21112). We acknowledge the Gauss Centre for Supercomputing e.V. (`www.gauss-centre.eu`) for providing computing time on the GCS Supercomputer SuperMUC-NG at Leibniz Supercomputing Centre (`www.lrz.de`), in project pr63qo.

Year	Earthquake	Magnitude
587	Antelope Valley	7.2
700	Pyramid Lake	7.0
913	Fish Lake (Leidy Creek)	6.8
950	Fish Lake (Oasis)	6.7
1170	Benton Springs	7.2
1375	Incline Village	7.1
1508	Mojave (San Andreas)	7.5[201, 145]
1540	Garlock	7.7
1557	Panamint Valley	7.1
1600	Mount Rose	7.0
1605	Genoa	7.2
1715	Furnace Creek	7.2
1812	Wrightwood	7.5[132]
1857	Fort Tejon	7.9[130]
1872	Owens Valley	7.5
1915	Pleasant Valley	7.5
1932	Cedar Mountain	7.2
1952	Kern County	7.3[18]
1954	Rainbow Mountain	7.0
1954	Fairview Peak	7.1
1954	Dixie Valley	7.2
1992	Landers	7.2[236]
1995	Ridgecrest	5.8 & 4.9[94]
1999	Hector Mine	7.1[108]

Table 3.1: Past earthquakes incorporated in the pre-Ridgcerest co- and post-seismic cumulative Coulomb failure stress change model ΔCFS. The model of [234] has here been updated by incorporating the contribution of 8 additional events, highlighted in blue.

Parameter	Symbol	Value
Direct-effect parameter	a	0.01-0.02
Evolution-effect parameter	b	0.014
Reference slip rate	V_0	10^{-6} m/s
Steady-state low-velocity friction coefficient at the slip rate V_0	f_0	0.6
Characteristic slip distance of the state evolution	L	0.2 m
Full weakened friction coefficient	f_w	0.1
Initial slip rate	V_{ini}	10^{-16} m/s
Weakened slip rate	V_w	0.1 m/s

Table 3.2: Rate-and-state frictional fault properties.

Time	Latitude (°)	Longitude (°)	Depth (km)	Magnitude
2019-07-12T13:11:38	35.638	-117.585	9.95	4.9
2019-07-07T05:38:15	35.768	-117.578	10.57	4.52
2019-07-06T08:32:58	35.639	-117.491	3.14	4.56
2019-07-06T04:13:07	35.587	-117.617	7.94	4.8
2019-07-06T04:07:05	35.555	-117.524	5.58	5.01
2019-07-06T03:29:29	35.704	-117.511	11.13	4.51
2019-07-06T03:25:28	35.860	-117.668	11.21	4.97
2019-07-06T03:23:51	35.800	-117.605	12.43	5.37
2019-07-06T03:19:53	35.770	-117.599	8.00	7.1
2019-07-06T03:16:32	35.725	-117.554	0.88	4.97
2019-07-05T11:07:53	35.760	-117.575	6.95	5.36
2019-07-04T18:56:06	35.716	-117.560	1.92	4.58
2019-07-04T18:39:44	35.601	-117.597	2.81	4.59
2019-07-04T17:33:49	35.705	-117.506	10.71	6.4

Table 3.3: List of earthquakes used for back-projection calibration. Event information is taken from the Advanced National Seismic System (ANSS) Comprehensive Earthquake Catalog.

Event	Latitude (°)	Longitude (°)	Depth (km)
Foreshock	35.70421	-117.49392	10.5
Mainshock	35.77623	-117.59286	8.0

Table 3.4: Assumed hypocenter location from the QTM catalog[189].

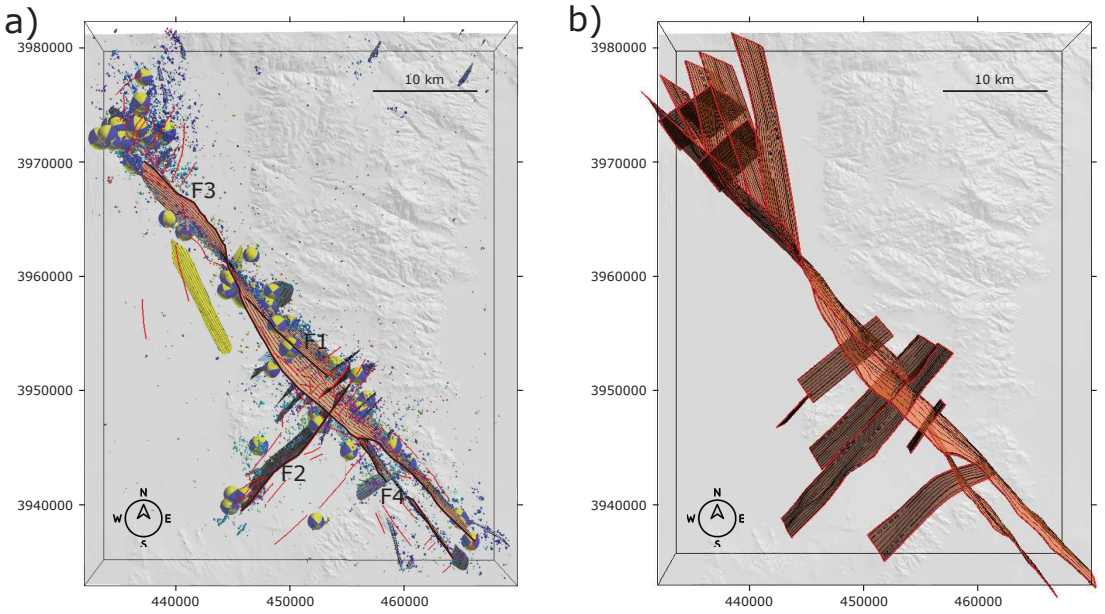

Figure 3.6: Top-view of (a) the constructed 3D fault network and (b) fault representations for the Ridgecrest earthquake sequence from the SCEC community fault model CFM, version 5.3[175]. Topography is overlain in transparent grey. In (a), focal mechanisms of aftershocks of magnitude larger than M_w4 are represented as 3D spheres[174]. When viewed from above, these are equivalent with the lower hemisphere stereographic projection representation typically plotted in tectonic maps. The three NW-SE trending right-lateral faults, F1, F3, and F4, and the conjugate NE-SW trending left-lateral fault, F2, are labeled.

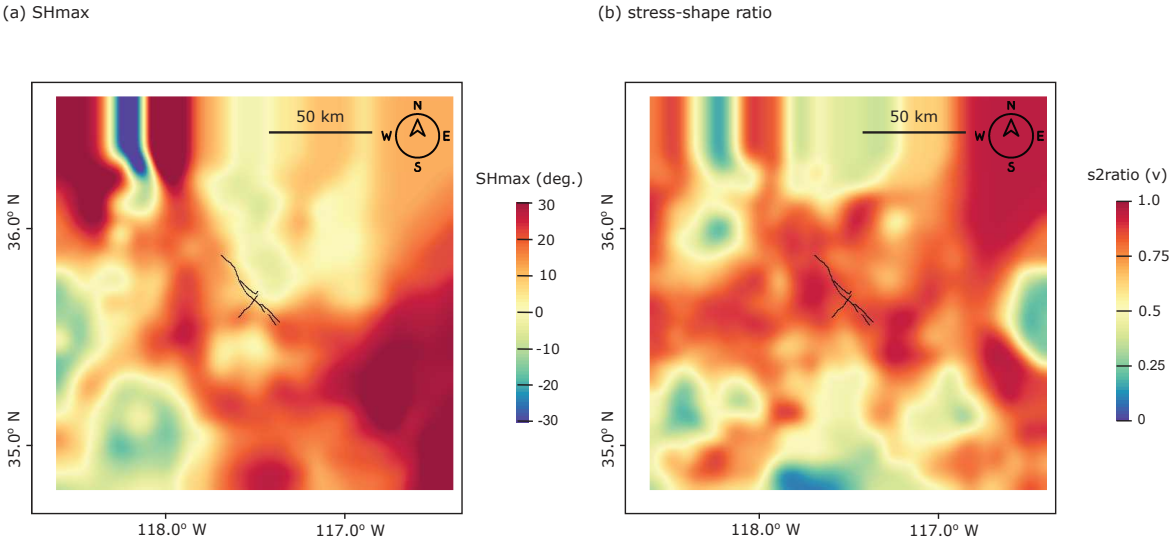

Figure 3.7: (a) SH_{max} and (b) stress-shape ratio ν computed from the YHSM-2013 dataset[253]. Note that the data from YHSM-2013 are projected, and smoothed, as detailed in Methods Section 3.7.4.

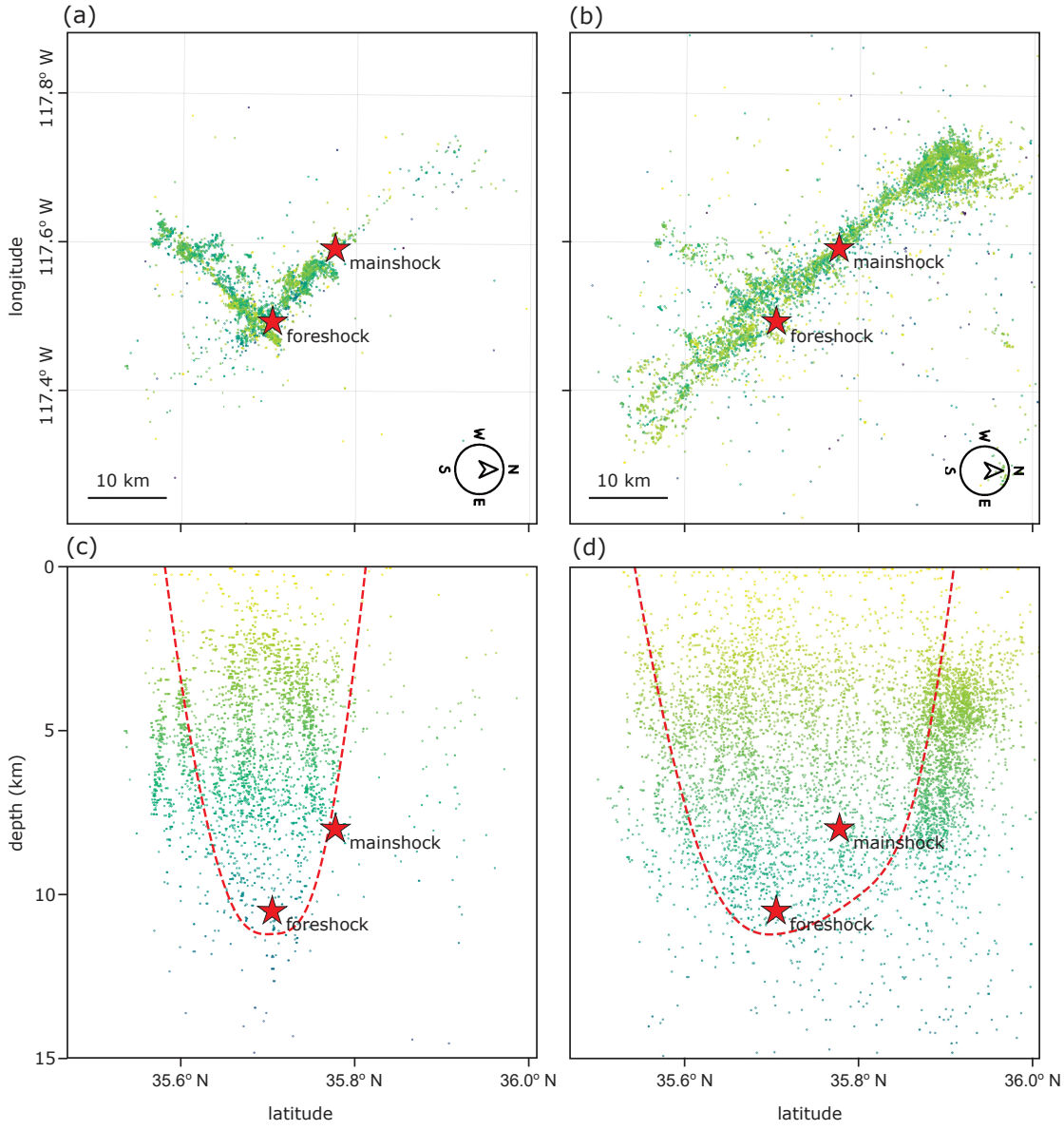

Figure 3.8: Assumed variations of seismogenic depth z_{seis} with latitude, constrained from aftershock locations[189]. Deviatoric stresses smoothly tapper below z_{seis} (see 3.7). Aftershock locations of (a) the foreshock and (b) the mainshock, using the same latitude x-axis as c) and d). Distribution of aftershocks with depth and latitude and assumed variation of z_{seis} (red dashed line) for (c) the foreshock and (d) the mainshock. The red stars are the hypocenter locations of both earthquakes.

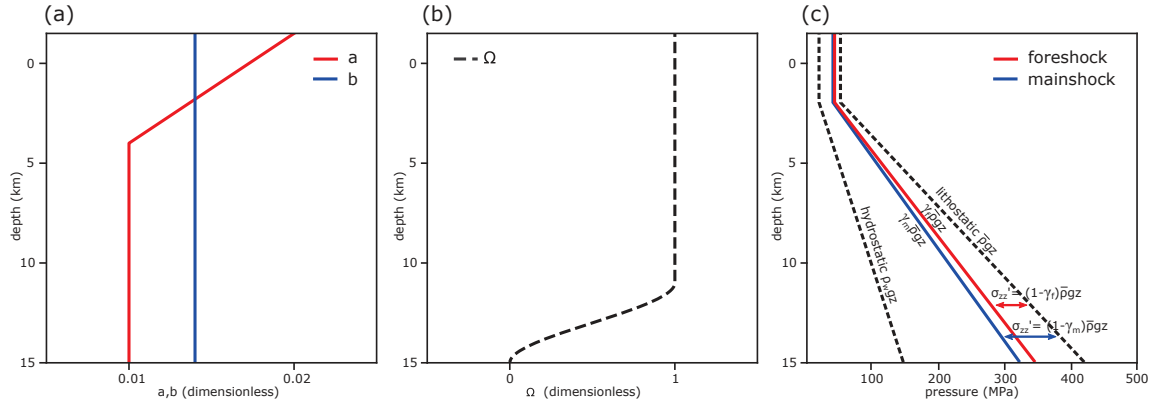

Figure 3.9: Depth-dependent friction and stress parameters. (a) a and b friction parameters. (b) Stress tapering function Ω. Ω tappers the deviatoric stresses below the seismogenic depth z_{seis} (see 3.7). Ω is here exemplarily represented with z_{seis}=11 km. (c) The foreshock effective vertical stress $\sigma'_{\mathrm{zz}} = (1-\gamma_{\mathrm{f}})\bar{\rho}gz$ and the mainshock effective vertical stress $\sigma'_{\mathrm{zz}} = (1-\gamma_{\mathrm{m}})\bar{\rho}gz$, with $\gamma_f\bar{\rho}gz$ and $\gamma_m\bar{\rho}gz$ being the pore fluid pressures both below lithostatic pressure $\bar{\rho}gz$ but above hydrostatic pressure $\rho_{\mathrm{w}}gz$, with $\bar{\rho}$ as average density and ρ_{w} as water density. Pore fluid pressure ratio γ_{f} and γ_{m} are 0.83 and 0.77, respectively.

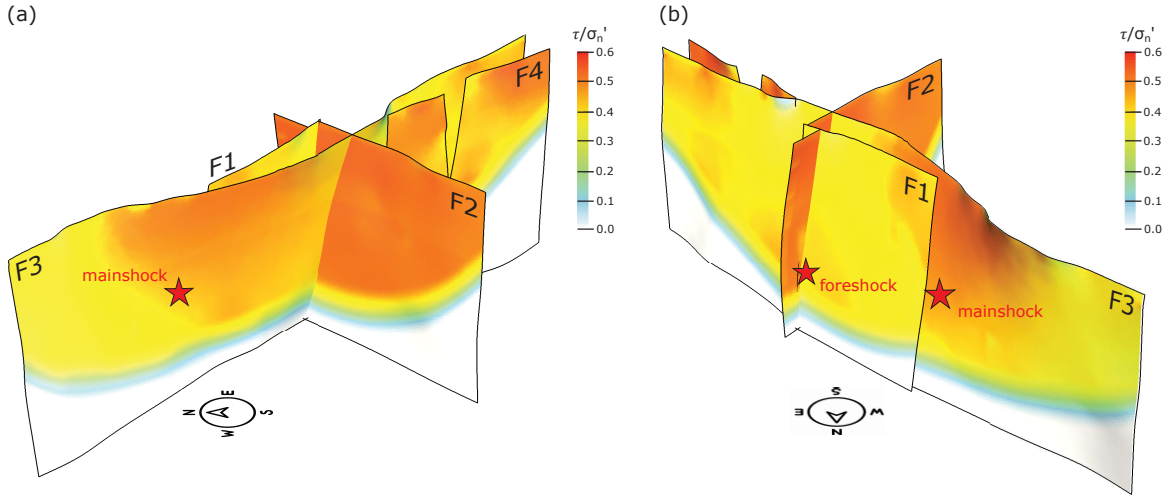

Figure 3.10: Ratio of initial shear stress τ over effective normal stress σ_{n}'. (a) View from west and (b) from north.

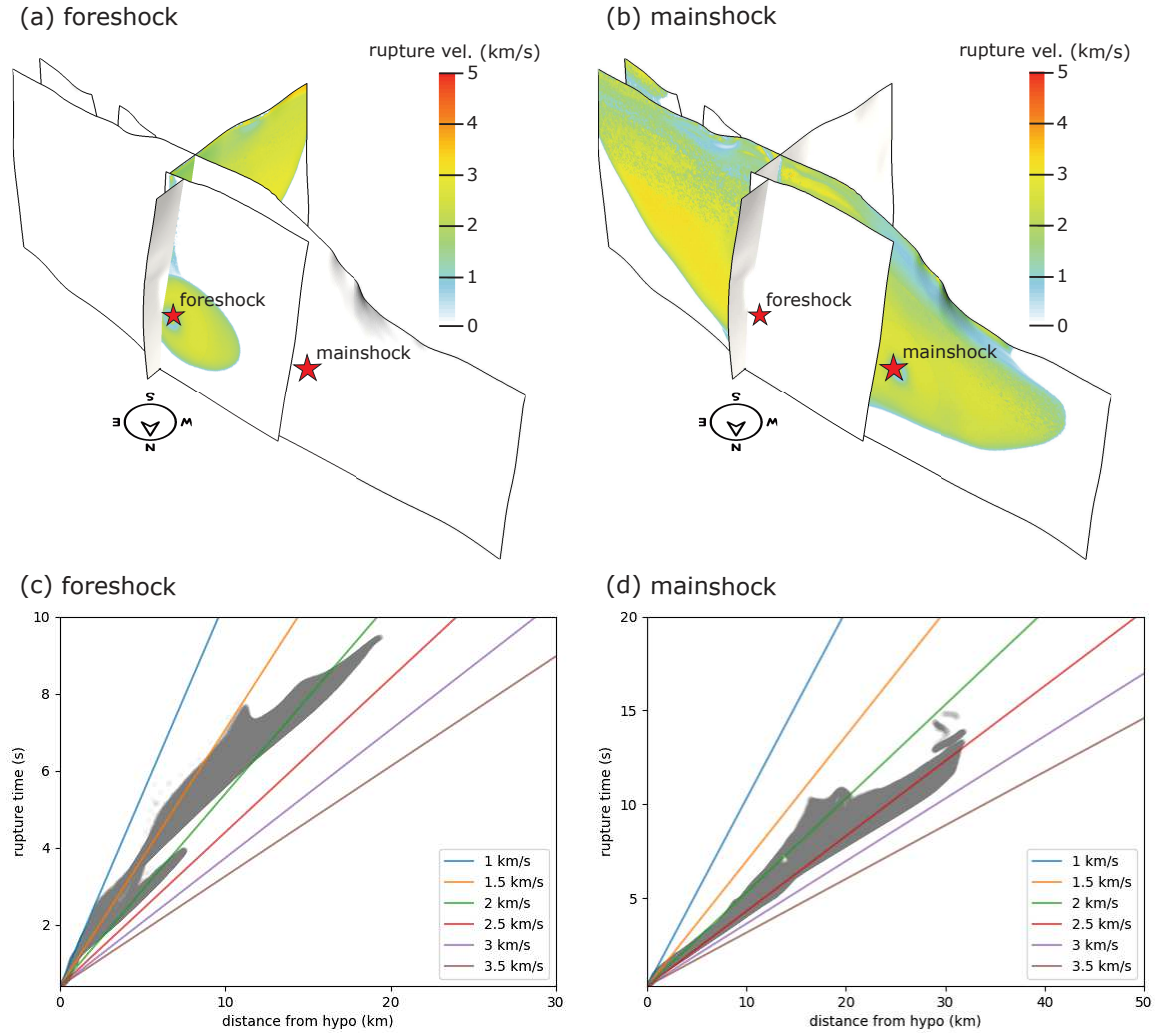

Figure 3.11: Rupture velocity distribution in the foreshock (a) and the mainshock (b) dynamic rupture scenarios. Distribution of rupture location relative to distance from (c) the foreshock and (d) the mainshock hypocenters with their rupture time (grey) across our complex fault system compared to constant rupture velocities (colored lines) We note that validation of dynamic rupture speed and moment release rate is challenged by the complexity of the dynamic rupture model. Also observational estimates may contain apparent slow initiation phases and lengthened slip duration, potentially due to secondary phase contamination and location uncertainties.

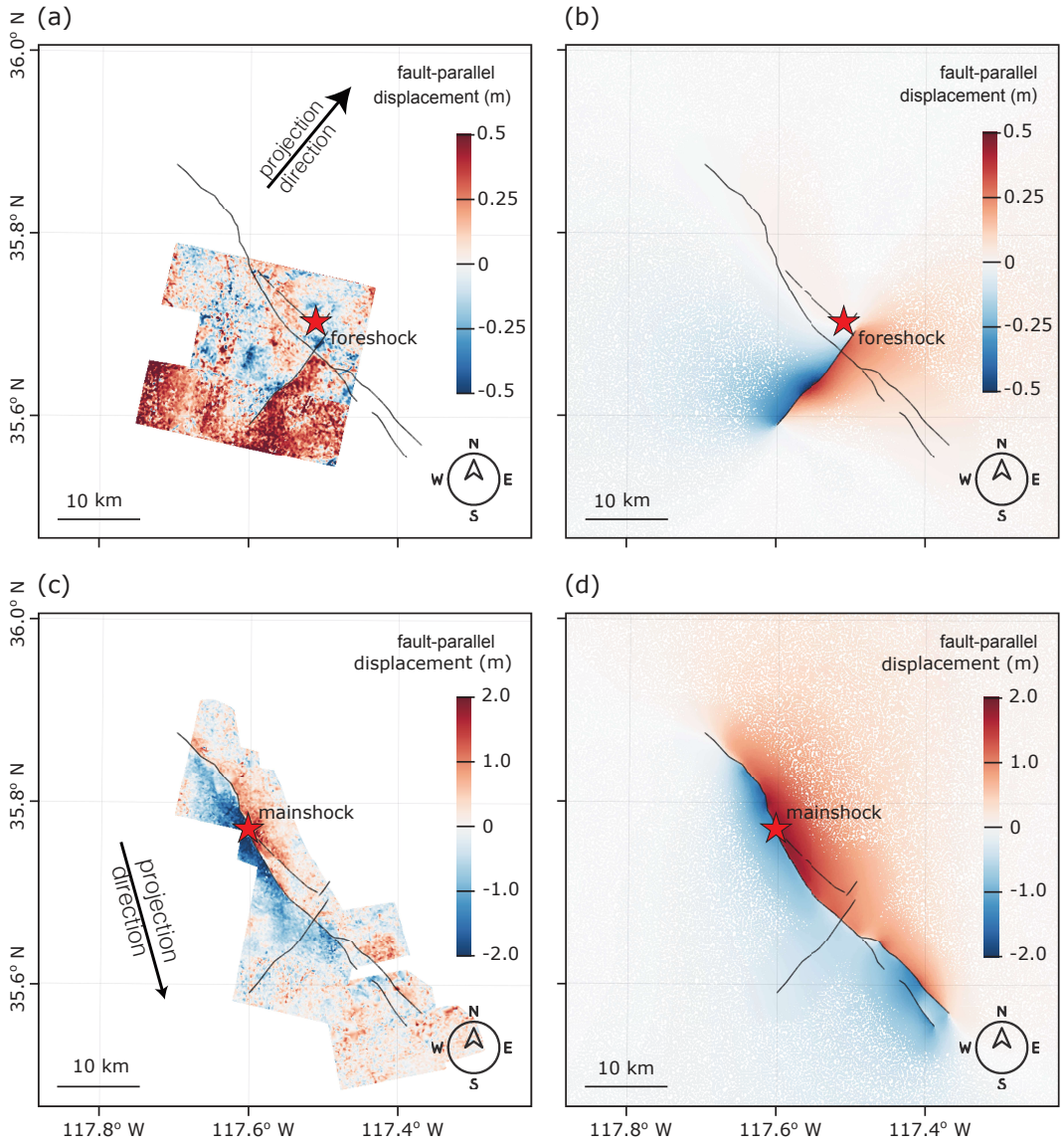

Figure 3.12: Comparison of the modeled and inferred surface displacements projected into fault parallel direction (with direction shown by arrow). Observations are from sub-pixel correlation of optical images from the PlanetScope imagery[151]. (a) observation and (b) modeled surface displacements for the foreshock. (c) observation and (d) modeled surface displacements for the mainshock.

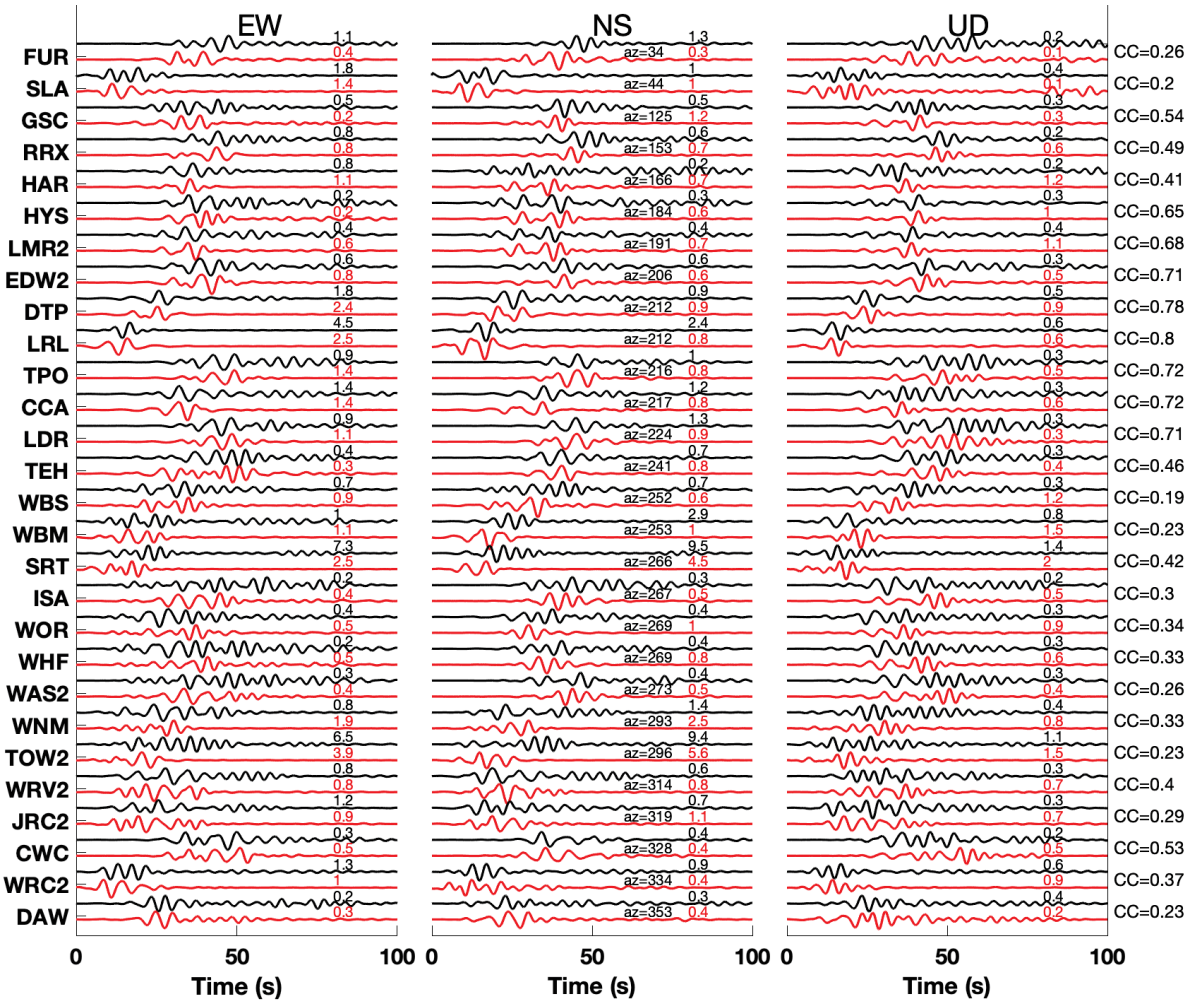

Figure 3.13: Comparison of modeled and observed ground motion time series for the Searles Valley foreshock. Synthetic (red) and observed (black) strong ground velocity at regional strong-motion stations shown in Figure 3.1, band-pass filtered between 0.1-0.3 Hz. CC are calculated from 300 s three-component waveforms. We normalize waveforms by their peak amplitudes (black numbers) to facilitate comparison and only consider unspoiled waveforms.

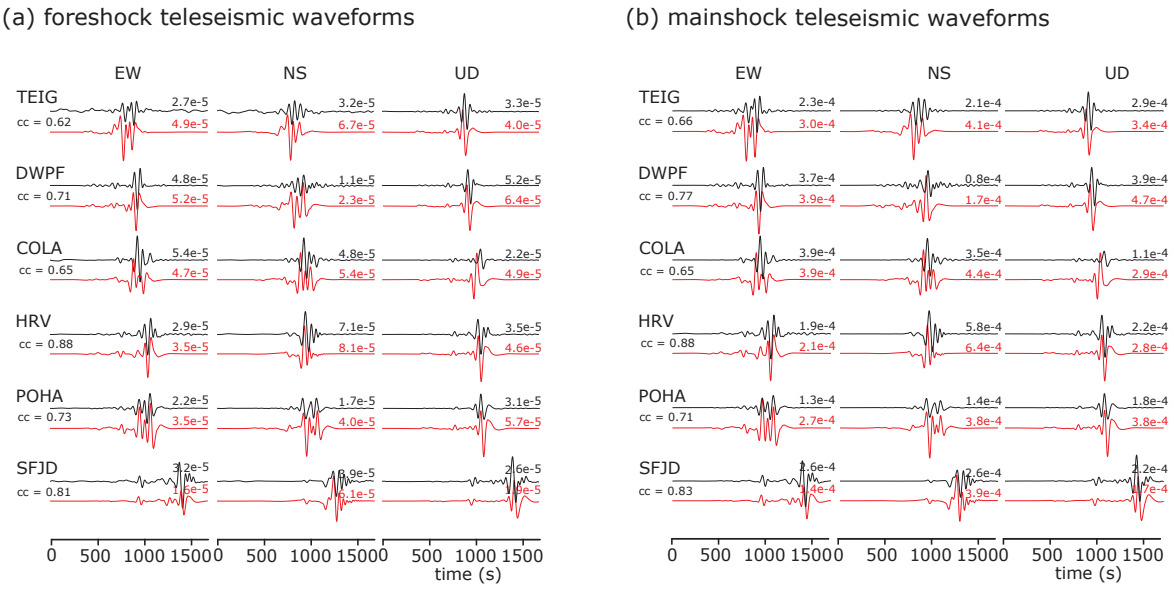

Figure 3.14: Comparison of synthetic (red) and observation (black) teleseismic waveforms at receiver locations shown in Figure 3.1a. A 0.002-0.02 Hz band-pass filter is applied. Synthetics are generated using Instaseis[48] and the PREM model including anisotropic effects, and accurate to a shortest period of 2 s (see 3.7). At these 6 stations teleseismic observations for periods 50–500 s are matched across a wide azimuthal range with an average cross-correlation coefficient of ≈0.73.

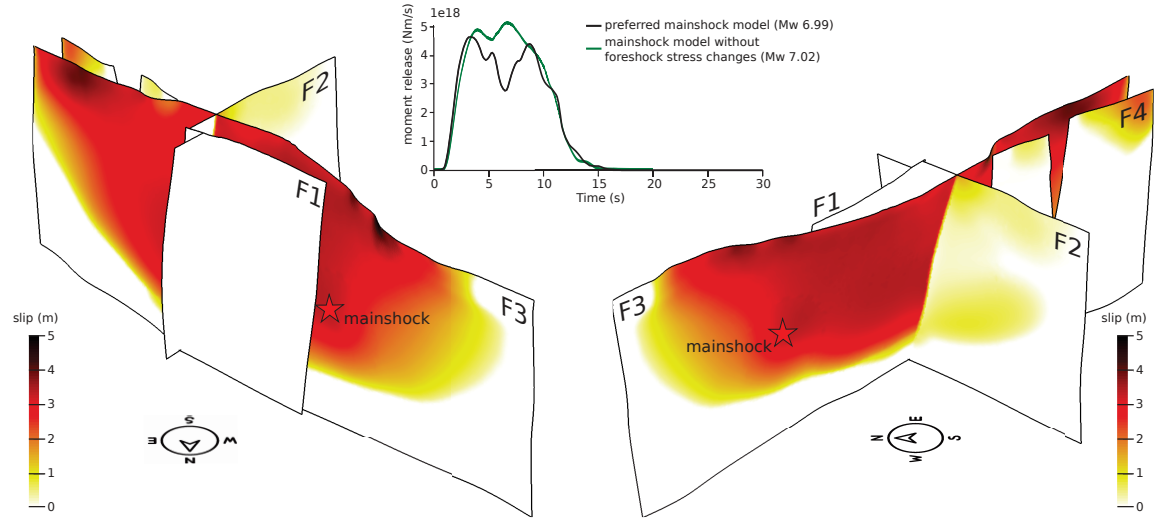

Figure 3.15: Alternative dynamic rupture scenario (i) of the mainshock which is not incorporating the foreshock dynamic and static stress changes. Final fault slip from two perspectives and moment rate compared to the preferred mainshock dynamic rupture scenario of Fig. 3.27. The reported moment magnitudes are calculated from slip on the faults, not accounting for the additional seismic moment due to off-fault deformation. See Video S3 for the evolution of absolute slip rate (m/s) across the fault network from 4 perspectives.

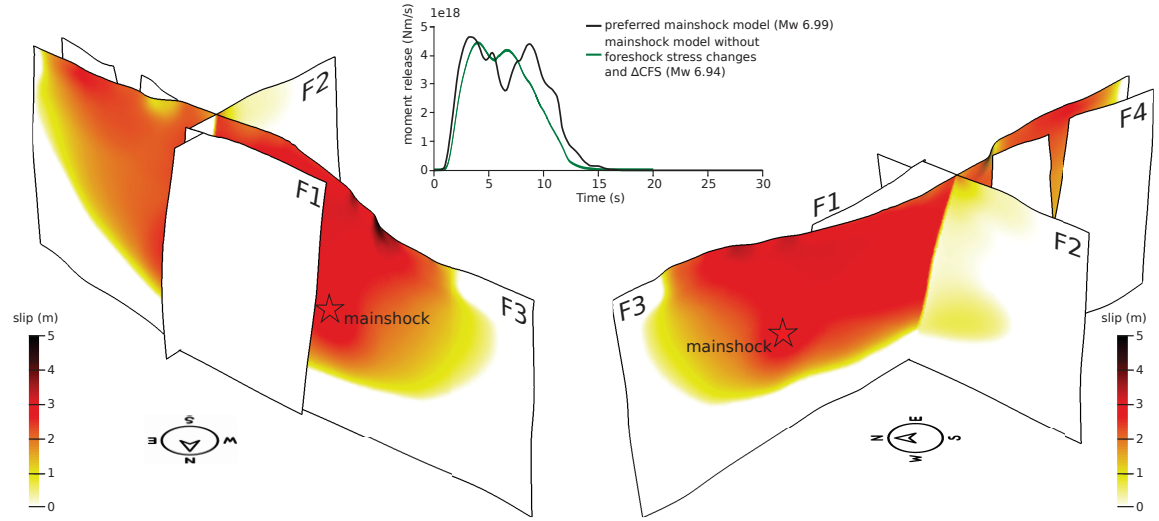

Figure 3.16: Alternative dynamic rupture scenario of the mainshock (ii) which is not incorporating the foreshock dynamic and static stress changes and in addition not incorporating the long-term ΔCFS. Final fault slip from two perspectives and moment rate compared to the preferred mainshock dynamic rupture scenario of Fig. 3.27. The reported moment magnitudes are calculated from slip on the faults, not accounting for the additional seismic moment due to off-fault deformation. See also Video S4 of the evolution of absolute slip rate (m/s) across the fault network from 4 perspectives.

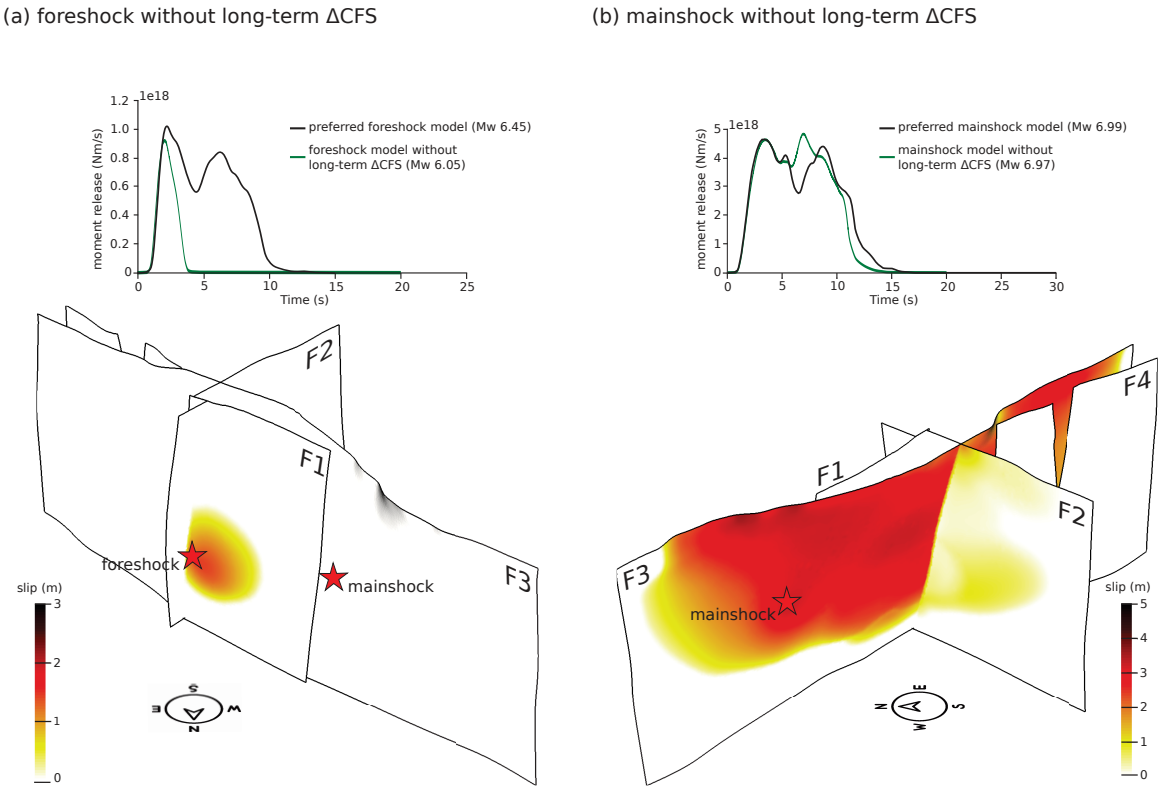

Figure 3.17: Alternative combined dynamic rupture models (iii) of foreshock and mainshock both not incorporating long-term ΔCFS. Final fault slip from two perspectives and moment rate compared to the preferred foreshock and mainshock dynamic rupture scenario of Fig. 3.27. The reported moment magnitudes are calculated from slip on the faults, not accounting for the additional seismic moment due to off-fault deformation. See Videos S5 and S6 for the evolution of absolute slip rate (m/s) across the fault network from 4 perspectives.

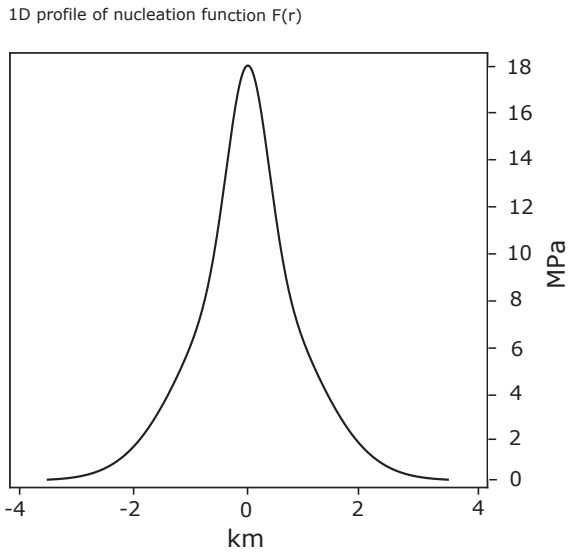

Figure 3.18: 1D profile of the dynamically required additional nucleation shear stress for the mainshock dynamic rupture scenario. The average nucleation stress is ∼3 MPa over the circular nucleation area of radius r_{nuc}=3.5 km.

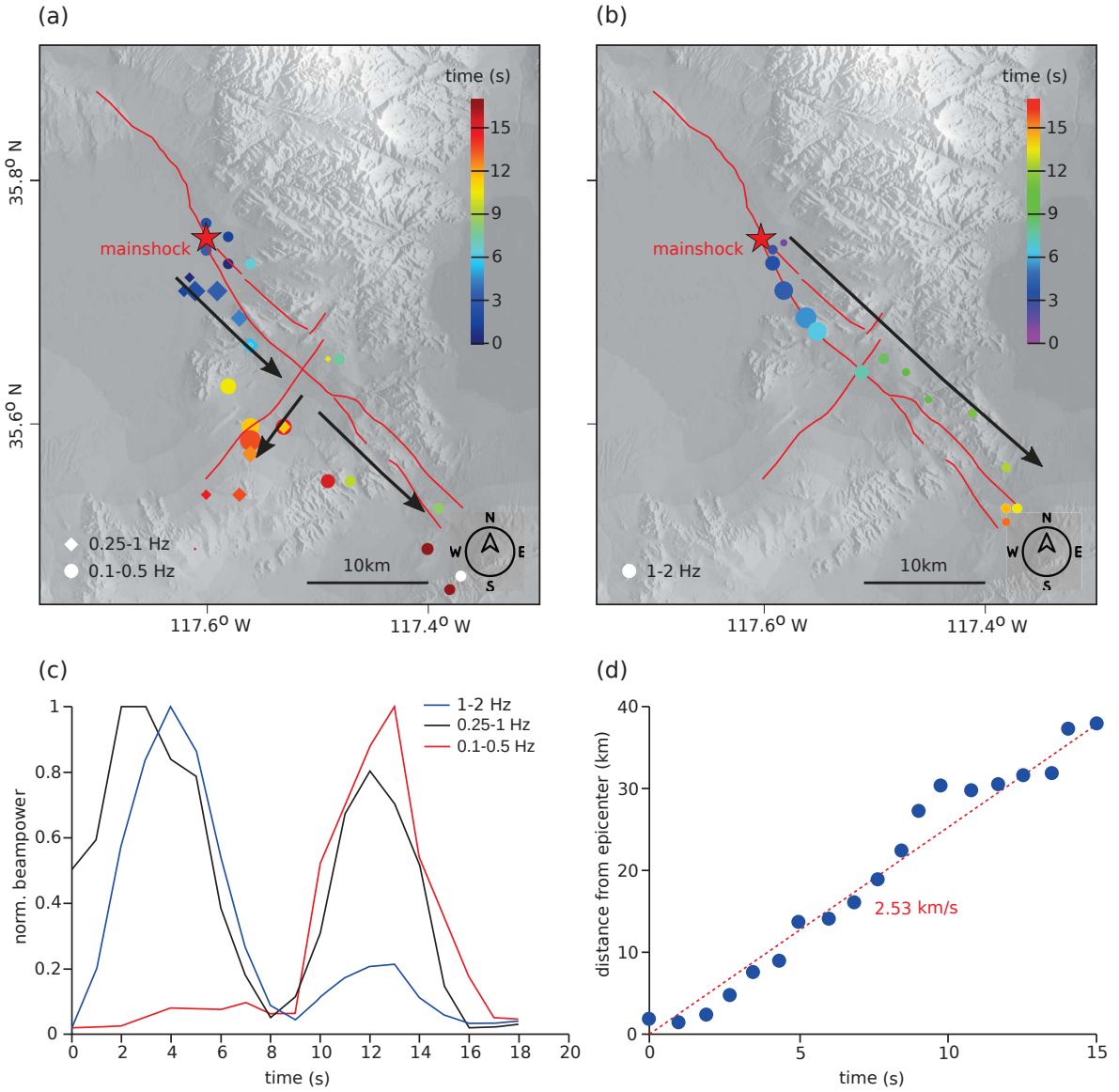

Figure 3.19: Frequency dependence of back-projection results (see 3.7) when imaging the mainshock event. (a) High-frequency radiators imaged from data recorded by the Alaska array, in the frequency range 0.25–1 Hz and 0.1–0.5 Hz, mapped with diamonds and circles, respectively. (b) High-frequency radiators (circles) from data in the frequency range 1–2 Hz. The symbol sizes are proportional to the relative radiated energy and their colour represent the rupture time with respect to the event origin time. (c) Normalized beam-power for the three frequency bands represented in (a) and (b). (d) Projected location along the mainshock average trend N330 of high-frequency radiators for the frequency band 1–2 Hz versus time, suggesting a rupture speed of about 2.5 km/s.

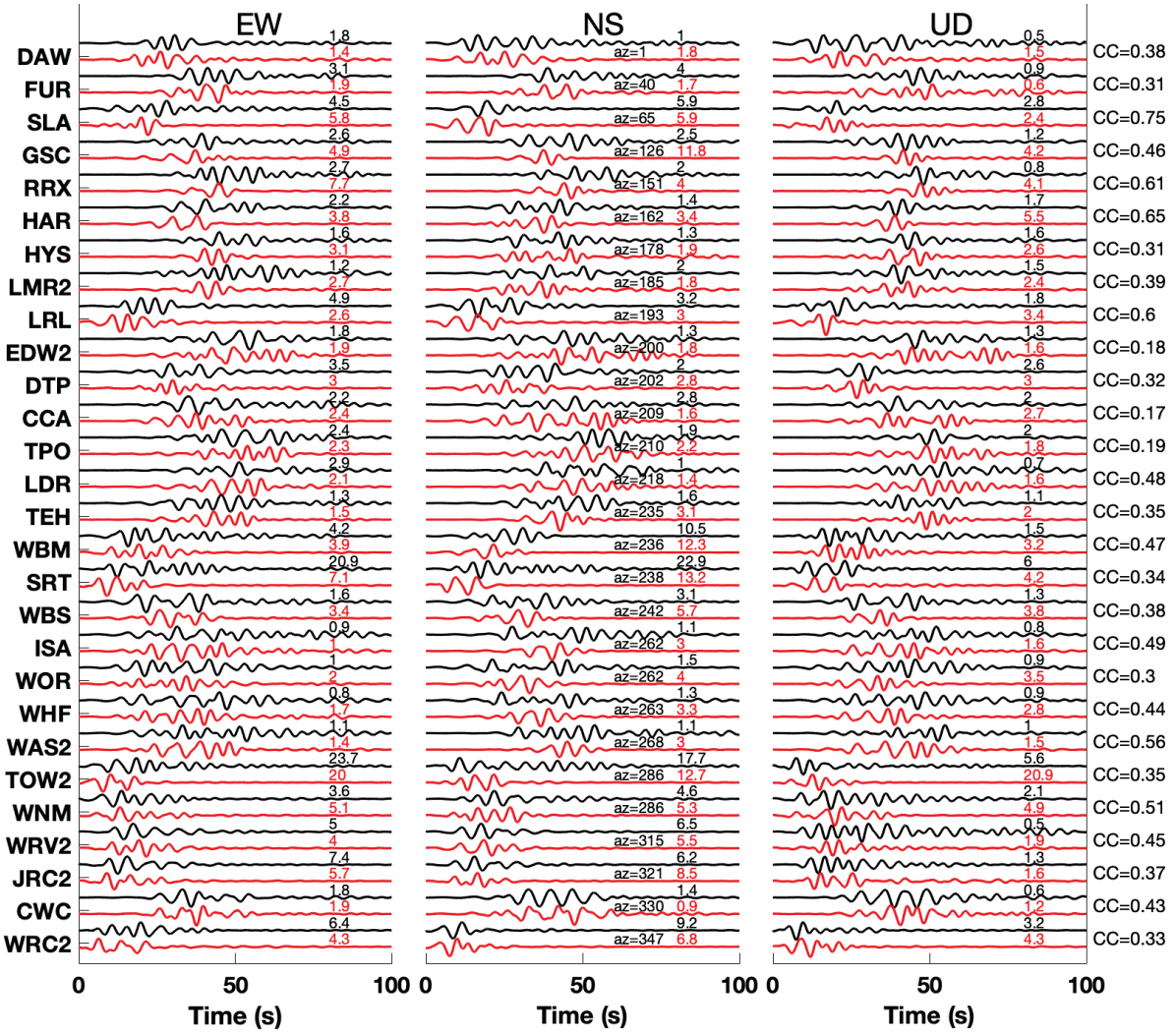

Figure 3.20: Comparison of modeled and observed strong ground motions for the Ridgcrest mainshock. Synthetic (red) and observed (black) ground velocity time series at regional strong-motion stations shown in Figure 3.1, band-pass filtered between 0.1-0.3 Hz. CC are calculated from 300 s three-component waveforms. We normalize waveforms by their peak amplitudes (black numbers) to facilitate comparison and only consider unspoiled waveforms.

(a) foreshock stress drop

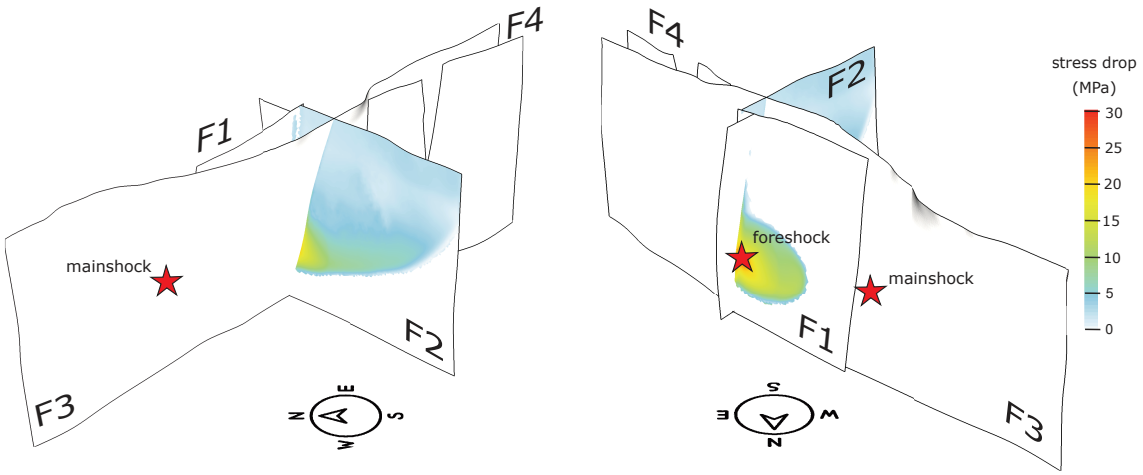

(b) mainshock stress drop

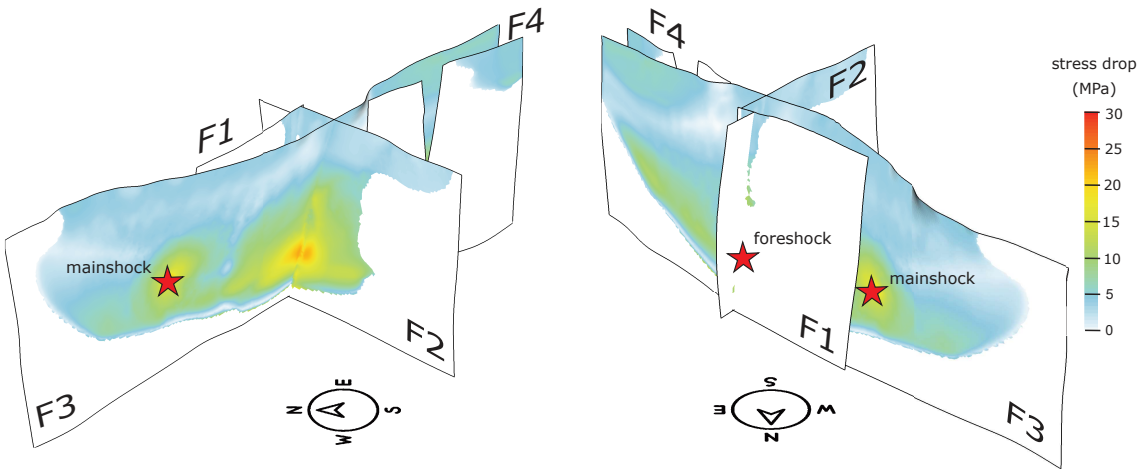

Figure 3.21: (a) Stress drop of the foreshock and (b) the mainshock dynamic rupture scenario. Left: view from west. Right: view from north.

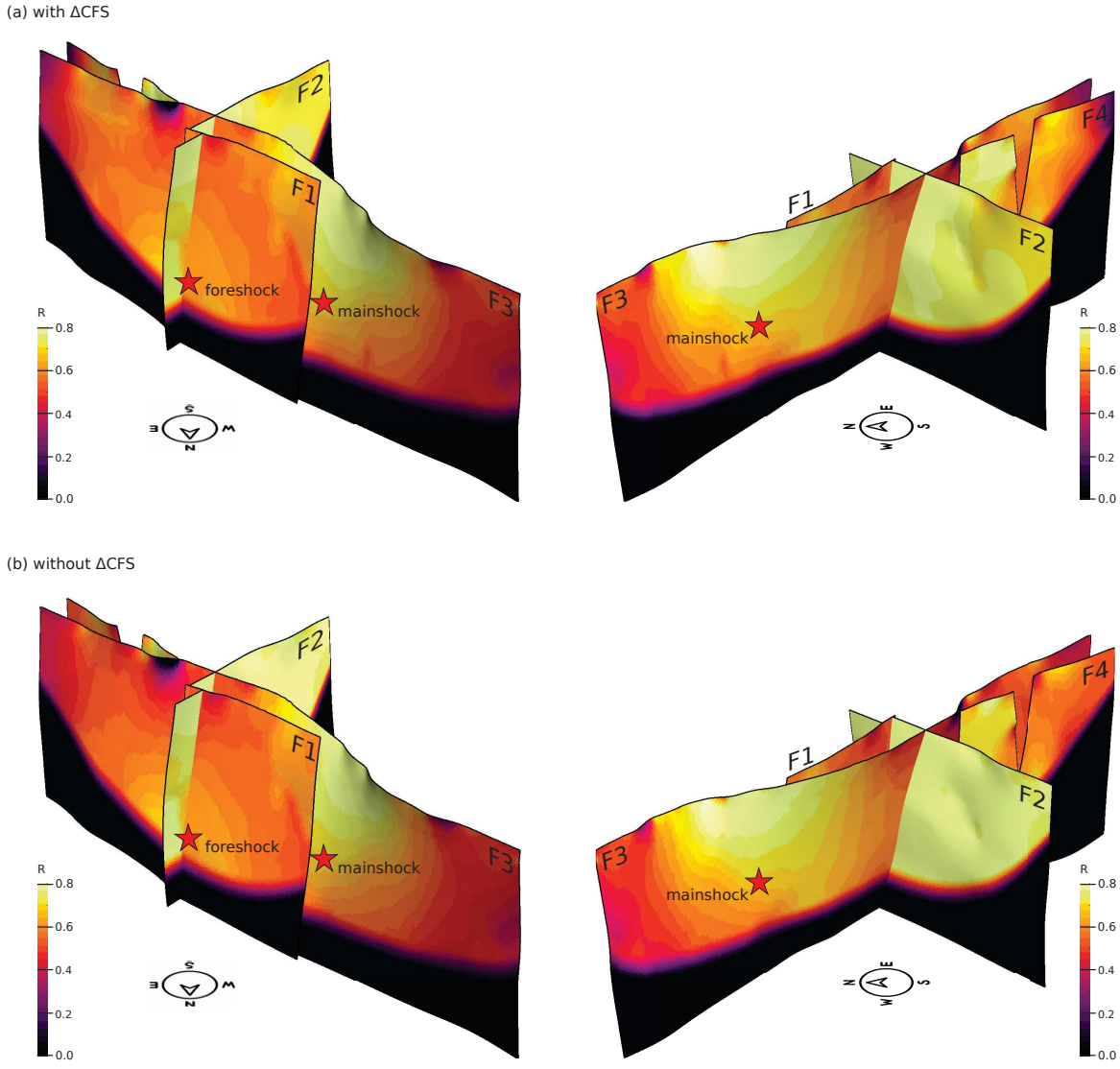

Figure 3.22: Relative prestress ratio R across the fault system for the preferred scenarios with long-term ΔCFS (left) and for alternative model (iii) without long-term ΔCFS (right). Mainshock and foreshock hypocenters are denoted by black stars.

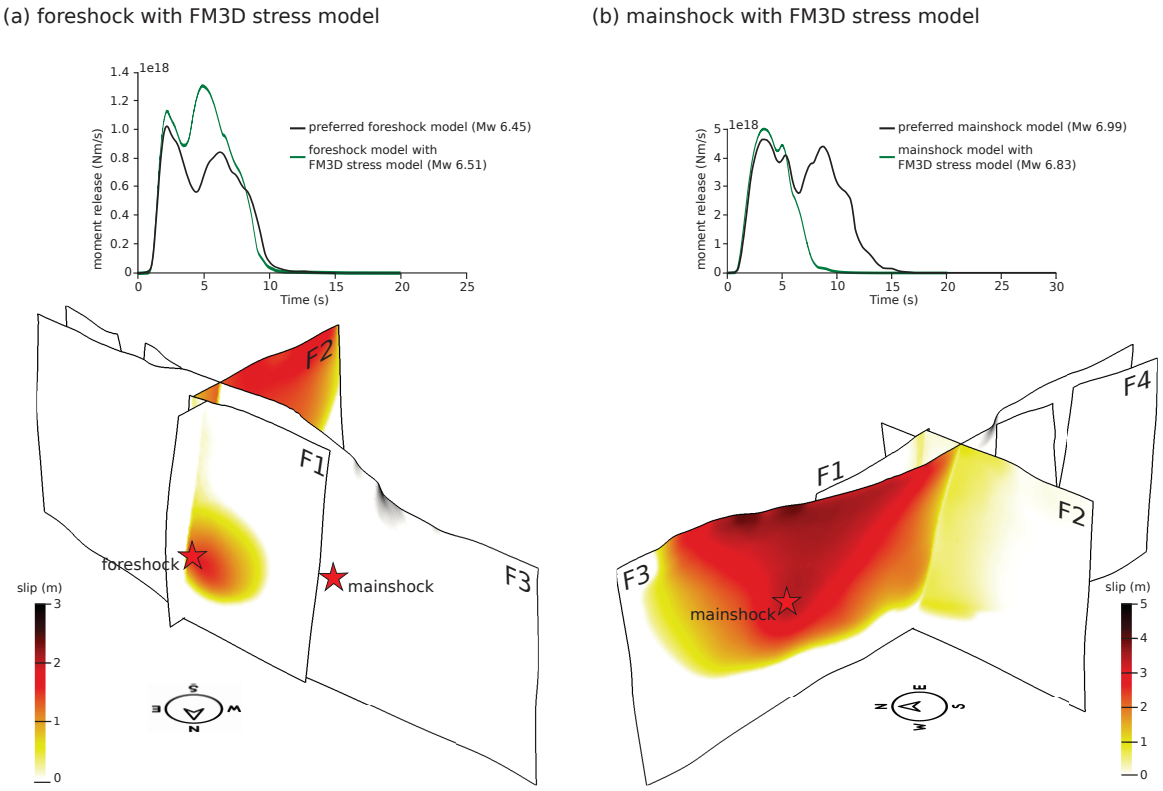

Figure 3.23: Alternative combined dynamic rupture models (iv) of foreshock (a) and mainshock (b), both incorporating the community stress model FM3D [88]. Final fault slip and moment rate compared to the preferred foreshock and mainshock dynamic rupture scenarios, that adapt the community stress model YHSM-2013[253] instead. The reported moment magnitudes are calculated from slip on the faults, not accounting for the additional seismic moment due to off-fault deformation. See Videos S7 and S8 for the evolution of absolute slip rate (m/s) across the fault network from 4 perspectives.

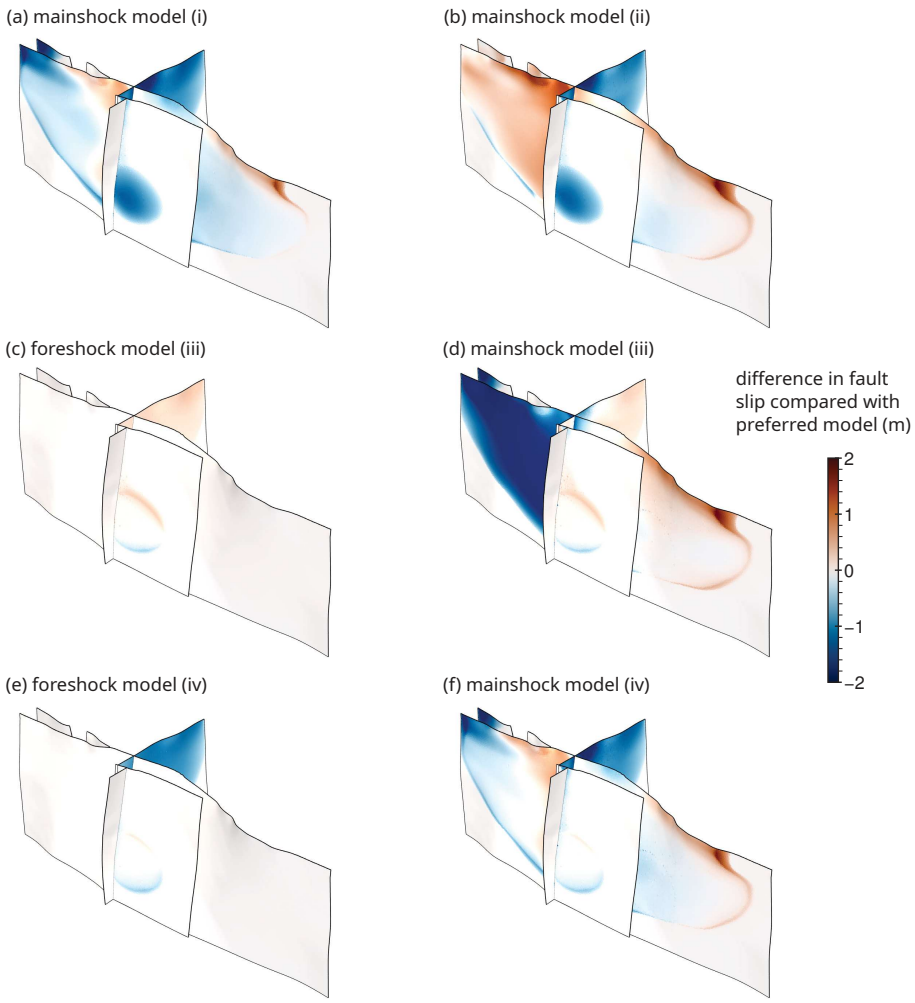

Figure 3.24: Difference in fault slip for models (i) to (iv) compared with preferred model in (m). Model (i) is not incorporating the foreshock stress changes. Model (ii) is not incorporating the foreshock stress changes and the long-term ΔCFS. Model (iii) is not incorporating the long-term ΔCFS. Model (iv) incorporates the community stress model FM3D [88].

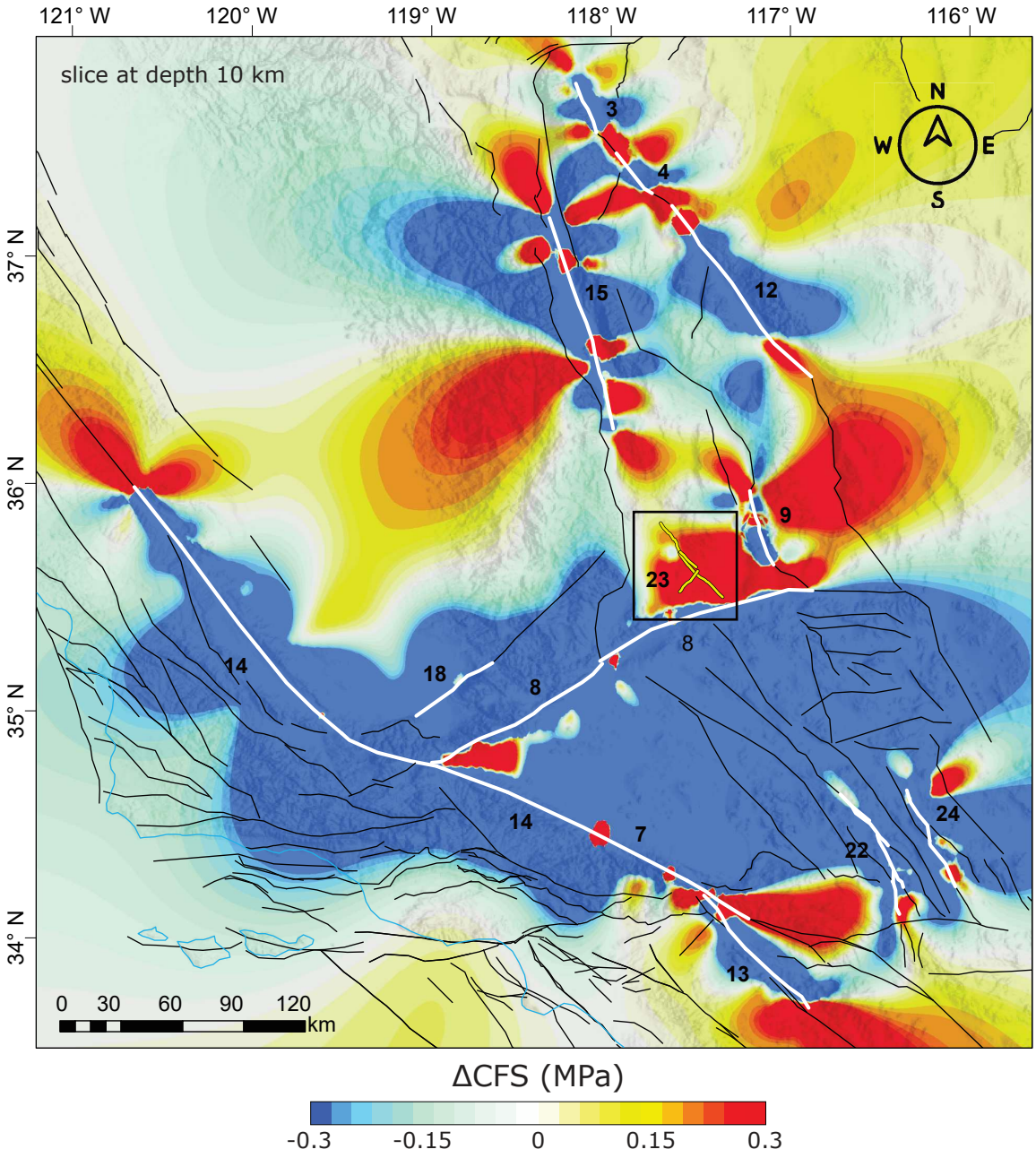

Figure 3.25: Pre-Ridgecrest cumulative Coulomb failure stress change (ΔCFS) from the events listed in Table 3.1, here plotted with white lines, at 10 km depth computed assuming a NW-striking fault plane of strike=318°, dip=88°, and rake=-170° and an effective friction coefficient f'=0.4, illustrating the 3D cumulative co- and post-seismic stress change model.

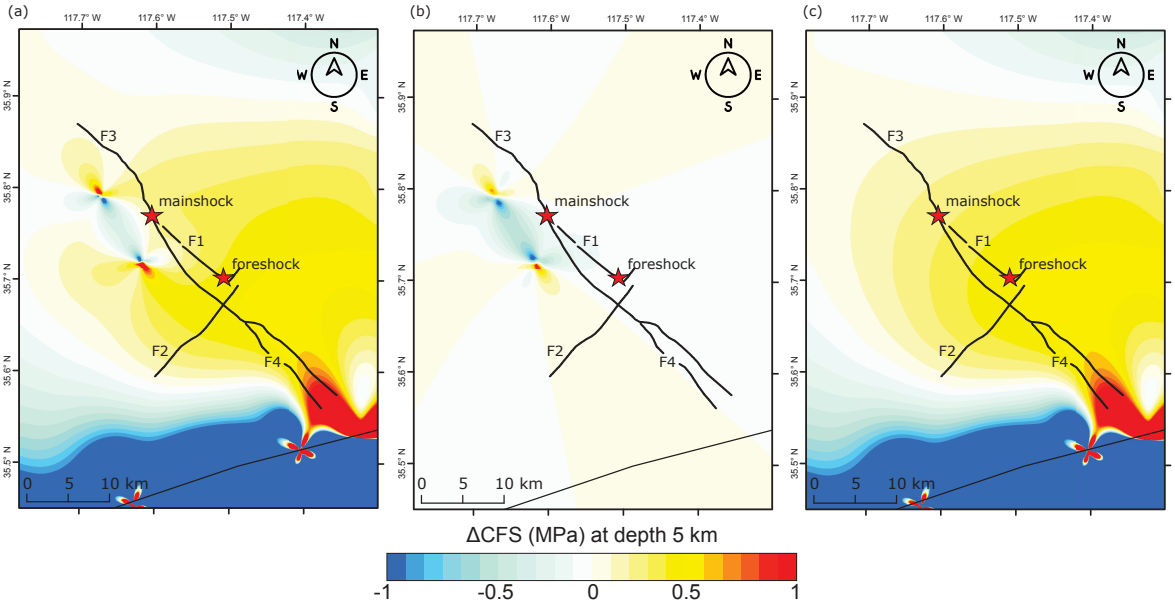

Figure 3.26: Pre-Ridgecrest cumulative Coulomb failure stress change (ΔCFS) isolating the effects of the two 1995 M_w 5.8 and M_w 4.9 earthquakes. (a) same as Figure 1b but with a smaller data range, ΔCFS of all events listed in Table 3.1 sliced at 5 km depth computed assuming a NW-striking fault plane of strike=318°, dip=88°, and rake=-170° and an effective friction coefficient f'=0.4. (b) ΔCFS of only the 1995 Ridgecrest M_w 5.8 and M_w 4.9 events. (c) ΔCFS of all events omitting the 1995 M_w 5.8 and M_w 4.9 events.

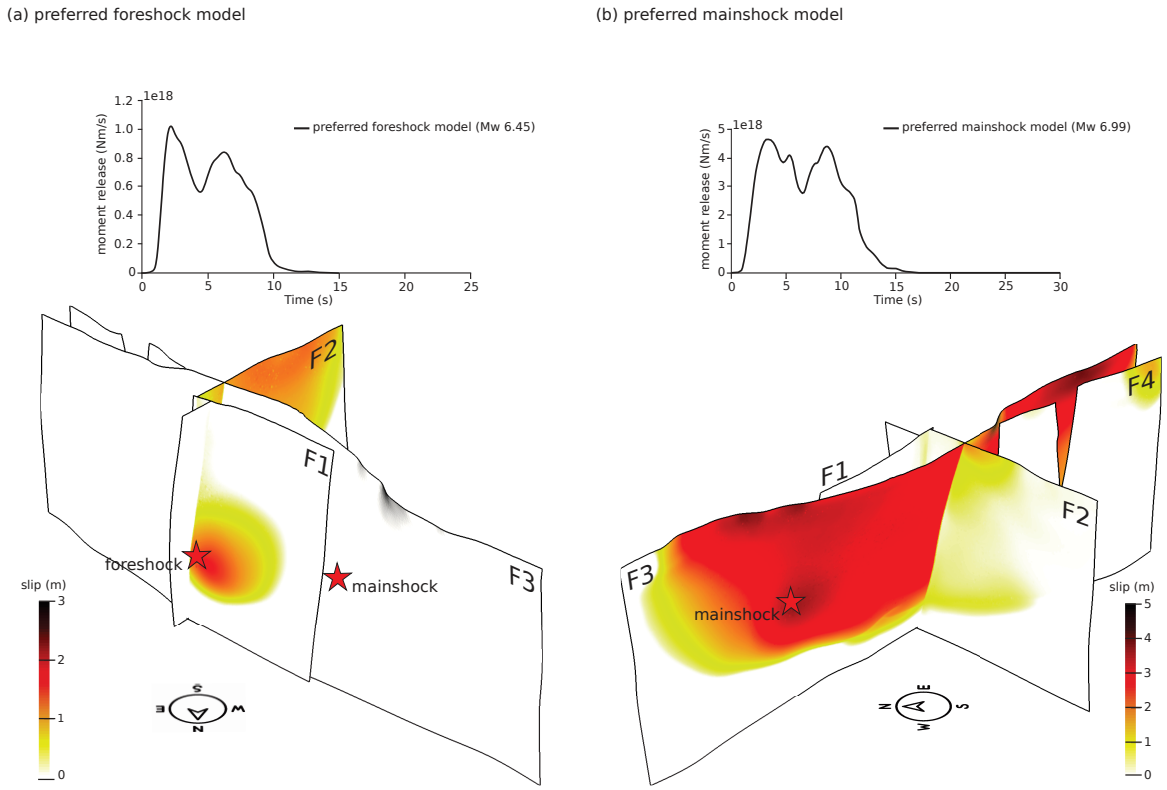

Figure 3.27: Preferred foreshock (a) and mainshock (b) dynamic rupture scenarios. Final fault slip from two perspectives and moment rate release.

Chapter 4

Constraining families of dynamic models using geological, geodetic and strong ground motion data: the Mw 6.5, October 30th, 2016, Norcia earthquake, Italy

4.1 Abstract

The 2016 Central Italy earthquake sequence is characterized by remarkable rupture complexity, including highly heterogeneous slip across multiple faults in an extensional tectonic regime. The dense coverage and high quality of geodetic and seismic data allow us to image intriguing details of the rupture kinematics of the largest earthquake of the sequence, the Mw 6.5 October 30th, 2016 Norcia earthquake, such as an energetically weak nucleation phase. Several kinematic models suggest multiple fault planes rupturing simultaneously, however, the mechanical viability of such models is not guaranteed. Using 3D dynamic rupture and seismic wave propagation simulations accounting for two fault planes, we constrain "families" of spontaneous dynamic models informed by a high-resolution kinematic rupture model of the earthquake. These families differ in their parameterization of initial heterogeneous shear stress and strength in the framework of linear slip weakening friction. First, we dynamically validate the kinematically inferred two-fault geometry and rake inferences with models based on only depth-dependent stress and constant friction coefficients. Then, more complex models with spatially heterogeneous dynamic parameters allow us to retrieve slip distributions similar to the target kinematic model and yield good agreement with seismic and geodetic observations. We discuss the consistency of the assumed constant or heterogeneous static and dynamic friction coefficients with mechanical properties of rocks at 3-10 km depth characterizing the Italian Central Apennines and their local geological and lithological implications. We suggest that suites of well-fitting dynamic rupture models belonging to the same family generally exist and can be derived by exploiting the trade-offs between dynamic parameters. Our approach will be applicable to validate the viability of kinematic models and classify spontaneous dynamic rupture scenarios that match seismic and geodetic observations as well as geological constraints.

4.2 Introduction

Kinematic modeling is a standard tool to image the slip behavior of faults during earthquakes of moderate-to-large magnitude. Kinematic models [93] prescribe the spatio-temporal evolution of slip on a fault as a result of solving data-driven inverse problems. Automated procedures deriving kinematic models within a few hours after significant events are an established part of rapid earthquake response information. Refined kinematic models often emerge during the months and years after an event using seismic and geodetic data and more advanced numerical methods to closely fit observations with a large number of free parameters [238]. Therefore, most significant earthquakes are characterized by several kinematic models that describe the complexity of the seismic process in terms of slip distribution, activated fault planes, fault geometry, and rupture time evolution.

More recently, kinematic modelers aim to take uncertainties into account, using, for example, a Bayesian approach [182] to mitigate errors and assumptions in the forward modeling, in the adopted Greens' function [250], in data coverage, and in data resolution. Despite recent advances, kinematic models are characterized by an inherent non-uniqueness of the problem (strong trade-offs among kinematic parameters) in addition to aforementioned significant uncertainties and the often required predefinition of fault geometries with notable exceptions, e.g., [182, 208].

However, it is uncommon to analyse whether kinematic models are dynamically consistent, i.e., if it is possible to find a configuration of dynamic parameters that yield the same spontaneous rupture history. The scaling and distribution of dynamic source properties can be evaluated from kinematic source models as a solution of the elastodynamic equation when the rupture history is prescribed a-priori on a fault plane. Distributions of the corresponding dynamic parameters can thus be retrieved without the need to use any constitutive law and to assess if the models would propagate spontaneously [219, 30].

Fully dynamic modeling of earthquakes provides a physics-based understanding of how earthquakes start, propagate, and stop. Earthquake dynamic rupture simulations couple the non-linear interaction of fault yielding and sliding behavior to seismic wave propagation [89]. Using modern numerical methods and computing infrastructure allows for realistic 3D dynamic rupture scenarios of complex, multi-fault earthquakes [3, 246]. Initial conditions, such as geometry, frictional fault strength, tectonic stress state and regional lithology, control rupture propagation style (e.g., pulse vs. crack-like dynamics and sub-Rayleigh vs. super-shear speeds), stress transfers (dynamic triggering, branching), and earthquake arrest [62, 14, 122, 89].

Since it is challenging to constrain fault stresses and strengths from direct observation, it is common to prescribe fault normal and shear stress as constant or linearly increasing with depth [73]. While matching strong motion records with dynamic rupture simulations can be formulated as an inverse problem with stress and friction as model parameters [68], to date, only simplified dynamic rupture simulations are computationally tractable for dynamic source inversion [61].

Dynamic models can be affected by parameter trade-offs [83, 202] and the choice of

constitutive law [46, 157]. Nevertheless, by reconciling findings from experiments [45, 37] and increasingly dense observations, dynamic models can bridge scales and geophysical disciplines to provide insight into the mechanic viability of competing hypothesis for a specific event [224, 241] or fault system [154, 91].

Few dynamic rupture models have been proposed of moderate size normal faulting events [68, 12]. Surface breaching reverse and normal faulting dynamic models are challenged by free-surface induced normal stress, strength, loss of ground motion symmetry, trapped waves in the hanging wall, and other dynamic and quasi-static effects [156, 10, 137].

In this work we develop a systematic approach to constrain spontaneous dynamic models based on a given kinematic model, allowing us to evaluate its dynamic consistency. Such data-driven physics-based models can complement rapid earthquake response and further the fundamental understanding of complex earthquake rupture processes.

Specifically, we design and analyze "families" of complex multi-fault dynamic models, each recovering main kinematic characteristics but varying in terms of their initial dynamic parameters which determine frictional strength and stress drop. We consider the well-recorded 2016 Mw 6.5 Norcia (Italy) normal faulting earthquake as a case study (Figure 4.1). This event is an example of a normal faulting earthquake with a moderate magnitude involving a complex set of intersecting faults. Several models proposed for this event [34, 31, 172, 203, 237, 22] generally agree on the location of the main slip release. However, most recent models require two or more connected faults to match all observations available from diverse dataset.

The inferred multi-fault geometries are not conflicting; a consensus [203, 148, 22, 237] is emerging for a multiple-fault model composed of a main normal fault parallel to the Apennines backbone, confined to the southeast by an oblique fault, unfavorably oriented with respect to the current tectonic regime [144]. The proposed composite models suggest that these fault planes slipped simultaneously, posing questions about the dynamic plausibility of co-seismic fault interaction.

Here, we focus on the complex kinematic model proposed by [203], "S18" hereinafter. In particular, for each family, we conduct dynamic rupture scenarios of the Norcia earthquake yielding the same kinematic features as the target "S18" model. We validate them with seismic and geodetic observations, overall slip distribution, rake direction, and moment magnitude. We derive a parametrization leading to friction coefficients (static and dynamic) consistent with the mechanical properties of rocks in the Italian Central Apennines.

Our approach helps to overcome the difficulties in assigning initial modeling conditions for dynamic rupture models in absolute terms and to discuss the lithological meaning of the derived friction parameters.

4.3 The Mw 6.5 October 30th 2016 Norcia earthquake

The Amatrice-Visso-Norcia (AVN) seismic sequence [34, 148, 203] started on August 24th, 2016, with the Mw 6.0 Amatrice earthquake [218]. The largest event, which occurred

on October 30th, struck the region close to Norcia village with magnitude Mw 6.5 and was preceded only four days earlier, on October 26th, by the Mw 5.9 Visso earthquake (Figure 4.1). For the Mw 6.0 Amatrice event, simplified dynamic rupture inferences from strong ground motion data [68, 12] reveal complex dynamics (e.g., two asperities and a slow nucleation phase) and imply that rupture arrested south of the secondary fault activated during the Norcia earthquake.

Similarly, the Norcia earthquake exhibited a large degree of complexity. Our starting point here is the kinematic model "S18" that involves, in addition to the main normal fault parallel to the Monte Vettore-Monte Bove fault systems, a second fault. This secondary fault is ascribed to the inherited Olevano-Antrodoco-Sibillini Thrust and dislocates as a NNE trending normal fault with a significant strike-slip component (Figure 4.1). The "S18" model is obtained from jointly inverting strong motion and GPS data, and is validated using InSAR data [203] and relocated aftershocks [148].

The main kinematic characteristics of the "S18" model (Figure 4.1) are the following: i) both faults dislocate almost simultaneously, reaching a maximum slip of 3 m; ii) the location of the high-slip patches is about 5 km shallower than the hypocenter while less than 20 cm of slip is inferred in the nucleation region; iii) the secondary fault is characterized by a predominantly left-lateral strike-slip mechanism within its largest slip patch, but also features local rake variations; iv) the southern part of the main fault, located behind the secondary fault and activated during the first event of the AVN sequence (the Mw 6.0 Amatrice earthquake), is partially reactivated during the Norcia event, with a locally significant amount of slip ($\approx$1 m).

4.4 Model setup

We use the open-source software package *SeisSol* (`www.seissol.org`) to model spontaneous dynamic earthquake rupture across intersecting faults and seismic wave propagation with high-order accuracy in space and time (Figure 4.2, for details see Supporting information 4.10.1).

Modeling complex fault interaction during dynamic rupture propagation is challenging, specifically across fault junctions and interpenetrating fault surfaces [47]. *SeisSol*, which is based on the Arbitrary high-order Derivatives Discontinuous Galerkin method [49], naturally allows for discontinuities and fault branching geometries [165].

4.4.1 Constitutive law

We adopt a simple constitutive relationship (Figure 4.3) to focus on the effects of heterogeneities in fault strength and stress. The linear slip-weakening (LSW) friction law [17] is a simple and widely used constitutive equation derived from theoretical and numerical models [5] of shear crack propagation from a macroscopic perspective [36]. This constitutive relation is completely characterized by the yield strength $\tau_y = \mu_s \sigma_n$, the dynamic frictional resistance $\tau_f = \mu_d \sigma_n$, and the critical slip distance D_c, where μ_s and μ_d are the static

and dynamic friction coefficients, respectively, and σ_n is the effective normal stress. The fault begins to rupture when shear stress locally exceeds τ_y and frictional fault strength decreases linearly from a static to a dynamic level over a critical slip distance D_c. For a slip greater than D_c, fault strength remains constant equal to τ_f (i.e., no healing). The distribution across the fault plane of the strength excess $(\tau_y - \tau_0)$, with the initial shear stress τ_0 , and the dynamic stress drop $\Delta\sigma = \tau_0 - \tau_f$, influences the ratio of strain energy and fracture energy, and determines local acceleration or deceleration of the rupture front.

Inference of the magnitude and direction of initial stresses is only possible from kinematic slip models in which the temporal rake rotation is well defined [210] otherwise, additional assumptions are required. Here we assume that the initial traction is co-linear with the accumulated slip in kinematic models to ensure physical plausibility [219].

Our spontaneous dynamic rupture model is fully defined in an elastic material by the spatial distributions of initial on-fault shear stress, normal stress, static and dynamic friction coefficients, and D_c in addition to the prescribed fault geometry and subsurface structural model. Using the LSW law permits us to potentially relate co-seismic fault-constitutive properties directly to observations, e.g., associating friction coefficients of different rocks with inferred values from laboratory experiments. However, scale-invariances and trade-offs between LSW dynamic parameters are well known [216, 78]: dynamic rupture models based on various dynamic parameter choices can fit seismological data equally well [83]. Dynamic parameters cannot be measured in-situ and often lack physical constraints rendering it difficult to determine them prior to (or after) an earthquake. This yields a wide and high-dimensional parameter space which is challenging to fully explore and constrain in a data-driven manner.

Therefore, assumptions have to be made when pre-assigning frictional parameters as well as the absolute amplitudes of initial stresses, which both may be heterogeneously distributed acting across the fault planes [185, 30]. This motivates our classification of "families" of dynamic models (section 4.4.4).

4.4.2 Fault geometry

We use a two-planar-fault geometry (Figures 4.1 and 4.2) derived from [203]. It consists of a main fault branch N155° trending along the Apennines (hereinafter F155), and a second fault plane striking N210° oblique to the Apennines (hereinafter F210). The main fault geometry aligns well with the SAR interferograms, the TDMT moment tensor solution, and the observed surface rupture [203]. The secondary fault plane geometry is supported by geodetic observations,the aftershock distribution, the inferred non–double-couple component of the mainshock moment tensor, and by moderate earthquakes of NE-SW trending focal mechanisms in the main fault hanging wall [148]. The dynamic activation of F210, which is shallowly dipping is a major challenge for this model.

4.4.3 Weak dynamic rupture nucleation

We assume the hypocenter adopted by [203] and located at 42.84°N, 13.11°E at a depth of 9.52 km to prescribe the onset of rupture in all our models. The nucleation region is located on fault F155 and intersects the bottom left corner of the F210 fault (see Figure 4.1). For the Norcia earthquake, similar to the Amatrice event, only small amounts of slip have been inferred in the hypocentral regions implying a transient, weak nucleation process [218, 68]. Weak nucleation in dynamic rupture models is controlled by spatial heterogeneities and the local closeness to failure of the hypocentral region. We find that locally over-stressing the fault (i.e., assuming the initial stress just above yield stress as e.g.[161]) tends to create artificially large fault slip in the hypocentral area and unrealistic strong pulses in the synthetic seismograms.

Instead, we gradually reduce the yield strength in an elliptical area centered at the hypocenter expanding at time-decreasing speed [89] which allows a smooth transition to fully spontaneous dynamic rupture propagation. In conjunction with assuming locally initial shear stresses very close to frictional strength, fault slip in the nucleation area remains limited, matching observations. To dynamically capture the low energy release and small slip during the weak nucleation phase, requires us to carefully balance the sensitive rupture initiation with spontaneous rupture across both activated fault planes. Low energy released in the nucleation zone does not promote spontaneous rupture towards the favourably stressed shallow fault region. Therefore, a large but weak nucleation area is required. For the models proposed, we choose a nucleation initial forcing speed of 2.8 km/s ($0.7V_s$) and a nucleation radius of 3-6 km, which is of similar size to inferences for the Amatrice event [172]. The forced nucleation phase contributes in our models during less than 2 seconds with little moment release.

4.4.4 Families of initial dynamic parameters

Dynamic models can be initialized assuming homogeneous or heterogeneous spatial distributions of one or more dynamic parameters governing frictional fault-weakening behavior and initial stresses on the fault plane [199].

To limit the complexity of the dynamic parameterization, it is common to attribute all heterogeneities either only to the initial shear stress distribution or to the yield strength [68] while considering the other dynamic parameters constant or homogeneously depth-dependent. In fully elastic dynamic models, the radiated waves are only sensitive to the dynamic stress drop but not to the absolute initial stress.

The main characteristics of the rocks that belong to a specific seismic zone can add lithology-controlled constraints [91]. Laboratory experiments on friction coefficients conducted on different types of rocks [45, 204, 44] provide possible ranges of frictional parameters for weak and strong faults [37]. Taking laboratory results into account can limit the parameter space to be explored in dynamic models.

Based on these considerations, we identify “families” of dynamic models, consistent with field and laboratory observations but differing in their parameterization of heterogeneous

fault stress and strength in the framework of a LSW friction law (Figure 4.3):

- Family (Hom) are models based on uniformly depth-dependent stress and strength conditions with constant static (μ_s) and dynamic (μ_d) friction coefficient.
- Family (A), the "family of heterogeneous stress", includes all models with constant static and dynamic friction coefficient, linearly depth-dependent initial normal stress but variable initial shear stress τ_0.
- Family (B), the "family of heterogeneous strength and stress", includes all models with constant dynamic friction coefficient, depth-dependent initial normal stress but heterogeneous static friction and initial shear stress.
- Family (C), the "family of heterogeneous dynamic friction", includes all models with uniform depth-dependent static friction and initial shear stress but heterogeneous dynamic friction. Family (C) ensures also depth-dependent strength excess.

A fully heterogeneous Family (D), the "family of heterogeneous strength, stress and friction", is here omitted given the high risk of severe data over-fitting.

We assume that the effective normal stress increases linearly with depth according to a fixed gradient based on an assumed fluid pressure ratio λ (defined as the fluid pressure over the lithostatic stress, e.g. [224]). The adopted near-hydrostatic fluid pressure ratio λ is 0.4, corresponding to an average gradient around 15 MPa/km. The associated stress and strength parameters (τ_0, τ_y, and τ_f) also vary linearly as a function of depth (see Figure 4.3).

Family (A) is our group of simple heterogeneous models: static and dynamic friction coefficients are homogeneous while the initial shear stress is heterogeneous. In this group of models, regions with kinematically constrained low fault slip have very high strength excess and small dynamic stress drop. Such areas, if large enough, do not favor sustained spontaneous rupture since they require more energy than available to overcome the strength excess. This family potentially allows using laboratory-consistent values for both static and dynamic frictions ($\mu_d \approx 0.2$ and $\mu_s \approx 0.6$, e.g., [37]]), but is not suited to all kinematic models. Specifically, the "S18" model cannot be reproduced using models belonging to Family (A) due to its low fault slip in the nucleation region: the resulting high strength excess prevents spontaneous rupture propagation.

Moreover, models of this family have a very small strength excess in regions of kinematically inferred high fault slip, such as at the center of the main slip patches (illustrated by the local closeness of τ_0 to τ_y in Figure 4.3). Thus, Family (A) dynamic models are also prone to a-causal ruptures, that is, failure may happen at many patches instantaneously. Thus, we refrain from further analysis of Family (A) in the remainder of this paper.

Family (B) is a group of heterogeneous models which are frequently proposed for dynamic source inversions [68]. Heterogeneities are attributed to the initial shear stress and yield strength, assuming a constant dynamic friction value. The heterogeneity of stress drop is then completely associated with the initial shear stress. Stress drop corresponding

to a prescribed distribution of slip can be retrieved in different ways: for example, by relating stress drop and slip in the wavenumber domain (originally proposed by [6] and updated by [185]) or by solving the elastodynamic equation using the entire slip-time history at each point of the fault [219, 30].

In this work, we explore two simple approaches. First, we estimate stress drop by assuming direct proportionality with fault slip. In the second approach, we infer the stress drop distribution from the stress change, by imposing the "S18" slip distribution everywhere on the fault (using an arbitrary smooth-step slip-rate function during 1 s), and measuring the final shear stress distribution [219, 30].

We constrain Family (B)'s yield strength, by assuming a strength excess radially increasing from the hypocenter, with a minimum value of 0.1 MPa at the hypocenter. In addition to the smooth nucleation procedure (Sec.4.4.3), this parametrization facilitates nucleation and yields realistic rupture growth.

Family (C) includes models with constant static friction, linearly depth-dependent initial shear stress, and heterogeneous dynamic friction. The resulting yield strength τ_y is only depth-dependent because the effective normal stress is depth-dependent. Heterogeneities in the dynamic friction coefficient stem from the target stress drop distribution, which is retrieved following two different procedures, as in Family (B).

While Family (B) has variable μ_s and constant μ_d, Family (C) has variable μ_d and constant μ_s.

We adopt friction values typical of many lithologies (i.e. 0.5-0.6 for μ_s and 0.1-0.2 for μ_d) [37] for the constant friction in Family (B) and (C). In contrast, variable μ_s and μ_d are obtained respectively from the assumed heterogeneous stress drop, derived from the "S18" fault slip. We further validate the dynamic models belonging to these two families by assuring that the variable friction values are compatible with the expected rocks in the modeled region and their depths. Introducing Family (C), which is often disregarded among kinematically constrained dynamic models, is motivated by the fact that most rocks favoring the occurrence of seismic events may share similar μ_s around 0.5-0.6 [28].

4.5 Results

The complex spatio-temporal evolution of the AVN sequence, and in particular the distribution and location of the main slip patches of the three main events may suggest strongly heterogeneous initial stress and/or frictional strength and weakening conditions. We first analyze simple models of Family (Hom), based on homogeneous friction, only depth-dependent stress assumptions, to understand which overall conditions favor a spontaneous multi-fault rupture across the assumed fault geometry. Next, we introduce more realistic heterogeneous dynamic models of Family (B) and (C).

4.5.1 Homogeneous initial conditions

Figure 4.4 (top panels) shows the on-fault distribution of the most important initial conditions and resulting dynamic parameters for three illustrative dynamic scenarios of Family (Hom). We assume constant static and dynamic friction coefficients of 0.6 and 0.2, respectively. Furthermore, we set the initial shear stress τ_0 as 65% of the yield strength τ_y, which allows dynamic rupture to spontaneously propagate while limiting rupture speed to sub-Rayleigh velocities for most of the fault area. For simplicity, we use on each fault plane a constant shear stress orientation, informed by the average faulting mechanism in the "S18" model: pure normal faulting for the F155 (-90°) and almost pure left-lateral strike faulting (-10°) for the F210 fault.

The magnitude of the initial shear stress τ_0 varies on the two fault planes only as a function of depth (Figure 4.4) following the normal stress gradient. Figure 4.4 (second row) shows the depth-variations of τ_y, τ_0 and τ_f as cross-sections. Small offsets are the result of the layered density profile. The nucleation is imposed inside a sphere of radius 3 km. Fixing all other parameters, we here explore how dynamic rupture viability on the main and secondary fault is depending on the choice of D_c. We confirm that smaller D_c, i.e. smaller fracture energy with other dynamic parameters kept unchanged, favors dynamic rupture propagation while larger D_c inhibits it. We also find that fault interaction branching, dynamic triggering, shadowing, and co-seismic static slip effects (e.g. [120]) is highly sensitive to choices of D_c.

For the assumed initial conditions and fault geometries, we find that values of $D_c \approx$1-2 m on the F155 main fault allow rupture propagation at sub-Rayleigh velocity (<3 km/s) across most of the slipping area. However, due to the linear depth-dependence of the initial stress, the rupture velocity tends to reach super-shear speeds at shallow depths [213]. At the same time, lower values of D_c on F210 (<0.8 m), are needed to allow dynamic rupture propagation there.

In Figure 4.4 (top row) we show three D_c combinations to illustrate the model sensitivity to this parameter. In the bottom panel, we compare snapshots of slip distributions after a rupture time of 6.75 s for these three models. Their elliptical slip distributions generated by crack-like dynamics, e.g., [62], are aided by LSW friction and homogeneous initial conditions. These models are characterized by high slip (> 10 m) in the hypocentral region and by magnitudes much larger than Mw 6.5 (between Mw7.14 and Mw7.35, see the right-most panel in the second row of Figure 4.4).

Assuming $D_c = 1.2$ m and $D_c = 1.0$ m for F155 and F210, respectively, rupture is not simultaneously propagating along both faults (see snapshot at t=6.75 s in panel a) but breaking only the main fault including the area beyond the fault intersection. At a later simulation time ($> 8s$, not shown in the figure) slip is observed also on F210, which is dynamically initiated by reflections at the free surface and at the interfaces of the layered velocity structure. Assuming $D_c = 1.2$ m and $D_c = 0.8$ m (panel b) for F155 and F210, respectively, both faults rupture simultaneously. Interestingly, rupture of F155 behind the intersection is initially prevented due to stress shadowing [19] from the F210 rupture. Finally, assuming $D_c = 1.8$ m and $D_c = 0.8$ m for F155 and F210 (panel c), respectively,

shows again simultaneous rupture on both fault planes. Initially, this model features a slower rupture (the rupture front is closer to the hypocenter at 6.75 s compared with panel b). Again, rupture propagation beyond the intersection with F210 is hindered. In the models of panels b and c, the rupture is able to propagate beyond the fault intersection with a delay of several seconds, which makes this secondary propagation more akin to a triggered event rather than a slow rupture.

We find that $D_c^{F210} > 0.8\ m$ prevents dynamic rupture on F210 (for the here assumed stress conditions and nucleation). As an additional constraint, if dynamic rupture on F210 is prevented, F155 can host spontaneous rupture propagation only if $D_c^{F155} < 1.2\ m$. Therefore, high values of D_c on the main fault need to be combined with low values of D_c on the secondary fault to allow rupture across both fault planes in the dynamic rupture Family (Hom). Assuming pure normal faulting for both faults results in even less favorable conditions for sustained rupture on F210 and very small D_c values are required to dislocate both fault planes (models not presented).

The presented models have the same ratio of initial shear stress τ_0 over yield strength τ_y. Exploring alternative ratios, as well as different ratios on each fault, will likely influence the critical D_c values that allow rupture on one or both faults. A full analysis of this variability, as well as variations in nucleation, is possible but beyond the scope of this study.

Fracture energy, defined as $G_c = 1/2\,(\tau_y - \tau_f)\,D_c$ [162], increases with depth in Family (Hom) and varies linearly with D_c between models. The average fracture energy in the examples is ≈20.6-29.3 MJ/m^2 (see right-most panel in the second row of Figure 4.4) which is comparable to estimates inferred for past earthquakes of similar magnitude [235]. We note that fracture energy on both fault planes is roughly equivalent for both models in panels a and b, despite their distinct rupture dynamics [83].

Using simple forward dynamic rupture models of Family (Hom) we show that a multi-fault rupture is plausible. Assuming homogeneous, depth-dependent stress and strength conditions can lead to left-lateral strike-slip faulting on the secondary fault (F210) and normal faulting on the main fault (F155). The synthetic waveforms resulting from dynamic rupture models of Family (Hom) are very different from observations. While we do not systematically explore the parameter space of all possible constant values of μ_s, μ_d, and D_c, this nevertheless suggests that the real dynamic initial conditions may have been strongly heterogeneous. We next explore the space of the dynamic parameters with heterogeneous stress and/or strength conditions to propose dynamic models that reproduce the main features of the "S18" model.

4.5.2 Heterogeneous initial conditions

We here investigate models of Families (B) and (C) having heterogeneous stress and strength as defined in Section 4.4.4. We identify plausible rupture models, representative of their respective family. These models are consistent with the "S18" inverted kinematic characteristics and with observations (Supporting information 4.10.2). We do not claim that these models are the dynamic models that best fit the data, due to trade-offs between

the dynamic parameters. Instead, we suggest that suites of well-fitting models belonging to the same family exist and can be derived by exploiting the trade-offs between their dynamic parameters. We first show models that assume a direct proportionality between fault slip and stress drop (Sec. 4.5.2) and, secondly, models in which the stress drop is kinematically inferred as the stress change associated with the "S18" model (Sec. 4.5.2).

Stress drop proportional to fault slip

In Figure 4.5 we show the dynamic parameter distributions of two representative models belonging to Family (B) and (C), respectively. Family (B) (panel a) has heterogeneous distributions of initial shear stress and yield strength. The latter is parameterized as a heterogeneous distribution of μ_s in the range of [0.2, 0.7] while μ_d is kept constant at 0.2. Family (C) (panel b) has heterogeneous distribution of dynamic friction μ_d with values between 0.1 and 0.45 and constant μ_s =0.5.

In computing the stress drop for both families (B) and (C), we slightly adapt the "S18" slip distribution at shallow depths (< 2 km) to prevent fault reactivation due to rupture-free-surface interaction mediated by small normal stress. To further prevent near-surface supershear rupture in the uppermost 2 km we use higher values of μ_s (0.7) in Family (B) and we add frictional cohesion $c = 2$ MPa to the yield strength ($\tau_y = \mu_s\sigma_n + c$) in Family (C) as often assumed in dynamic rupture models [91]. The resulting range of the dynamic parameters τ_y, τ_f and τ_0 for the representative models of the two families is very different (see Figure 4.5).

As we have seen in Sec. 4.5.1 the choice of D_c is fundamental. Yet, D_c is one of the most difficult dynamic parameters to constrain [216, 83]. We find in numerical experiments conducted for both heterogeneous Families (B) and (C) that a constant D_c value on each fault plane does not allow realistic rupture dynamics. In fact, imposing a smaller D_c ($D_c <$ 50 cm) on both fault planes leads to supershear rupture velocities. On the other hand, imposing larger D_c values ($D_c >$ 50 cm) tends to prevent the rupture from propagating spontaneously. These strong dynamic trade-offs are also due to the very small slip in and around the nucleation area [68]. Thus, we here decide to assume D_c proportional to slip [216] which is a common assumption to ensure spontaneous rupture propagation. We note that the velocity toughening friction law of [7], aiming at mimicking the effect of off-fault yielding, yields an equivalent linear scaling of D_c. Based on few trial simulations, we set $D_c = 0.3S_{final}$ (S_{final} is the slip distribution of the "S18" model) in the shallow part of the fault (down to 4.5 km depth) where the main patch of slip is located. Below 4.5 km depth, we set $D_c = 0.1S_{final}$, which aids spontaneous rupture to migrate to the shallow region of larger fault slip (see Figure 4.5). The choice of D_c affects the width of the cohesive zone, which has to be numerically well resolved [246]. We limit D_c to values larger than 0.02-0.06 m (depending on the family) which ensures that the median of the cohesive zone distribution remains numerically well resolved (Appendix 4.10.1).

In Figure 4.6 we show snapshots of fault slip (top) and slip rate (bottom) for one model of Family (B). Rupture propagates simultaneously on both fault planes. Moreover, rupture is also able to propagate beyond F210. The interaction of the main rupture front

with the free surface produces back-propagating rupture fronts interface waves [50] of small amplitudes. The nucleation area (Sec. 4.4.3) results in a weak nucleation, as desired. The slip distribution features a large patch of slip of up to 3 m located just above the hypocenter on F155 with a dominant normal component, as well as a smaller patch of slip with similar maximum amplitude on the F210 fault with a dominant strike-slip component. The final slip distribution resembles the "S18" model, but is less heterogeneous. This arises mainly from the assumed proportionality between slip and stress drop as will become apparent in comparison to models initialized with the stress change computed from the "S18" model (see Sec. 4.5.2).

The rupture evolution of a representative dynamic rupture model belonging to Family (C), characterized by heterogeneous dynamic friction, is shown in Figure 4.7 using fault slip and slip rates snapshots. The final slip distribution is very similar to the presented Family (B) model, despite the different dynamic conditions, due to comparable stress drop. Approximately, when neglecting dynamic under- and overshooting, the stress drop is indeed the same in both families, with heterogeneity in initial pre-stress parameterized as spatially variable μ_s or μ_d in Family B and C, respectively. Rupture speed, as well as the peak slip velocity, are also similar in the main area of slip. The Family (C) model features a slightly higher rupture velocity than the Family (B) model towards the northern end of the main fault. Again, this model allows the rupture to propagate behind the secondary fault.

The total inferred seismic moments are 1.05e+19 Nm and 1.3e+19 Nm for the representative models of Family (B) and (C), respectively. These values agree with the seismic moment inferred from kinematic inversion in [203] (0.88e+19 Nm). The average fracture energy computed accounting only for fault cells with slip larger than 20% of average slip is $0.7MJ/m^2$ for Family (B) and $0.61MJ/m^2$ for Family (C). These averages are smaller than those obtained for models of Family (Hom) (Section 4.5.1) and consistent with proposed scaling laws between fracture energy and seismic moment [235, 219].

Figure 4.8 compares synthetic velocity waveforms, with selected observed data in the near-source region. We obtain a surprisingly good fit in both amplitude and phase for both families, given our synthetics are not resulting from a dynamic source inversion. We underline that no static correction has been applied. Moreover, the synthetics of the two families are very similar to each other. Synthetic waveforms at the CNE station, located northwest of the main patch, have similar pulses and amplitudes to the recorded data in both models but are slightly delayed indicating directivity effects not fully captured in either scenario.

Kinematically inferred stress change

We now present models that belong to Family (B) and (C) in which the stress drop distribution is initialized from the stress change kinematically computed from the "S18" model. We call these models "stress change" models. The stress change models differ from the previously presented models only in their (potential) stress drop distribution. Figure 4.9 shows the imposed heterogeneous distributions of μ_s and μ_d for two models belonging to

Families (B) and (C), respectively. Both friction parameters are distributed within the same range (0.2-0.7) but more heterogeneous compared to the models of Section 4.5.2. Note that the large values of μ_d ($\approx$0.7) in Figure 4.9 are fictitious since they are located in areas where rupture does not propagate. Both stress change models show a more heterogeneous distribution also of all other dynamic and kinematic parameters, which is reflected in the complex rupture history shown in Figures 4.14 and 4.15. In these models the peak slip on F210 is higher, while on average the final slip distribution is more similar to the original model "S18" than the models presented in Figures 4.6 and 4.7. Also, the rupture evolution is more complex than the circular propagation assumed in the kinematic model, due to the highly heterogeneous pre-stress distribution in the stress-change models.

In Figure 4.9 we show the waveform fits for these models. Both stress change models align well with observations. Synthetics of the two models are again similar to each other although differences are more clearly noticeable than in the models shown previously. The more pronounced variability between the models of the two families is expected because they have different and complex slip rate histories.

Geodetic validation

Even if we here do not aim at identifying a best dynamic model for the Norcia earthquake, we validate all four exemplary heterogeneous dynamic rupture models also with geodetic GPS and InSAR data. We compare in Figure 4.10 the synthetic deformation along line of sight for the descending and ascending ALOS2 InSAR data and the synthetic coseismic displacements with GPS observations [31].

The target "S18" model, inverted from strong-motion and GPS data, offers, as expected, the best fit to the GPS data. The dynamic rupture models having the same stress drop assumption yield similar geodetic fits. The "stress change" models, having slip distributions very similar to the original "S18" model, offer the best fit for InSAR data, and reproduce the GPS reasonably well in amplitude and direction, except for a large observed displacement in the footwall region.

Models inferred by assuming stress drop proportional to slip (Section 4.5.2), show in general the largest deformation values, still consistent with inversion results, but at worse orientation. This is mainly due to their slip distributions, which reproduce the large-scale features of the target model but not its shallow smaller-scale heterogeneities. Comparison with both ascending and descending InSAR data yields similar conclusions (Figure 4.10 and Figure 4.18). Note that this dataset can only be discussed qualitatively, as the observed data contain also the deformation produced by the Mw 5.9 Visso earthquake.

While our results suggest the existence of dynamic models within both heterogeneous families able to support the dynamic viability of the "S18" kinematic model, model validation with seismological and geodetic data does not identify a preferred family of models. Additional constraints are needed to assign heterogeneities to dynamic parameters, e.g. using friction values consistent with rock properties in the area.

4.6 Discussion

We present several dynamic rupture models for the Norcia earthquake to assess if the kinematic model "S18" proposed by [203] is dynamically viable (i.e. if the earthquake can propagate spontaneously on both faults). To this end, we design families of dynamic parameters. Family (Hom), the simplest possible distribution of dynamic parameters, allows us to dynamically validate the fault geometry and the average rake values inferred in the "S18" model. Specifically, we find parameter sets that allow for simultaneous spontaneous dynamic rupture of both fault planes (even if the secondary fault is dynamically more challenging to activate). However, homogeneous dynamic conditions lead to earthquake scenarios not agreeing well with observations.

The models of Family (B) and (C) with spatially heterogeneous dynamic parameters permit to dynamically retrieve slip distributions similar to model "S18", yielding a satisfactory fit of the observed waveforms and geodetic observations. We suggest the existence of suites of dynamic models in both families that are able to validate the target kinematic model.

However, the dynamic conditions of Family (B) and (C) are very different. In Family (B), we assume constant dynamic friction (μ_d =0.2) and heterogeneous static friction, which varies between μ_s=0.2 and 0.7. In Family (C), we assume constant static friction (in the showed model, we assume $\mu_s = 0.5$) while the dynamic friction is heterogeneous and varies between μ_d =0.1 and 0.45.

Geological data and results from laboratory experiments provide strong evidence for structural and frictional heterogeneities within crustal faults [37]. However, the different dynamic parameter assumptions made for Families (B) and (C) have implications for the physical processes occurring on the fault plane during the coseismic stage. In particular, the choice of reliable friction coefficients may be related to the rocks where the event nucleates, propagates, and finally generates the large slip patches.

For the Norcia earthquake, the integration of seismic reflection profiles with seismological data shows that the mainshock nucleated within the Triassic Evaporites and propagated through the overlaying carbonates [177]. The Triassic Evaporites consist of anhydrites and dolostones and laboratory data on these fault rocks show static friction in the range of 0.5-0.6 [204] with a reduction to 0.4 with increasing temperatures. In addition, the main patch of slip seems to be located within carbonates [203, 177], where the static friction is around the Byerlee's values (0.6) and dynamic friction at high slip rates can be as low as 0.2 [44]. Experiments conducted at high slip velocities ($> 1m/s$) [45] show that dynamic friction of different rocks ranges between 0.1 and 0.4. Static friction as low as 0.3-0.2 can be found only in clay-rich rocks (e.g., phyllosilicates). However, friction experiments on carbonates-clay mixtures show that the increase of clay content promotes a clear transition from velocity weakening to velocity strengthening behavior [194]. In consideration of these experimental values, the models of Family (B) may be plausible when considering rocks rich in phyllosilicates. Such low static friction values retrieved for Family (B) are located in and around the nucleation zone. Since these conditions may lead to velocity strength-

ening, this area would be less prone to nucleate [194]. Finding clay-rich rocks at depths similar to the hypocentral depth is unlikely [177]. Since small slip in the nucleation area is a specific earthquake characteristic, we may hypothesize that weak nucleation can result from pre-seismic creep.

Following the results of [177] and laboratory values, it seems that models belonging to Family (C) are promising candidates to represent the friction values of the seismogenic area in the Central Apennines. This family shows the lowest values of dynamic friction (0.1) in the areas of highest slip rate, consistent with laboratory experiments, while the highest dynamic friction values characterize areas of small slip.

While we here show that the S18 kinematic model can constrain reasonable dynamic rupture scenarios under certain assumptions (e.g., assuming weak nucleation), we note that both, kinematic and dynamic earthquake source models, may be highly non-unique when considered in isolation. Due to the vast size of the null space of the inverse problem and incomplete data coverage, kinematic combinations of source parameters may be acceptable that include opposite rake angles of multiple faults and fault geometries that may not favor dynamic fault interaction. On the other hand, dynamic trade-offs, e.g., between strength excess and slip-weakening distance, challenge an intuitive assessment of the physical consistency of a given kinematic model. We believe that adding physics-based constraints (i.e., by the assumed friction law) and combining dynamic rupture modeling and kinematic source inversion will reduce uncertainty of both kinds of proposed models.

4.7 Conclusions

We propose families of dynamic models for the Mw 6.5 October 30th, 2016 Norcia earthquake that aim to reproduce the main characteristics of the "S18" kinematic model inferred by [203] and to assess its mechanical viability. We detail representative models of two families: either with constant dynamic friction coefficient and heterogeneous initial stress and yield strength or with constant static friction coefficient, homogeneous depth-dependent initial stress, and heterogeneous dynamic friction coefficient.

In addition to the goodness of fit of seismic waveforms and geodetic deformation (GPS and InSAR) and the ability to reproduce characteristics of the target kinematic model (such as the slip distribution), we propose that geological constraints, e.g. ensuring compatibility of the assumed friction values with experimental values from near-fault rocks, can help to discriminate among plausible dynamic rupture scenarios.

Despite the limited resolution of seismological and geodetic data, we believe that future efforts shall be directed towards a new generation of dynamic models of real events including constraints from interdisciplinary geophysical observations. For example, using models of Family (B) or (C), the static and dynamic friction parameters may be chosen based on available geological and lithological constraints, while future high-resolution, near-fault seismic and geodetic data can help to constrain fault characteristics, e.g. D_c, and relative initial shear loading, in-situ. Reducing the trade-offs among the dynamic parameters by improving the resolution of the seismological data and the knowledge of friction properties

of fault rocks are definitely ingredients to combine.

The developed approach can be readily applied to various types of earthquakes using kinematic models to constrain dynamic rupture scenarios and enhance data-driven approaches with physics-based implications.

4.8 Data and resources

SeisSol is openly available at https://github.com/SeisSol/SeisSol. We use commit 24b71e4b0b1501782f0369c068dfcc99f57d1bcb. All simulation input files and the jupyter notebooks are accessible at https://github.com/git-taufiq/NorciaMultiFault.

4.9 Acknowledgements

We would like to thank M. Scuderi and C. Collettini for helpful discussions. We thank the editor R. Bendick, reviewers R. Harris and T. Ragon for their helpful and detailed reviews. T.U., T., D.L., and A.-A. Gabriel are supported by the European Research Council (ERC) under the European Union's Horizon 2020 research and innovation programme (TEAR, agreement No. 852992 and ChEESE, grant no. 823844), the German Research Foundation (DFG project grants no. GA 2465/2-1 and GA 2465/3-1) and by KAUST-CRG (grant no. ORS-2017-CRG6 3389.02). Computing resources were provided by the Leibniz Supercomputing Centre (LRZ, project no. pr63qo on SuperMUC-NG).

4.10 Supporting information

4.10.1 Numerical method and computational mesh

We use SeisSol, a powerful open-source software package (`https://github.com/SeisSol/SeisSol`), to perform dynamic rupture simulations at the supercomputer SuperMUC-NG at the Leibniz Supercomputing Centre, Germany. *SeisSol* solves the 3-D elastodynamic problem of spontaneous frictional failure across prescribed fault surfaces nonlinearly coupled to seismic wave propagation based on an the Arbitrary high-order accurate DERivative Discontinuous Galerkin (ADER-DG) method [49, 97].

SeisSol reaches scalable performance up to several thousand nodes on modern supercomputers [97, 230] and has been applied in large-scale, data-integrated earthquake models, including crustal events [246, 224], intraplate [161] and megathrust earthquakes [230]. SeisSol uses unstructured tetrahedral meshes enabling geometrically complex models, such as branching and intersecting faults[165]. Aided by a clustered local time-stepping scheme, mesh resolution can be adapted to ensure fine sampling of the faults while satisfying the requirements regarding numerical dispersion of pure wave propagation away from the fault. End-to-end computational optimizations [230], allows for high efficiency on high-

performance computing infrastructure. *SeisSol* is verified in a wide range of community benchmarks [165] by the SCEC/USGS Dynamic Rupture Code Verification project [89].

Our model domain is discretized into an unstructured computational mesh of four-node linear tetrahedral elements. We use an on-fault spatial discretisation h of 250 m for all models shown in the paper (corresponding to ∼16 million elements). In the volume, we parametrize the mesh size based on the velocity structure: we allow 3 cells per wavelength of shear waves to ensure resolving a maximum frequency of at least 1 Hz. In most of our simulations, we use basis functions of polynomial order p =4 which leads to fifth-order numerical accuracy in time and space. In SeisSol, each triangular fault interface is sub-sampled by $(p+2)^2$ Gaussian integration points.

We ensure all simulation results are sufficiently resolved by following the procedure established in [247], following [43]. We measure the cohesive zone size, the region behind the rupture front where the fault strength drops from its static to dynamic level, everywhere on both faults. In a purely elastic setup with depth-dependent heterogeneous initial conditions it is sufficient to resolve the median cohesive zone size Λ by ≈1-2 elements (for $p = 5$) or ≈2-3 elements (for $p = 4$). With $h = 250$ m we ensure that the median cohesive zone size is correctly resolved ($\Lambda > 600$ m) for all our models, except Family (C).

Adopting the same mesh for Family (C) models, we increase the resolution by using $p = 5$ (order 6 space-time accuracy). We verify that the fault dynamics of the more heterogeneous Family C models are sufficiently resolved by comparing the on-fault results with results from a finer mesh of fault mesh size h =100 m (corresponding to ∼33 million elements and median $\Lambda = 253$ m). Rupture arrival time, peak slip-rate, and final slip differ by about 1.5%, 1.4% and 1%, respectively, between these two simulations. Such errors are well within the recommended criteria of [43]. Simulating 30 s of each earthquake scenario using 5th order accuracy in space and time and on fault mesh size $h = 250$ m requires about 600 CPU hours in single precision.

4.10.2 Model validation data

The Mw 6.5 October 30th, 2016 Norcia earthquake has been recorded by a dense network of strong-motion stations (Figure 4.1), by Global Positioning System (GPS) stations, and by ALOS-2 satellites. The strong motion stations belong to the National Accelerometric Network (`http://ran.protezionecivile.it`) of the Italian Department of Civil Protection and the National Seismic Network of INGV [150]. Strong motion recordings were processed to remove the instrument response, band-pass filtered in the frequency range of 0.02 - 0.5 Hz (Butterworth filter with 2 passes 2 poles), and integrated to obtain ground velocity waveforms. The location of the used stations is shown in Figure 4.1. The maximum station-epicenter distance is within 45 km. These recorded waveforms are compared with synthetics computed using SeisSol, filtered in the same frequency band. The three-components coseismic displacements recorded by campaign GPS stations have been downloaded from the RING website (`http://ring.gm.ingv.it`), and the location of the closest stations is shown in Figure 4.10.

The satellite data (InSAR) acquired by the ascending and descending orbits along the

line of sight of ALOS-2 [31] has a time interval covering both the October 30th Norcia event and the Mw 5.9 Visso earthquake (October 26th). It does not allow discrimination between the surface displacement effects produced by the two earthquakes separately in the northern region (Figure 4.10). All these data-set have been used in this work to validate the proposed dynamic models.

4.10.3 Velocity structure

We adopt the 1D layered model for the Central Apennines of [98] (nnCIA model), constrained by deep crustal profiles, surface-wave dispersion, and teleseismic P-wave receiver functions. This model consists of five crustal layers above the Moho, including a thin (1.5 km) shallow layer with a relatively low shear wave velocity of 2.14 km/s and a velocity inversion at a depth of 4.5 km (see Figure 4.2 and Figure 4.11). The model is routinely adopted for moment tensor inversion for Italian earthquakes and kinematic finite fault inversions in the Apennines Region, including the "S18" model.

4.10.4 Movies

Below are additional movies as supporting information:

- Movie FB_SLIP.mp4: animation of the slip dynamics for Family (B)
- Movie FC_SLIP.mp4: animation of the slip dynamics for Family (C)
- Movie FB_SLIPVEL.mp4: animation of the slip velocity dynamics for Family (B)
- Movie FC_SLIPVEL.mp4: animation of the slip velocity dynamics for Family (C)

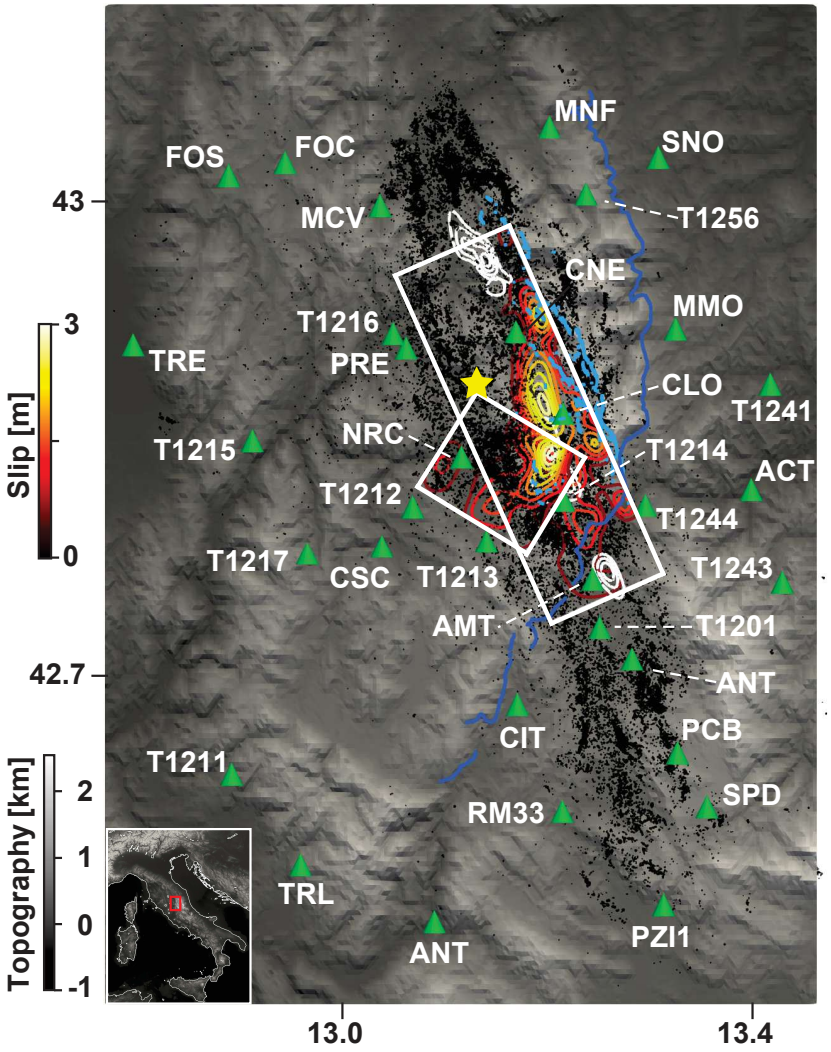

Figure 4.1: Map of the study area. Black dots: Amatrice–Visso–Norcia seismic sequence relocated earthquakes from [148]; darker blue lines: fault traces of OAS (Olevano-Antrodoco-Sibillini) thrust fronts; light blue lines: observed surface offsets. Green triangles denote the strong motion stations. Yellow star shows the epicenter of the 2016 Norcia event adopted in this study. White contours are the slip distribution for Visso and Amatrice events, from [218, 34]. The slip distribution of the Norcia event inferred by [203] - model S18 - is shown by coloured contours. Important characteristics of S18 are the weak nucleation, the main slip patches occurring updip from the nucleation on the two differently oriented faults (white boxes) and the rupture beyond the fault intersection.

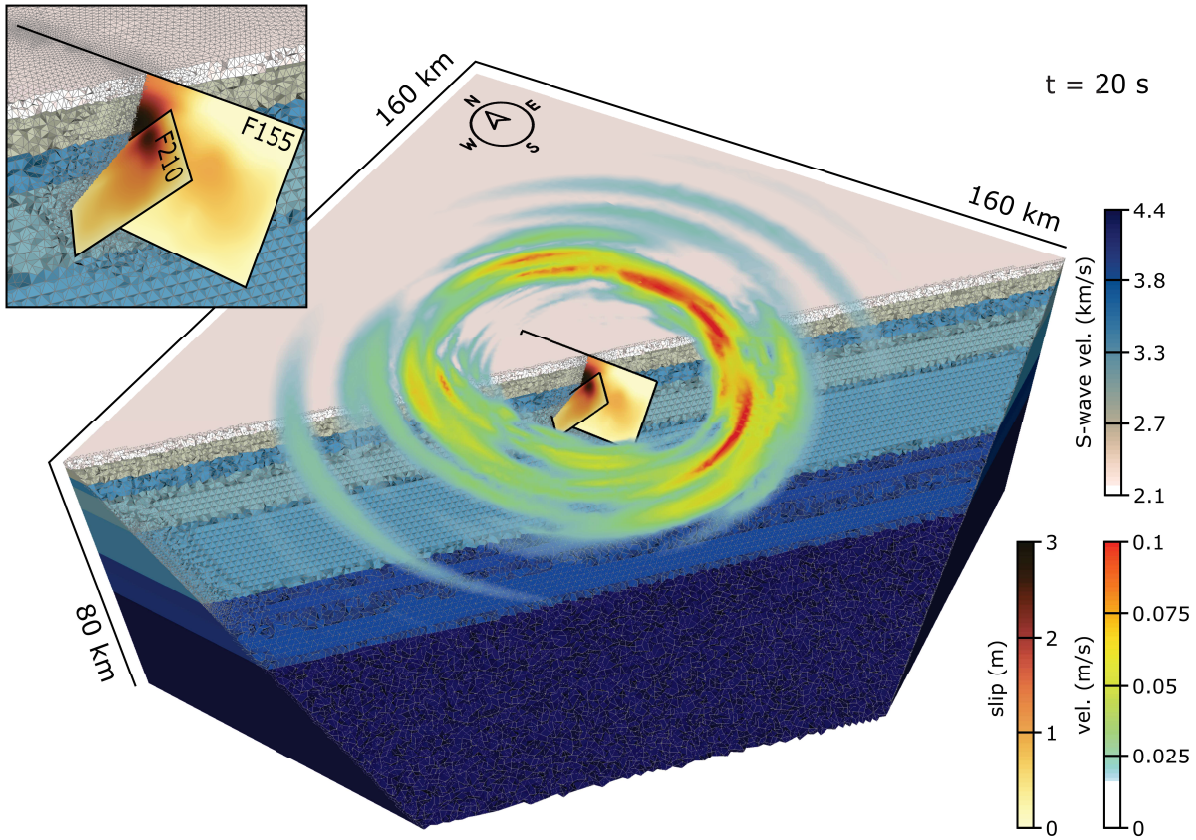

Figure 4.2: Snapshot of the ground surface wavefield (absolute particle velocity in m/s) at a simulation time of 20 s. The two-faults model, as well as the unstructured mesh incorporating the interface layers of the 1D layered velocity model (nnCIA model, [98]) and featuring refined resolution in the vicinity of the faults, are also shown. The inset provides a zoomed view on the two fault planes, colored by the slip distribution of the exemplary model of Family (B) in which stress drop is assumed proportional to slip. The two-planar-fault geometry [203] consists of a main fault branch N155° trending along the Apennines and dipping 47° to the SW (hereinafter F155), and a second fault plane striking N210° oblique to the Apennines and dipping 36° to the NW (hereinafter F210). The main fault is 34 km long and 16 km wide (downdip), while the secondary fault is 10 km long and 14 km wide. F155 reaches the modeled free surface, while the top border of F210 is 1.8 km below the modeled ground surface.

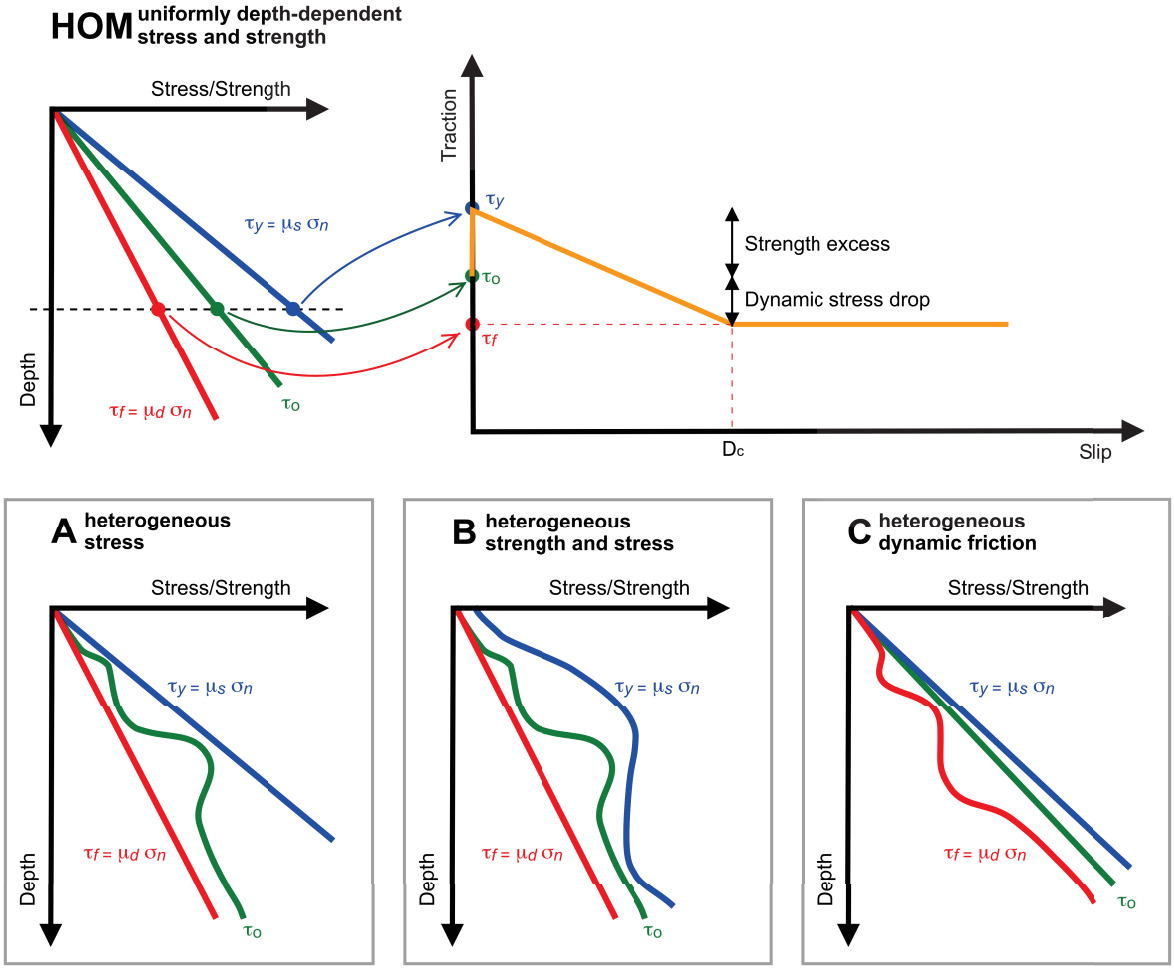

Figure 4.3: Variation with depth of dynamic parameters describing the LSW law, classified in four families of dynamic rupture models proposed in this work. Family (Hom) encompasses models based on laterally-invariant and linearly depth-dependent stress and strength conditions with constant static and dynamic friction coefficients. Family (A), called "family of heterogeneous stress", includes models with constant static and dynamic friction, linearly depth-dependent normal stress, and variable initial shear stress τ_0. Family (B), called "family of heterogeneous strength and stress", includes all models with constant dynamic friction, linearly depth-dependent normal stress, and heterogeneous static friction and initial shear stress. Family (C), called "family of heterogeneous dynamic friction", includes all models with linearly depth-dependent normal stress and initial shear stress, constant static friction, and heterogeneous dynamic friction.

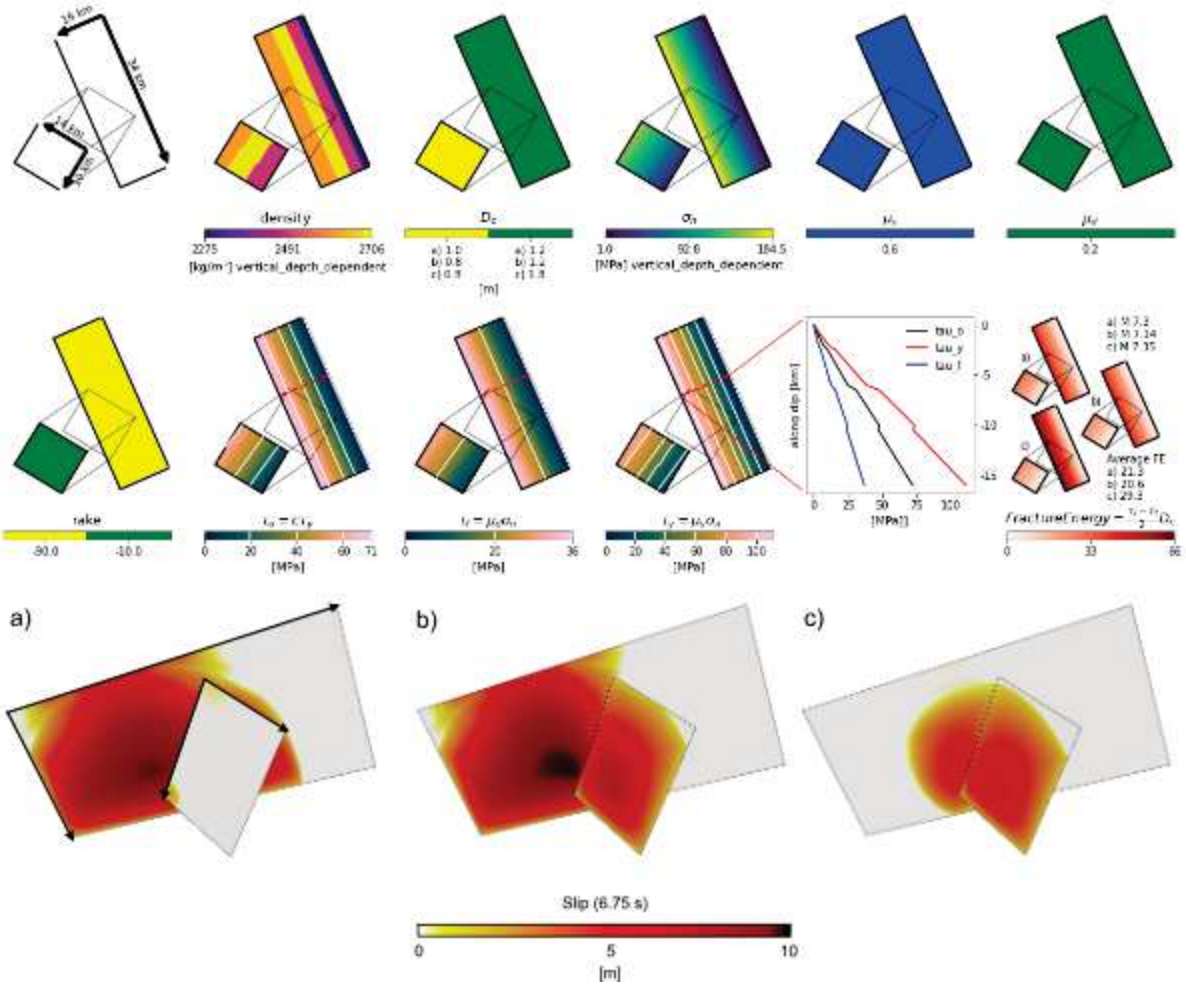

Figure 4.4: Parametrization and rupture dynamics of representative dynamic rupture models belonging to Family (Hom). Upper panels: example of distribution of dynamic parameters in homogeneous stress conditions on both the fault planes (Family (Hom)). Bottom panels: slip distribution after 6.75 s of rupture initiation for models with: a) $D_c^{F155} = 1.2$ m and $D_c^{F210} = 1.0$ m ; b) $D_c^{F155} = 1.2$ m and $D_c^{F210} = 0.8$ m; c) $D_c^{F155} = 1.8$ m and $D_c^{F210} = 0.8$ m . The fracture energy panel indicates the average values of fracture energy E_g and the moment magnitude Mw values after the ruptures termination.

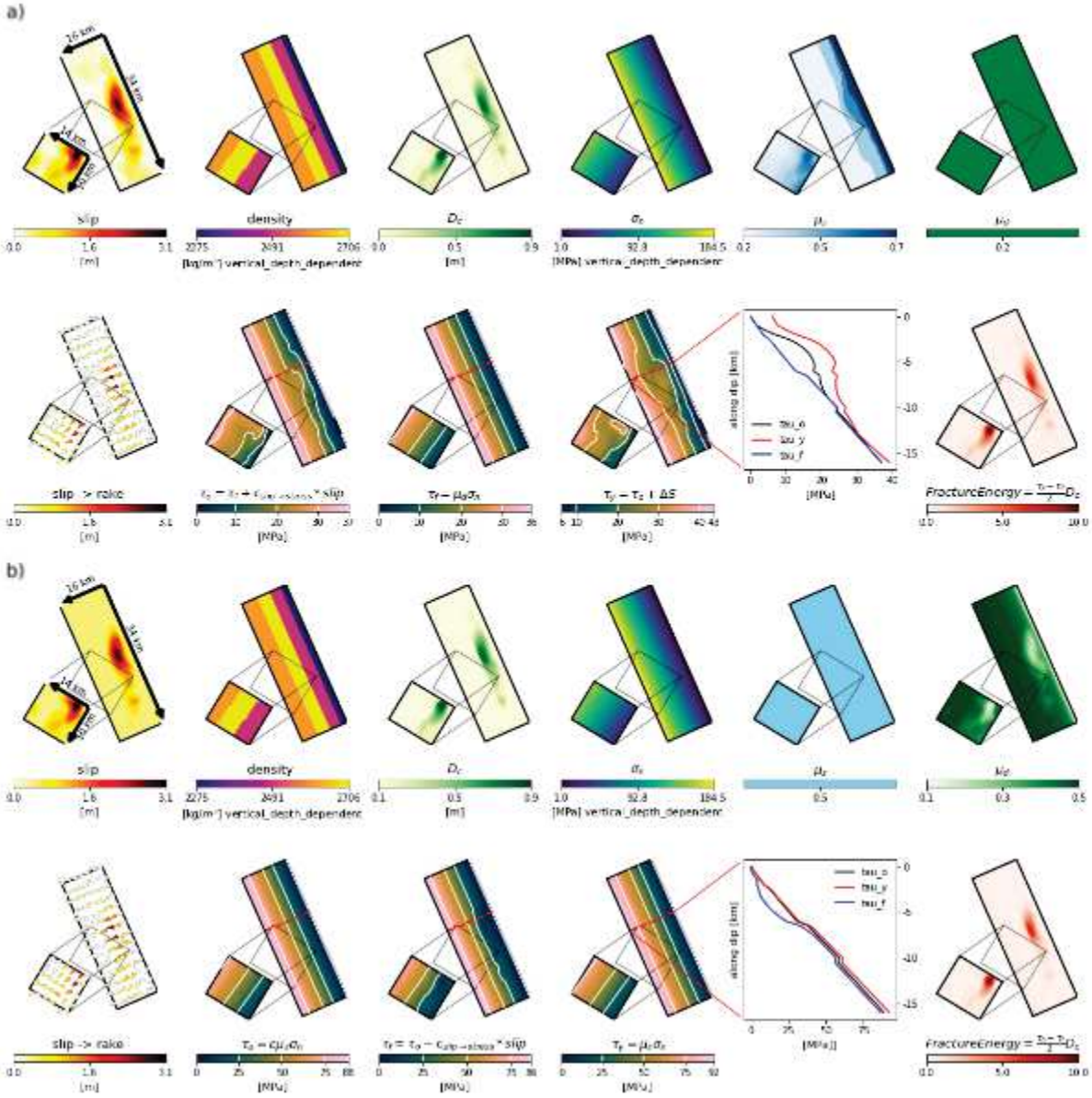

Figure 4.5: Distribution of the dynamic rupture parameters of the two exemplary models of Family (B) (panel a) and (C) (panel b)

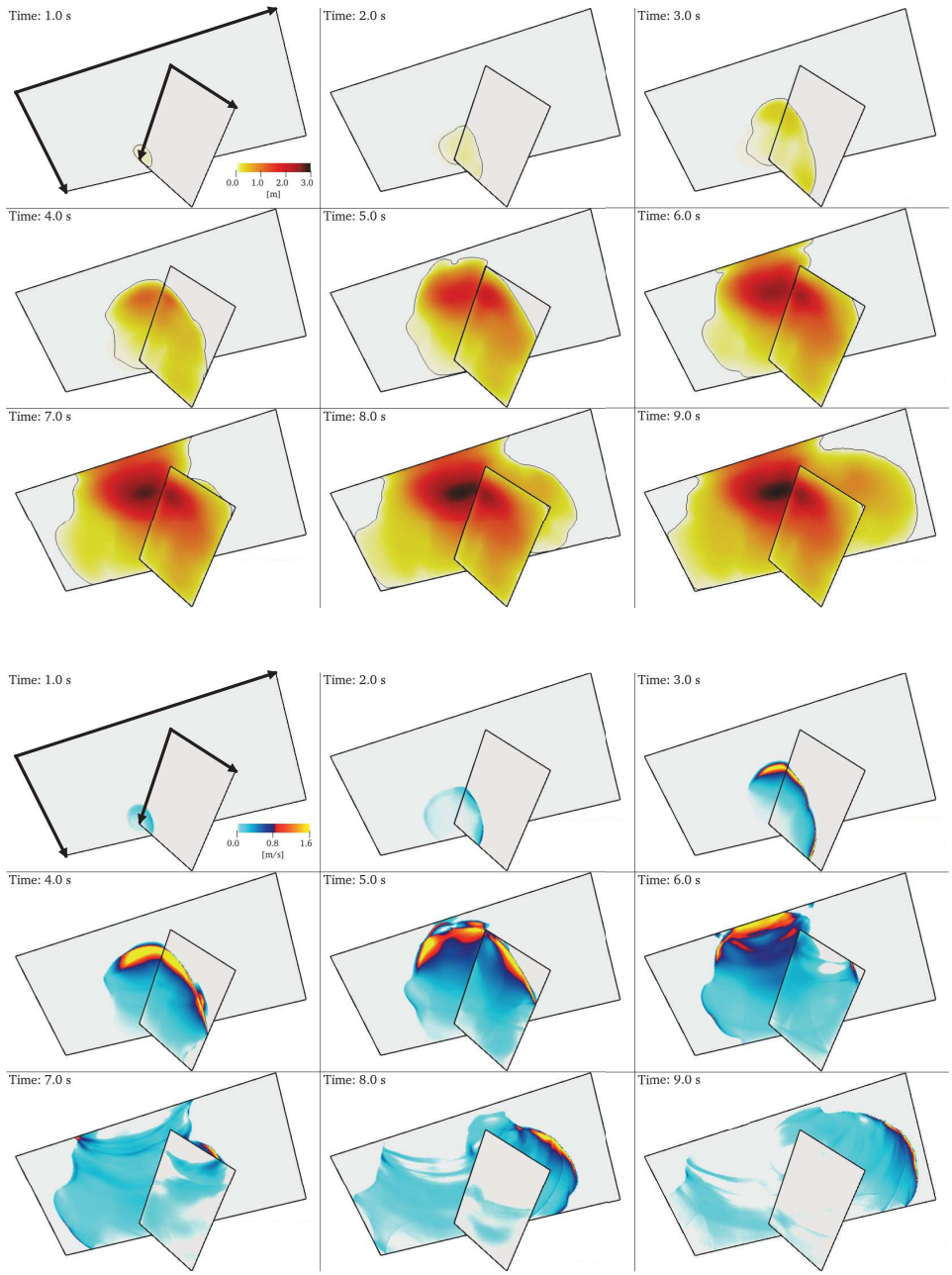

Figure 4.6: Dynamics of the exemplary model belonging to Family (B) inferred by assuming stress drop proportional to slip. Snapshots, every one second, of slip (m, top) and slip rate (m/s, bottom). Corresponding animations are available in supplementary material

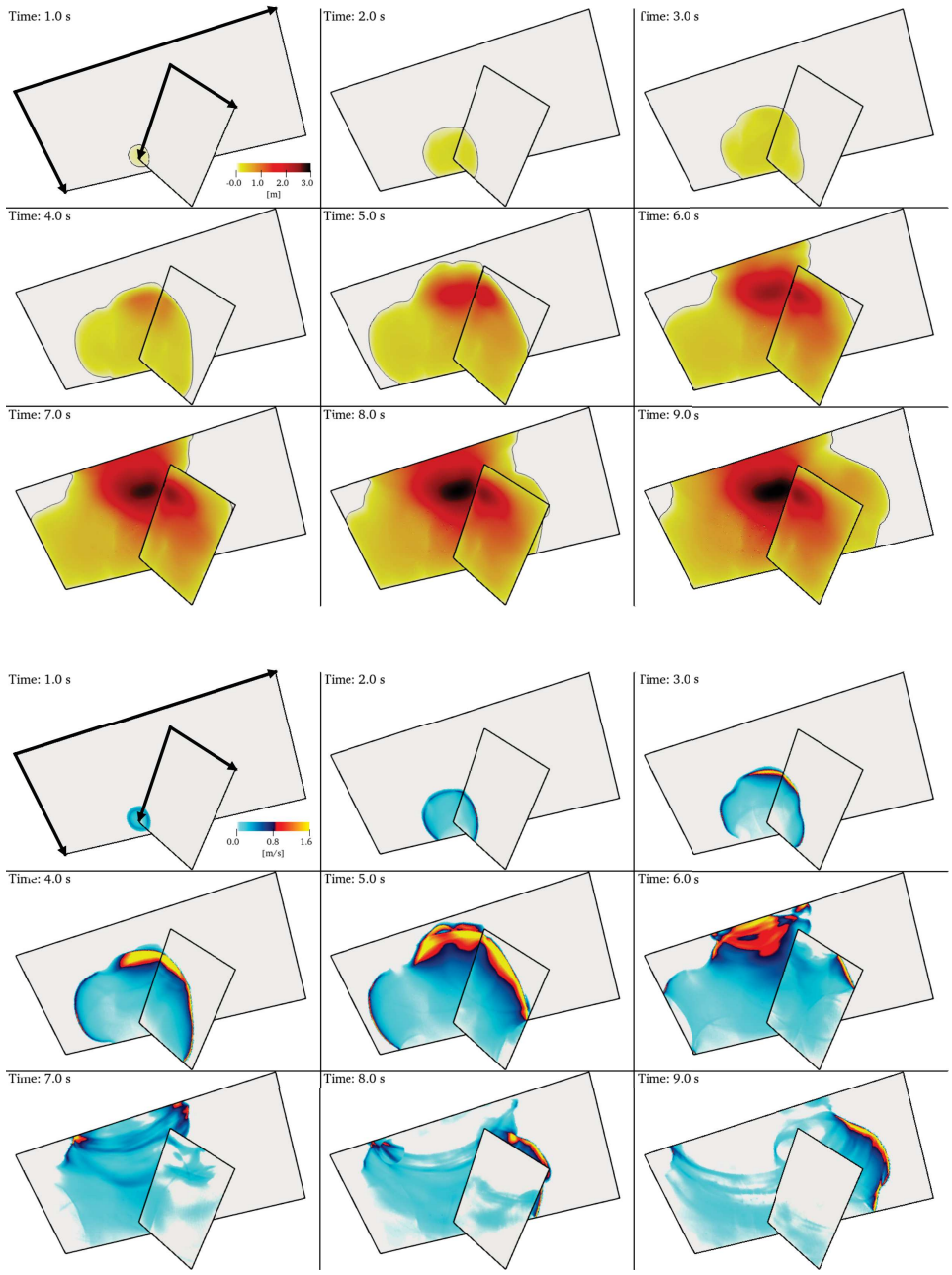

Figure 4.7: Dynamics of the exemplary model belonging to Family (C) inferred by assuming stress drop proportional to slip. Snapshots, every one second, of slip (m, top) and slip rate (m/s, bottom). Corresponding animations are available in supplementary material

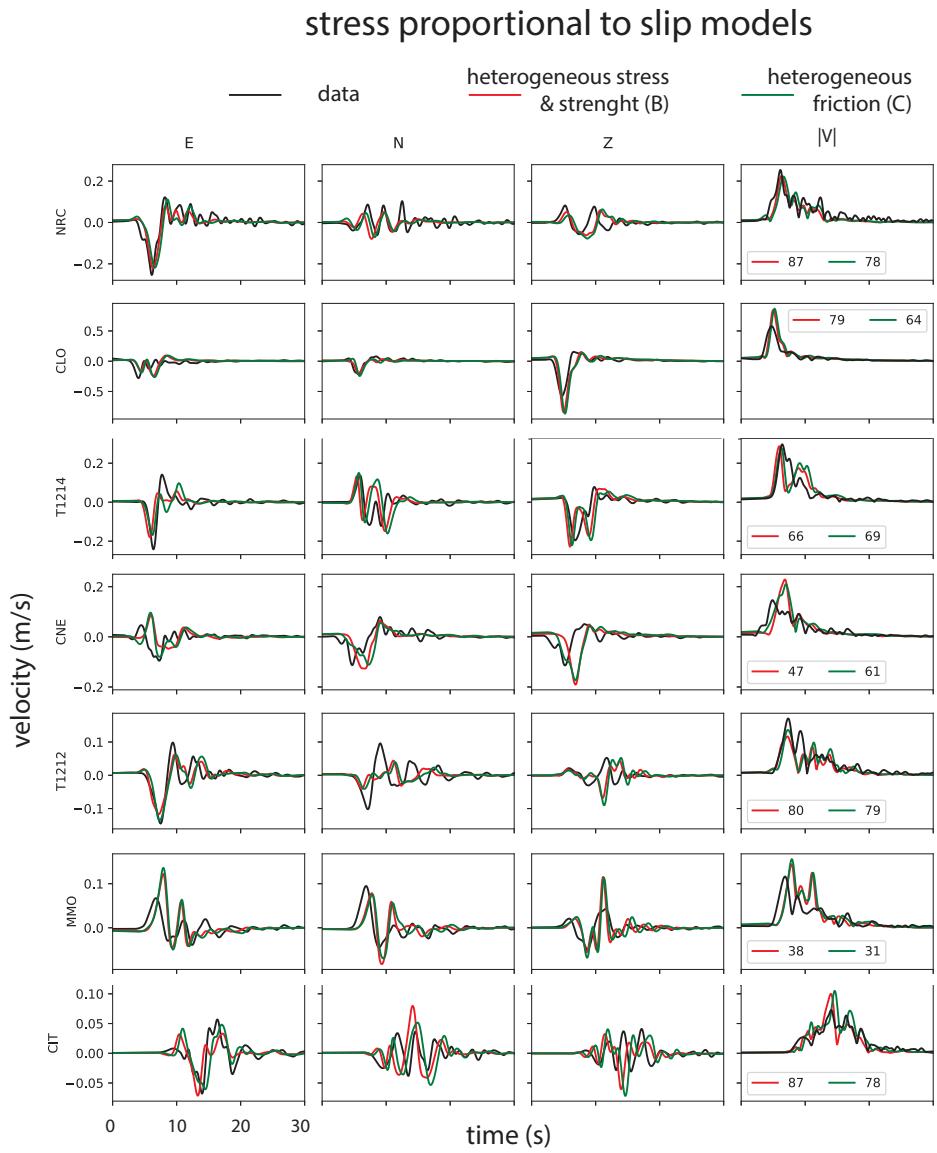

Figure 4.8: Comparison of synthetics strong-motion velocity waveforms (red and green for Family (B) and (C) models, respectively) inferred by assuming stress drop proportional to slip with observations (black) at selected stations. We quantify the waveform fit using the metric equation suggested by [16] on the time-history of the 3D absolute velocity vector. The fit can vary between -100% to $+100\%$ from worst to best, respectively. Both families give similar goodness of fit ($VR_B = 55.5\%$ for Family (B) and $VR_C = 49.7\%$ for Family (C)). Numbers in the fourth column represent goodness of fit for each station and model. Station location is shown in figure 4.1. Additional waveform comparisons are shown in Figure 4.12 and 4.13.

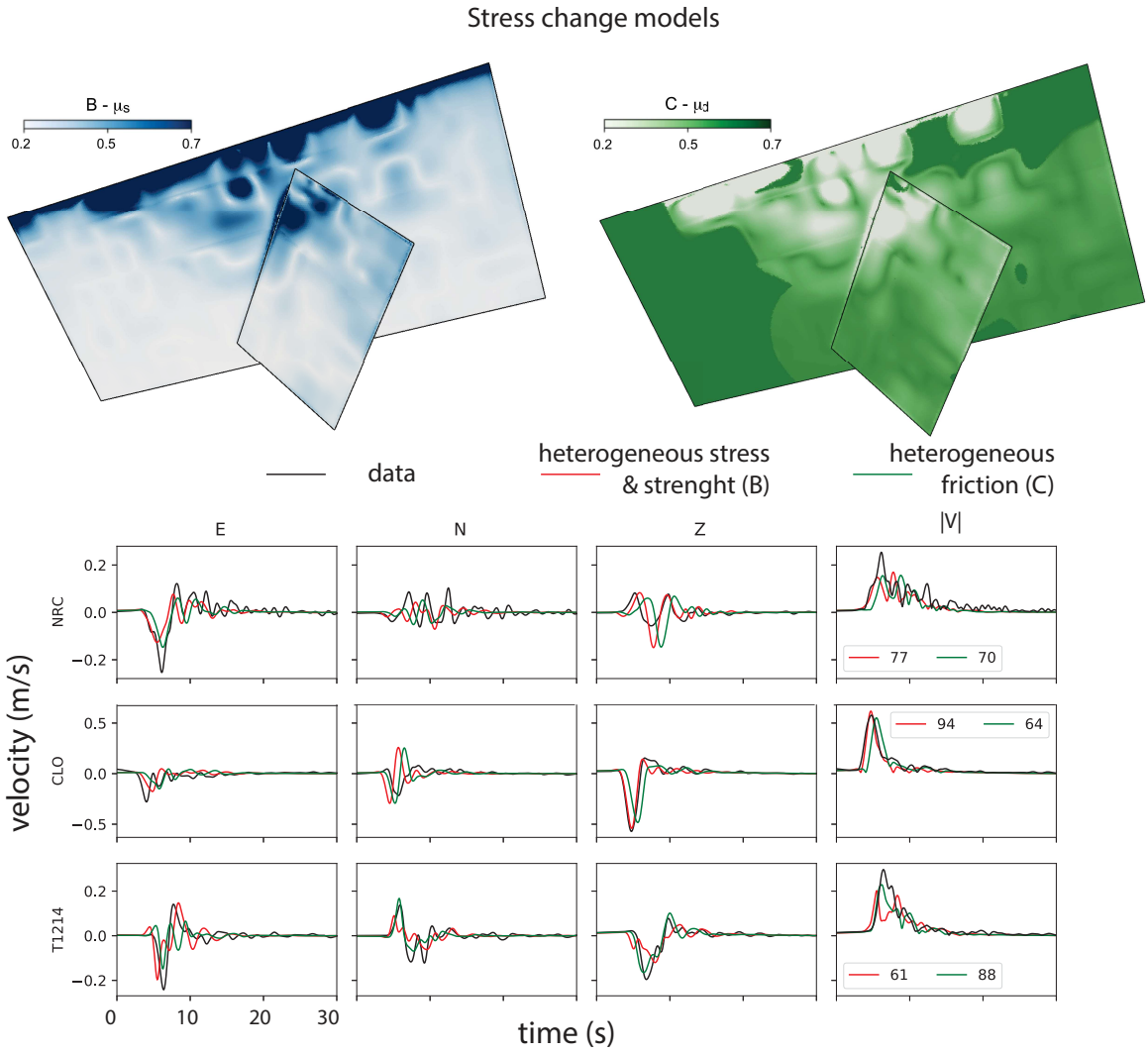

Figure 4.9: Top: distribution of static (left) and dynamic (right) friction parameters for exemplary models of Family (B) and (C), respectively, obtained with the stress change procedure (Section 4.5.2). Bottom: comparison of synthetics velocity waveforms (red, green for for Family (B) and (C) models, respectively) obtained with the stress change procedure with observation (black) at selected stations. Numbers in the fourth column represent goodness of fit for each station and model. Station locations are shown in figure 4.1. Additional waveform comparisons are shown in Figure 4.16 and 4.17.

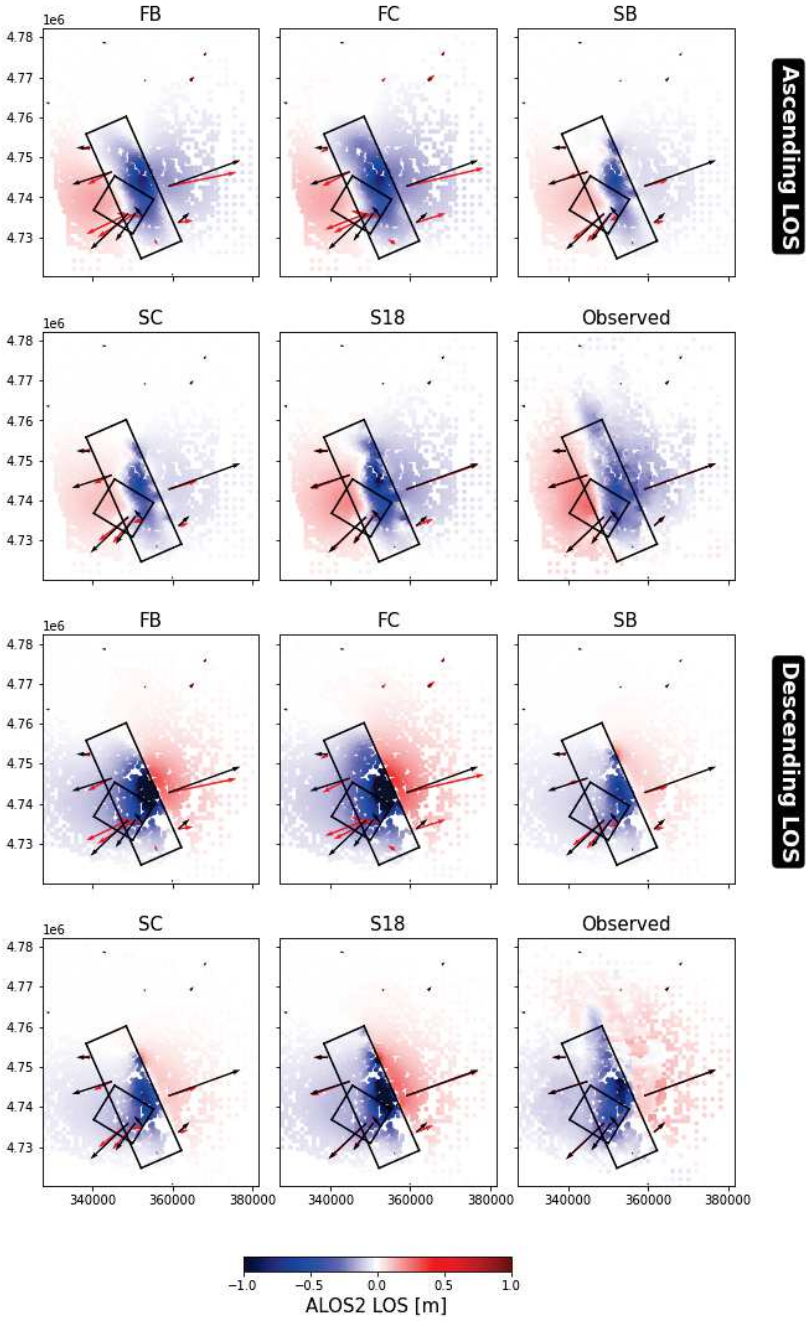

Figure 4.10: Measured ground displacements along line of sight for the ascending and descending ALOS2 InSAR data [31] compared with synthetics of all four presented dynamic models and of the original "S18" kinematic model. Each panel reports also the observed ground displacements at GPS stations (black arrows) and the synthetics the corresponding model (colored arrows). Geographical coordinates are expressed in UTM (zone 33). InSAR residuals among the models are shown in Figure 4.18

.

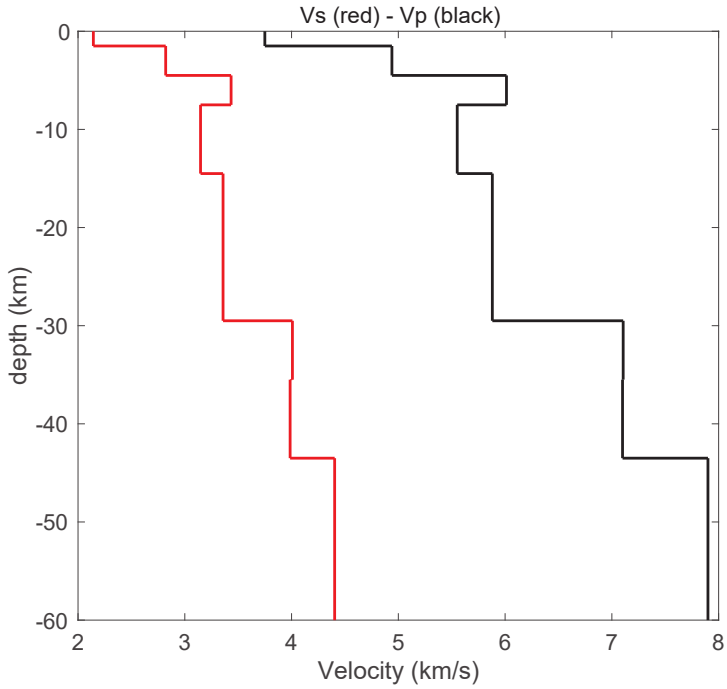

Figure 4.11: Velocity model by [98], adopted in this study (Supporting information 4.10.3)

.

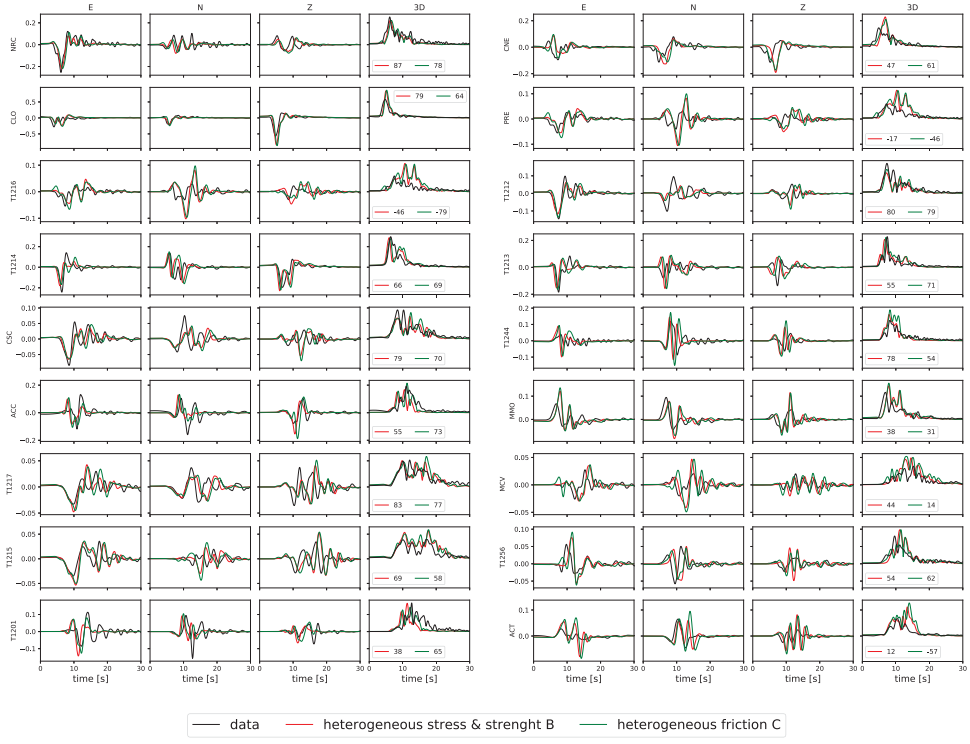

Figure 4.12: Comparison of synthetics strong-motion velocity waveforms (red and green for Family (B) and (C) models, respectively) at all stations inferred by assuming stress drop proportional to slip with observation (black). The variance reduction (VR) for both model are: $VR_B = 55.5$ and $VR_C = 49.7$ (1/2)

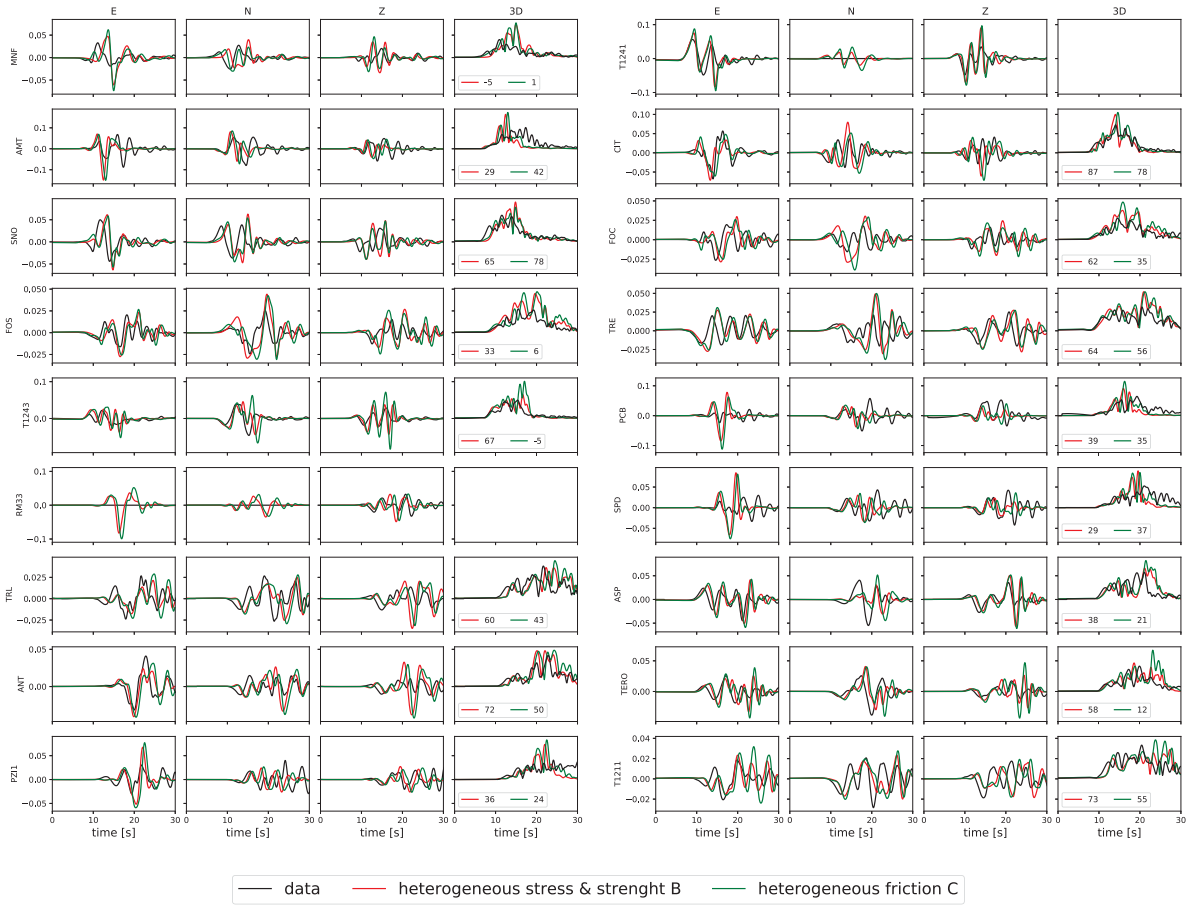

Figure 4.13: Comparison of synthetic strong-motion velocity waveforms (red and green for Family (B) and (C) models, respectively) at all stations inferred by assuming stress drop proportional to slip with observation (black). The variance reduction (VR) for both models are: $VR_B = 55.5$ and $VR_C = 49.7$ (2/2)

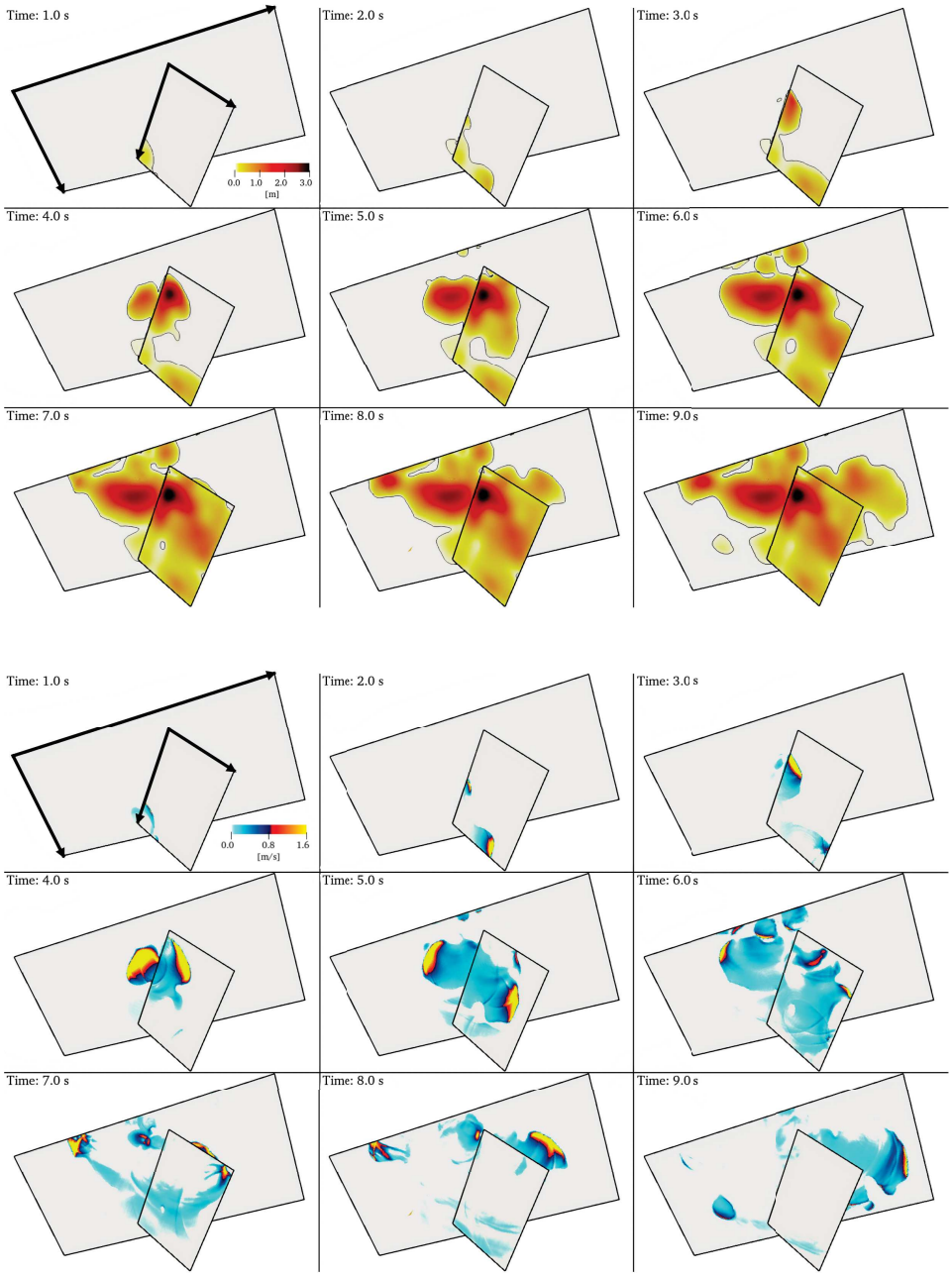

Figure 4.14: Dynamics of the exemplary model belonging to Family (B) based on the stress change procedure. Snapshots, every one second, of slip (m, top) and slip rate (m/s, bottom).

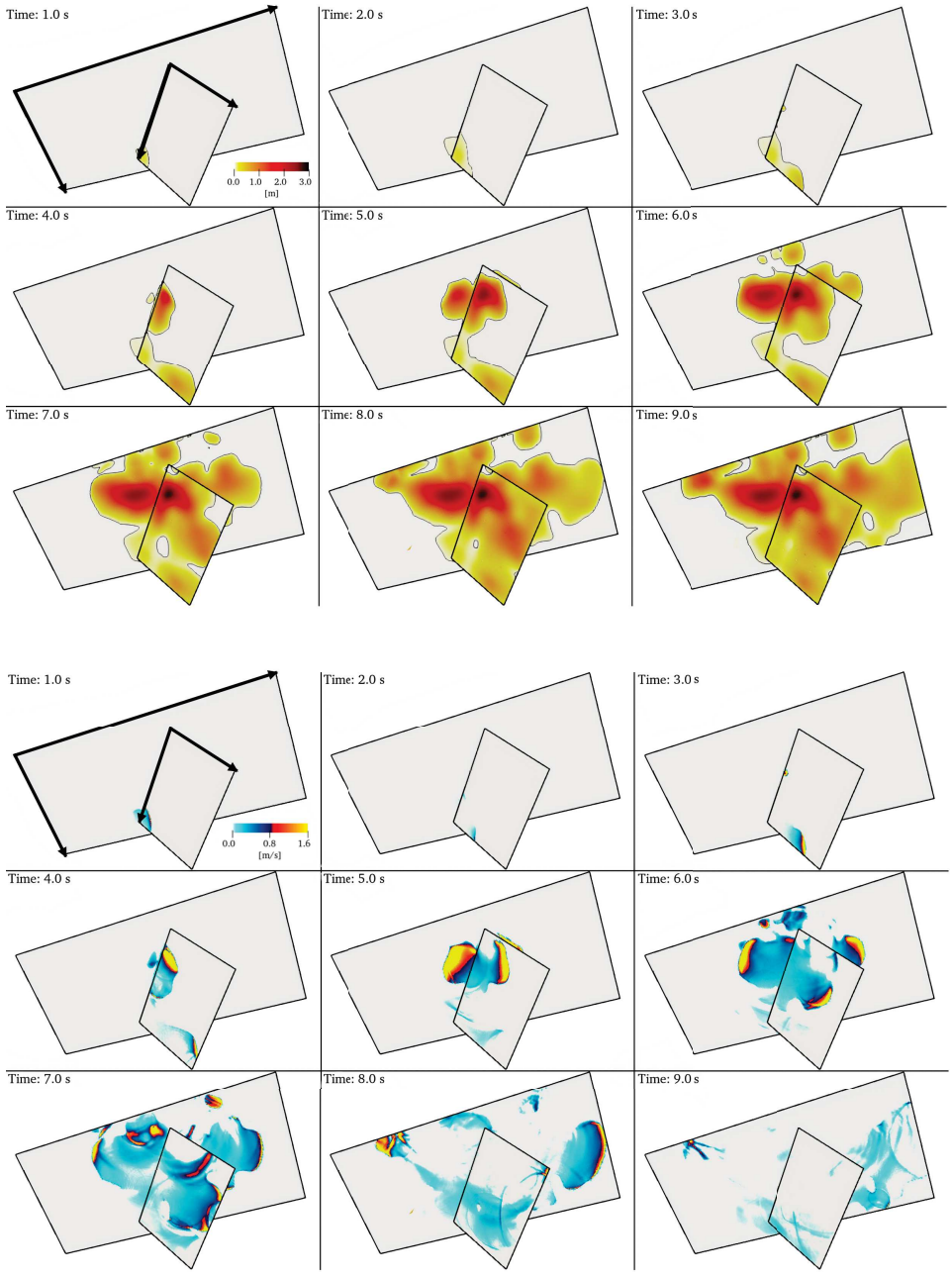

Figure 4.15: Dynamics of the exemplary model belonging to Family (C) based on the stress change procedure. Snapshots, every one second, of slip (m, top) and slip rate (m/s, bottom).

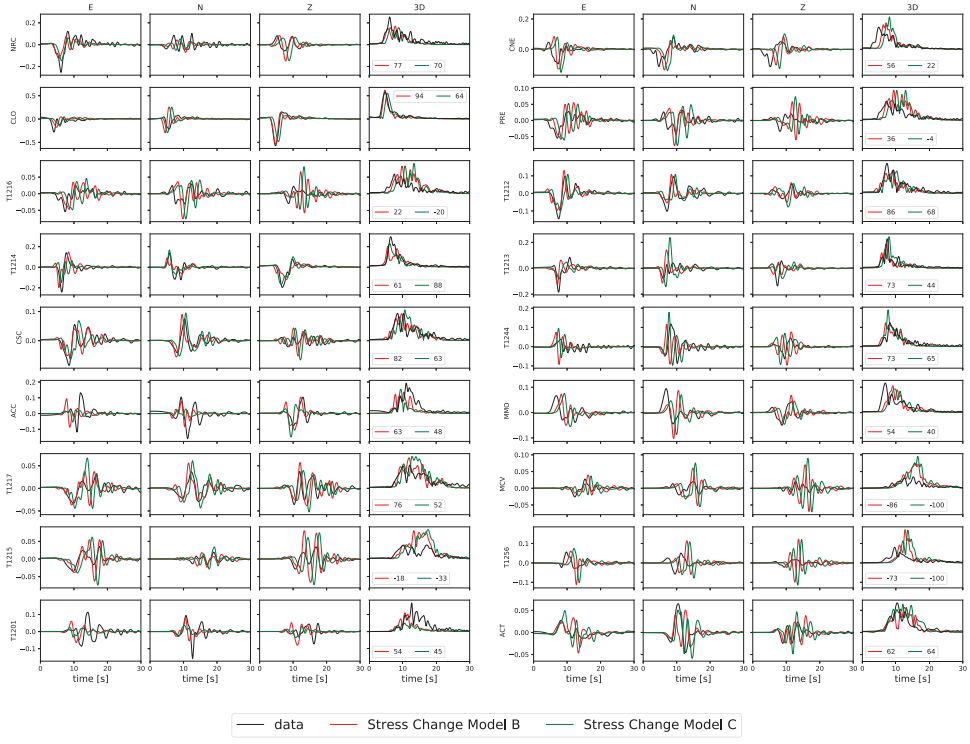

Figure 4.16: Comparison of synthetic strong-motion velocity waveforms (red and green for Family (B) and (C) models, respectively) at all stations derived from the stress change procedure with observation (black). The variance reduction (VR) for both models are: $VR_B = 58.0$ and $VR_C = 48.6$ (1/2)

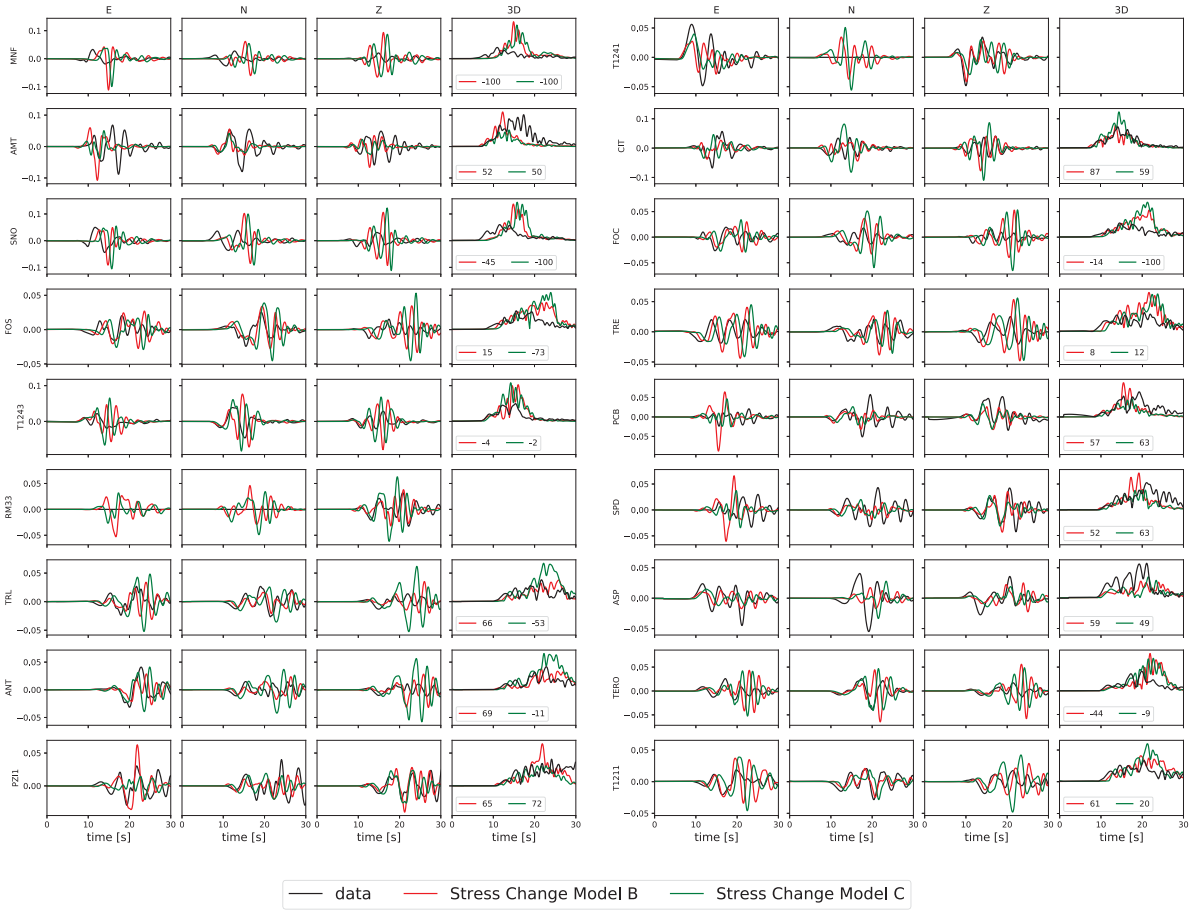

Figure 4.17: Comparison of synthetic strong-motion velocity waveforms (red and green for Family (B) and (C) models, respectively) at all stations derived from the stress change approach with observations (black). The variance reduction (VR) for both models are: $VR_B = 58.0$ and $VR_C = 48.6$ (2/2)

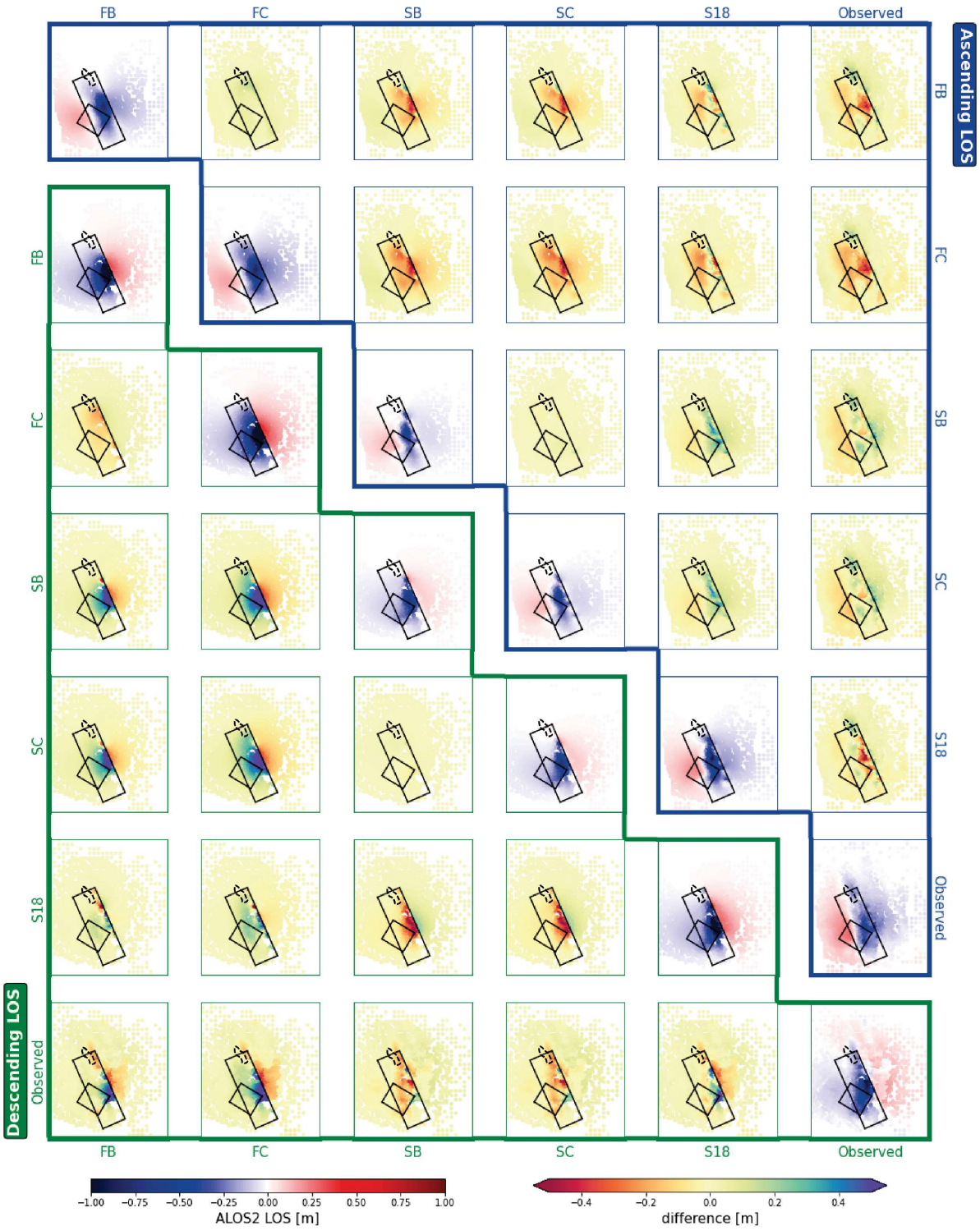

Figure 4.18: Measured ground displacements along line of sight for the descending and ascending ALOS2 InSAR data compared with synthetics of all four presented dynamic models and of the original "S18" kinematic model. Off diagonal subplots show the difference in displacements (row less column). Dotted contours show the isoline displacement at 20 cm on fault plane of Visso earthquake.

Chapter 5

Conclusions

The first chapter demonstrates the successful implementation of 3D physics-based, broadband earthquake ground-motion simulations constrained by data-driven dynamic earthquake source inversion. This study quantifies the first-order role of large- and small-scale dynamic source heterogeneities in the broadband seismic wavefield. Future developments may focus on incorporating 3D and site-specific wave propagation effects for realistic, fully physics-based acceleration synthetics suitable for engineering applications.

The second chapter showcases the assimilation of models and data from various sources to constrain multi-fault dynamic rupture scenarios that self-consistently intertwine earthquake dynamics and unify seismic, geodetic, and geological observations. The study demonstrates the effectiveness of combining data-driven and physics-based modeling to illuminate the underlying physics of cascading multi-fault earthquake sequences. This study emphasizes the importance of long-term and short-term interactions between fault systems. Also, it highlights the need for future seismic hazard assessments to consider these interactions in active multi-fault systems.

Lastly, the third chapter proposes families of dynamic models for a specific earthquake event, aiming to reproduce the main characteristics of a kinematic model while assessing its mechanical viability. Geological constraints are proposed to discriminate among plausible dynamic rupture scenarios by ensuring compatibility with experimental values from near-fault rocks. Future efforts should focus on developing a new generation of dynamic models of actual events that integrate interdisciplinary geophysical observations, improved resolution of seismological data, and knowledge of friction properties of fault rocks.

These studies offer a comprehensive framework for understanding the mechanics of complex fault systems and earthquake sequences. Integrating advanced physics-based simulations, high-performance computing, and data-driven earthquake imaging paves the way for more accurate assessments of seismic hazards, ultimately contributing to the development of more effective geohazard mitigation strategies and the increased resilience of communities and infrastructure to seismic events

5.1 Future outlook

Building upon the analysis of complex fault systems, earthquake sequences, and efficient seismic simulations using supercomputers, Digital twins hold great potential for future earthquake research. This promising approach aims to integrate advancements in physics-based simulations, data-driven earthquake imaging, and Bayesian dynamic source inversion techniques to revolutionize our understanding of earthquake processes and seismic hazard assessments. Digital twin models are anticipated to incorporate friction laws for more accurate fault behavior and rupture dynamics analysis. Researchers could investigate the effects of various friction laws on earthquake scenarios to gain insights into the role of friction in seismic event generation and propagation, refining digital twin models and enhancing seismic hazard assessments.

Digital twin technology can improve geometrical earthquake source imaging by combining high-resolution seismic and geodetic data with advanced imaging techniques. This would enable better comprehension of complex fault interactions, seismic hazard implications, and earthquake risk assessment. Employing Bayesian dynamic source inversion within digital twins could provide a robust statistical framework for inferring earthquake source parameters from observational data, resulting in more accurate models of earthquake sources.

Digital twins could be a powerful platform for simulating and analyzing earthquake scenarios, such as rupture mechanics and ground motion characteristics. They may be able to monitor and analyze real-time data from seismic networks, geodetic measurements, and other sources. This technology could foster collaboration among researchers, policymakers, and stakeholders through a shared, interactive platform, aiding in developing effective geohazard mitigation strategies and resilient infrastructure design.

Bibliography

[1] G. Ameri, F. Gallovič und F. Pacor, *Journal of Geophysical Research* **117** (2012), 4308.

[2] E.M. Anderson, *Trans. Edinburgh Geol. Soc* **8** (1905), 387.

[3] R. Ando und Y. Kaneko, *Geophysical Research Letters* **45** (2018), 875.

[4] D. Andrews, *Bull. Seismol. Soc. Am.* **94** (2004), 769.

[5] D.J. Andrews, *Journal of Geophysical Research* **81** (1976), 3575.

[6] D.J. Andrews. *A stochastic fault model: 1. Static case*. Technischer Bericht B7, 1980.

[7] D.J. Andrews, *Bulletin of the Seismological Society of America* **94** (2004), 769.

[8] D.J. Andrews, *J. Geophys. Res. Solid Earth* **110** (2005), B01307.

[9] S.L. Antoine, Y. Klinger, A. Delorme, K. Wang, R. Bürgmann und R.D. Gold, *Bull. Seismol. Soc. Am.* **111** (2021), 2275.

[10] H. Aochi, *Geophysical Journal International* **215** (2018), 2134.

[11] H. Aochi und R. Madariaga, *Bulletin of the Seismological Society of America* **93** (2003), 1249.

[12] H. Aochi und C. Twardzik, *Pure and Applied Geophysics* **177** (2020), 1931.

[13] A. Ascione, S. Mazzoli, P. Petrosino und E. Valente, *The Geological Society of America Bulletin* **125** (2013), 1239.

[14] K. Bai und J.P. Ampuero, *Journal of Geophysical Research: Solid Earth* **122** (2017), 280.

[15] G. Baltzopoulos, L. Luzi und I. Iervolino, *Bull. Seismol. Soc. Am.* **110** (2020), 1495–1505.

[16] M. Barall und R.A. Harris, *Seismological Research Letters* **86** (2015), 223.

[17] G.I. Barenblatt, *Journal of Applied Mathematics and Mechanics* **23** (1959), 622.

[18] G.W. Bawden, *J. Geophys. Res. Solid Earth* **106** (2001), 771.

[19] H.S. Bhat, M. Olives, R. Dmowska und J.R. Rice, *Journal of Geophysical Research* **112** (2007), B11309.

[20] A. Bizzarri, *Bull. Seismol. Soc. Am.* **100** (2010), 923.

[21] M.L. Blanpied, D.A. Lockner und J.D. Byerlee, *Geophys. Res. Lett.* **18** (1991), 609.

[22] L. Bonini, R. Basili, P. Burrato, V. Cannelli, U. Fracassi, F.E. Maesano, D. Melini, G. Tarabusi, M.M. Tiberti, P. Vannoli und G. Valensise, *Tectonics* **38** (2019), 990.

[23] M. Bouchon. *The state of stress on some faults of the San Andreas system as inferred from near-field strong motion data*. Technischer Bericht B6, 1997.

[24] A. Breuer, A. Heinecke, S. Rettenberger, M. Bader, A.A. Gabriel und C. Pelties. In *Supercomputing. ISC 2014. Lecture Notes in Computer Science, vol 8488*. Springer, Cham (2014), Seiten 1–18.

[25] L. Bruhat, Y. Klinger, A. Vallage und E.M. Dunham, *Geophysical Journal International* **220** (2020), 1857.

[26] J. Burjánek und J. Zahradník, *Geophysical Journal International* **171** (2007), 1082.

[27] S.A. Bydlon und E.M. Dunham, *Geophysical Research Letters* **42** (2015), 1701.

[28] J. Byerlee. In *Rock Friction and Earthquake Prediction*. Birkhäuser Basel (1978), Seiten 615–626.

[29] S. Carena und J. Suppe, *J. Geol. Soc.* **24** (2002), 887.

[30] M. Causse, L.A. Dalguer und P.M. Mai, *Geophysical Journal International* **196** (2014), 1754.

[31] D. Cheloni, V. De Novellis, M. Albano, A. Antonioli, M. Anzidei, S. Atzori, A. Avallone, C. Bignami, M. Bonano, S. Calcaterra, R. Castaldo, F. Casu, G. Cecere, C. De Luca, R. Devoti, D. Di Bucci, A. Esposito, A. Galvani, P. Gambino, R. Giuliani, R. Lanari, M. Manunta, M. Manzo, M. Mattone, A. Montuori, A. Pepe, S. Pepe, G. Pezzo, G. Pietrantonio, M. Polcari, F. Riguzzi, S. Salvi, V. Sepe, E. Serpelloni, G. Solaro, S. Stramondo, P. Tizzani, C. Tolomei, E. Trasatti, E. Valerio, I. Zinno und C. Doglioni, *Geophysical Research Letters* **44** (2017), 6778.

[32] K. Chen, J.P. Avouac, S. Aati, C. Milliner, F. Zheng und C. Shi, *Nat. Commun.* **11** (2020), 22.

[33] Y. Cheng und Y. Ben-Zion, *Geophys. Res. Lett.* **47** (2020), e2020GL089650.

[34] L. Chiaraluce, R. Di Stefano, E. Tinti, L. Scognamiglio, M. Michele, E. Casarotti, P. De Gori, V. Augusti, L. Valoroso, C. Tiberi, A. Govoni, G. Monachesi, S. Mariano, E. D'Alema, G. D'Anna, A. Massucci, G. Di Giulio, F. Cara, M. Anselmi, D. Latorre, L. Abruzzese und C. Chiarabba, *Seismological Research Letters* **88** (2017), 757.

[35] A. Cirella, G. Pezzo und A. Piatanesi, *Geophysical Research Letters* **45** (2018), 12302.

[36] M. Cocco und E. Tinti, *Earth and Planetary Science Letters* **273** (2008), 123.

[37] C. Collettini, T. Tesei, M.M. Scuderi, B.M. Carpenter und C. Viti, *Earth and Planetary Science Letters* **519** (2019), 245.

[38] A. Copley, *J. Geol. Soc.* **175** (2017), 1.

[39] S.M. Corish, C.R. Bradley und K.B. Olsen, *Bulletin of the Seismological Society of America* **97** (2007), 901.

[40] J.T. Cortez, D.D. Oglesby, C. Kyriakopoulos, B. Wu, K. Chaudhuri, A. Ghosh und R. Douilly, *Geophys. Res. Lett.* **48** (2021), e2020GL090659.

[41] F. Cotton und O. Coutant, *Geophys. J. Int.* **128** (1997), 676.

[42] S.M. Day und C.R. Bradley, *Bull. Seismol. Soc. Am.* **91** (2001), 520.

[43] S.M. Day, L.A. Dalguer, N. Lapusta und Y. Liu, *Journal of Geophysical Research: Solid Earth* **110** (2005), 1.

[44] N. De Paola, R.E. Holdsworth, C. Viti, C. Collettini und R. Bullock, *Earth and Planetary Science Letters* **431** (2015), 48.

[45] G. Di Toro, R. Han, T. Hirose, N. De Paola, S. Nielsen, K. Mizoguchi, F. Ferri, M. Cocco und T. Shimamoto, *Nature* **471** (2011), 494.

[46] J.H. Dieterich, *Journal of Geophysical Research* **84** (1979), 2161.

[47] R. Douilly, D.D. Oglesby, M.L. Cooke und J.L. Hatch, *Geosphere* **16** (2020), 474.

[48] M. van Driel, L. Krischer, S. Stähler, K. Hosseini und T. Nissen-Meyer, *Solid Earth* **6** (2015), 701.

[49] M. Dumbser und M. Käser, *Geophysical Journal International* **167** (2006), 319.

[50] E.M. Dunham, *Journal of the Mechanics and Physics of Solids* **53** (2005), 327.

[51] E.M. Dunham, D. Belanger, L. Cong und J.E. Kozdon, *Bulletin of the Seismological Society of America* **101** (2011), 2308.

[52] Z. Duputel, J. Jiang, R. Jolivet, M. Simons, L. Rivera, J.P. Ampuero, B. Riel, S.E. Owen, A.W. Moore, S.V. Samsonov, F. Ortega Culaciati und S.E. Minson, *Geophysical Research Letters* **42** (2015), 7949.

[53] C.B. DuRoss, R.D. Gold, T.E. Dawson, K.M. Scharer, K.J. Kendrick, S.O. Akciz, S.J. Angster, J. Bachhuber, S. Bacon, S.E.K. Bennett, L. Blair, B.A. Brooks, T. Bullard, W.P. Burgess, C. Chupik, M. DeFrisco, J. Delano, J.F. Dolan, E. Frost, N. Graehl, E.K. Haddon, A.E. Hatem, J.L. Hernandez, C. Hitchcock, K. Hudnut, J. Thompson Jobe, R. Koehler, O. Kozaci, T. Ladinsky, C. Madugo, D.S. McPhillips, C. Milliner, A. Morelan, B. Olson, J. Patton, B. Philibosian, A.J. Pickering, I. Pierce, D.J. Ponti, G. Seitz, E. Spangler, B. Swanson, K. Thomas, J. Treiman, F. Valencia, A. Williams und R. Zinke, *Bull. Seismol. Soc. Am.* **110** (2020), 1400.

[54] K. Duru und E.M. Dunham, *Journal of Computational Physics* **305** (2016), 185.

[55] E.. (EC8). *EN 1998-1: Design of structures for earthquake resistance, part 1: General rules, seismic actions and rules for buildings*. European Committee for Standardization (CEN), 2004.

[56] Z. Fang und E.M. Dunham, *Journal of Geophysical Research: Solid Earth* **118** (2013), 3642.

[57] T.G. Farr, P.A. Rosen, E. Caro, R. Crippen, R. Duren, S. Hensley und et al., *Reviews of Geophysics* **45** (2007), RG2004.

[58] A. Frankel, E. Wirth, N. Marafi, J. Vidale und W. Stephenson, *Bulletin of the Seismological Society of America* **108** (2018), 2347.

[59] L.B. Freund: *Dynamic fracture mechanics*. Cambridge University Press, 1998.

[60] E. Fukuyama, *Earth Planet Sp.* **67** (2015), 38.

[61] E. Fukuyama und T. Mikumo, *Journal of Geophysical Research: Solid Earth* **98** (1993), 6529.

[62] A.A. Gabriel, J.P. Ampuero, L.A. Dalguer und P.M. Mai, *J. Geophys. Res.* **117** (2012), B09311.

[63] A.A. Gabriel, J.P. Ampuero, L.A. Dalguer und P.M. Mai, *J. Geophys. Res. Solid Earth* **118** (2013), 4117.

[64] A.A. Gabriel, D. Li, S. Chiocchetti, M. Tavelli, I. Peshkov, E. Romenski und M. Dumbser, *Philosophical Transactions of the Royal Society A: Mathematical, Physical and Engineering Sciences* **379** (2021), 20200130.

[65] F. Galadini, P. Galli und M. Moro, *Annals of Geophysics* **46** (2003), 815.

[66] M. Galis, C. Pelties, J. Kristek, P. Moczo, J.P. Ampuero und P.M. Mai, *Geophys. J. Int.* **200** (2015), 890.

[67] F. Gallovič, W. Imperatori und P.M. Mai, *Journal of Geophysical Research: Solid Earth* **120** (2015), 428.

[68] F. Gallovič, Valentová, J.P. Ampuero und A.A. Gabriel, *Journal of Geophysical Research: Solid Earth* **124** (2019), 6970.

[69] F. Gallovič, G. Ameri, J. Zahradník, J. Janský, V. Plicka, E. Sokos, A. Askan und M. Pakzad, *Bulletin of the Seismological Society of America* **103** (2013), 3164.

[70] F. Gallovič und J.P. Ampuero, *Seismological Research Letters* **86** (2015), 1679.

[71] F. Gallovič, Valentová, J.P. Ampuero und A.A. Gabriel, *Journal of Geophysical Research: Solid Earth* **124** (2019a), 6949.

[72] F. Gallovič, Valentová, J.P. Ampuero und A.A. Gabriel, *Journal of Geophysical Research: Solid Earth* **124** (2019b), 6970.

[73] P. Galvez, J.P. Ampuero, L.A. Dalguer, S.N. Somala und T. Nissen-Meyer, *Geophysical Journal International* **198** (2014), 1222.

[74] P. Galvez, A. Petukhin, K. Irikura und P. Somerville, *Pure and Applied Geophysics* **177** (2020), 2143.

[75] D.I. Garagash, *Phil. Trans. R. Soc. A.* **379** (2021), 20200129.

[76] A. Ghosh, J.E. Vidale und K.C. Creager, *J. Geophys. Res. Solid Earth* **117** (2012), B10301.

[77] D.E. Goldberg, D. Melgar, V.J. Sahakian, A.M. Thomas, X. Xu, B.W. Crowell und J. Geng, *Geophys. Res. Lett.* **47** (2020), e2019GL086382.

[78] H. Goto und S. Sawada, *Bulletin of the Seismological Society of America* **100** (2010), 910.

[79] R. Graves, T.H. Jordan, S. Callaghan, E. Deelman, E. Field, G. Juve und et al., *Pure and Applied Geophysics* **168** (2011), 367.

[80] R.W. Graves, B.T. Aagaard, K.W. Hudnut, L.M. Star, J.P. Stewart und T.H. Jordan, *Geophys. Res. Lett.* **35** (2008), L22302.

[81] R.W. Graves und A. Pitarka, *Bulletin of the Seismological Society of America* **100** (2010), 2095.

[82] M. Guatteri, P.M. Mai und G.C. Beroza, *Bulletin of the Seismological Society of America* **94** (2004), 2051.

[83] M. Guatteri und P. Spudich, *Bulletin of the Seismological Society of America* **90** (2000), 98.

[84] M. Guatteri, P. Spudich und G.C. Beroza, *Journal of Geophysical Research: Solid Earth* **106** (2001), 26511.

[85] M. Hallo und F. Gallovič, *Geophys. J. Int.* **207** (2016), 1012.

[86] M. Hallo und F. Gallovič, *J. Geophys. Res. Solid Earth* **125** (2020), e2019JB018703.

[87] I.J. Hamling, H. Sigrún, C. Kate, E. John, L. Cunren, F. Eric, L. Nicola, V. Pilar, W. Laura, W. Tim J., D. Elisabetta, B. Stephen, B. David, D. Paul, G. Paula, H. Jamie, M. Christof, P. Neville, P. Chris, P. William, B. Philip, B. David J. A., V.D. Russ, L. Robert, L. Tim, N. Andrew, P. Jarg, R. Julie und S. Mark, *Science* **356** (2017), eaam7194.

[88] J.L. Hardebeck und A.J. Michael, *J. Geophys. Res. Solid Earth* **111** (2006), B11310.

[89] R.A. Harris, M. Barall, B. Aagaard, S. Ma, D. Roten, K. Olsen und et al., *Seismological Research Letters* **89** (2018), 1146.

[90] R.A. Harris, M. Barall, D. Andrews, B. Duan, S. Ma, E. Dunham, A.A. Gabriel, Y. Kaneko, Y. Kase, B. Aagaard et al. , *Seismol. Res. Lett.* **82** (2011), 638.

[91] R.A. Harris, M. Barall, D.A. Lockner, D.E. Moore, D.A. Ponce, R.W. Graymer, G. Funning, C.A. Morrow, C. Kyriakopoulos und D. Eberhart-Phillips, *Journal of Geophysical Research: Solid Earth* **126** (2021), e2020JB020577.

[92] S. Hartzell, L. Ramírez-Guzmán, M. Meremonte und A. Leeds, *Bulletin of the Seismological Society of America* **107** (2016), 344.

[93] N.A. Haskell, *Bulletin of the Seismological Society of America* **54** (1964), 1811.

[94] E. Hauksson, K. Hutton, H. Kanamori, L. Jones, J. Mori, S. Hough und G. Roquemore, *Seismol. Res. Lett.* **66** (1995), 54.

[95] E. Hauksson, L.M. Jones, K. Hutton und D. Eberhart-Phillips, *J. Geophys. Res. Solid Earth* **98** (1993), 19835.

[96] T.H. Heaton, *Phys. Earth Planet. Inter.* **64** (1990), 1.

[97] A. Heinecke, A. Breuer, S. Rettenberger, M. Bader, A.A. Gabriel, C. Pelties, A. Bode, W. Barth, X.K. Liao, K. Vaidyanathan, M. Smelyanskiy und P. Dubey: *Petascale high order dynamic rupture earthquake simulations on heterogeneous supercomputers. Petascale high order dynamic rupture earthquake simulations on heterogeneous supercomputers*, In *International Conference for High Performance Computing, Networking, Storage and Analysis, SC*. (2014).

[98] R.B. Herrmann, L. Malagnini und I. Munafò, *Bulletin of the Seismological Society of America* **101** (2011), 975.

[99] F. Hu, H. Huang und X. Chen, *Earthq. Sci.* **30** (2017), 91.

[100] Z. Hu, K.B. Olsen und S.M. Day, *Geophysical Journal International* **230** (2022), 2162.

[101] Y. Ida, *Journal of Geophysical Research* **77** (1972), 3796.

[102] S. Ide und M. Takeo, *Journal of Geophysical Research: Solid Earth* **101** (1996), 5661.

[103] I. Iervolino, C. Galasso und E. Cosenza, *Bulletin of Earthquake Engineering* **8** (2010), 339.

[104] W. Imperatori und P. Mai, *Geophysical Journal International* **202** (2015), 2163.

[105] W. Imperatori und P.M. Mai, *Geophysical Journal International* **192** (2013), 725.

[106] S. Inc. *SimModeler: Simulation modeling suite 11.0 documentation*, 2017.

[107] K. Irikura und H. Miyake: *Progress of strong motion prediction. Progress of strong motion prediction*, In *17th World Conference on Earthquake Engineering, Sendai, Japan—September 27th to October 2nd, 2021.* (2021).

[108] C. Ji, D.J. Wald und D.V. Helmberger, *Bull. Seismol. Soc. Am.* **92** (2002), 1208.

[109] J. Jiang, B.A. Erickson, V.R. Lambert, J.P. Ampuero, R. Ando, S.D. Barbot, C. Cattania, L.D. Zilio, B. Duan, E.M. Dunham et al. , *J. Geophys. Res. Solid Earth* **127** (2022), e2021JB023519.

[110] J. Jiang und N. Lapusta, *Science* **352** (2016), 1293.

[111] Z. Jin und Y. Fialko, *Bull. Seismol. Soc. Am.* **110** (2020), 1660.

[112] Y. Kaneko, N. Lapusta und J.P. Ampuero, *J. Geophys. Res. Solid Earth* **113** (2008), B09317.

[113] M. Käser, V. Hermann und J. de la Puente, *Geophysical Journal International* **173** (2008), 990.

[114] A. Kato, S. Sakai, S. Matsumoto und Y. Iio, *Commun. Earth. Environ.* **2** (2021), 13.

[115] B.L.N. Kennett und E.R. Engdahl, *Geophys. J. Int.* **105** (1991), 429.

[116] N. Kheirdast, A. Ansari und S. Custódio, *Journal of Geophysical Research: Solid Earth* **126** (2021), e2020JB020773.

[117] K. Konno und T. Ohmachi, *Bulletin of the Seismological Society of America* **88** (1998), 228.

[118] L. Krenz, C. Uphoff, T. Ulrich, A.A. Gabriel, L. Abrahams, E. Dunham und M. Bader: *3D acoustic-elastic coupling with gravity: the dynamics of the 2018 Palu, Sulawesi earthquake and tsunami. 3D acoustic-elastic coupling with gravity: the dynamics of the 2018 Palu, Sulawesi earthquake and tsunami*, In *Proceedings of the International Conference for High Performance Computing, Networking, Storage and Analysis*SC '21. ACM, New York, NY, USA (2021).

[119] L. Krischer, T. Megies, R. Barsch, M. Beyreuther, T. Lecocq, C. Caudron und J. Wassermann, *Comput. Sci. Discov.* **8** (2015), 014003.

[120] C. Kyriakopoulos, D.D. Oglesby, T.K. Rockwell, A.J. Meltzner, M. Barall, J.M. Fletcher und D. Tulanowski, *Journal of Geophysical Research: Solid Earth* **124** (2019), 3680.

[121] A.H. Lachenbruch und J. Sass, *J. Geophys. Res. Solid Earth* **85** (1980), 6185.

[122] V. Lambert, N. Lapusta und S. Perry, *Nature* **591** (2021), 252.

[123] G. Lanzano, L. Luzi, C. Cauzzi, J. Bienkowski, D. Bindi, J. Clinton und et al., *Seismological Research Letters* **92** (2021), 1642.

[124] N. Lapusta und Y. Liu, *Journal of Geophysical Research: Solid Earth* **114** (2009).

[125] E.J. Lee, P. Chen, T.H. Jordan, P.B. Maechling, M.A.M. Denolle und G.C. Beroza, *J. Geophys. Res. Solid Earth* **119** (2014), 6421.

[126] S.J. Lee, D. Komatitsch, B.S. Huang und J. Tromp, *Bulletin of the Seismological Society of America* **99** (2009), 314.

[127] B. Li und A. Ghosh. In *The Chile-2015 (Illapel) Earthquake and Tsunami*. Springer (2017), Seiten 33–43.

[128] B. Li, B. Wu, H. Bao, D.D. Oglesby, A. Ghosh, A.A. Gabriel, L. Meng und R. Chu, *J. Geophys. Res. Solid Earth* **127** (2022), e2021JB022663.

[129] C. Liang, J.P. Ampuero und D. Pino Muñoz, *Geophys. Res. Lett.* **48** (2021), e2020GL090744.

[130] J. Lin und R.S. Stein, *J. Geophys. Res. Solid Earth* **109** (2004), B02303.

[131] C. Liu, T. Lay, E.E. Brodsky, K. Dascher-Cousineau und X. Xiong, *Geophys. Res. Lett.* **46** (2019), 11820.

[132] J.C. Lozos, *Sci. Adv.* **2** (2016), e1500621.

[133] J.C. Lozos und R.A. Harris, *Geophys. Res. Lett.* **47** (2020), e2019GL086020.

[134] B. Luo, B. Duan und D. Liu, *Bulletin of the Seismological Society of America* **110** (2020), 2619.

[135] L. Luzi, R. Puglia, E. Russo, M. D'Amico, C. Felicetta, F. Pacor und et al., *Seismological Research Letters* **87** (2016), 987.

[136] S. Ma, *Geochem. Geophys. Geosyst.* **9** (2008), Q11009.

[137] S. Ma und G.C. Beroza, *Bulletin of the Seismological Society of America* **98** (2008), 1642.

[138] S. Ma, S. Custodio, R.J. Archuleta und P. Liu, *Journal of Geophysical Research* **113** (2008), B02301.

[139] R. Madariaga, *Geophysical Journal International* **51** (1977), 625.

[140] E.H. Madden, T. Ulrich und A.A. Gabriel, *J. Geophys. Res. Solid Earth* **127** (2022), e2021JB023382.

[141] Y. Magen, A. Ziv, A. Inbal, G. Baer und J. Hollingsworth, *Bull. Seismol. Soc. Am.* **110** (2020), 1627.

[142] P.M. Mai, W. Imperatori und K.B. Olsen, *Bulletin of the Seismological Society of America* **100** (2010), 2124.

[143] P.M. Mai, D. Schorlemmer, M. Page, J.P. Ampuero, K. Asano, M. Causse und et al., *Seismological Research Letters* **87** (2016), 690.

[144] M.T. Mariucci und P. Montone. *IPSI 1.4, Database of Italian Present-day Stress Indicators*, 2020.

[145] L.J. McAuliffe, J.F. Dolan, E. Kirby, C. Rollins, B. Haravitch, S. Alm und T.M. Rittenour, *J. Geophys. Res. Solid Earth* **118** (2013), 5126.

[146] D. Melgar, T.I. Melbourne, B.W. Crowell, J. Geng, W. Szeliga, C. Scrivner, M. Santillan und D.E. Goldberg, *Seismol. Res. Lett.* **91** (2019), 1943–1951.

[147] Q. Meng und B. Duan, *Seismological Society of America* **94** (2023), 206.

[148] M. Michele, L. Chiaraluce, R. Di Stefano und F. Waldhauser, *Journal of Geophysical Research: Solid Earth* **125** (2020), e2019JB018440.

[149] M. Michele, R. Di Stefano, L. Chiaraluce, M. Cattaneo, P. De Gori, G. Monachesi und et al., *Annals of Geophysics* **59** (2016), 1.

[150] A. Michelini, L. Margheriti, M. Cattaneo, G. Cecere, G. D'Anna, A. Delladio, M. Moretti, S. Pintore, A. Amato, A. Basili, A. Bono, P. Casale, P. Danecek, M. Demartin, L. Faenza, V. Lauciani, A. Giovanni Mandiello, A. Marchetti, C. Marcocci, S. Mazza, F. Mariano Mele, A. Nardi, C. Nostro, M. Pignone, M. Quintiliani, S. Rao, L. Scognamiglio und G. Selvaggi, *Advances in Geosciences* **43** (2016), 31.

[151] C. Milliner und A. Donnellan, *Seismol. Res. Lett.* **91** (2020), 1986–1997.

[152] D. Monelli und P.M. Mai, *Geophysical Journal International* **173** (2008), 220.

[153] M.P. Moschetti, S. Hartzell, L. Ramírez-Guzmán, A.D. Frankel, S.J. Angster und W.J. Stephenson, *Bulletin of the Seismological Society of America* **107** (2017), 1704.

[154] S. Murphy, G. Di Toro, F. Romano, A. Scala, S. Lorito, E. Spagnuolo, S. Aretusini, G. Festa, A. Piatanesi und S. Nielsen, *Earth and Planetary Science Letters* **486** (2018), 155.

[155] S. Nielsen und R. Madariaga, *Bull. Seismol. Soc. Am.* **93** (2003), 2375.

[156] D.D. Oglesby, R.J. Archuleta und S.B. Nielsen, *Science* **280** (1998), 1055.

[157] M. Ohnaka, Y. Kuwahara und K. Yamamoto, *Tectonophysics* **144** (1987), 109.

[158] K. Okubo, H.S. Bhat, E. Rougier, S. Marty, A. Schubnel, Z. Lei und et al., *Journal of Geophysical Research: Solid Earth* **124** (2019), 11771.

[159] K.B. Olsen, R. Madariaga und R.J. Archuleta, *Science* **278** (1997), 834.

[160] K.B. Olsen und J.E. Mayhew, *Seismological Research Letters* **81** (2010), 715.

[161] K.H. Palgunadi, A.A. Gabriel, T. Ulrich, J.A. Lopez-Comino und P.M. Mai, *Bulletin of the Seismological Society of America* **110** (2020), 2328.

[162] A. Palmer, J.R. Rice und R. Hill, *Proceedings of the Royal Society of London A. Mathematical and Physical Sciences* **332** (1973), 527.

[163] L. Passone und P.M. Mai, *Bulletin of the Seismological Society of America* **107** (2017), 2980.

[164] M.E. Pasyanos, D.S. Dreger und B. Romanowicz, *Bull. Seismol. Soc. Am.* **86** (1996), 1255.

[165] C. Pelties, A.A. Gabriel und J.P. Ampuero, *Geoscientific Model Development* **7** (2014), 847.

[166] C. Pelties, J. de la Puente, J.P. Ampuero, G.B. Brietzke und M. Käser, *Journal of Geophysical Research* **117** (2012), B02309.

[167] M.D. Petersen, A.M. Shumway, P.M. Powers, C.S. Mueller, M.P. Moschetti, A.D. Frankel, Y. Zeng, M.L. Zoback, O.S. Boyd, E.H. Field et al. , *Earthquake Spectra* **36** (2019), 5.

[168] S. Peyrat, K. Olsen und R. Madariaga, *Journal of Geophysical Research: Solid Earth* **106** (2001), 26467.

[169] S. Peyrat und K.B. Olsen, *Geophysical Research Letters* **31** (2004), L05608.

[170] M. Pischiutta, A. Akinci, E. Tinti und A. Herrero, *Geophysical Journal International* **224** (2021), 1753.

[171] A. Pitarka, A. Akinci, P. De Gori und M. Buttinelli, *Bulletin of the Seismological Society of America* **112** (2021), 262.

[172] A. Pizzi, A. Di Domenica, F. Gallovič, L. Luzi und R. Puglia, *Tectonics* **36** (2017), 2370.

[173] Planet. *Planet data application program interface: in space for life on Earth*, 2019.

[174] A. Plesch, *Harvard University* (2021).

[175] A. Plesch, J.H. Shaw, Z.E. Ross und E. Hauksson, *Bull. Seismol. Soc. Am.* **110** (2020), 1818–1831.

[176] D.J. Ponti, J.L. Blair, C.M. Rosa, K. Thomas, A.J. Pickering, S. Akciz, S. Angster, J. Avouac, J. Bachhuber, S. Bacon, N. Barth, S. Bennett, K. Blake, S. Bork, B. Brooks, T. Bullard, P. Burgess, C. Chupik, T. Dawson, M. DeFrisco, J. Delano, S. DeLong, J. Dolan, A. Donnellan, C. DuRoss, T. Ericksen, E. Frost, G. Funning, R. Gold, N. Graehl, C. Gutierrez, E. Haddon, A. Hatem, J. Helms, J. Hernandez, C. Hitchcock, P. Holland, K. Hudnut, K. Kendrick, R. Koehler, O. Kozaci, T. Ladinsky, R. Leeper, C. Madugo, M. Mareschal, J. McDonald, D. McPhillips, C. Milliner, D. Mongovin, A. Morelan, S. Nale, J. Nevitt, M. O'Neal, B. Olson, M. Oskin, S. Padilla, J. Patton, B. Philibosian, I. Pierce, C. Pridmore, N. Roth, D. Sandwell, K. Scharer, G. Seitz, D. Singleton, B. Smith-Konter, E. Spangler, B. Swanson, J.T. Jobe, J. Treiman, F. Valencia, J. Vanderwal, A. Williams, X. Xu, J. Zachariasen, J. Zimmerman und R. Zinke, *Seismol. Res. Lett.* **91** (2020), 2942–2959.

[177] M. Porreca, G. Minelli, M. Ercoli, A. Brobia, P. Mancinelli, F. Cruciani, C. Giorgetti, F. Carboni, F. Mirabella, G. Cavinato, A. Cannata, C. Pauselli und M.R. Barchi, *Tectonics* **37** (2018), 1116.

[178] W. Power und T. Tullis, *Journal of Geophysical Research* **96** (1991), 415.

[179] J. Premus, F. Gallovič und J.P. Ampuero, *Sci. Adv.* **8** (2022), eabq2536.

[180] J. Premus, F. Gallovič, L. Hanyk und A. Gabriel, *Seismological Research Letters* **91** (2020), 2881.

[181] Q. Qiu, S. Barbot, T. Wang und S. Wei, *Bull. Seismol. Soc. Am.* **110** (2020), 1701.

[182] T. Ragon, A. Sladen und M. Simons, *Geophysical Journal International* **214** (2018), 1174.

[183] M.D. Ramos, J.C. Neo, P. Thakur, Y. Huang und S. Wei, *Bull. Seismol. Soc. Am.* (2020).

[184] S. Rettenberger, O. Meister, M. Bader und A.A. Gabriel: *ASAGI: A Parallel Server for Adaptive Geoinformation. ASAGI: A Parallel Server for Adaptive Geoinformation*, In *Proceedings of the Exascale applications and Software Conference 2016*EASC '16. ACM, New York, NY, USA (2016) Seiten 2:1–2:9.

[185] J. Ripperger, J.P. Ampuero, P.M. Mai und D. Giardini, *Journal of Geophysical Research: Solid Earth* **112** (2007), 4311.

[186] J. Ripperger, P.M. Mai und J.P. Ampuero, *Bulletin of the Seismological Society of America* **98** (2008), 1207.

[187] A.J. Rodgers, A. Pitarka, R. Pankajakshan, B. Sjögreen und N.A. Petersson, *Bulletin of the Seismological Society of America* **110** (2020), 2862.

[188] A.M. Rodriguez Padilla, M.A. Quintana, R.M. Prado, B.J. Aguilar, T.A. Shea, M.E. Oskin und L. Garcia, *Seismol. Res. Lett.* **93** (2021), 494.

[189] Z.E. Ross, B. Idini, Z. Jia, O.L. Stephenson, M. Zhong, X. Wang, Z. Zhan, M. Simons, E.J. Fielding, S.H. Yun, E. Hauksson, A.W. Moore, Z. Liu und J. Jung, *Science* **366** (2019), 346.

[190] D. Roten, K.B. Olsen, S.M. Day, Y. Cui und D. Fäh, *Geophysical Research Letters* **41** (2014), 2769.

[191] D. Roten, K.B. Olsen, S.M. Day, Y. Cui und D. Fäh, *Geophys. Res. Lett.* **41** (2014), 2769.

[192] D. Roten, K.B. Olsen und J.C. Pechmann, *Bulletin of the Seismological Society of America* **102** (2012), 2008.

[193] A.M. Rubin und J.P. Ampuero, *J. Geophys. Res. Solid Earth* **110** (2005), B11312.

[194] R. Ruggieri, M.M. Scuderi, F. Trippetta, E. Tinti, M. Brignoli, S. Mantica, S. Petroselli, L. Osculati, G. Volontè und C. Collettini, *Tectonophysics* **807** (2021), 228811.

[195] A. Ruina, *J. Geophys. Res. Solid Earth* **88** (1983), 10359.

[196] S. Ruiz und R. Madariaga, *Geophysical Research Letters* **38** (2011), 2011GL047147.

[197] M. Sambridge, *Geophysical Journal International* **196** (2013), 357.

[198] M. Sambridge und K. Mosegaard, *Reviews of Geophysics* **40** (2002), 3.

[199] W.H. Savran und K.B. Olsen, *Journal of Geophysical Research: Solid Earth* **125** (2020), 1.

[200] SCEDC. *Southern California Earthquake Data Center*, 2013.

[201] K.M. Scharer, G.P. Biasi und R.J. Weldon II, *J. Geophys. Res. Solid Earth* **116** (2011), B12111.

[202] J. Schmedes, R.J. Archuleta und D. Lavallée, *Journal of Geophysical Research* **115** (2010), B03304.

[203] L. Scognamiglio, E. Tinti, E. Casarotti, S. Pucci, F. Villani, M. Cocco, F. Magnoni, A. Michelini und D. Dreger, *Journal of Geophysical Research: Solid Earth* **123** (2018), 2943.

[204] M.M. Scuderi, A.R. Niemeijer, C. Collettini und C. Marone, *Earth and Planetary Science Letters* **369-370** (2013), 220.

[205] D.R. Shelly, *Seismol. Res. Lett.* **91** (2020), 1971–1978.

[206] Q. Shi und S. Wei, *Geophys. Res. Lett.* **47** (2020), e2020GL089827.

[207] Z. Shi und S.M. Day, *Journal of Geophysical Research: Solid Earth* **118** (2013), 1122.

[208] K. Shimizu, Y. Yagi, R. Okuwaki und Y. Fukahata, *Geophysical Journal International* **220** (2020), 1055.

[209] P. Somerville, K. Irikura, R. Graves, S. Sawada, D. Wald, N. Abrahamson, T. Iwasaki, T. Kagawa und N. Smith, *Seismological Research Letters* **70** (1999), 59.

[210] P. Spudich, M. Guatteri, K. Otsuki und J. Minagawa. *Use of Fault striations and Dislocation Models to Infer Tectonic Shear Stress during the 1995 Hyogo-ken Nanbu (Kobe) Earthquake*. Technischer Bericht 2, 1998.

[211] J. Suppe, *J. Struct. Geol.* **69** (2014), 481.

[212] S. Takemura, T. Furumura und T. Maeda, *Geophysical Journal International* **201** (2015), 459.

[213] R. Tang, J. Yuan und L. Gan, *Geophysical Research Letters* **48** (2021), e2020GL091621.

[214] T. Taufiqurrahman, A.A. Gabriel, T. Ulrich, L. Valentova und F. Gallovič, *Geophys. Res. Lett.* (2022), 31.

[215] E. Tinti, E. Casarotti, T. Ulrich, T. Taufiqurrahman, D. Li und A.A. Gabriel, *Earth and Planetary Science Letters* **576** (2021), 117237.

[216] E. Tinti, M. Cocco, E. Fukuyama und A. Piatanesi, *Geophysical Journal International* **177** (2009), 1205.

[217] E. Tinti, E. Fukuyama, A. Piatanesi und M. Cocco, *Bulletin of the Seismological Society of America* **95** (2005), 1211.

[218] E. Tinti, L. Scognamiglio, A. Michelini und M. Cocco, *Geophysical Research Letters* **43** (2016), 10745.

[219] E. Tinti, P. Spudich und M. Cocco, *Journal of Geophysical Research* **110** (2005), B12303.

[220] S. Toda und R.S. Stein, *Bull. Seismol. Soc. Am.* **110** (2020), 1765–1780.

[221] E. Tondi, D. Jablonská, T. Volatili, M. Michele, S. Mazzoli und P.P. Pierantoni, *GSA Bulletin* **133** (2020), 1679.

[222] S. Tung und T. Masterlark, *Bulletin of the Seismological Society of America* **108** (2018), 553.

[223] C. Twardzik, S. Das und R. Madariaga, *Journal of Geophysical Research: Solid Earth* **119** (2014), 7010.

[224] T. Ulrich, A.A. Gabriel, J.P. Ampuero und W. Xu, *Nature Communications* **10** (2019), 1.

[225] T. Ulrich, A.A. Gabriel und E.H. Madden, *Nature Geosci.* **15** (2022), 67.

[226] T. Ulrich, S. Vater, E.H. Madden, J. Behrens, Y. van Dinther, I. van Zelst, E.J. Fielding, C. Liang und A.A. Gabriel, *Pure Appl. Geophys.* **176** (2019), 4069–4109.

[227] T. Ulrich, S. Vater, E.H. Madden, J. Behrens, Y. van Dinther, I. van Zelst, E.J. Fielding, C. Liang und A.A. Gabriel, *Pure and Applied Geophysics* **176** (2019), 4069.

[228] C. Uphoff und M. Bader: *Generating high performance matrix kernels for earthquake simulations with viscoelastic attenuation. Generating high performance matrix kernels for earthquake simulations with viscoelastic attenuation*, In *2016 International Conference on High Performance Computing & Simulation (HPCS)*. IEEE (2016) Seiten 908–916.

[229] C. Uphoff, D.A. May und A.A. Gabriel, *Geophys. J. Int.* (2022).

[230] C. Uphoff, S. Rettenberger, M. Bader, E. Madden, T. Ulrich, S. Wollherr und A.A. Gabriel: *Extreme scale multi-physics simulations of the tsunamigenic 2004 Sumatra megathrust earthquake. Extreme scale multi-physics simulations of the tsunamigenic 2004 Sumatra megathrust earthquake*, In *Proceedings of the International Conference for High Performance Computing, networking, Storage and Analysis, SC 2017*. (2017).

[231] Valentová, F. Gallovič und S. Hok, *Bulletin of the Seismological Society of America* **111** (2021), 2559.

[232] S. Valkaniotis. *Subpixel optical correlation co-seismic offsets for the Mw 6.4 and Mw7.1 Ridgecrest, California earthquakes, from Copernicus Sentinel 2 data*, 2019.

[233] A. Verdecchia und S. Carena, *Tectonics* **34** (2015), 213.

[234] A. Verdecchia und S. Carena, *Tectonics* **35** (2016), 1793.

[235] R.C. Viesca und D.I. Garagash, *Nature Geoscience* **8** (2015), 875.

[236] D.J. Wald und T.H. Heaton, *Bull. Seismol. Soc. Am.* **84** (1994), 668.

[237] R.J. Walters, L.C. Gregory, L.N. Wedmore, T.J. Craig, K. McCaffrey, M. Wilkinson et al. , *Earth and Planetary Science Letters* **500** (2018), 1.

[238] K. Wang, D.S. Dreger, E. Tinti, R. Bürgmann und T. Taira, *Bulletin of the Seismological Society of America* **110** (2020), 1603.

[239] X. Wang und Z. Zhan, *J. Geophys. Res. Solid Earth* **124** (2020), e2020JB019577.

[240] M. Wei, Y. Kaneko, Y. Liu und J.J. McGuire, *Nature Geosci.* **6** (2013), 566.

[241] H. Weng und H. Yang, *Journal of Geophysical Research: Solid Earth* **123** (2018), 6658.

[242] E.A. Wirth, A.D. Frankel, N. Marafi, J.E. Vidale und W.J. Stephenson, *Bulletin of the Seismological Society of America* **108** (2018), 2370.

[243] K.B. Withers, M.P. Moschetti und E.M. Thompson, *Geophysical Research Letters* **47** (2020), e2019GL086690.

[244] K.B. Withers, K.B. Olsen, S.M. Day und Z. Shi, *Bulletin of the Seismological Society of America* **109** (2018), 229.

[245] K.B. Withers, K.B. Olsen, Z. Shi und S.M. Day, *Bulletin of the Seismological Society of America* **109** (2018), 212.

[246] S. Wollherr, A.A. Gabriel und P.M. Mai, *Journal of Geophysical Research: Solid Earth* **124** (2019), 6666.

[247] S. Wollherr, A.A. Gabriel und C. Uphoff, *Geophysical Journal International* **214** (2018), 1556.

[248] Y. Xie, H. Bao und L. Meng, *J. Geophys. Res. Solid Earth* **126** (2021), e2020JB021396.

[249] X. Xu, D.T. Sandwell und B. Smith-Konter, *Seismol. Res. Lett.* **91** (2020), 1979–1985.

[250] Y. Yagi und Y. Fukahata, *Geophysical Journal International* **186** (2011), 711.

[251] T. Yamashita, *Geophysical Journal International* **143** (2000), 395.

[252] J. Yang, H. Zhu und D. Lumley, *Geophys. Res. Lett.* **47** (2020), e2020GL087181.

[253] W. Yang und E. Hauksson, *Geophys. J. Int.* **194** (2013), 100.

[254] J. Yin und M.A. Denolle, *Geophys. J. Int.* **217** (2019), 729.

[255] H. Yue, J. Sun, M. Wang, Z. Shen, M. Li, L. Xue, W. Lu, Y. Zhou, C. Ren und T. Lay, *Earth Planet Sci. Lett.* **570** (2021), 117066.

[256] Y. Zeng und Z. Shen, *Bull. Seismol. Soc. Am.* **106** (2016), 766.